Calcium carbonate-naphthoquinone hybrid pigments inspired by biomineral coloration in sea urchins

Vaskar Sardhalia

Sorbonne Université

Doctoral School 397: Physics and Chemistry of Materials

Laboratoire de Chimie de la Matière Condensée de Paris (LCMCP)

Calcium carbonate-naphthoquinone hybrid pigments inspired by biomineral coloration in sea urchins

by Vaskar Sardhalia

Degree of Doctor of Philosophy

Supervised by Dr. Marie Albéric and Prof. Thierry Azaïs

Presented and defended at Sorbonne University, on 15th December 2023

To a committee composed of:

Carole Perry	Professor, Nottingham Trent University	Referee
Christèle Combes	Professor, Institut National Polytechnique de Toulouse	Referee
Boaz Pokroy	Professor, Technion - Israel Institute of Technology, Haifa	Examiner
Yael Politi	Professor, Technische Universität Dresden	Examiner
Laurent Billon	Professor, Université de Pau et des Pays de l'Adour	Examiner
Nadine Nassif	Director of Research, CNRS, LCMCP	President
Thierry Azaïs	Professor, Sorbonne Université, LCMCP	Co-supervisor
Marie Albéric	Researcher, CNRS, LCMCP	Supervisor

Formal Acknowledgments and Project Contributions

The research conducted in this thesis encompasses collaborative endeavors with colleagues in the field, conducted under the supervision of Professor Dr. Thierry Azaïs and CNRS Researcher Dr. Marie Albéric from LCMCP at Sorbonne University. Throughout the subsequent chapters, Vaskar Sardhalia, the author of this thesis, offers comprehensive elucidations of each contribution to these collaborative projects. Unless expressly indicated otherwise, the content presented within this thesis is solely attributable to Vaskar Sardhalia.

In collaboration with Dr. Shahrouz Amini at the Max Planck Institute for Colloids and Interfaces, we conducted in-situ colorimetry measurements, FIB-SEM, and Raman spectroscopy analyses. STEM EELS analysis was performed in collaboration with Dr. Marta de Frutos from LPS, University Paris-Saclay. We obtained FEG-SEM micrographs with assistance from David Montero at Sorbonne University. Mathieu Fregnaux performed XPS measurements and subsequently analyzed by Dr. Anne Vallée at Institut Lavoisier de Versailles, France. In addition, lamella section preparation on an ultramicrotome and STEM analysis were executed by Chakib Djediat at Muséum National d'Histoire Naturelle, Paris, France. For solution state NMR experiments, we had the privilege of collaborating with Dr. Isabelle Correia at Sorbonne University. Dyeing experiments on different textiles were performed in collaboration with by Tony Jouanneau T. founder of ATELIER SUMBIOSIS, a lab merging science and textiles.

Personal Acknowledgments

First and foremost, this project is the outcome of collaborative efforts by numerous individuals whose essential contributions have made it all possible. I wish to convey my profound and heartfelt appreciation to my supervisors, Dr. Thierry Azaïs and Dr. Marie Albéric, for granting me the opportunity to engage in research at the LCMCP, Sorbonne University. Their patient mentorship, invaluable guidance, positive attitude, and friendly demeanor, combined with their unwavering dedication, have not only inspired me but also made my work highly productive and enjoyable. Having the opportunity to work under their tutelage has been an exceptional privilege. It's a testament to their expertise and mentorship and a rare chance to learn and grow in a unique enviro nment.

I would like to extend my heartfelt gratitude to all the individuals at LCMCP and our collaborative institutions who have been instrumental in assisting me with various experiments, their meticulous analysis, and the invaluable feedback and insights they've provided. Your expertise, dedication, and willingness to lend a helping hand have played a significant role in the success of my work. I am truly fortunate to have had such a supportive and knowledgeable network of colleagues and collaborators. Your contributions have been indispensable, and I am deeply thankful for your unwavering assistance.

During my PhD journey, the friends (Tristan, Ieva, Claudio, Camille, Amel, Mathilda) I made have been like rays of sunshine on cloudy days. Their unwavering support, shared laughter, and stupid talk sessions have made the academic challenges bearable and added a warmth and sense of camaraderie to this incredible adventure. These friendships have been essential to my PhD experience, and I'm endlessly grateful for the bonds I have formed.

I want to express my heartfelt gratitude to all the wonderful administration people who've been there for me throughout my PhD journey. Your help and, of course, the many shared jokes, especially with our delightful Hélène, have made my stay at LCMCP so much more enjoyable.

I am immensely grateful to my parents for their love and support. Without the unwavering support of my family, the past three years of my life would not have been as wonderful. I also want to express my gratitude to my brother for his support and constant support. I extend my thanks to my friends in India for constantly pushing me and helping me realize my potential.

Last but not least, I send lots of love to my Happy family (Master’s) for making the past five years colorful and filling them with beautiful memories.

Table of Contents

Abbreviations

ACC	Amorphous Calcium Carbonate
ACC.H_2O	Amorphous Calcium Carbonate, hydrated
CA	Carbonic anhydrase
CF	Calcifying Fluid
CCHH	Calcium Carbonate Hemihydrate
DIC	Dissolved Inorganic Carbon
DTA	Differential Thermal Analysis
ECF	Extracellular calcifying fluid
ECM	Extracellular calcifying medium
FEG-SEM	Field Emission Gun Scanning Electron Microscope
FIB-SEM	Focused Ion Beam Scanning Electron Microscope
HETCOR	Heteronuclear Correlation Spectroscopy
IA	Ion Attachment
ICF	Intracellular Calcifying Fluid
ISE	Ion Selective Electrode
MAS	Magic Angle Spinning
NMR	Nuclear Magnetic Resonance
PA	Particle Attachment
PDF	Pair Distribution Function Analysis
PHNQ	Polyhydroxylated Naphthoquinone
PM	Physical Mixing
SEM	Scanning Electron Microscope
ss NMR	Solid-State Nuclear Magnetic Resonance
STEM	Scanning Transmission Electron Microscope
STEM-EELS	Scanning Transmission Electron Microscope Electron energy Loss Spectroscopy
VD/ADM	Vapour Diffusion/Ammonium carbonate Degradation Method
UV-vis	Ultraviolet – visible
XRD	X-rays diffraction

Δ [Ca], ΔpH, ΔDIC, $\Delta\Omega_{CaCO3}$ Difference observed when comparing the CF with seawater, in calcium concentration, pH, DIC, and supersaturation with respect to relevant $CaCO_3$ mineral

Introduction

Color is a ubiquitous trait intertwined with numerous interactions in the natural world, such as communication, mating, camouflage, and warning signals among living organisms. It serves as vital visual cues that have evolved to fulfill specific functions, playing a crucial role in shaping various ecological relationships such as mimicry, territorial displays, thermoregulation, and more (Stuart-Fox and Moussalli, 2009). More specifically, many mineralizing organisms are consistently engaged in the production of a multitude of vibrantly colored biominerals, which can be found throughout the natural world, and the phenomenon wherein living entities generate minerals is known as biomineralization (Lowenstam and Weiner, 1989).

In biominerals, colors can arise from: 1) structural coloration, where nanostructures (1-100 nm) interact with light to create different colors (Kinoshita and Yoshioka, 2005); 2) pigmentation, caused by organic pigments incorporated into the mineral phase, which also contributes to diverse colors in biominerals (Goodwin and Srisukh, 1950; Shikov *et al*., 2018; Williams, 2017); 3) elemental impurities (Ti, V, Cr, Mn, Fe, Co, Ni, Cu, *etc*.) influence coloration by absorbing and emitting light at distinct wavelengths (Fritsch and Rossman, 1987). The aforementioned processes lead to the rich tapestry of colors seen in biominerals such as the ones produced by invertebrates, *e.g.*, sea urchins and mollusks. In addition to beauty, some organic pigments have been shown to function as protection from UV (polyhydroxylated

naphthoquinones in sea urchins), defense against fouling organisms (pigment variolins, discorhabdins, isoquinoline metabolite in sponges), predators (Bandaranayake, 2006) and even enhancing mechanical properties (Williams, 2017).

Sea urchin biominerals illustrate Nature's capacity to create an extensive spectrum of colors by utilizing a specific group of organic compounds called polyhydroxylated naphthoquinones (PHNQs) (Anderson *et al*., 1969). Synthesized within one type of the immune coelomocytes, the so-called red-spherule cells, about 40 different PHNQ molecules (*e.g.,* echinochrome A, spinochromes A, B, C, D, and E) have already been identified in different sea urchin species (Vasileva *et al*., 2021). Sea urchin biominerals consist of calcium carbonate ($CaCO_3$) in the form of calcite enriched with Mg (2-12 mol%) (Magdans and Gies, 2004) and a small fraction (approximately 1-2 wt.%) (Kanold *et al*., 2015) of intracrystalline organic molecules, including lipids, proteins, glycoproteins, polysaccharides, and PHNQs. It is intriguing to note that PHNQs have inherent light sensitivity. However, when encapsulated within calcite, they remarkably demonstrate stability against sunlight and oxidizing agent exposure like sodium hypochlorite (NaClO). This property paved the way for harnessing colored biominerals as a source of inspiration to engineer stable biohybrid pigments.

These biohybrid alternatives could provide an alternative to synthetic dyes and chemicals (Lellis *et al*., 2019). Historical hybrid pigments include cave frescoes (Iron oxide + aluminosilicate clays + fat) and the famous Maya blue pigment (Morris *et al*., 1931). This ancient blue pigment, composed of indigo (organic) and palygorskite (mineral), boasts enduring color and photostability in Mesoamerican art, proposed to be due to indigo molecules displacing water within the channels and assuming stable positions (Fois *et al*., 2003).

To enhance the durability of organic dyes, a promising approach has emerged in the form of organic-inorganic hybrid pigments, engineered to resist the fading effects of sunlight exposure. These hybrids rely on matrices like silica and clays to encapsulate and shield organic dyes from environmental stressors. The synthesis of these innovative pigments is either by sol-gel chemistry (Schottner, 2001) or solid-state grinding (Ghannam *et al*., 2005). The former involves two primary reactions: precursor hydrolysis in acidic or basic conditions, followed by the polycondensation of hydrolyzed products. This method creates mass-colored, photo-stable amorphous materials by meticulously blending pigment components in a solution that undergoes controlled chemical reactions to produce a stable, homogeneous substance. In contrast, “solid-state grinding" yields surface-colored crystalline pigments with relatively

lower photo-stability. An intriguing facet of this research, as mentioned above, is the ability of adult sea urchins to produce mass-colored crystalline biominerals, exhibiting impressive photostability.

Therefore, it is anticipated that the integration of PHNQs and commercially available natural naphthoquinones during ACC crystallization will result in significant inorganic-organic interactions resulting in a comprehensive range of new bio-based hybrid colorants offering a diverse palette. This research offers a pathway to environmentally friendly and durable pigments and deepens our understanding of the intricate relationship between living organisms and their mineralized structures.

Apart from giving color to sea urchins, PHNQs have demonstrated antioxidant, antimicrobial, and anti-inflammatory effects (Hou *et al*., 2018b; Kim *et al*., 2015) through combating bacterial infections, reducing inflammation, and protecting against cardiovascular diseases and eye conditions, showing therapeutic potential, especially for echinochrome A which belongs to PHNQS family found in sea urchins.

The potential interplay between biomineralization and pigmentation mechanisms has been suggested in many studies regarding mollusks (Bauchau, 2001; Cusack *et al*., 1992; Sun *et al*., 2015). However, for sea urchins, only one study by (Zito *et al*., 2015) indicated that pigment production and biomineralization pathways might be connected as they share one common enzyme, carbonic anhydrase. In parallel, an earlier study (Towe, 1967) mentioned that "organic pigments are irrelevant to biomineralization, also obviously trapped within the crystal during its growth". Therefore, the exact role or the involvement of organic pigments in biomineralization remains unknown.

In contrast, the formation of biogenic calcite in sea urchins has been extensively studied from the cellular pathways to mineral deposition ((Kahil *et al*., 2020; Politi *et al*., 2004). In adult sea urchin spines, calcite is formed through the initial deposition of hydrated amorphous calcium carbonate (ACC) nanoparticles that transform into anhydrous ACC before crystallizing (Albéric *et al*., 2019; Politi *et al*., 2004). Thermodynamically and kinetically unstable under ambient conditions, the temporary stabilization of ACC has been ascribed to the presence of macromolecules and Mg^{2+} ions (Raz *et al*., 2003). During biomineralization processes, likely during ACC crystallization, some of these macromolecules together with Mg^{2+} ions, are entrapped in the final mineral structure. These organic molecules were shown to precisely

control the polymorphism, morphology, size of the crystalline $CaCO_3$ blocks (J. Aizenberg *et al*., 1995; Albeck *et al*., 1996) and seemingly also contribute towards the color of the biominerals.

Sea urchin mineralized tissues, particularly their spines, present a wide range of colors from green to purple, even within the same species and within one single spine. For example, *Paracentrous lividus* green spines present a purple tip most of the time (Goodwin and Srisukh, 1950). It is, however, not clear if those differences in colors among and within individuals originate from different PHNQs composition or other mechanisms such as specific organic-inorganic interactions or different developmental stages, as already suggested (Goodwin and Srisukh, 1950). The latter is potentially related to the different extent of ACC crystallization.

In this context, this doctoral research aims to:

1) elucidate the **physicochemical mechanisms** that underlie the chromatic manifestation displayed by sea urchin spines known to be formed through **ACC precursors** likely in the presence of **naphthoquinone pigments** and,

2) better understand the **processes that drive the incorporation of naphthoquinones into calcite** and result in the formation of biogenic hybrid pigments with stable colors,

3) propose bio-inspired and bio-sourced pigments for the coloring industry, particularly textile finishing.

In order to do so, we studied:

i) the **effect of naphthoquinone on ACC composition, local structure, stability, and crystallization** pathways into calcite and,

ii) the **multi-level organic-inorganic interactions** present in the bioinspired hybrid pigments.

A bio-inspired synthesis was considered here that entails forming ACC nanoparticles in the presence of biogenic PHNQs previously extracted from sea urchin spines and commercially available natural naphthoquinone molecules (naphthazarin, lawsone, juglone).

The content of this thesis has been systematically arranged into five chapters, with a conclusion and perspectives section, each serving a specific purpose and contributing to the overall flow and organization of the thesis.

Chapter I: State of the art is dedicated to a comprehensive bibliographical analysis of the accessible data about $CaCO_3$ biomineralization with a focus on ACC precursors, biomineral pigmentation, giving most attention to sea urchins and biohybrid pigments. This chapter also explores synthetic $CaCO_3$ formation, crystallization mechanisms, and the impact of additives and environmental conditions.

Chapter II: Methodology consolidates all the preparatory, technical procedures, and experimental methodologies employed throughout this thesis.

Chapter III: Role of naphthazarin on ACC formation and crystallization explores the role of readily available natural naphthoquinone pigments in providing ACC's coloration, composition, structure, and ability to control crystallization kinetics. In particular, we demonstrate the dynamic evolution of ACC's color throughout its formation and crystallization process. This unveils potential mechanisms that might also contribute to the pigmentation of biominerals formed through ACC precursors.

Chapter IV: Multi-scale investigation of naphthazarin-calcite interfaces comprehensively examines multiple facets of naphthazarin-calcite pigments obtained from different syntheses. It studies naphthazarin's influence on crystal morphology and investigates the intricate mechanisms underlying its incorporation. The chapter analyzes the distribution patterns of naphthazarin within calcite structures from micron to atomic scales, providing a comprehensive understanding of naphthazarin's role in shaping the properties of the resulting crystalline hybrid pigments.

Chapter V: $CaCO_3$-naphthoquinone biohybrid pigments deals with studying lawsone, juglone, and biogenic PHNQ molecules extracted from sea urchin spines. The focus is on how these molecules affect ACC color and crystallization, the shape and structure of calcite. By examining this, the chapter provides insights into why certain PHNQ molecules are preferred for incorporation into sea urchin spines.

The **conclusion** summarizes the findings and insights gained during this work and the perspectives that present future research and potential areas of exploration.

1

State of the art

This chapter reviews some of our current knowledge about biogenic and synthetic calcium carbonate ($CaCO_3$) systems, colors in the living world, (poly)hydroxylated naphthoquinone pigments in sea urchins and plants, and synthetic hybrid pigments. In particular, it delves into the world of biominerals, mainly focusing on the diversity and the formation of $CaCO_3$ structures and morphologies observed in shells and skeletons of different species, explicitly focusing on sea urchin spines. This chapter also explores the intricate mechanisms involved in the crystallization of amorphous calcium carbonate (ACC) into calcite during biomineralization processes in sea urchins. After describing the different origins of colors in the living world, including pigmentation mechanisms, biomineral pigmentation in sea urchins involving polyhydroxylated naphthoquinones is also addressed as a source of inspiration for this doctoral research work. In addition, synthetic $CaCO_3$ systems are extensively explored, focusing on syntheses involving ACC formation and crystallization. The role of organic molecules on ACC stability, crystallization mechanisms, calcite crystal morphology, and atomic structure is particularly reviewed. Lastly, dyes and pigments, including

naphthoquinones found in plant and hybrid pigments, are described. The latter provides great stability, has a smaller impact on the environment, might be compatible with living systems, and can imitate natural colors, making them suitable for various uses such as textile finishing.

1.1. Biomineralization and biominerals

Biominerals are minerals formed by living organisms through complex biological processes, referred to as biomineralization (Mann, 1988; Lowenstam and Weiner, 1989). These processes control the deposition of inorganic and organic materials to create solid structures. Understanding the mechanisms of $CaCO_3$ biomineral formation is, for example, essential for interpreting its evolutionary significance, environmental impact, sensitivity to past and future environmental changes but also for designing bio-inspired research aiming at developing new materials (Gilbert *et al*., 2022).

1.1.1. Mechanistic models for biomineralization

Biominerals were first described as being either formed by biologically induced or organic-matrix-mediated mineralization (Lowenstam, 1981). Biologically induced mineralization occurs externally to cells or on their surfaces, commonly observed in algae and most bacterial species. On the other hand, organic-matrix-mediated mineralization, later termed biologically controlled mineralization, is prevalent in many animals (Lowenstam, 1981). An essential characteristic of biologically controlled mineralization is that it takes place within well-defined and confined spaces or compartments (Bazylinski and Frankel, 2003; Veis, 2003).

Later, some researchers sought to consolidate all known biomineralization mechanisms into universally applicable models, emphasizing commonalities among diverse species.

Based on several seminal results in the field of biomineralization from the 1950s to 2011 (Weiner and Addadi, 2011) proposed a general model for mineralization pathways in various organisms involving (i) an extracellular matrix, (ii) a vesicle-confined space (syncytium), and (iii) the formation of mature mineralized elements within a vesicle inside the cell (Figure 1.1). According to this model, eight main steps (1-8), labeled in Figure 1.1, are involved in the crystallization pathways. Extracellular matrix mineralization occurs, for example, in radial foraminifera shell formation, bone, dentin, enamel, mollusk shells, and crustacean cuticles (Figure 1.1i). Mineralization occurs within a large vesicle or syncytium, as found in

echinoderms like the sea urchin larval spicule (Figure 1.1ii). In the case of pathway iii, the mature mineralized product might remain within the cell (*e.g.*, guanine crystals in fish skin) or be moved to the cell surface (*e.g.*, Coccolithophoridae and miliolid foraminifera).

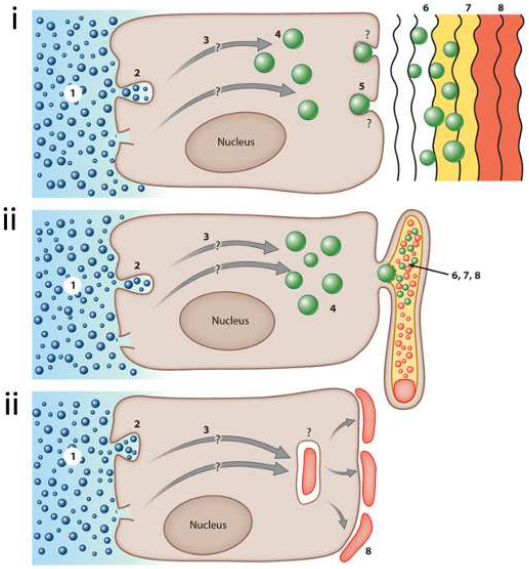

Figure 1.1. Illustrations of general crystallization pathways encompassing (i) an extracellular matrix, (ii) confinement within vesicles (syncytium), and (iii) the development of fully mineralized elements within intracellular vesicles (image adapted from (Weiner and Addadi, 2011)).

A more recent model introduced by (Gilbert *et al*., 2022) describes the $CaCO_3$ crystallization pathways in five main steps (1-5) occurring in marine organisms, including foraminifera, coccolithophorids, corals, echinoderms, brachiopods, and mollusks (Figure 1.2).

Step 1 gathers calcium (Ca^{2+}) and dissolved inorganic carbon (DIC) into the internal and external cellular environments while removing protons. Carbon dioxide (CO_2) is also acquired by passive diffusion through cell and vesicle membranes and through mitochondrial respiration, which leads to CO_2 partial diffusion into seawater, into the external cellular fluid (ECF), and into the internal cellular fluid (ICF). Part of this CO_2 is quickly transformed into bicarbonate ions (HCO_3^-), thanks to the action of carbonic anhydrase (CA) in the cytosol, the ICF, and the ECF and further transforms into carbonate ions (CO_3^{2-}) due to the higher pH of these environments. Carbonate ions subsequently bind to calcium (Ca^{2+}). In addition to calcium and carbonate ions, organic molecules produced by the organism are also introduced into

vesicles and the ECF, forming the organic framework enclosed within the biomineral. Like Weiner's model, biomineral formation occurs in a privileged space, which may be intra- or extracellular and is separated from but partly open to seawater, and its chemical composition is biologically controlled. In addition, this model suggests that the ICF is either endocytosed seawater (Figure 1.2 step 1a), as observed in foraminiferans but not in corals, or endocytosed ECF (Figure 1.2 step 1b), as observed in corals.

Step 2 involves the release of solid particles consisting of hydrated amorphous calcium carbonate (ACC-H_2O) into the extracellular fluid (Figure 1.2 step 2) through exocytosis. The presence of ACC-H_2O was first reported in sea urchin larvae (Politi *et al*., 2008; Gong *et al*., 2012), as detailed in Section 1.1.3. In steps 3 and 4, these ACC particles, along with the Ca^{2+} and CO_3^{2-} ions that are present, attach to the leading edge of the growing mineral structure (Figure 1.2 steps 3 and 4). Finally, step 5 consists of ACC crystallization (Beniash *et al*., 1997; Gong *et al*., 2012; Mass *et al*., 2017; Schmidt *et al*., 2022) through particle attachment (PA) (De Yoreo *et al*., 2015; Gong *et al*., 2012) and ion attachment (IA) (Gal *et al*., 2018, 2016; Walker *et al*., 2020). Depending on the specific conditions, the crystalline form can be calcite, aragonite, or vaterite. Finally, both particle attachment (PA) (De Yoreo *et al*., 2015; Gong *et al*., 2012) and ion attachment (IA) (Gal *et al*., 2018, 2016; Walker *et al*., 2020) are proposed to occur at the front of the growing mineral structure, as indicated by PA + IA (Figure 1.2).

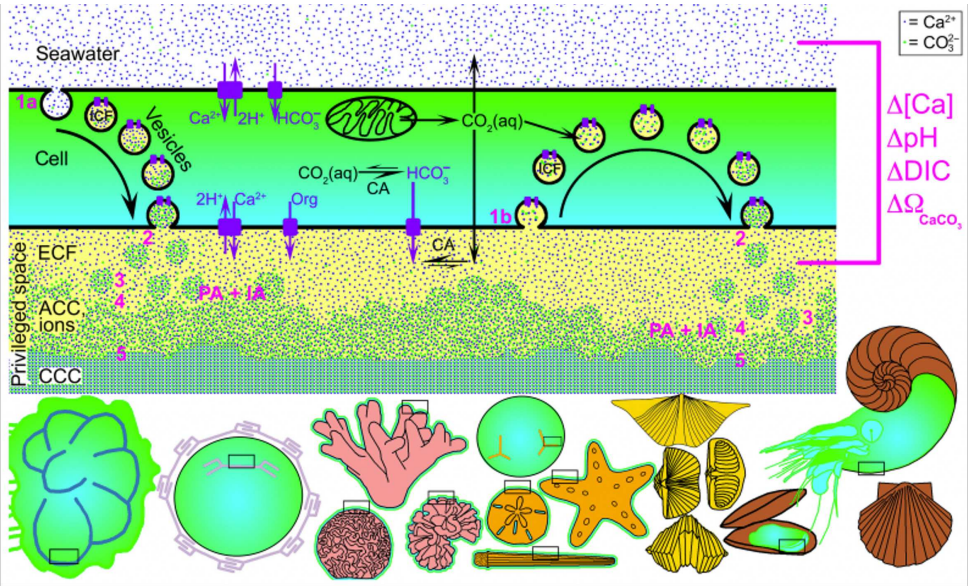

Figure 1.2. An integrated model for the molecular mechanisms of $CaCO_3$ biomineralization in some marine organisms with different steps (1-5) (image adapted from (Gilbert *et al*., 2022)).

1.1.2. Biomineral function, composition, structure and properties

Biominerals are composite materials formed by living organisms, consisting of both an organic and a mineral phase (Aizenberg *et al*., 2005; Fratzl *et al*., 2004; Fratzl and Weinkamer, 2007), and are thus also called organic-inorganic hybrid materials (Chujo, 2007; García-Martínez and Collar, 2021). Hybrid materials consist of a minimum of two components, typically organic and inorganic entities, intricately blended at the molecular or nanoscopic level. The wide array of compositions and structures in these materials engenders diverse physicochemical properties that extend beyond a mere amalgamation of the individual precursor traits depending upon the interaction between organic and inorganic components (Figure 1.3) (Chujo, 2007; Unterlass, 2016; Zhu and Yuan, 2015).

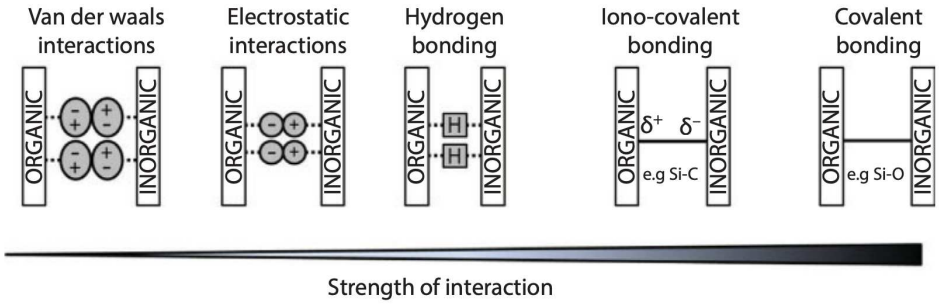

Figure 1.3. The relative strength of typical interactions observed in hybrid materials (image adapted from (Saad *et al*., 2018)).

In particular, biominerals can be both amorphous or/and crystalline and have been shown to serve many functions, such as navigation, mechanical support, photonics, and protection of soft body parts (Raz *et al*., 2003). These biominerals exhibit remarkable complexity and properties that exceed those of synthetic analogs and differ greatly from geological minerals, thanks to the organism's ability to regulate composition, structure, size, and morphology (Lowenstam and Weiner, 1989; Nudelman and Sommerdijk, 2012). Biological regulation of crystal deposition and growth may also lead to the formation of biominerals that diffract like single-crystals (Addadi *et al*., 1999) *i.e.,* sea urchins diffract light akin to single crystals, thanks to the intricate arrangement of structures in their skeletons.

More than 50 mineral phases have been identified to date as biominerals, which are present across all kingdoms of life (Weiner and Dove, 2003). The inorganic component is typically a mineral phase such as calcium carbonate ($CaCO_3$), hydroxyapatite ($Ca_{10}(PO_4)_6(OH)_2$), silica,

magnetite (Fe_3O_4), and iron sulfides. Additionally, the organic component may include proteins, lipids, polysaccharides, enzymes, peptides, amino acids, pigments, carbohydrates, DNA/RNA, glycoproteins, chitin, *etc.* (Crichton, 2012). Within different organisms, both intra-crystalline and inter-crystalline organic molecules play important roles. Inter-crystalline organics provide an environment for crystal growth and nucleation sites (Aizenberg *et al*., 1997; Joanna Aizenberg *et al*., 1995; Marin *et al*., 2016), whereas intra-crystalline organics enhance the mechanical strength and flexibility of biological minerals (Metzler *et al*., 2008). The latter are described in more detail in Section 1.1.3.2. The precise regulation of both inter- and intra-crystalline organic molecules by organisms during biomineralization allows for shaping and manipulating the growth of these complex biominerals with specific polymorph, morphology, orientation, and size, contributing to their unique properties and functionality (Berman *et al*., 1988; Falini *et al*., 1996; Yang *et al*., 2020).

1.1.3. $CaCO_3$ biominerals

1.1.3.1. Crystalline and stable amorphous $CaCO_3$ biominerals occurrence

$CaCO_3$ is a prevalent mineral, constituting approximately 4% of the Earth's crust. Calcium carbonate is widely present in the natural environment and can be found in freshwater and saltwater environments, soils, sediments, mineral dust particles, and geological structures.

Calcium carbonate exists in six distinct crystalline polymorphs, including anhydrous phases like calcite, aragonite, and vaterite, as well as hydrated phases such as monohydrocalcite ($CaCO_3 \cdot H_2O$), ikaïte ($CaCO_3 \cdot 6H_2O$) (Addadi *et al*., 2003; Mann, 1988), as well as, a recently discovered *in vitro* form, the hemihydrate polymorph $CaCO_3.0.5H_2O$ (Zou *et al*., 2019).

Many living organisms contain crystalline $CaCO_3$ biominerals in the form of calcite, aragonite, and vaterite. Some examples are reported in Table 1.1. $CaCO_3$ biominerals can serve various purposes, such as providing structural support (*e.g.,* sponges, corals), offering protection (*e.g.*, shells), functioning as hard buoyancy tanks (*e.g.*, cuttlebone), or being part of photoreceptor systems (*e.g.*, light-focusing eye lenses of chitons). However, the biological function of some biominerals is still unclear, and understanding the biological benefits of their convoluted crystal shapes is still challenging. One hypothesis for the design of such convoluted shapes that often diffract as single crystals is that amorphous minerals lack specific internal structure, are uniformly strong in all directions, and are more adaptable to the available space. However, it’s

worth noting that amorphous minerals are less thermodynamically stable and more soluble than their crystalline counterparts (Addadi *et al*., 2003). Biogenic ACC has been categorized into two types: stable and transient. The stable form is often hydrated and has the composition $CaCO_3 \cdot H_2O$ (Levi-Kalisman *et al*., 2000), while the transient form was first reported to contain little to no water, with less than one-third of a water molecule per calcium carbonate molecule (Raz *et al*., 2003). Later, hydrated ACC, which subsequently transforms into anhydrous ACC, was also evidenced in sea urchin larvae (Politi *et al*., 2004), as described in more detail in Section 1.1.3.3.1.

(Weiner *et al*., 2003) summarized that various organisms, spanning different biological kingdoms and phyla, have been identified as producers of stable ACC. These organisms can be found in diverse taxonomic groups, including Echinodermata, Arthropoda, Mollusca, Platyhelminthes, Plantae, and Porifera. Bacteria can also internally produce stable ACC nanoparticles, even under highly challenging biomineralization conditions, as demonstrated by (Blondeau *et al*., 2018). It's important to note that the list of ACC-producing organisms may evolve and expand as ongoing research uncovers more examples.

In biominerals, ACC was proposed to serve three main roles: first, as a moldable amorphous precursor phase for crystalline $CaCO_3$ polymorphs, as mentioned before; second, as a dense ion-storage phase that can dissolve to meet calcium deficiencies; and third, as a structural material with isotropic properties and the ability to incorporate trace elements. Due to its versatile properties, such as moldability and intriguing mechanical features in biomineral hybrid structures, ACC further presents promising opportunities for designing new materials (Gower, 2008).

Table 1.1. Distribution of some stable biogenic crystalline and amorphous $CaCO_3$.

Kingdom/ phylum/ Class/Order/ Family/Genus/ Species	**Organism**	**Form of deposit**	**$CaCO_3$ deposited by organisms**	**References**
Plantae	Mulberry tree	Cystoliths in leaves	Calcite, aragonite, vaterite, ACC	(Jahren *et al*., 1998; Levi-Kalisman *et al*., 2002; Nitta *et al*., 2006; Wu *et al*., 2006)
Arthropoda/ Crustacea	Lobsters Crabs Shrimps	Cuticle, Gastroliths, storage structure	ACC, Calcite	(Ismail *et al*., 2022; Mergelsberg *et al*., 2019; Rødde *et al*., 2008)
Porifera	Sponges	Spicule core	ACC Calcite	(Taylor *et al*., 2007)
Ascidiacea	Sea squirt	Spicule (body)	Calcite, aragonite, vaterite, ACC, monohydrocalcite	(Aizenberg *et al*., 2002; Lambert, 1998; Mann, 2001)
Chordates	Fishes	$CaCO_3$ aggregates to absorb water and get rid of excess Ca	ACC, Calcite	(Aizenberg *et al*., 2002; Foran *et al*., 2013; Lambert, 1998)
Echinodermata	Sea urchins Sea stars Sea cucumbers	Spines and test Ossicles	Calcite, ACC	(Albéric *et al*., 2018b, 2019; Bechtel *et al*., 2013; Blowes *et al*., 2017; Drozdov *et al*., 2016; Gong *et al*., 2012; Seto *et al*., 2012)
Mollusks Bivalvia	Clams Oysters Mussels Scallops	Shells	ACC, vaterite Calcite Aragonite	(Huang and Zhang, 2022; Mohamed *et al*., 2012; Piwoni-Piórewicz *et al*., 2019)
Gastropoda (Nudibranchia)	Snails	Shell	Aragonite	(Parveen *et al*., 2020)
Platyhelminthes	Flatworms	Corpuscles	ACC, Calcite	(Señorale-Pose *et al*., 2008)
Bacteria	Cyanobacteria	Shell against light or sink against pH change	ACC, Aragonite, Calcite	(Benzerara *et al*., 2014; Blondeau *et al*., 2018; Couradeau *et al*., 2012; Obst *et al*., 2009)

Placozoa	*Trichoplax adhaerens*	Crystals deposition in cells	Aragonite	(Mayorova *et al*., 2018)
Cnidaria	Corals Anemone	Coral structure Spicules(Sclerites)	ACC, Calcite, aragonite	(Mass *et al*., 2017; Rahman and Oomori, 2008)
Chlorophyta	Green algae	Micropearls	ACC, Calcite	(Natsi and Koutsoukos, 2022; Wefer, 1980)
Annelids	Earthworms	Granules secretion	ACC Calcite	(Hodson *et al*., 2015)
Fungus	Fungal fruiting bodies	Nanofibres	ACC, Calcite	(Bindschedler *et al*., 2016; Elkhateeb *et al*., 2022; Hodson *et al*., 2015; Versteegh *et al*., 2014, 2013; Vinn, 2021)
Brachiopoda	Trochozoans	Shells	ACC, Calcite	(Simonet Roda *et al*., 2019)
Bryoza	Moss animals	Cell spaces	Calcite	(Swatland, 2010)
Cocco-lithophores	Single-celled algae	Intricate plates	Calcite	(Haunost *et al*., 2021)

1.1.3.2. Inorganic-organic interactions in $CaCO_3$ biominerals

Originally, intra-crystalline organics referred to organic molecules that resist prolongated chemical oxidation such as NaClO treatments (Crenshaw, 1972; Penkman *et al*., 2008) and are thus considered occluded within the crystal lattice (Lu 2009, Marin 2016), which protect them from degradation. On the other hand, inter-crystalline organics do not resist oxidative treatment because they are localized at the crystal surfaces. In other words, intra-crystalline organics refer to the organics present within individual crystallites, whereas inter-crystalline represents the organic interfaces existing between adjacent crystallites (Weber and Pokroy, 2015).

In the 1970s, the application of TEM allowed for the examination of bubbly and frothy morphologies within nacre tablets, shedding light on intra-crystalline organics (Towe and Thompson, 1972). In the late 1980s, (Berman *et al*., 1988) demonstrated that calcite crystals grown with acidic glycoproteins from sea urchins had conchoidal fractured surfaces, unlike the smooth surfaces of abiotic calcite. This was attributed to the presence of intra-crystalline organic molecules. Further studies, including single-crystal X-ray diffraction, explored the impact of these organics on calcite crystallite size and orientation in sea urchin and mollusk shells (Berman *et al*., 1993, 1990). The results confirmed that biomacromolecules could be incorporated into the crystal structure while modifying its microstructure and morphology, allowing organisms to exert control over these aspects.

Biomineral composites typically have higher inter-crystalline organics, approximately 5 wt%, compared to intra-crystalline organics, around 0.4 wt% in the prismatic layer of *A. rigida*. Intra-crystalline organics consist mainly of proteins and chitin, with varying concentrations across species (Nudelman *et al*., 2007). Amino acid compositions in *A. rigida* prisms differ significantly from those in *P. fucata* and *A. pectinata* prisms (Okumura *et al*., 2013). It is essential to note that intra-crystalline organics usually carry negative charges, which attract cations like Ca^{2+} in calcium-based minerals, aligning them with charged crystal lattice planes (Gilow *et al*., 2011).

While the compositions of intra-crystalline organics may differ in various biogenic calcites, mechanical properties remain consistent, suggesting minimal influence on mechanical performance (Deng *et al*., 2022). Nevertheless, the chemical compositions of intra-crystalline organics play a significant role in controlling nucleation, growth, and biomineral shapes. *In vitro* experiments reveal that intra-crystalline organics from different biominerals induce

unique modifications in crystal structures. For instance, calcite crystals grown in the presence of intra-crystalline organics from mollusk prisms exhibit flattened morphologies, while those from sea urchin spines result in elongated crystals (Aizenberg *et al*., 1997; Albeck *et al*., 1993).

(Younis *et al*., 2012) employed high-angle annular dark-field scanning electron microscopy (HAADF-STEM) in tomography mode and electron tomography reconstruction to directly visualize organic macromolecules within biogenic crystal hosts. Their findings elegantly demonstrated that the organic patches observed were not uniformly scattered within a single crystal but rather aligned along the (001) plane (Figure 1.4).

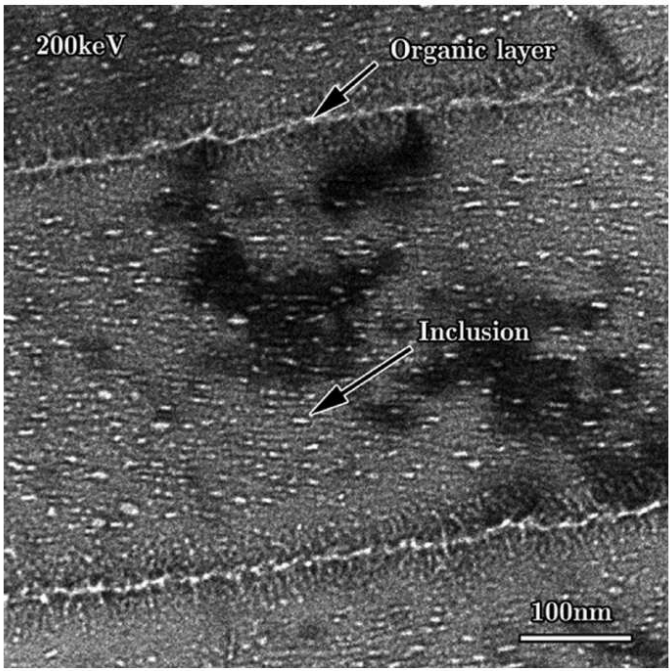

Figure 1.4. Transmission electron micrographs (TEM) captured in bright field mode reveals organic inclusions within nacre lamellae, distinguished by their bright appearance (image adapted from (Younis *et al*., 2012)).

Many biominerals have various residual strains and stresses, stemming from factors like organic lattice distortions, trace element substitutions, and ACC crystallization. These can be detrimental or beneficial. Three types of residual stress/strain exist: composite-level, atomic-scale, and nano-aggregation induced (Deng *et al*., 2022; Zolotoyabko, 2017). While composite-level stress can be relieved mechanically, atomic-scale stress persists until lattice damage releases stress. Comparing residual-stress removed samples is complex due to associated

compositional changes from processes like heat treatment (Deng *et al.*, 2022; Zolotoyabko, 2017).

Figure 1.5 summarizes the structural characteristics within a mineral that can influence the properties of the material. In particular, incorporating intra-crystalline organics strengthens biominerals through dislocation impediment and induces local lattice distortions and residual stress, further enhancing strength. Crystalline features (crystal size, porosity, *etc.*) also affect different cracking behaviors, *e.g.,* in polycrystalline minerals, cracks propagate along grain boundaries, while single-crystal minerals exhibit cleavage cracks. In addition, twinning boundaries impede and deflect cracks (Deng *et al*., 2022; Zolotoyabko, 2017).

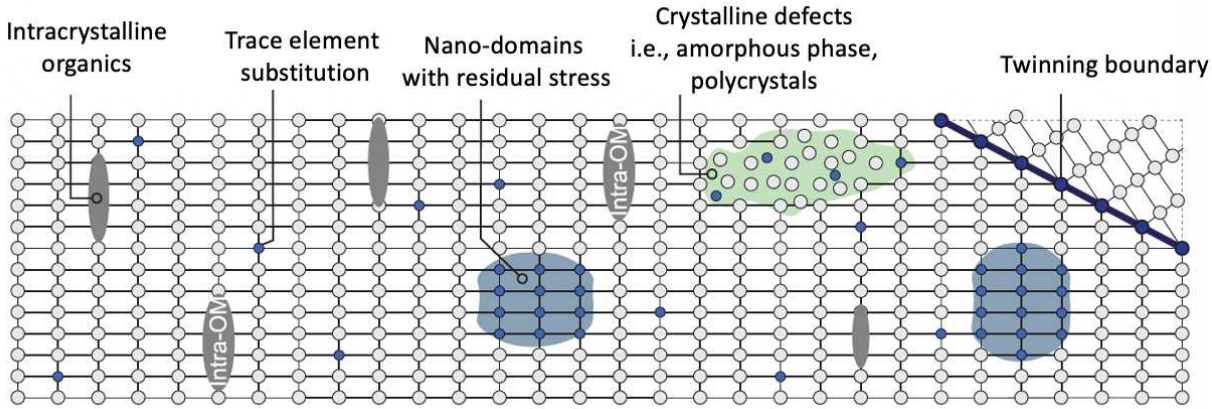

Figure 1.5. A schematic depiction of the structural characteristics within the mineral building blocks (lattice) is shown, encompassing intra-crystalline organic materials (intra-OMs), trace element substitutions, nano-heterogeneity domains, crystalline imperfections, and twinning boundaries (image adapted from (Deng *et al*., 2022)).

Lattice distortions are linked to phase transformation, with an inverse relationship to the remaining amorphous phase in biogenic calcium carbonate: less amorphous phase corresponds to higher lattice distortions. Comparing calcitic biocomposites, sea urchin spines exhibit smaller lattice distortions than mollusk shells like *Pinna nobilis* and *Atrina rigida* (Zolotoyabko *et al*., 2006) (Figure 1.6). This is supported by varying levels of residual amorphous phase, reaching up to 10 wt.% in sea urchin spines but notably lower in mollusk shells (Albéric *et al*., 2018).

Additional support for the impact of the remaining amorphous phase on lattice distortions is evident in the variation of lattice distortions with annealing temperature. In skeletal structures,

particularly for sea urchins rather than mollusks, lattice distortions are observed when annealing temperatures rise from 25°C to 150–200 °C, primarily due to the crystallization of any remaining ACC. As the annealing temperature exceeds 200°C, lattice distortions gradually diminish because of the removal of organics, leading to lattice relaxation (Figure 1.6) (Albéric *et al*., 2018b; Pokroy *et al*., 2006).

Unlike mollusk shells, Coccoliths show minimal lattice distortions, possibly due to their different intra-crystalline organics. Mollusk shells contain acidic proteins, while coccoliths have acidic polysaccharides, which interact with growing calcite crystallites, exerting smaller forces on mineral blocks (Frølich *et al*., 2015).

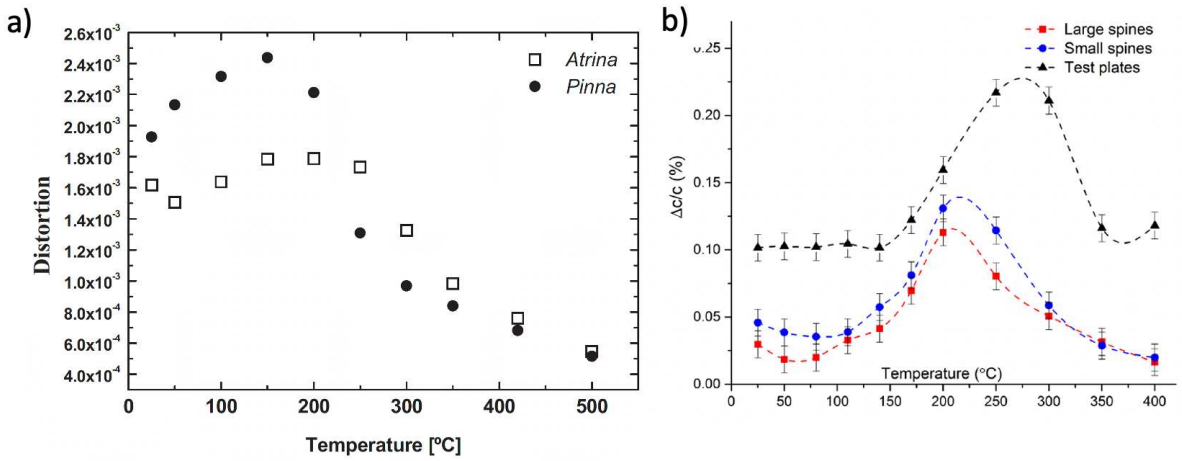

Figure 1.6. a) Temperature-induced lattice distortions along the c-axis in biogenic calcite. The lattice distortions are calculated concerning a control calcite sample (geological) and account for varying Mg concentrations in the studied samples (image adapted from (B. Pokroy *et al*., 2006)). The second graph, b) shows temperature-dependent lattice distortions (Δc/c) on sea urchin test and spines (Image adapted from (Albéric *et al*., 2018b)).

1.1.3.3. Case study of sea urchin biominerals

Sea urchin biominerals serve as intriguing models for studying mineralization processes due to their intricate skeletal structures and potential applications in biomimetic materials.

1.1.3.3.1. Adult sea urchin spines

Sea urchins have spiky appendages called spines that protrude from their body shells, serving as both protection and a means of movement. These spines are primarily made of calcite, with

small amounts of stable anhydrous amorphous calcium carbonate (ACC), very little amount of water, and organic molecules incorporated into their crystalline structure (Albéric *et al*., 2018b). The skeletal part of the spines consists of an inner meshwork called the stereom and outer radial wedges called septa (Figure 1.7B, 1.7C). Within the spines, there are soft tissues, including the epidermis and dermis (or stroma), which contain various types of cells distributed throughout the spine. The fenestrated stereom contributes to the relative strength of echinoid spines by preventing crack propagation, while the compact septa enhance bending stress resistance (Dubois and Ameye, 2001).

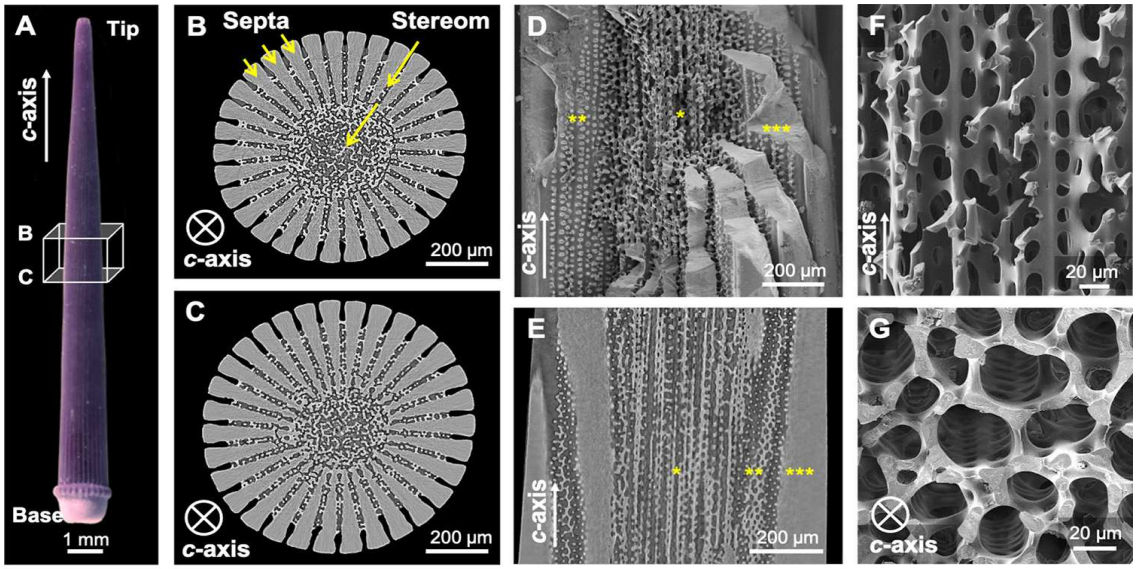

Figure 1.7. Sea urchin spines of *P. lividus*, devoid of organic matter using NaClO. CT scans unveil labeled zones B and C, perpendicular to the c-axis – B at the tip and C near the base. An SEM micrograph (D) shows a base-fractured spine. E) Further insights arise from a CT image along the c-axis I. SEM images (F and G) display inner laminar stereom from diverse angles. Laminar and labyrinthic stereom denoted as * and **, septa as ***. Calcite c-axis orientation is indicated by a white arrow or crossed circle (image adapted from (Albéric *et al*., 2022)).

As for many other biominerals, sea urchin skeletal elements exhibit behavior akin to single crystals when observed in both polarized light and measured by X-ray diffraction (Donnay and Pawson, 1969). Unlike the cleavage seen in geological calcite, their conchoidal fractured surfaces are a result of hindered crack propagation (Figure 1.8) caused by intra-crystalline organic molecules (Towe, 1967). The presence of coherent organic/inorganic interfaces generates diffraction spots resembling those of single crystals, although atomic organic-inorganic interactions introduce small calcite lattice distortions as described before in Section

1.1.3.2. Initially, Towe (1967) thought sea urchin spines were a mix of single crystals and polycrystalline formations. However, Blake *et al*. (1984) found, using HRTEM, that sea urchin spines are mainly single crystals with a mosaic-like structure. This was confirmed by (Berman *et al*., 1990) and (Aizenberg *et al*., 1997) with synchrotron radiation. They showed that sea urchin spines consist of coherent blocks, typically 100-200 nm in size, with an angular spread of around 130 millidegrees. Finally, recent studies on *Paracentrotus lividus* sea urchin spines have provided insights into their nano-structure, suggesting the presence of nano-pores filled with hydrated organic materials and a thin layer of ACC positioned between the intra-crystalline organics and the crystalline calcite (Albéric *et al*., 2018, Albéric *et al.*, 2022).

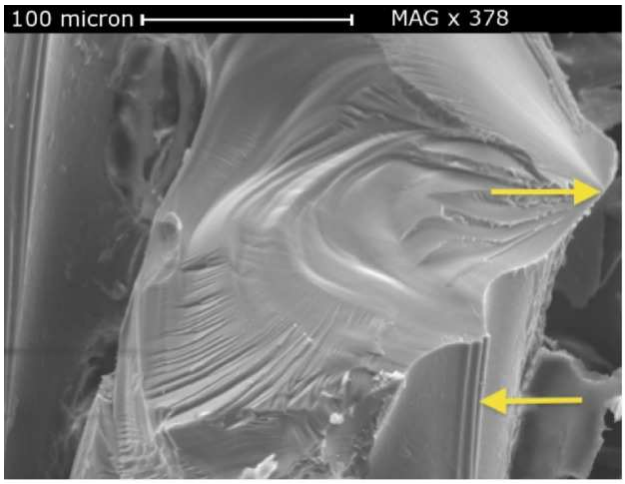

Figure 1.8. The fractured surface of a spine wedge is shown, which shares similarities with fracture patterns observed in glass. The upper arrow marks the point of crack initiation, while the lower arrow draws attention to a feature on the outer surface of the wedge, confirming that the crack started from the exterior surface (image adapted from (Tsafnat *et al*., 2012)).

1.1.3.3.1. Transient ACC phases in the formation of sea urchin biominerals

Amorphous precursors for biomineral formation were initially proposed by Towe and Hamilton in 1968; the idea was considered inconclusive at the time, and attention shifted to conventional crystallization pathways (Towe and Hamilton, 1967). However, the first widely accepted demonstration of the amorphous precursor pathway in biomineralization came from chiton teeth, where the first-formed calcium phosphate mineral was found to be amorphous, gradually transforming into dahllite (Lowenstam and Weiner, 1985). Regarding $CaCO_3$, the existence of an amorphous precursor remained less apparent. Although certain organisms, such

as sea urchins, mollusks, could generate and stabilize ACC, its connection to crystalline biominerals had not been acknowledged. However, in the late 1990s, Aizenberg *et al.* observed an intriguing composite of a crystalline calcitic core and outer amorphous $CaCO_3$ in the sponge *Clathrina* (Aizenberg *et al*., 1996). Further *in vitro* experiments with polypeptides mimicking biomineral-associated proteins revealed the involvement of a transient amorphous precursor pathway (Gower and Tirrell, 1998). *In-situ* examinations and focused research efforts led to discovering and recognizing the amorphous precursor pathway in biomineralization.

The first report of a transient ACC phase in biominerals was by Beniash *et al*. in 1997, where they observed its presence alongside single-crystalline calcite in sea urchin larvae spicules. Proteins and magnesium ions were then identified as playing a role in forming and stabilizing the ACC phase in the larval spicules. Notably, the biogenic transient ACC phase exhibited structural and compositional differences from the stable ACC phase, and surprisingly, it did not contain bound water (Raz *et al*., 2003). By utilizing X-ray photoelectron emission spectromicroscopy. Politi *et al.*, 2008) additionally revealed the presence of three distinct mineral phases: an initial short-lived, presumably hydrated ACC phase, followed by an intermediate transient form of ACC, and finally, the biogenic crystalline calcite phase. This was later confirmed by (Gong *et al*., 2012), and a two-step reaction was proposed from $ACC{\cdot}H_2O$ to ACC to calcite. Interestingly, their research uncovers the presence of $ACC{\cdot}H_2O$-rich nanoparticles that persist even after the surrounding mineral has undergone dehydration and crystallization. This persistence is attributed to protein matrix components occluded within the mineral, which inhibit the dehydration of $ACC{\cdot}H_2O$.

In parallel, *ex vivo* evidence of an amorphous precursor (Figure 1.9) was identified in the regenerating tip of adult urchin spines (Politi *et al*., 2004) and teeth (Ma *et al*., 2007), suggesting the importance of transient amorphous phases in producing biominerals diffracting like single crystals but exhibiting a complex morphology. More recently, the same two-step reaction $ACC{\cdot}H_2O$ to ACC to calcite as for the larvae was also evidenced for the spines (Albéric *et al*. 2019).

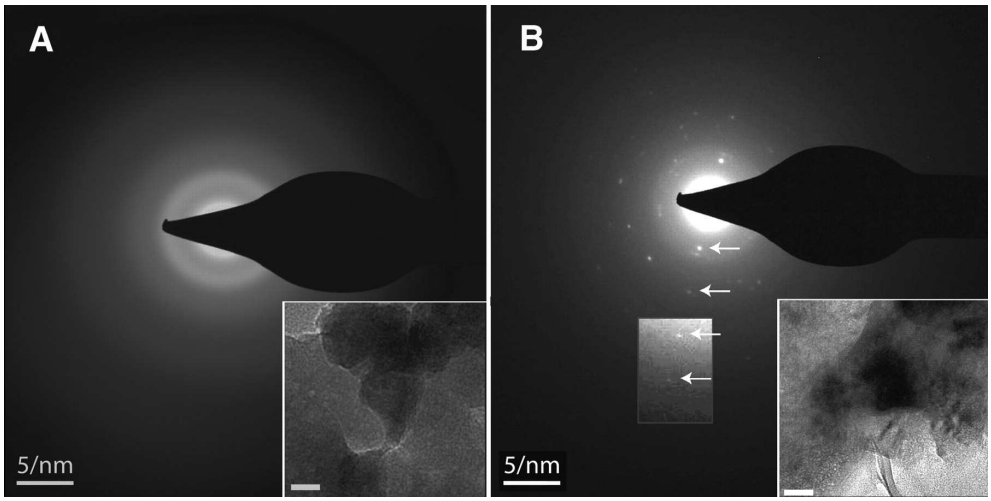

Figure 1.9. TEM and electron diffraction patterns of particles from freshly regenerated spines. (A), the diffraction pattern suggests amorphous material, while (B), taken after 3 weeks, displays diffraction peaks characteristic of calcite, indicating a transition from amorphous to crystalline. The freshly regenerated spines underwent freeze shock and sonication, with the same particles re-examined after 3 weeks to capture the transformation process (image adapted from (Politi *et al*., 2004)).

1.2. Colors in the living world

1.2.1. Some examples of colors and patterns in different organisms

Color and pattern integration in diverse organisms highlights the intricate connection between biology and colors. This interplay involves at least three distinct mechanisms: 1) structural colors from nanostructures causing iridescence, like in butterflies and fish (Fudouzi, 2011); 2) pigment-based colors from molecules like carotenoids and melanin found in the tissues or specific cellular compartments as well as in biominerals; and 3) photoluminescence (Rosário *et al*., 2019; Shawkey and D'Alba, 2017). Table 1.2 showcases the remarkable occurrence of colors and patterns for various organisms grouped according to their mechanisms of color formation.

Table 1.2. Some colors and patterns integrated within diverse organisms.

Color mechanisms	Organisms	Molecules/ structures involved	Source	References
Biomineral pigmentation (skeleton and shells)	Sea urchins, Crinoids	Polyhydroxylated naphthoquinones	Dietary sources and synthesized by organisms	(Goodwin and Srisukh, 1950; Hou *et al*., 2018b),
	Avian eggs	Heme based Pigments	Dietary source	(Ostertag *et al*., 2019)
	Mollusks	Carotenoids, melanin, and tetrapyrroles, including porphyrins and bile pigments	Dietary sources and synthesized by organisms	(Williams, 2017)
	Crusteceans	Fat-soluble carotenoids	Dietary sources	(Bandaranayake, 2006)
	Red corals	Carotenoids	produced by organisms	(Smith *et al*., 2007)
Tissues/ Cells pigmentation	Brittle stars	Melanin	Dietary source and synthesized by organism	(Fontaine, 1962a, 1962b)
	Corals	Coral polyps and chromoprotein	Zooxanthellae algae impart the color	(Bandaranayake, 2006)
	Algal bloom	Chlorophyll, astaxanthin, lutein, fucoxanthin, canthaxanthin, zeaxanthin, β-cryptoxanthin	Synthesized by organisms	
Bio-luminescence	Fireflies Brittle star	Bioluminescent compounds and heavy metal ions Green fluorescent photoprotein	Synthesized by organisms and dietary source	(Bandaranayake, 2006)
Pigmentation	Plants	Chlorophylls, carotenoids, and flavonoids	Synthesized by organisms	(Sudhakar *et al*., 2016)

Pigmentation and Structural color (Diffraction and interference effects)	Butterfly wings	Papiliochromes, pterins, and monochromes	Synthesized by organisms	(Hashimoto *et al*., 2021; Shamim *et al*., 2014)
	Bird feathers	Carotenoids, melanins, and porphyrines	Synthesized and dietary sources	(Jeon *et al*., 2021)
	Fish Scales	Melanophores, bluish iridophores, yellowish iridophores and mature xanthophores (orange).	Synthesized by organisms	(Nüsslein-Volhard and Singh, 2017)
Exoskeleton coloration	Beetles	Chitin and melanins, monochromes, pteridines, tetrapyrroles, carotenoids, flavonoids, papiliochromes, and quinones	Dietary source and synthesized by organisms	(Noh *et al*., 2016)

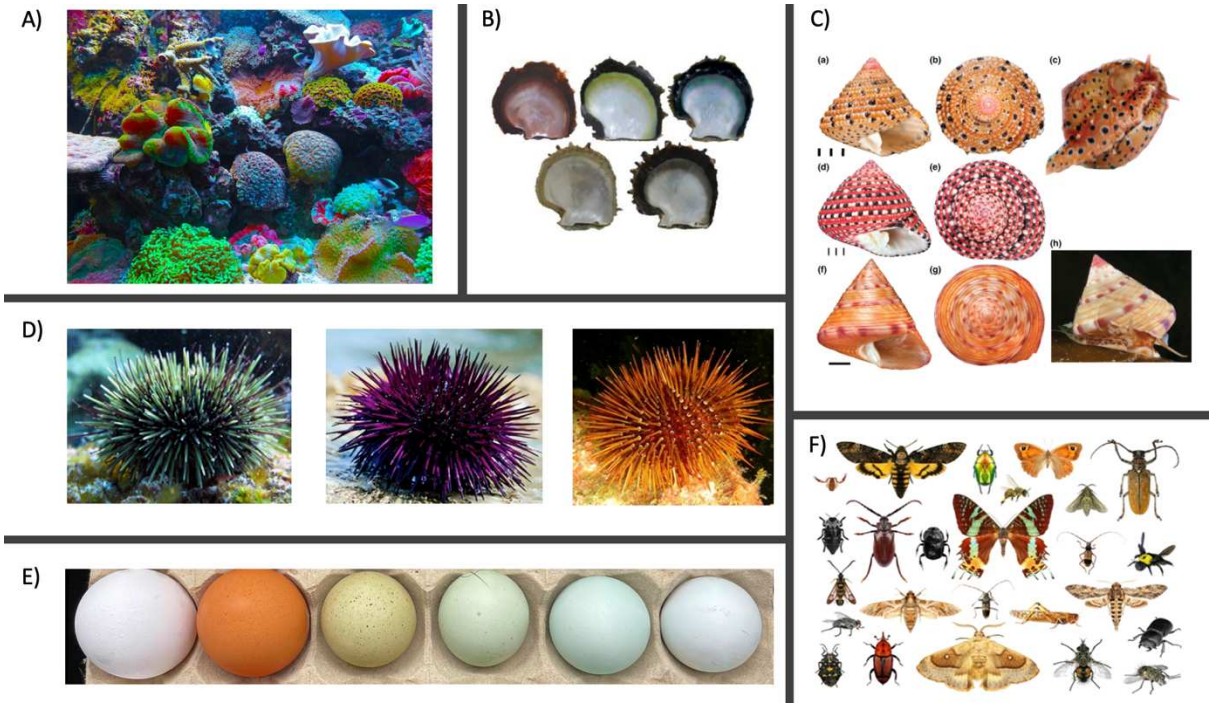

Figure 1.10 An array of hues exhibited by various organisms is shown. The diverse spectrum of colors found in nature, from the vibrant plumage of sea corals to the intricate patterns adorning the wings of butterflies, each organism contributes to a rich tapestry of color.

1.2.2. Pigmentation in sea urchin biominerals

1.2.2.1. The PHNQ family and its properties

The phenomenon of color variations in sea urchin biominerals manifests across its test and spines, generating a wide range of colors across species, such as purple, green, and red hues (Wise, 2011). The prevailing consensus among researchers is that polyhydroxylated naphthoquinones (PHNQs) serve as the primary pigment in the test and spines of sea urchins (Fox and Hopkins, 1966). Similarly to other naphthoquinones, PHNQs lead to intense colors because of important electron delocalization in their quinoid structure (Dulo *et al*., 2021), which vary in solution according to pH due to successive deprotonations of their numerous hydroxyl groups. About forty different PHNQs have been identified in different sea urchin species (Anderson *et al*., 1969; Vasileva *et al*., 2021), including echinochrome A and spinochromes (Figure 1.11). These molecules are incorporated within the biogenic calcite phase, making them resistant to sunlight and pH change. PHNQs have attracted significant attention due to their diverse biological activities (Hou *et al*., 2019, 2018a; Shikov *et al*., 2018). They have been shown to possess strong antioxidant properties, capable of scavenging free radicals and inhibiting lipid peroxidation, making them potential candidates for protecting cells and tissues from oxidative damage (Hou *et al*., 2018a; Kuwahara *et al*., 2010; Li *et al*., 2013; Powell *et al*., 2014). In addition, PHNQs possess antibacterial activity against various strains of bacteria, including both common human pathogens and marine bacteria (Brasseur *et al*., 2017; Hou *et al*., 2020). PHNQs have also been found to suppress inflammatory responses and reduce the production of pro-inflammatory molecules, indicating their potential as anti-inflammatory agents. Finally, research has revealed their protective effects against cardiovascular diseases and eye conditions (Brasseur *et al*., 2017; Egorov *et al*., 1999).

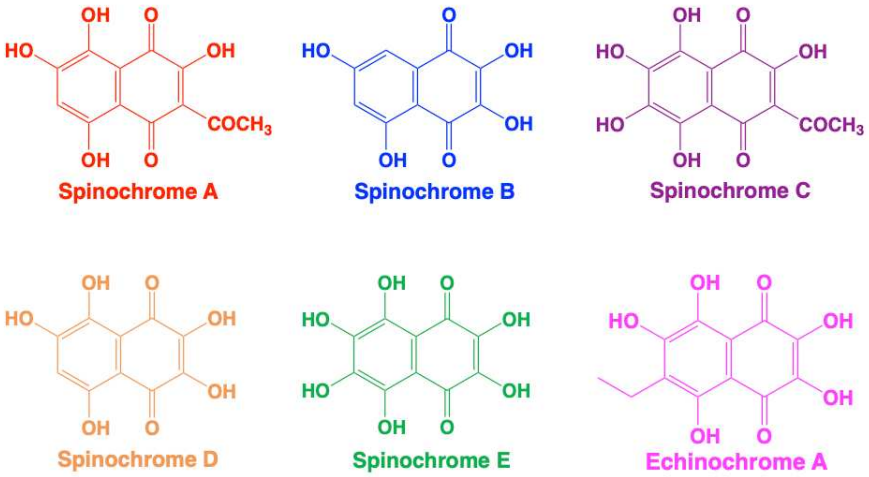

Figure 1.11. The chemical structures of pigments found in the sea urchins: echinochrome and spinochromes.

1.2.2.2. Pigmentation mechanisms

1.2.2.2.1. PHNQ production, storage, release, and incorporation to the growing spines

We do not yet fully understand how biomineral pigmentation works, but various studies conducted over time provided valuable information on PHNQ production and storage in the so-called red-spherule cells (RSC), which are one type of the immune coelomocytes of sea urchins.

In particular, a study conducted by (Hira *et al*., 2020) revealed that live RSCs in the green sea urchin (*Strongylocentrotus droebachiensis)* display distinctive multi-color autofluorescence compared to other coelomocytes. Employing fluorescence-activated cell sorting (FACS) and successful isolation of pure live RSC populations facilitated the analysis of PHNQ content in these cells. They identified sulfated derivatives of spinochrome C, D, E, and spinochrome dimers, suggesting that RSCs may play a significant role in the biogenesis of naphthoquinone compounds and regulating their bioactivity.

In addition, specific genes related to pigment production and coloration, including the pks gene cluster, flavin-containing monooxygenase family genes, and the *sult* gene (Calestani *et al*., 2003), were found in the pigment cells. Notably, reducing Sppks gene expression in sea urchin embryos led to albino specimens, indicating its crucial role in the final steps of pigment production.

Furthermore, (Coates *et al*., 2018) evidenced that red spherule cells from sea urchins (*Paracentrotus lividus* and *Psammechinus miliaris*), when exposed to microbial ligands, intact microbes and damage signals, exhibited cellular degranulation and an increased release of cell-free echinochrome A into the coelomic fluid.

In a 1975 study conducted by Heatfield and Travis, the investigation focused on the fine structure of spherulocytes, which are cell types containing large intracellular membrane-bound vacuoles known as spherules. This examination was carried out in the regenerating tips of spines in the sea urchin *Strongylocentrotus purpuratus,* and RSC were identified in close contact with the growing micro-spines.

In essence, sea urchins can control the production of PHNQs in RSC and their release during a defense mechanism against foreign species or during the regeneration of spines, which imparts color to the biomineral.

1.2.2.2.2. Interplay between biomineralization and pigmentation in sea urchins

Various studies focused on mollusks have explored the potential connection between biomineralization and pigmentation mechanisms (Bauchau, 2001; Cusack et al., 1992;. However, limited research has addressed this relationship in the context of sea urchins. Nevertheless, an important study conducted by (Zito *et al*., 2015), suggests that pigment production and biomineralization pathways in sea urchins might be interlinked due to the important role of carbonic anhydrase in both processes. In addition, a study by Towe in 1967 challenged the notion that "organic pigments are irrelevant to biomineralization, also obviously trapped within the crystal during its growth" (Towe, 1967). This perspective introduces an element of debate regarding the potential correlation between organic pigments and the biomineralization process.

Interestingly, some spines undergo color changes that depend on the biomineralization stage during sea urchin spine growth. This transition is observed from white to pinkish to the final color, which varies among sea urchin species. Notably, color differences between septa and stereom have been documented in *Paracentrotus lividus* green spines during biomineralization, as reported by Goodwin and Srisukh, 1950. In the case of green spines, the stereom exhibited a purple color, while the septa appeared green. The exact mechanism behind the origin of these

colors remains unknown. However, this does indicate that organic pigment might be involved in biomineral formation.

As discussed previously, sea urchin biominerals exhibit a diverse color spectrum, resulting from using polyhydroxylated naphthoquinones (PHNQs), synthesized within red-spherule cells. (Figure 1.12) highlights the homogenous and quite vibrant color within sea urchins despite the very low amount (>0.1 wt.%) of organic pigments. Their ability to maintain coloration under extensive bleaching sets sea urchin spines apart. This resilience is attributed to the hybrid pigment nature of the spines, where the interplay of inorganic and organic components protects and preserves their colors. These spines serve as a natural model for developing bio-inspired materials and pigments with exceptional color stability.

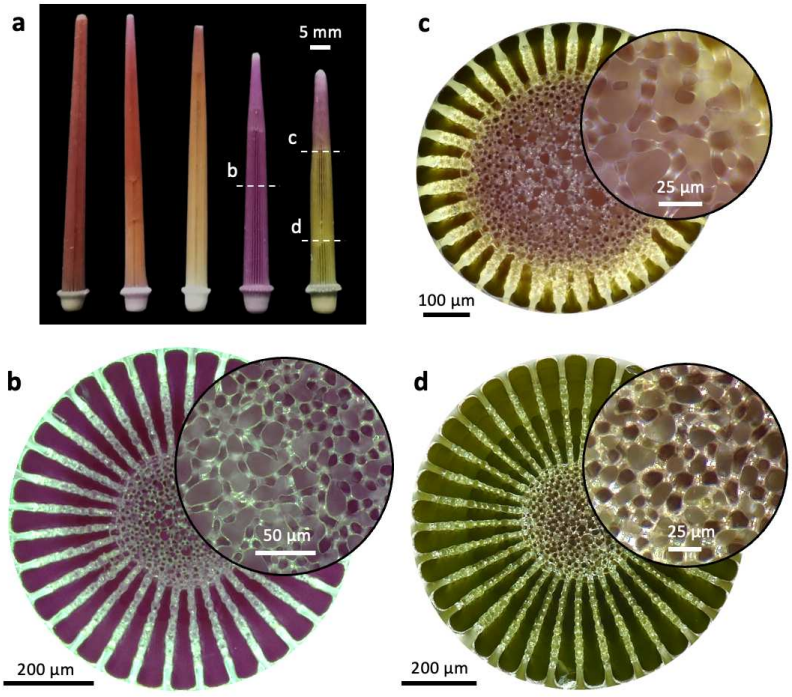

Figure 1.12. a) Sea urchin spines, b) cross-sectional view of purple spine, c,d) cross-sectional view of green spine.

1.3. Synthetic $CaCO_3$

1.3.1. Different $CaCO_3$ syntheses

Calcium carbonates can be synthesized using many methods, such as precipitation, carbonation, hydrothermal, and more advanced methods. By breaking down these complex processes, the goal is to understand how calcium carbonate is made in various forms, each with its unique qualities and properties. Table 1.3 compares different $CaCO_3$ synthesis methods with specific advantages and limitations to suit various needs and product preferences.

Table 1.3. Comparison of different strategies developed for the controlled synthesis of $CaCO_3$. References can be found at the bottom of the table, along with the explanation of the abbreviations.

	Conditions				Characteristics		
Strategies	pH	Additives	Temp. (°C)	Other	Morphology	Polymorph	Size (μm)
Ca^{2+}–CO_3^{2-} reaction system	–	DSS, PSSS	–	$[CaCl_2]$ = $[Na_2CO_3]$ = 5×10^{-4} -5×10^{-2} M	Spherical, toroidal, ellipsoidal	Vaterite, calcite	0.5 - 1.8
	9.0	EG	25	$[CaCl_2]$ = $[Na_2CO_3]$ = 0.05, 0.1, 0.33 M; EG/ H_2O ratios: 1:1, 4:1, 6:1	Spherical, ellipsoidal	Vaterite	0.4 – 2.7
	8.0–10.0; 11.0–12.0	EG	23	$[Ca^{2+}]$:$[CO_3^{2-}]$ ratios: 5:1, 2:1, 1:1, 1:2, 1 :3	Ellipsoidal, spherical, spheroidal, rhombohedral, flower-like, irregular	Vaterite, calcite	–
	–	SDS; PAA	80	PAA (M_w = 8000g mol^{-1}), [PAA] = 0.5gL^{-1}, [SDS]= 10 mM	Hollow microspheres	Calcite	4-7
Solid-liquid-gas carbonation	–	Urea	150	High-pressure CO_2: 12 MPa, mass ratios: $Ca(OH)_2$/urea = 1:6	Spherical	94.2% vaterite	–
	8.0-12.0	DMCHA, DBU, DBAE, BDA, EP	40-90	$[Ca(CH_3COO)_2]$ = 1.0 M	Rhombohedral , spherical, rod-like, shuttle-like	Calcite, vaterite, aragonite	–
	–	EDTA-2Na	120	Pressurized - CO_2	Hierarchical hollow microspheres	Calcite	4-6
Water-in-oil reverse emulsion	–	AOT	25	AOT/isooctane/ water reverse microemulsion, $[CaCl_2]$ = $[Na_2CO_3]$ = 0.05M	Rod -like, irregular, spherical	Calcite, vaterite	1-3
	–	–	65	CO_2 /N_2 switch-able surfactant reverse micelles	Spherical, rhombohedral, dendrite-like	Vaterite, calcite	–
	–	Tween-80, Span-80	22	US	Spherical	Vaterite	0.02-0.03
Carbonation of $Ca(OH)_2$	12	Phe	25		Spherical, Rhombohedral dendritic	ACC, calcite, vaterite aragonite	0.02-0.5 2-5

Microwave-hydrothermal	9	VHVEVS peptide	60-180		Nanosphere	ACC	0.23
Sono-atomization	9		60-180	Na_2CO_3 and $CaCl_2$ 0.2-1.0 mol/dm³	Nanosphere	ACC	0.02-0.04
Electrochemical deposition	7	ATP	21	Ca^{2+} 40-200 mol/dm³	Rhombohedral Dendritic	Calcite, Vaterite	2-5
Vapor diffusion	6-9		25	$(NH_4)_2CO_3$ and $CaCl_2$	Nanosphere Rhombohedral Dendritic	ACC Calcite Vaterite Aragonite	0.02-0.4 2-10
Deposition			25		Spherical	ACC	1-2
Hydrothermal method		amino acids	140	Na_2CO_3 and $CaCl_2$: 0.15M	Rhombohedral scalenohedral	Calcite	10-100
Double deco-mposition	12.1	Pyrophosphates	25	$NaHCO_3$ and $CaNO_3$	Spherical Rhombohedral	ACC Calcite	100 nm 1-10
PILP			25	$(NH_4)_2CO_3$ and $CaCl_2$. polyaspartate	Spherical Spherulite Distorted rhombohedral	ACC Vaterite Calcite	- 10-20 50-60

Abbreviations and references for the method of synthesis for Table 1.3:

N^1-Dodecyl-N,N-dimethyl acetamidine bicarbonate; AOT: sodium bis(2-ethylhexyl) sulfosuccinate; BDA: N-butydimethylamine; DBAE: 2-(dibutylamino)ethanol; DBU: 1,8-diazabicycloundec-7-ene; DMCHA: N,N-dimethylcyclohexylamine; DSS: dextran sodium sulfate; EDTA-2Na: disodiumsalt of ethylenediaminetetraacetic acid; EG: ethylene glycol; EP: N-Ethylpiperidine; PAA: poly(acrylic acid); Phe: L-phenylalanine; PSSS: poly(styrenesulfonate) sodium; SDS: sodium dodecyl sulfonate; US: ultrasonication; VHVEVS: Ac-Val-His-Val-Glu-Val-Ser-$CONH_2$, PILP: Polymer induced liquid precursor.

Ca^{2+}–CO_3^{2-}reaction system (Bahrom *et al*., 2019; Oral and Ercan, 2018; Svenskaya *et al*., 2018), Solid–liquid–gas carbonation (Rugabirwa *et al*., 2019a, 2019b), Water-in-oil reverse emulsion (Jiang *et al*., 2015; Tai and Chen, 2008), Carbonation of $Ca(OH)_2$ (Camerini *et al*., 2019; Xto *et al*., 2019), Microwave hydrothermal (Qi *et al*., 2014), Sono atomization (Kojima *et al*., 2012), Electrochemical deposition (Tlili *et al.*, 2003), Vapour diffusion (Chen *et al*., 2013), Deposition (Xu *et al*., 2005), Hydrothermal method (Lang *et al*., 2020), Double decomposition method (Merle *et al*., 2022), PILP (Gower and Odom, 2000).

For *in-vitro* synthesis of $CaCO_3$, Ca^{2+} and CO_3^{2-}ions are reacted, usually using calcium salts (*e.g.*, $CaCl_2$ or $Ca(NO_3)_2$) and carbonate salts (*e.g.*, Na_2CO_3, $NaHCO_3$, K_2CO_3, or $(NH_4)_2CO_3$). The precipitate's size, morphology, and polymorphism depend on initial supersaturation, ion concentration, pH, temperature, and additives (details in Section 1.3.3). Higher supersaturation leads to metastable and amorphous phases along with calcite, while lower supersaturation favors calcite formation. The transition and crystallization of ACC can proceed along an energetically favorable pathway: ACC → vaterite → aragonite → calcite (Radha *et al*., 2010).

1.3.1.1. Characterizing ACC: structure and hydration level

ACC formation is influenced by the synthesis conditions like time, solute concentration, pH, temperature, solvent, and confinement, which determine the ACC's structure and hydration level. ACC hydration levels (n) refer to the extent to which ACC has absorbed or incorporated water molecules into its structure $CaCO_3.nH_2O$. It can also vary depending on the environment where it is stored, such as temperature, humidity, vacuum and other chemical species. Hydration levels have been reported to range from 0.4 to 1.6 (Michel *et al*., 2008; Khouzani *et al*., 2015; Gebauer *et al*., 2010; Du *et al*., 2018; Jensen *et al*., 2018). A 3D atomic model shows channels rich in calcium ions filled with carbonate ions and water. These channels contain both mobile and less mobile water types (Goodwin *et al*., 2010). However, the exact dimensions of the nanochannels with mobile water are uncertain because no experimental evidence is available. Debate surrounds the presence of mobile water-rich channels, approximately nanometer-sized. High hydration (above 0.8) leads to water networks, while lower levels reduce mobility, suggesting rigid content. Dehydration-induced changes in ACC are accompanied by rearrangement of ions (Bushuev *et al*., 2015). During the process of dehydration, H_2O molecules located within the first coordination shell around calcium ions are replaced by carbonate (CO_3^{2-}) groups. This substitution leads to minimal changes in the coordination number of calcium ions in the first coordination shell and the average distance between oxygen and calcium atoms.

As a result, it becomes challenging to quantitatively measure structural variations among amorphous calcium carbonate (ACC) particles with different hydration levels using commonly employed techniques like calcium K-edge extended X-ray absorption fine structure (EXAFS). However, qualitative assessments of these differences can be made by comparing calcium K-edge X-ray absorption near-edge structure (XANES) or pair distribution function (PDF) of ACC particles that undergo changes *in situ*, such as exposure to elevated temperatures or pressures, leading to alterations in their degree of dehydration.

XANES techniques show distinct features between hydrated and anhydrous ACC, allowing differentiation based on the short-range order (Politi *et al*., 2008; Gong *et al*., 2012; Mass *et al*., 2017; Zou *et al*., 2019; Albéric *et al*., 2019). Employing specific photon energies spanning the Ca $L_{2,3}$-edge (340 to 360 eV), an array of X-ray absorption images was acquired, comprehensively encompassing the Ca $L_{2,3}$-edge spectrum for each image pixel. The

fundamental underpinning of these maps lies in the acquisition of reference spectra for ACC-H_2O, ACC, and calcite, meticulously derived through the fitting of averaged spectra from each distinct phase (Figure 1.13a and 1.13b) (Albéric *et al*., 2019; Gong *et al*., 2012). In calcite, the primary peaks corresponding to the Ca L_2 and L_3 peaks exhibit splitting, resulting in the emergence of two minor peaks. In synthetic ACC, minor displays reduced intensity and are positioned nearer to the main peaks, resembling shoulders.

Using atomic pair distribution function (PDF) analysis (Figure 1.13c), the local structure can be probed from short-range order to long-range order, including the medium-range order (Goodwin *et al*., 2010; Michel *et al*., 2008). The partial pair distribution functions (PDF) reveal average bond distances between intricately connected atom pairs in the solid lattice. The computation of PDFs, as described by Michel *et al.,* 2008, allows the separation of individual atomic pair contributions. In the context of ACC, the visible 2.4 Å peak arises mainly from Ca-O pairs, while the prominent 2.9 Å peak mainly involves O-O pairs. The notable 4.1 Å peak indicates both Ca-O and Ca-Ca pairs, and the conspicuous 6.2 Å peak mainly results from Ca-Ca interactions (Figure 1.13c) (Michel *et al*., 2008; Saharay *et al*., 2013)

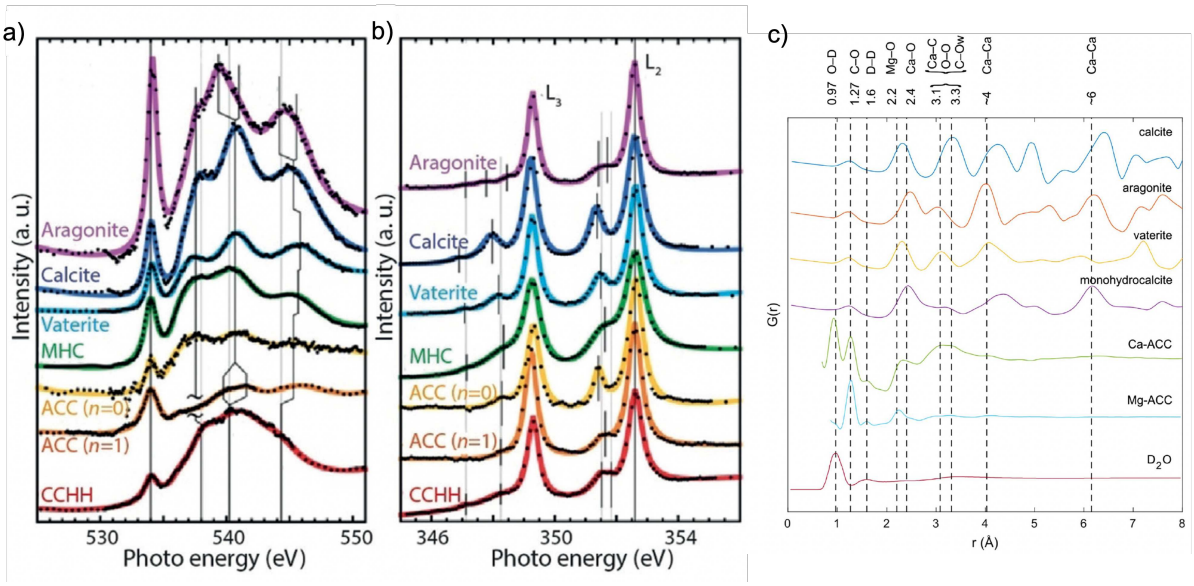

Figure 1.13. a) O K-edge and Ca L-edge XANES spectra of ACC with varying hydration levels and different $CaCO_3$ crystalline forms (Zou *et al*., 2019). b) Comparison of experimental total pair distribution functions for various calcium carbonate variations, including hydrated forms, pure ACC, magnesium-stabilized ACC, and pure heavy water (Clark *et al*., 2022).

1.3.2. ACC crystallization mechanisms

In literature, two main mechanisms have been proposed for the transformation of ACC into crystalline calcium carbonate. The first mechanism is the "dissolution and crystallization" route, where ACC dissolves partially, followed by the reprecipitation of dissolved ions to form the crystalline phase. This pathway is strongly influenced by the bulk water's presence, which further determines the resulting crystal structure and morphology. In the absence of bulk water, the second mechanism is the "solid-state rearrangement," the locally ordered ACC acts as the basic unit and undergoes a rearrangement to transform into the corresponding crystalline polymorphs (Gal *et al*., 2013). Additionally, a third route composed of both main mechanisms mentioned above has been proposed in *in vitro* studies (Ihli *et al*., 2014), where the transformation of ACC into crystalline polymorphs was first observed *via* partial dissolution/ recrystallization mechanism, mediated by surface water, followed by a solid-state rearrangement of the majority of the ACC nanoparticles. A better understanding of these mechanisms holds significant potential for designing and developing novel materials with unique properties inspired by nature. The following subsections will focus on the two main types of amorphous to crystal transformations reported in the literature.

1.3.2.1. Dissolution-precipitation crystallization mechanism

During the dissolution-crystallization (D/C) transformation, ion species diffuse from the dissolution site to the nucleation and growth area of the new crystal. Figure 1.14 illustrates that upon mixing $CaCl_2$ and Na_2CO_3 solutions (0.01 M), a structure resembling an emulsion form was observed under cryo-transmission electron microscopy combined with a special quenching technique (Rieger *et al*., 2007). This emulsion-like structure subsequently undergoes decomposition, leading to the formation of $CaCO_3$ nanoparticles. These nanoparticles then aggregate to create vaterite spheres with dimensions on the order of a few micrometers. Although initially spherical, these vaterite spheres undergo a transformation through a series of dissolution and crystallization events. As a result of these dynamic processes, the vaterite spheres gradually evolve into calcite, which exhibits a distinct rhombohedral shape (Figure 1.14) (Rieger *et al*., 2007).

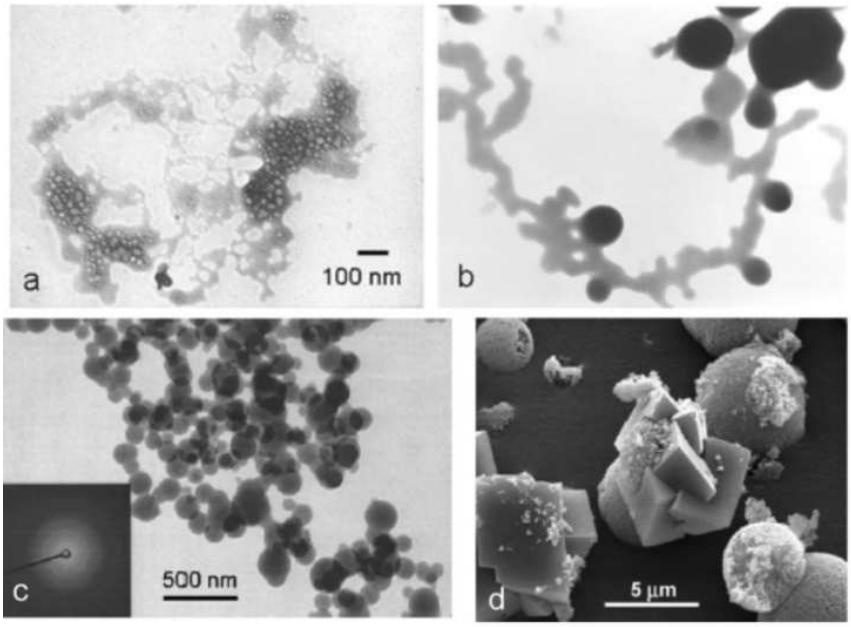

Figure 1.14. Cryo-TEM images reveal an "emulsion-like" precipitate forming within a) 100 ms, b) over minutes, the precipitate undergoes densification and breaks down into nanoparticles, c) nanoparticles are identified as nondiffracting ACC after 1 minute, d) as time progresses to 60 minutes, SEM images show the formation of vaterite spheres and calcite rhombs. Images have been adapted from (Rieger *et al*., 2007).

(Han and Aizenberg, 2008) observed the transformation of ACC particles into calcite rhombohedra by finding ACC-depleted areas surrounding each crystal, indicating that ACC particles had dissolved to support the growth of the new crystals. Similarly, in support of the D/C process, Rodriguez-Navarro *et al.* and Zou *et al.* noticed changes in morphology and an increased concentration of dissolution products in solution during the transformation (Rodriguez-Navarro *et al*., 2014; Zou *et al*., 2015).

The structure of $CaCO_3$ crystals formed from ACC particle-containing solutions depends on the kinetics of dissolution and crystal formation that are influenced by particle size, hydration, and crystallization conditions like pH, temperature, and solvent (Rodriguez-Navarro *et al*., 2014; Zou *et al*., 2015). It has been shown that a higher ethanol fraction prolongs dissolution, while smaller particles from supersaturated solutions dissolve faster, showing lower kinetic stability (Chen *et al*., 2013). Smaller ACC particles dissolve quickly, favoring vaterite, while larger particles dissolve more slowly and tend to transform into calcite. Surprisingly, higher pH increases kinetic stability with decreased solubility and reduced size (Tobler *et al*., 2016).

Confinement in restricted volumes enhances ACC's kinetic stability and controls $CaCO_3$ crystal morphology and structure (Stephens *et al*., 2011; Tester *et al*., 2011). Limited ion transport slows ACC dissolution and new crystal formation. Slower crystallization allows for the creation of metastable crystal forms with unique morphologies, such as single-crystalline vaterite and aragonite nanowires, when ACC is confined in track-etched nanopores (Schenk *et al*., 2014a; Zeng *et al*., 2018).

It has been proposed that the dissolution process is preceded by ACC dehydration, but high activation energies raise doubts about the order of events (Gal *et al*., 2014; Ihli *et al*., 2014; Rodriguez-Blanco *et al*., 2011; Rodriguez-Navarro *et al*., 2014). TGA measurements on the ACC particles coated with lipid bilayers confirmed the ACC dehydration before dissolution. Further, IR studies have shown the water evolution of the ACC phase from 18-20 wt.% to 10-13 wt.%. These findings suggested that the lipid bilayer stabilizes ACC and confirms dehydration before crystallization (Ihli *et al*., 2014).

Atmospheric water is crucial in triggering the D/C transformation of ACC in the air. Konrad *et al.* found that a specific threshold of atmospheric water (around 0.25 mol per $CaCO_3$ unit) is needed to initiate crystallization in dry and additive-free ACC (Konrad *et al*., 2016). The role of atmospheric moisture in triggering crystallization led to investigating the impact of humidity (RH). Crystallization at all RH values resulted in pore formation within the dense ACC nanoparticle arrangement in the film. As RH increased, pores enlarged, and nanoparticle fusion occurred, demonstrating matter displacement and dissolution (Xu *et al*., 2006). Albéric *et al.* 2018a performed *in situ* total X-ray scattering during a high RH transformation from amorphous to crystal phase, detecting reorganization at short and long-range scales, supporting the involvement of the D/C transformation(Albéric *et al*., 2018a). This research suggests that the crystallization process is intricately influenced by relative humidity, leading to distinct morphological features and confirming the importance of the D/C mechanism in the amorphous-to-crystal transformation.

1.3.2.2. Solid-state transformation

Solid-state crystallization is the process of transforming an amorphous or disordered solid into a crystalline structure without the presence of a liquid medium. During this transformation, atoms or molecules within the solid rearrange themselves to form ordered arrangements in the crystal lattice (Figure 1.15). (Nielsen *et al*., 2014) established that amorphous calcium

carbonate (ACC) serves as a precursor for the growth of crystalline phases. However, (Walker *et al*., 2017) observed the presence of both amorphous and crystalline materials coexisting within a single aragonite needle. This coexistence strongly suggested a solid-state transformation process in which amorphous material undergoes a transition to a crystalline state. In the initial stages, tiny ACC particles come into existence and subsequently join together to create larger particles. These aggregated particles further combine to take on a larger, elongated form. Within this amorphous framework, nanoscale crystals begin to develop, and over time, they mature into the ultimate needle-shaped structure (Figure 1.15). This process can be driven by diffusion-driven or diffusionless-driven crystallization mechanisms. However, diffusionless transformations do not apply to ACC due to its lack of a crystalline structure.

Dehydrating ACC particles is essential for transforming them into crystals *via* solid-state transformations (Ihli *et al*., 2014; Saharay *et al*., 2013) (Figure 1.15g). Initially considered thermodynamically favored, recent experiments and MD simulations show that dehydration might rather be kinetically driven (Albéric *et al*., 2018a; Bushuev *et al*., 2015; Saharay *et al*., 2013). External triggers like elevated temperatures, pressures, or an electron beam are required to overcome the energy barrier (Albéric *et al*., 2018a; Tobler *et al*., 2016; Zou *et al*., 2015). Dehydration of ACC involves ion rearrangement, hindered by water-ion interactions that reduce mobility (Goodwin *et al*., 2010; Saharay *et al*., 2013). Initially, highly hydrated ACC allows easier water removal. As dehydration progresses, stronger interactions raise the energy barrier. At low hydration (n=0.2), water becomes rigid, leading to a significantly higher activation energy for removal. Once fully dehydrated, crystalline $CaCO_3$ nuclei form, consuming the amorphous matrix. The kinetics of solid-state transformation determines $CaCO_3$ crystal structure and size, with faster transformations leading to larger crystallites and the formation of thermodynamically stable calcite, while slower transformations result in a mixture of calcite and metastable vaterite.

Shape-preserving crystallization, often called "pseudo-solid-state" transformation, has also been observed in synthetic $CaCO_3$. This phenomenon occurs during the crystallization of ACC in solution or under heat treatment, where the presence of water within ACC influences the reorganization of ions (Gower, 2008). When ACC films are generated through gas diffusion, they retain their microscale morphology at the air-solution interface during crystallization (Harris *et al*., 2015). These films maintain a granular structure while developing iso-oriented or polycrystalline domains. Recent *in-situ* transmission electron microscopy studies have

provided insights into the densification of ACC particles, showing their transformation into crystalline particles without altering their nanoscale morphology (Liu *et al.*, 2020). Finally, studies have demonstrated that the films undergo crystallization via a local dissolution/precipitation mechanism.

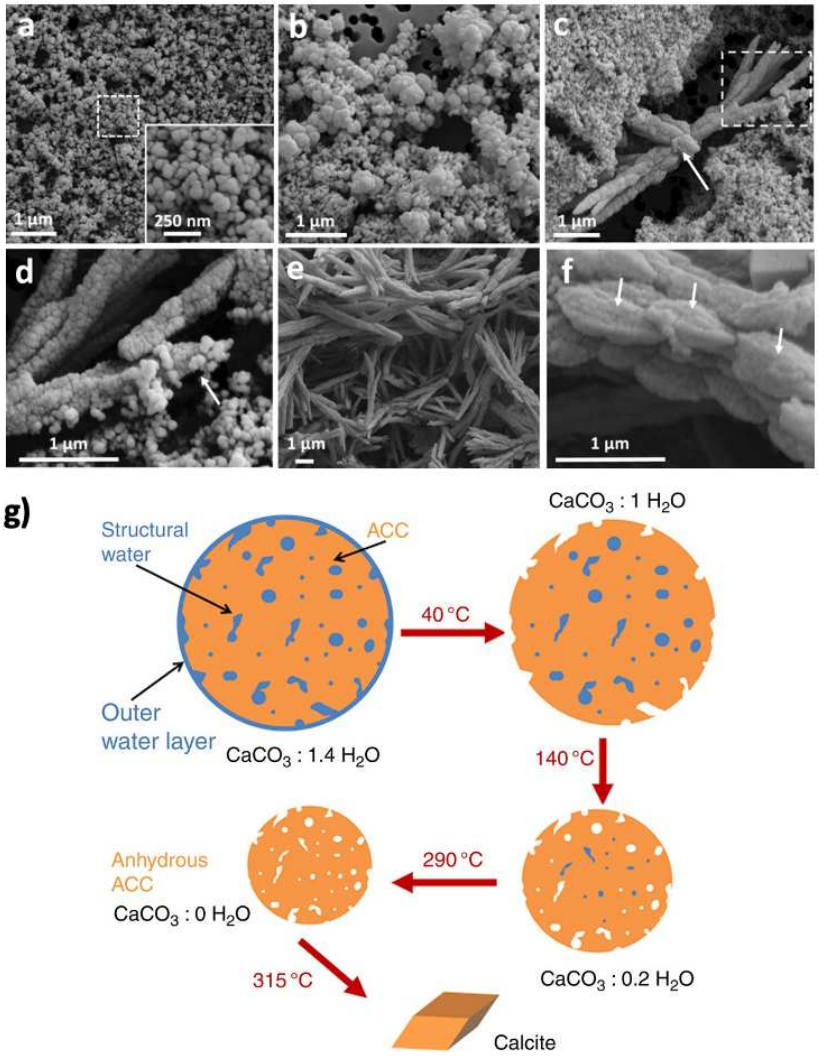

Figure 1.15. Time-resolved SEM images, a) after 1 minute of reaction, spherical ACC particles of 75-100 nm are observed. b) At 10 minutes, larger particles of 450-600 nm are present. c) At 20 minutes, aragonite sheaf-shaped crystals emerge. d) Higher magnification reveals spherical ACC particles attaching to the growing aragonite needle. e) After 1 hour, aragonite needles are formed. f) A higher magnification of an aragonite needle shows elongated particles of 900 nm to 1 µm, which assemble smaller units (arrows) (image adapted from (Walker *et al.*, 2017)). g) ACC crystallization into calcite via dehydration (image adapted from (Ihli *et al.*, 2014)).

1.3.3. Influence of the conditions of synthesis and the presence of organic additives on $CaCO_3$ formation

1.3.3.1. Conditions of synthesis

Environmental parameters like temperature and pH impact nucleation and growth, leading to distinct $CaCO_3$ crystal structures (Niu *et al*., 2022). Here, we focus on the influence of reactant concentrations and pH.

Initial reactant concentrations of Ca^{2+} and/or CO_3^{2-} impact $CaCO_3$ particle properties. For example, high CO_3^{2-} concentration yields anisotropic shapes, while low concentration forms isotropic spheroids. Excess Ca^{2+} or CO_3^{2-} alters reaction rates and particle growth, leading to specific particle characteristics. Moreover, controlled addition or mixing influences the size, shape, surface charge, and hydrophilicity of the synthesized $CaCO_3$ phase, *e.g.,* vaterite particles with diverse morphologies can be obtained using dropwise precipitation (Svenskaya *et al*., 2018).

Furthermore, the pH conditions during the formation of ACC significantly impact its stability, crystallization kinetics, and pathways. In an aqueous medium without stabilizing agents, the lifetime of ACC is typically very short (~300 s) unless it is synthesized under low temperatures (<10 ºC) or highly basic conditions (pH > 11). Indeed, ACC synthesized at a pH of around 12.5 exhibits greater stability against crystallization upon heating compared to ACC synthesized at pH values below 11.5. In addition, ACC synthesized at pH ~12.5 directly crystallizes into calcite, whereas ACC synthesized at pH values below 11.5 initially crystallizes into a vaterite-calcite mixture, which eventually transforms into calcite (Figure 1.16) (Oral and Ercan, 2018; Tobler *et al*., 2016). Figure 1.16 showcases the effect of pH on the morphology of the $CaCO_3$. At lower pH levels (8 and 10), the SEM images reveal the presence of ellipsoidal, spherical, and spheroidal vaterite particles. These vaterite particles exhibit a range of shapes, with some being elongated and others more spherical in nature. The diversity in shapes suggests that the pH conditions influence the morphology of the particles, resulting in the formation of various vaterite structures. However, as the pH level increases (to 11, 12, and 13), a notable transformation takes place. The vaterite particles observed at lower pH values change shape and structure. In these higher pH conditions, the vaterite particles transform into rhombohedral, flower-like, and irregular calcite particles (Figure 1.16).

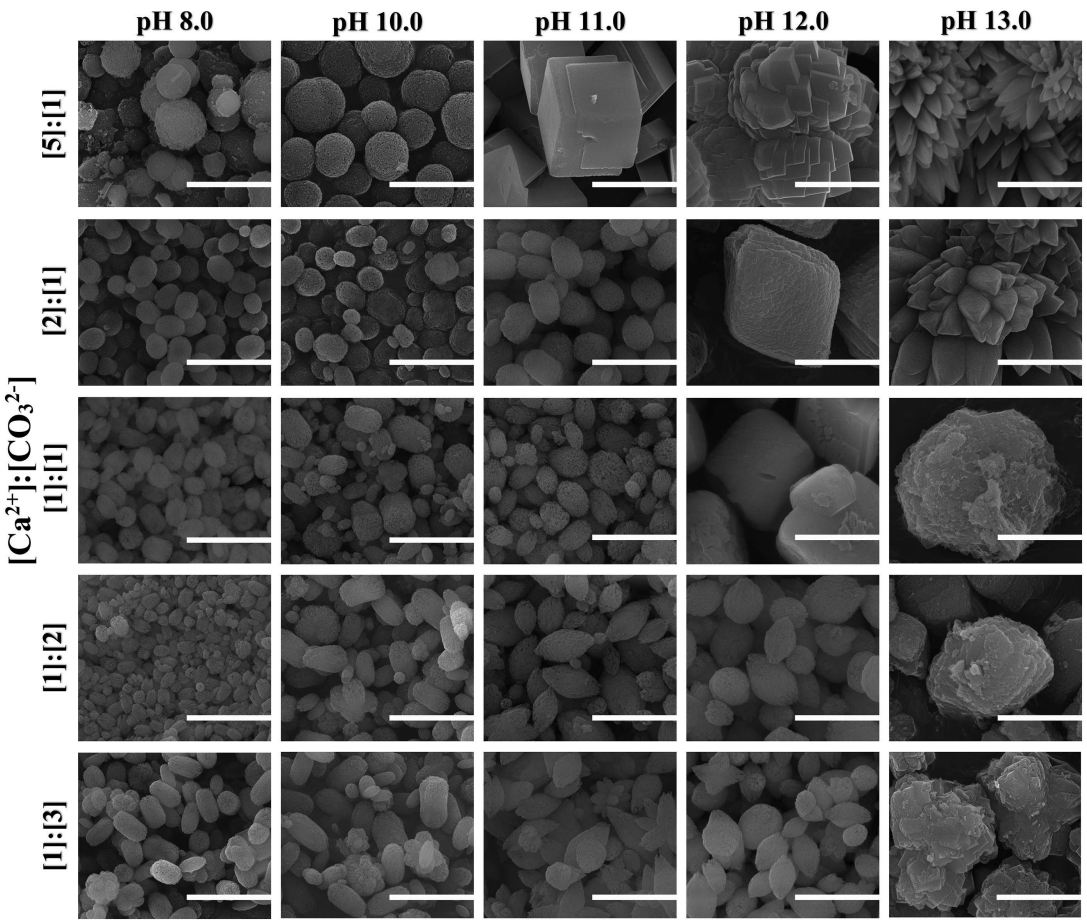

Figure 1.16. SEM images of $CaCO_3$ particles synthesized at various pH l (8, 10, 11, 12, and 13) using different ratios of calcium ions (Ca^{2+}) to carbonate ions (CO_3^{2-}). The scale bars are 3 μm (Oral and Ercan, 2018).

1.3.3.2. Organic additives

Organic and inorganic additives significantly influence $CaCO_3$ formation and crystallization (Meldrum and Cölfen, 2008). They act as templating or guiding agents of crystal shapes and polymorph selections. They affect stability and solubility, promoting ACC or specific crystalline phases. Here, we present the role of a few organic molecules: synthetic polymers, biogenic organics (amino acid, protein, and polysaccharides), and organic pigments.

1.3.3.2.1. Synthetic polymer and biogenic organics

When discussing the impact of organic (surfactants and polymers) but also inorganic (cations) additives on $CaCO_3$ crystallization, the classical approach considers the adsorption of these molecules to crystal growth surfaces, influencing growth rate and crystal shape. However,

emerging evidence suggests more intricate effects are at play. For example, polyacrylic acid (PAA) can control the shape of the calcite crystals from elliptical at low PAA concentration to spherical at high concentration (Kim *et al.*, 2022). Polystyrene sulfonate also influences $CaCO_3$ crystal shapes by affecting ion complexation, nucleation, stabilization of the intermediate amorphous particles, and controlling mesocrystal assembly (Geng *et al.,* 2010).

Researchers have also demonstrated that the activity of highly active polyamines relies on their ability to form complexes with carbonate ions present in the solution, highlighting that electrostatic attraction between carbonate and additives alone is insufficient (Schenk *et al.,* 2014b).

Zou *et al.,* 2018 hypothesized a mechanism of $CaCO_3$ formation in the presence and absence of polyaspartic acid. In the absence of additives, the binding between positively charged Ca^{2+} ions and negatively charged CO_3^{2-} ions results in the formation of $CaCO_3^0$ complexes, and the effective interaction between the complexes leads to the formation of ACC when the solution is unstable (Figure1.17a) and in the presence of additives, the first step is a cooperative ion-association process in which the additives attract either Ca^{2+} ions or CO_3^{2-} ions and also provides an additional effective interaction between the $CaCO_3^0$ complexes, inducing the formation of ACC with smaller particle size by destabilizing the solution (Figure 1.17b).

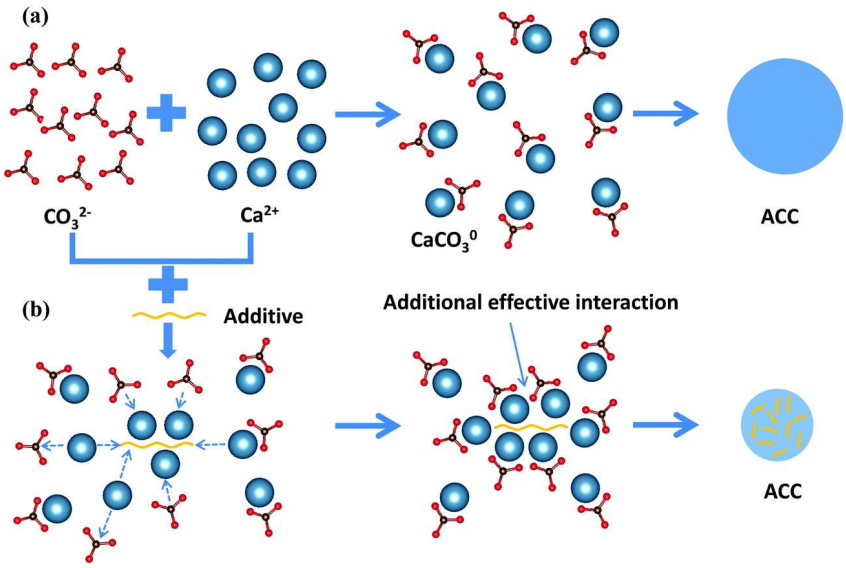

Figure 1.17. The formation of calcium carbonate, (a) In the absence of influential additives, the binding of Ca^{2+} and CO_3^{2-} ions lead to the formation of $CaCO_3$ complexes, resulting in the formation of ACC when the solution is unstable, (b) With influential additives present, a cooperative ion-association process occurs, destabilizing the solution and promoting the formation of smaller-sized ACC particles (image adapted from (Zou *et al*., 2018)).

In addition, several organic molecules, including amino acids, monosaccharides (Lang *et al*., 2020), and polysaccharides (Albeck *et al*., 1996) were shown to be incorporated within calcite crystals during crystal growth (Teng and Dove, 1997). Through single-crystal diffraction techniques, it was confirmed that these organic molecules are located at specific crystallographic planes within the crystal structure. As described in Section 1.3.2 for biogenic calcite, incorporating organics can also lead to anisotropic lattice distortions in synthetic calcite (Borukhin *et al*., 2012). The extent of lattice distortions induced by organics depends on factors such as charge, size, rigidity, and the relative pKa of functional groups. Molecules that strongly interact with the mineral phase are incorporated at higher concentrations, resulting in more pronounced lattice distortions (Borukhin *et al*., 2012).

In environments with low water activity, organic molecules play a crucial role in controlling the transport of ions to and from the mineral surface, restricting their movement to specific locations. This control enables organisms to influence the morphology of the mineral. Organic macromolecules can adhere to specific crystal planes and impede crystal growth, suggesting that organisms can shape the texture and shape of biogenic crystals (Berman *et al*., 1993, 1990, 1988). Figure 1.18 from (Aizenberg *et al*., 1997), showcases an example of organics inducing

growth along a specific axis. Firstly, pure synthetic calcite crystals exhibit the presence of stable {104} hexagonal faces. However, the introduction of macromolecules extracted from *P. lividus* spines induces the formation of new negative rhombohedral faces within the synthetic calcite crystals, which are slightly oblique to the crystal's c-axis. Furthermore, when observing the epitaxial overgrowth of calcite crystals on the lateral surface of a young spine, it becomes evident that the presence of released macromolecules exerts a significant influence on the morphological characteristics of these crystals. This influence is further confirmed in the case of mature spines, where the epitaxial overgrowth on the lateral surface yields similar morphological effects as observed in the earlier stages.

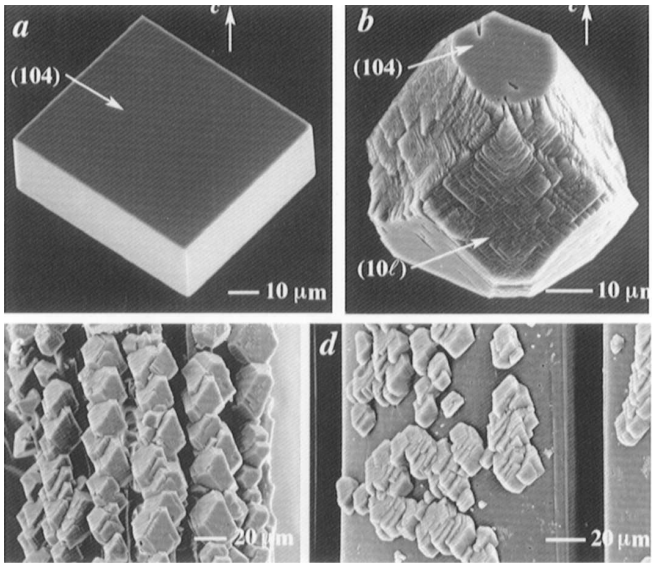

Figure 1.18. (a) Pure synthetic calcite crystal exhibits stable {104} hexagonal faces. (b) Macromolecules extracted from *P. lividus* spines induce the development of new negative rhombohedral faces slightly oblique to the c-axis in synthetic calcite crystals. (c) Epitaxial overgrowth of calcite crystals on the lateral surface of a young spine shows pronounced morphological effects influenced by released macromolecules. (d) Epitaxial overgrowth on the lateral surface of a mature spine exhibits similar morphological effects as in (c) (Aizenberg *et al*., 1997).

Additional crystal growth experiments have shown that specific soluble matrix components (SM) extracted from calcite or aragonite biominerals can induce the growth of the corresponding calcium carbonate polymorph. SM alone was initially thought to control crystal polymorph and morphology, but further studies revealed the important role of the insoluble matrix (IM) components. When combined with SM, IM can also affect crystal polymorphs

(Belcher *et al*., 1996; Falini *et al*., 1996; Feng *et al*., 2000). The diversity of these protein-mediated *in vitro* mineralization highlights the complexity of the natural processes.

1.3.3.2.2. Organic pigments

Very few studies have reported the effect of some organic pigment molecules, called "dyes" here, indifferently on calcite growth. Shan *et al.*, 2004 successfully produced $CaCO_3$ crystals using organic dyes featuring negatively charged functional groups by *in situ* hydrolysis of diethyl carbonate in a calcium-containing solution. They showed that some dyes are valuable for studying crystal morphology control through organic-inorganic interactions. In particular, the use of organic dyes with negatively charged functional groups results in $CaCO_3$ crystals with different polymorphs (calcite or vaterite), colors, and morphologies. Eosin Y yielded hexagonal carmine calcites with stepped faces, methyl blue generated twinned Y-shaped calcite crystals, fluorescein sodium produced brown calcite crystals, and alizarin red S led to violet dogbone-like calcites (Figure 1.19). Notably, the dye-infused $CaCO_3$ maintained its color stability even after enduring a 5-hour boiling process, underscoring a growth process akin to natural biomineralization where dyes were effectively occluded (Shan *et al*., 2004).

Marzec *et al.,* 2018 studied the tandem effects of amino acids and Brilliant Blue R, Brilliant Black, and Brilliant Blue G dyes by synthesizing calcite crystals by vapor diffusion method (Figure 1.20a). The use of these dyes only did not allow for the coloration of the calcite crystals, and the addition of amino acids was essential to obtain colored crystals. These results showed that amino acids, proficient occlusion in calcite, seemingly undertake the role of chaperones for singular or aggregated of these particular dye molecules (Figure 1.20b).

Notably, the method used for synthesizing $CaCO_3$ can also impact the incorporation of organics into the calcite crystals. In particular, vapor diffusion synthesis methods tend to introduce higher concentrations of organics into calcite crystals compared to direct precipitation methods, leading to more significant lattice distortions within the crystal lattice (Borukhin *et al*., 2012).

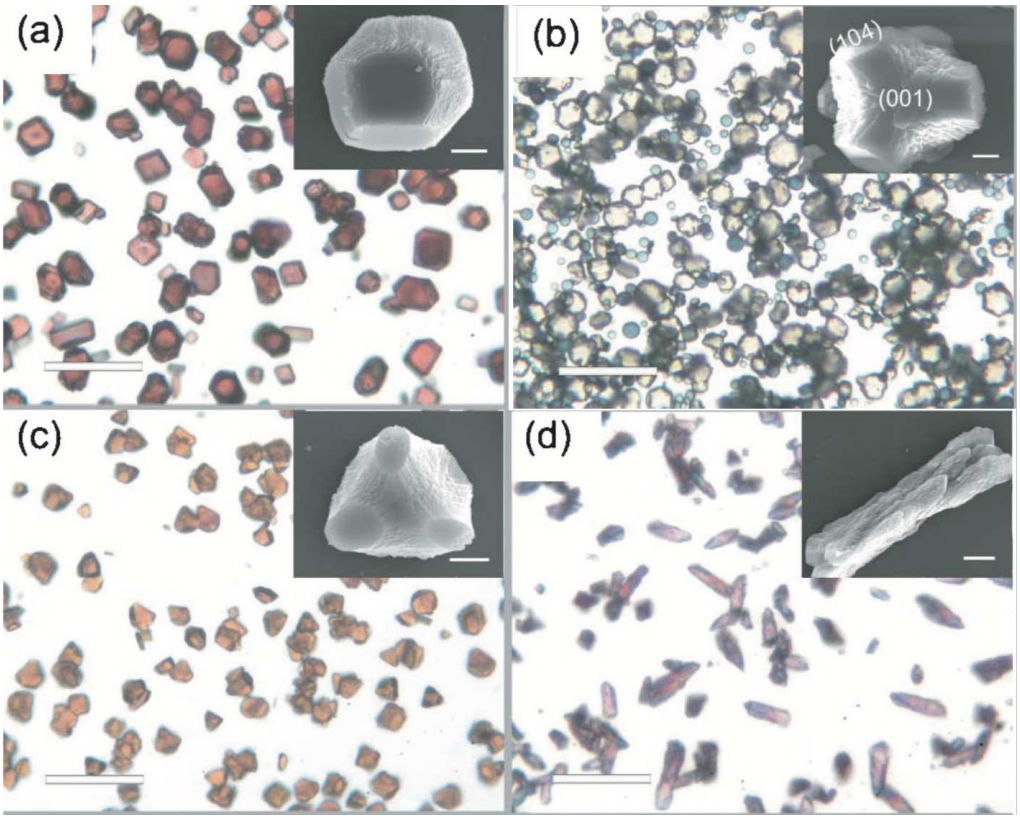

Figure 1.19. Optical micrographs and SEM images of calcite produced in the presence of (a) 1.50 g/L eosin Y, (b) 0.50 g/L methyl blue, (c) 2.00 g/L fluorescein sodium, (d) 0.25 g/L alizarin red S.(image adapted from (Shan *et al*., 2004))

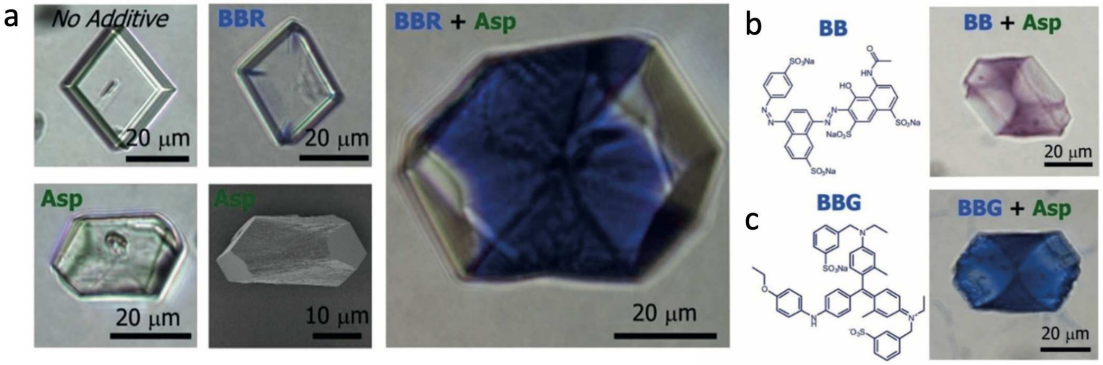

Figure 1.20. Calcite formed in the presence of a) Brilliant Blue R (BBR) with and without Asp (aspartic acid), b) Brilliant Black (BB) with Asp, and c) Brilliant Blue G (BBG) with Asp (adapted from (Marzec *et al*., 2018)).

1.4. Hybrid pigments

Hybrid pigments are composite materials consisting usually of two components: 1) organic dyes or pigments contributing to the color, and 2) mineral parts (clay, $CaCO_3$, silica, *etc*). These combined components interact synergistically, enhancing color effects, improved stability, and unique physical properties in various applications such as paints, coatings, plastics, and cosmetics.

1.4.1. Dyes and pigments

1.4.1.1. Definitions, classification, and mechanisms behind color

Dyes are vibrant compounds that dissolve in the media used during the dyeing procedure, imparting color through the selective absorption of light. They have the ability to blend with the medium they are applied to, such as textiles or liquids. Pigments are finely divided solid substances, either organic or inorganic (Singh and Bharati, 2014). Unlike dyes, pigments are typically insoluble in the medium they are incorporated into and remain chemically unaffected. They exist as discrete particles, adding color and visual appeal to various materials, such as paints, plastics, and inks (Broadbent, 2001; Gürses *et al*., 2016). Figure 1.21 showcases the classification and distribution of organic and inorganic colorants, including pigments and dyes, while Figure 1.22 displays the different families of organic pigments commonly used.

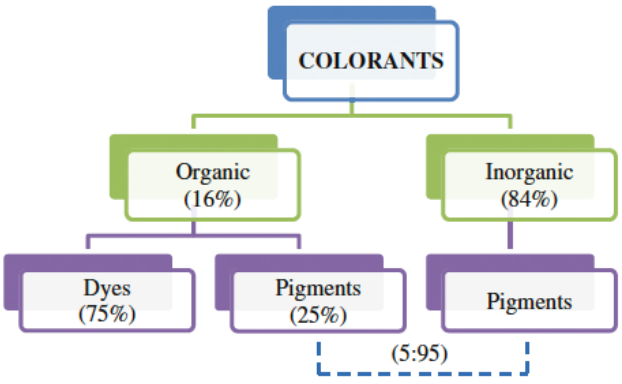

Figure 1.21. Illustrating the distribution of colorants, with the percentage indicating the proportion contributing to their usage (adapted from (Gürses *et al*., 2016)).

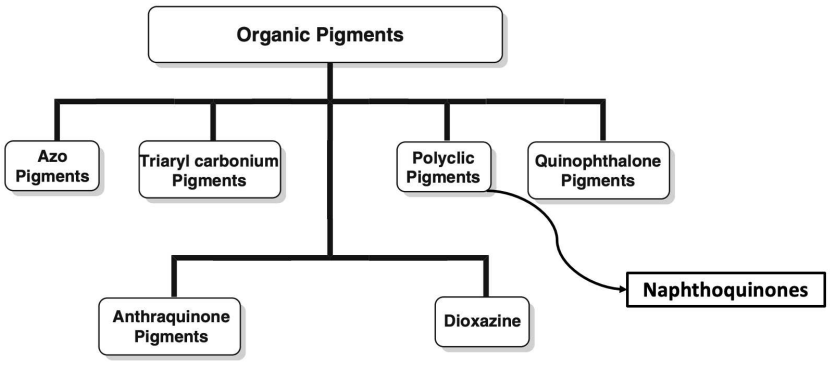

Figure 1.22. Classification of organic pigments (image adapted from (Gürses *et al*., 2016)).

Color is highly influenced by a substance's chemical and physical characteristics and arises from the intricate interplay between light and matter. When light interacts with an object, it undergoes a process known as absorption and reflection. The surface of the object absorbs certain wavelengths of light while reflecting others, giving rise to the perception of color. The specific chemical composition and physical properties of the substance determine which wavelengths of light are absorbed and which are reflected, thereby determining the color we observe (Broadbent, 2001).

When a molecule absorbs electromagnetic radiation in the UV or visible regions, an electron within it becomes excited and moves to a higher energy level. A chromophore, such as C=C, C≡C, C=O, C≡N, N=N, NO_2, *etc*., is a covalently unsaturated group responsible for this absorption. If a compound absorbs light in the visible region, it appears colored. However, the presence of a chromophore alone does not guarantee color; it depends on whether it absorbs visible or UV radiation. Chromophores with π electrons, like C=C or C≡C, undergo $\pi \rightarrow \pi^*$ transitions, while those with both π and non-bonding electrons, like C=O, C≡N, or N=N, undergo $\pi \rightarrow \pi^*$, $n \rightarrow \pi^*$, and $n \rightarrow \sigma^*$ transitions (Figure 1.23). Auxochromes, such as NH_2, -OH, -SH, halogens, *etc*., are covalently saturated groups that alter the absorption maximum wavelength and intensity when attached to a chromophore. They enhance color and extend conjugation *via* resonance. The combination of a chromophore and auxochrome creates a new chromophore with different absorption properties. For example, the addition of an OH group extends conjugation in phenol, resulting in increased absorption values (λ_{max} and ε_{max}) (Gürses *et al*., 2016).

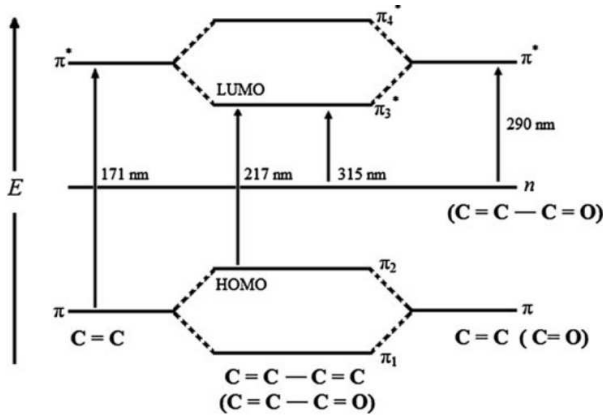

Figure 1.23. The relative energies of electronic transitions in conjugated systems refer to the varying energy levels associated with the movement of electrons within conjugated systems (adapted from (Gürses *et al*., 2016)).

1.4.1.2. Commercially available natural naphthoquinones and their properties

In our research, we faced the challenge of obtaining sufficient quantities of PHNQs through the extraction process, which is labor-intensive and results in low yields due to the low amount of PHNQs encapsulated in biominerals (< 0.1 wt.%).

To overcome this obstacle and enable us to perform a series of experiments, we turned to commercially available hydroxylated naphthoquinones (naphthazarin, lawsone, and juglone) (Figure 1.24). These compounds were chosen because they share a parent structure analogous to PHNQs, making them suitable substitutes for our research purposes. They also bear a few hydroxyl groups, allowing us to study the influence of the number and positions of -OH on $CaCO_3$ growth.

Naphthoquinones are naturally occurring compounds that are produced by bacteria, fungi, and higher plants as part of their metabolic processes and defense mechanisms (Babula *et al*., 2009; War *et al*., 2012). These compounds (Figure 1.24), particularly derivatives of 1,4-naphthoquinone such as juglone, lawsone, and naphthazarin, have been extensively studied in the fields of biology and medicine, both in their natural forms and as synthetic derivatives.

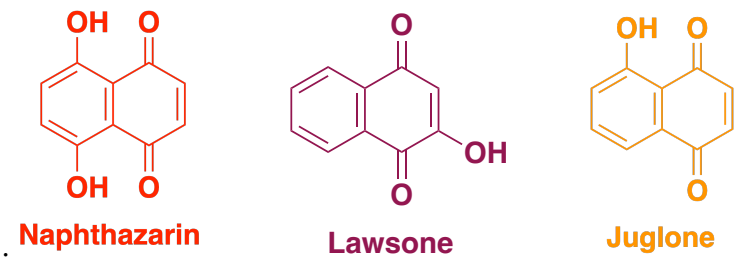

Figure 1.24. Chemical structure of commercially available naphthoquinones.

Naphthazarin: Naphthazarin, a member of the 1,4-naphthoquinone family, is naturally synthesized in various plant species belonging to the *Boraginaceae, Droseraceae*, and Nepenthaceae families. These plants produce naphthazarin and other secondary metabolites as a part of their defense mechanism against herbivores, as they possess inherent toxic properties that directly affect insect-infested plants (Devi *et al*., 2016). The initiation of redox cycles and the subsequent generation of reactive oxygen species (ROS) contribute to the toxic effects. These reactive molecules disrupt cellular processes and cause oxidative stress, ultimately impairing insect survival (Duffey and Stout, 1996). Interestingly, the synthesis of quinone derivatives, including naphthazarin, is often triggered as a response to herbivorous attacks. When plants are subjected to stress caused by herbivory, their secondary metabolism pathways become activated, producing defensive compounds (Eilenberg and Zilberstein, 2008). This makes them promising candidates for applications in biopesticides and bioherbicides (Dayan and Duke, 2014). Researchers have been particularly interested in naphthazarin and its derivatives due to their exceptional anticancer, anti-inflammatory, antibacterial, and antifungal properties. (Kim *et al*., 2015; Shen *et al*., 2002; Zhang *et al*., 2017).

Lawsone: Hydroxynaphthoquinones, such as lawsone (2-hydroxy-1,4-naphthoquinone), have gained recognition for their remarkable chemical and pharmacological properties (Lamoureux *et al*., 2008). Lawsone, also known as the principal active ingredient in henna plants (El-Shaer *et al*., 2007; Saeed *et al*., 2013), is a natural dye with a red-orange color. Henna plants are native to tropical and subtropical regions of Africa, India, Sri Lanka, and the Middle East, growing as tall flowering shrubs or trees. It exists in three tautomeric forms: 1,4-naphthoquinone (most stable), 1,2-naphthoquinone, and 1,2,4-naphthotrione. The 1,4-isomer exhibits greater stability due to the cancellation of carbonyl group dipolar moments and intramolecular hydrogen bonds (Lamoureux *et al*., 2008). This stability and tautomeric equilibrium play a role in its chemical behavior and properties (Figure 1.25). Additionally,

lawsone possesses strong UV-absorbing properties, making its aqueous extracts effective sunscreens (Ashnagar and Shiri, 1941). Lawsone's unique properties as a cosmetic dye and sunscreen make it a versatile and valued substance in personal care and cultural practices.

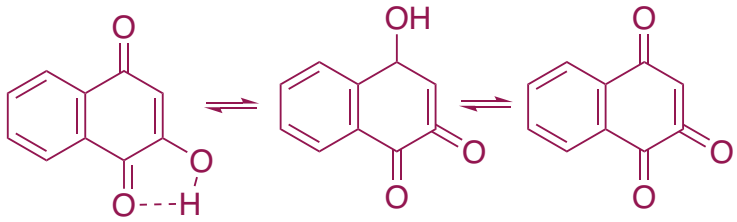

Figure 1.25. Depicts the three tautomeric forms of lawsone: 1,4-naphthoquinone (the most stable form), 1,2-naphthoquinone, and 1,2,4-naphthotrione.

Juglone: Juglone is found in walnut trees and other plant species and has diverse distribution in different parts of the tree. It is primarily produced by various walnut species, including *Juglans nigra, Juglans regia, Juglans sieboldiana*, and *Juglans cinerea*. Juglone is also present in Carya ovata, Proteaceae, Caesalpiniaceae, and Fabaceae (Colaric *et al*., 2005; Inbaraj and Chignell, 2004; Moir and Thomson, 1973). Juglans nigra is commonly used for juglone isolation and allelopathic studies due to its high juglone content (Soderquist, 1973).

Juglone displays diverse pharmacological effects, including depressant, anti-skin disease, antimicrobial, anti-cancer, anti-fungal, antioxidant, apoptotic, and anti-angiogenesis activities (Auyong *et al*., 1963; Clark *et al*., 1990; Fang *et al*., 2018; Liu *et al*., 2017; Wang *et al*., 2017). Juglone displays both pro-oxidant and antioxidant properties. It can generate reactive oxygen species (ROS) while also acting as a metal chelator, particularly for Fe^{2+}. Chelation prevents metal-catalyzed oxidation and contributes to its antioxidant effects. It also inhibits food degradation by resisting oxygen and reactive species (Bentes *et al*., 2011; Galano *et al*., 2016; Leopoldini *et al*., 2004; Tamafo Fouegue *et al*., 2016).

1.4.1.3. Halochromic properties of naphthoquinones: case of naphthazarin

Naphthoquinones are compounds with pH-dependent properties that demonstrate varying protonation states in different pH conditions. In mildly acidic and neutral pH, they exist as fully protonated. As the pH increases, naphthoquinones can undergo deprotonation, forming deprotonated species that change the solution's color (Figure 1.26). In the case of naphthazarin, it exists as fully protonated (NH_2) in mildly acidic and neutral pH. As the pH increases,

naphthazarin undergoes deprotonation, forming NH^- or N^{2-} species (Figure 1.26) (Land *et al*., 1983). Naphthazarin possesses two pKa values, with the first pKa around 7.8, indicating the dissociation of its first proton in slightly acidic conditions. The second pKa, approximately 10.7, represents the dissociation of its second proton at a higher pH (Land *et al*., 1983).

The color of a naphthazarin solution changes with pH variations. In mildly acidic and neutral pH ranges, the solution appears rose-red. In dilute alkali solutions, it exhibits a blue-violet color, while in strong alkali solutions, it turns deep blue. The observed color changes can be attributed to the electronic transitions occurring within the molecule. This color is a result of the absorption of certain wavelengths of light by the conjugated π-electron system within the molecule. However, under specific conditions or upon exposure to certain factors, naphthoquinones can change their electronic structure, leading to alterations in their absorption and reflection of light. Furthermore, the ionization of each hydroxy group in naphthazarin influences its optical absorption spectrum (Figure 1.26). As the hydroxy groups undergo ionization with increasing pH, the visible absorption band shifts towards longer wavelengths (redshift), and the extinction coefficient increases. This pH-dependent spectral behavior provides valuable insights into the electronic properties of naphthazarin and its interaction with its surroundings.

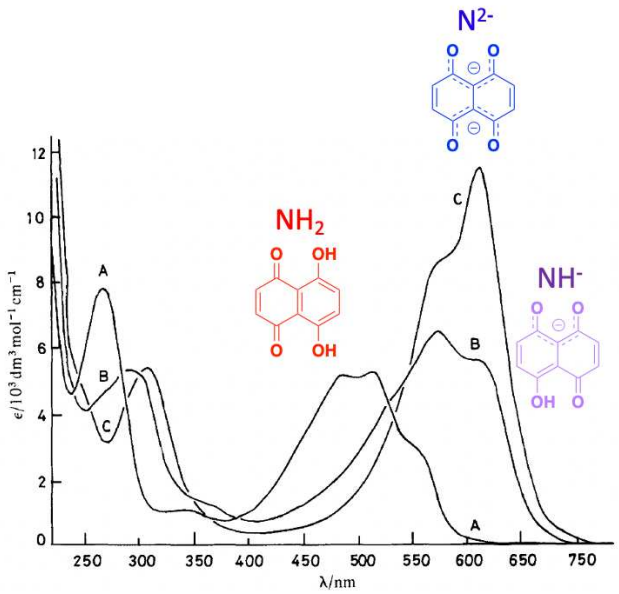

Figure 1.26. The absorption spectra of naphthazarin in aqueous solutions correspond to a specific pH condition. The spectrum A represents the absorption of naphthazarin in its fully protonated form (NH_2) at pH 4.3. Spectrum B shows the absorption of naphthazarin in the NH^- form at pH 9.5, indicating deprotonation of the compound. Finally, the spectrum labeled C, the absorption of naphthazarin in the N^{2-} form at approximately pH 11.5 (image adapted from (Land *et al*., 1983)).

1.4.2. Example of hybrid pigments and remarkable stability

Historical use of hybrid pigments dates back to antiquity, exemplified by the composite pigments adorning the Lascaux cave frescoes (13,000 BC). Each component served a distinct role: iron oxide for color, aluminosilicate clays for medium, and organic binders (marrow, fat, urine, saliva, blood) within clays for structural and chromatic effects. Silicates, predominantly clays, and various minerals, including metal oxides and carbonates, were pivotal inorganic precursors for hybrid materials, chosen for their abundance, malleability, and enhancement potential through organic integration. Figure 1.27 provides the timeline for the advancement in hybrid materials, including hybrid pigments.

Maya Blue, a pigment revered for its use by the Yucatan Maya civilization, has captivated the attention of researchers due to its remarkable durability (Morris *et al*., 1931). It is composed of indigo, which gives rise to the color, and palygorskite, which forms an integral part of its

composition (Figure 1.28). It has been proposed that attapulgite and natural indigo synergistically interact to bestow Maya Blue (Morris *et al*., 1931).

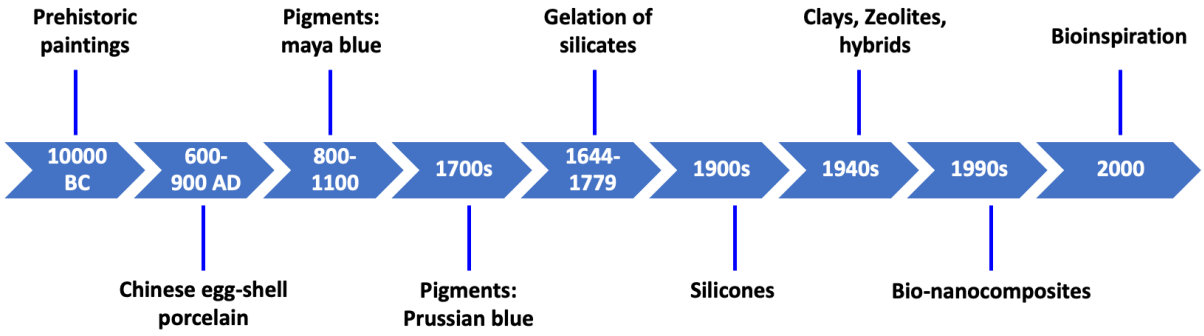

Figure 1.27. Chronicle of the progression and multidisciplinary advancement of organic-inorganic hybrid materials over time.

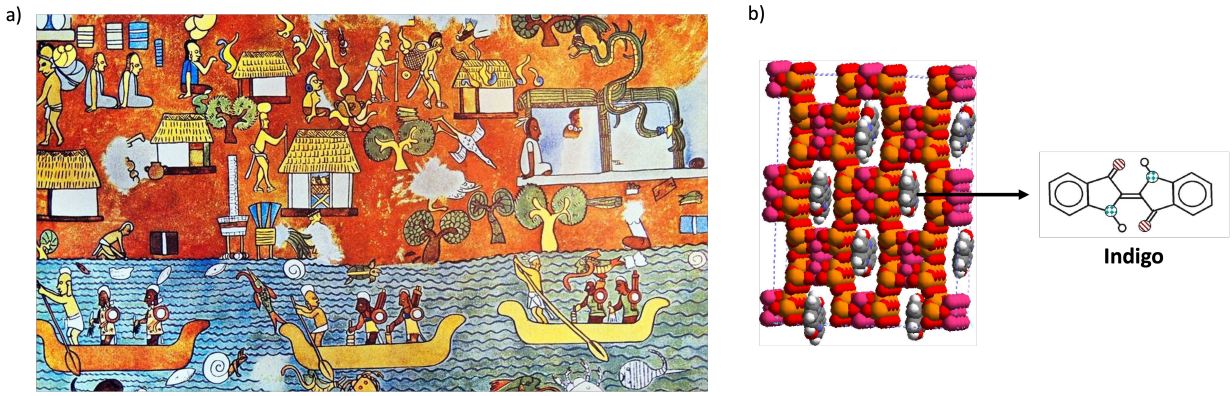

Figure 1.28. a) 1,600-year-old Mayan temple murals in Chichén Itzá retain vibrant, unfading blue colors, b) possible structure of maya blue where indigo molecules sit in the channels of palygorskite (image adapted from (Polette-Niewold *et al*., 2007)).

Notably, its vibrant hue remains unaffected under the influence of elevated temperatures, light, and potent concentrated mineral acids. On the one hand, (Hubbard *et al*., 2003) proposed that indigo molecules coat clay channel entrances and are attached *via* hydrogen bonding to silanol groups at micropore borders. On the other hand, (Fois *et al*., 2003) hypothesized that indigo molecules replace water within channels, assuming stable positions. It has also been suggested that the photostability of the Maya blue could be due to the photostability of the indigo molecule itself due to its planarity in trans geometry (Volkov *et al*., 2020).

1.4.3. Recent developments in hybrid pigments

Hybrid pigments result from combining organic or inorganic compounds sourced from nature/synthetic with other materials. This blending enables the creation of pigments with diverse colors, enhanced stability, and unique properties beyond traditional options. These pigments have garnered interest for their potential applications in cosmetics, textiles, paints and coatings, printing inks, biomedical, and food industries, offering sustainable and eco-friendly alternatives to conventional synthetic pigments and appealing to environmentally conscious practices (Sanchez *et al*., 2011).

For example, Ghannam *et al*. (2008) synthesized a range of vibrant P(S-co-A)-mica pigments *via* nitroxide-mediated polymerization directly onto mica's surface. These pigments, offering tunable colors, find applications as fillers in cosmetics and coatings when incorporated into nitrocellulose or acrylic bases. The color spectrum was intricately linked to macromolecular chain adsorption density and dye concentration, further fortified by covalent bonding between dye and polymer to prevent bleeding. Notably, extended polymerization time amplified color variations due to the proximity of the dye to the surface and its interaction with oxanions. Another example from Joubert *et al*. (2009) discerned that controlling anchored chain length and optimizing the styrene/dye ratio proved pivotal for creating colored hybrid materials, effectively mitigating light reflection and color consistency challenges. By adsorbing flavylium cations onto synthetic clays, (Silva *et al*., 2020) produced hybrid pigments with enhanced thermal stability and reduced color changes at higher pH. Interlayer adsorption in clay contributes to these improved properties, suggesting its potential as a matrix for durable and vibrant hybrid pigments based on cationic plant pigment analogs.

In another study, (Kogo *et al*., 2022) synthesized $CaCO_3$ employing food dye as a benign additive suitable for human use, further investigating the influence of citric acid on this hybrid material by reacting a prepared $Ca(OH)_2$ suspension with CO_2 gas (Figure 1.29). The incorporation of citric acid intricately impacted the crystallinity and morphology of the resulting calcite particles. Through the integration of dye during the synthesis process, $CaCO_3$ with diverse shapes and hues was successfully obtained.

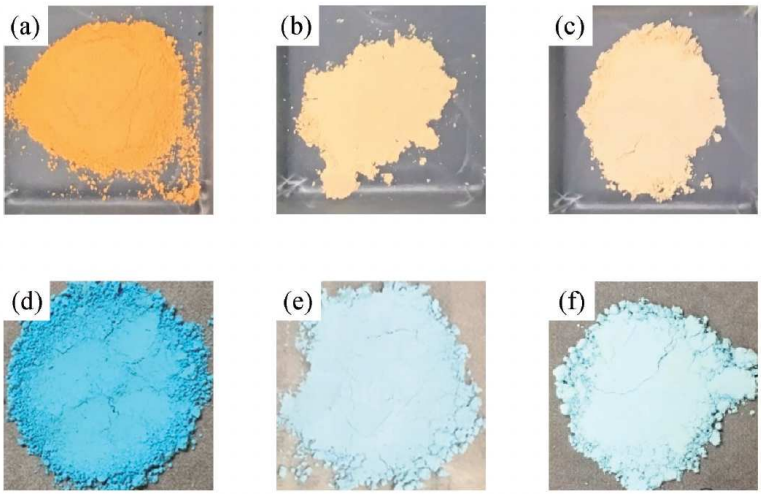

Figure 1.29. $CaCO_3$ with distinct colors produced through carbonation, with the introduction of dyes; (a), (b), (c): Sunset Yellow FCF, with citric acid aqueous solution additions of 0 cm^3, 5 cm^3, and 8 cm^3, respectively; (d), (e), (f): Brilliant Blue FCF, with citric acid aqueous solution additions of 0 cm^3, 5 cm^3, and 8 cm^3, respectively.

Exploring the field of ink-jet printing paper, Yoo *et al*. (2009) harnessed eggshell calcium carbonate particles as coating pigments. Their incorporation led to heightened optical density for cyan, magenta, and yellow inks, albeit resulting in reduced black ink density and paper gloss. Moreover, the potential of $CaCO_3$ as an environmentally friendly and cost-effective wastewater-sorbing material was underscored. (Zhao and Gao, 2010) effectively demonstrated $CaCO_3$'s proficiency as a sorbing agent through the occlusion of waste dye, shedding light on its promising applications in waste treatment. In another study by (De Queiroga *et al*., 2019), functionalized bentonites were obtained through microwave-assisted silylation at 50°C for 5 minutes, followed by glutaraldehyde treatment. Hybrid bentonites were then utilized as hosts for adsorbing the organic dye Violet 5R, serving both environmental applications and pigment creation. They successfully demonstrated robust pigment stability, enduring 450 hours of light exposure without significant photodegradation.

Recent advancements in hybrid pigments have sparked interest in harnessing nature-inspired solutions for coloration. The need for these developments arises from the demand for sustainable and environmentally friendly pigments. To address this, researchers are exploring modifications to enhance pigment properties, including color stability and durability. The majority of research in the field of hybrid pigments has predominantly utilized silica or clay as matrices. However, there is a growing interest in exploring calcite as a viable alternative as, in

nature, organisms create colorful and stable $CaCO_3$ biominerals, and this natural inspiration suggests that calcite could be a promising medium for bio-inspired pigment development.

This doctoral research aims to elucidate the physicochemical mechanisms behind the chromatic manifestation of sea urchin spines, potentially involving ACC precursors and naphthoquinone pigments. It also seeks to understand the incorporation of naphthoquinones into calcite, forming stable biogenic hybrid pigments. Additionally, the study aims to propose bio-inspired pigments for textile finishing. The research investigates the impact of naphthoquinones on ACC composition and explores organic-inorganic interactions in hybrid pigments.

2

Methodology

In this chapter, we describe the different methods used to synthesize the $CaCO_3$-naphthoquinone samples, both amorphous and crystalline, and the wide range of multiscale techniques used to characterize them. The complementarity analytical techniques employed here provided valuable comprehension of the composition, the color, the local structure, the atomic and molecular inorganic-organic interactions, and the nano-spatial distribution of the naphthoquinone pigments within the $CaCO_3$ crystals. This exploration unveils the origin of color variations during ACC crystallization and gives insights into the mechanisms of pigment incorporation within calcite crystals having stable-colored materials, ultimately contributing to a better understanding of biomineral pigmentation and the development of innovative and biohybrid pigments inspired by nature.

2.1 Bioinspired approach: direct precipitation synthesis and vapor diffusion method for $CaCO_3$ synthesis

Various synthesis techniques are available in synthesizing calcite through amorphous calcium carbonate (ACC) precursors (Niu *et al*., 2022). These methods differ, *e.g.,* in terms of the solvents used, the mixing procedure, the initial concentrations of the reactants, the presence of organic or inorganic additives and the handling/storage of the end products, which in turn lead to distinct ACC formation pathways and stability against crystallization into different $CaCO_3$ polymorphs (Du *et al*., 2018; Du and Amstad, 2020; Niu *et al*., 2022). We here explored two main well-known $CaCO_3$ synthesis models (described in detail below) in the presence of biogenic or synthetic naphthoquinone pigments in order to: 1) assess the mechanisms behind the origin of color variations in calcitic sea urchin biominerals known to be formed through ACC precursors; 2) study the potential role of naphthoquinone pigments on biomineralization pathways, and 3) allow for the development of biohybrid pigments with stable colors similar to sea urchin spines.

The biogenic naphthoquinones considered in this work are the ones found in sea urchins, *i.e.,* polyhydroxylated naphthoquinones (PHNQs). Because PHNQs are not commercially available, they were previously extracted from *P. lividus* biominerals as a mixture or pure compound (see Section 2.2.1). However, their extraction is a tedious process that yields only ~0.1 wt.%, the actual amount in *P. lividus* sea urchin spines. Therefore, synthetic and commercially available naphthoquinones exhibiting analogous structures to PHNQs were also extensively used. Also found in nature (Majdi *et al*., 2023), we chose to work with singly or doubly hydroxylated naphthoquinones (lawsone, juglone, and naphthazarin), which allows for a thorough investigation of the different $CaCO_3$–naphthoquinone syntheses and study the effect of the position and the number of hydroxyls on the mechanisms cited above.

The first $CaCO_3$ synthesis extensively investigated here was the direct precipitation method using water as the primary reaction medium. It allows for the production of stable ACC nanoparticles and subsequent crystalline $CaCO_3$ that, in our case, were synthesized in the presence of the different naphthoquinone pigments. In general, the ACC-naphthoquinone samples were obtained at around 30 s of the reaction, and the subsequent crystalline polymorphs after a few minutes (vaterite+calcite) up to several hours (calcite). This method is widely used (Rodriguez-Blanco *et al*., 2011; Tobler *et al*., 2016, 2015, 2014; Zou *et al*., 2015)

and allows for controlling particle size, crystal shape, and crystallinity degree, making it suitable for tailored material synthesis (Niu *et al*., 2022). In addition, it is relatively simple, green, cost-effective, and requires minimal specialized equipment. In addition, by using more specialized equipment such as a titration system, *e.g.,* by Metrohm® (see Section 2.4.1), ACC synthesis can be more controlled, *e.g.*, in terms of particle size distribution and be more reproducible. Finally, the simplicity of this technique allowed us to modify different parameters such as pH, and concentration of reactants and introduce various organic pigments to investigate their influence on the formation, stability, and crystallization behavior of $CaCO_3$.

The second method investigated was the vapor diffusion method, also called the ammonium carbonate degradation method. This method provides a versatile platform to tune the reaction conditions and explore various crystalline $CaCO_3$ phases (Liu *et al*., 2016), such as calcite and vaterite, in our case. This method is very common to study the effect of organic molecules on crystal growth (Aizenberg *et al*., 1997; Berman *et al*., 1988; Falini *et al*., 1996; Marin *et al*., 2005; Marzec *et al*., 2018). In particular, we used it to study the role of naphthoquinone pigments on $CaCO_3$ crystal morphology and color. Notably, this method also goes through ACC precursor (Ihli *et al*., 2013). Ihli *et al.* showcased that under slow growth conditions in vapor diffusion, where monocrystals are found, new material continues to form after the initial ACC nucleation. In addition, we could explore various concentrations of naphthoquinone pigments by increasing the pH of the starting solution, as naphthoquinone pigments are known to be poorly soluble in water, in particular at acidic pH (Land *et al*., 1983). Their solubility can drastically increase at alkaline pH. This approach provides valuable insights into the complex interplay between organic pigments and $CaCO_3$, leading to a deeper understanding of the underlying mechanisms governing the ultimate incorporation of these molecules within calcite.

2.2. Materials

2.2.1. Pigment molecules

Biogenic naphthoquinones

PHNQs were obtained from *Paracentrotus lividus* sea urchin spines from the Roscoff Biological Station (France). PHNQ molecules were extracted by Claudio Dos Reis Ferreira (PhD student) and Mathilda Béarez (L2 student) at the LCMCP. Briefly, the extraction performed by Claudio Dos Reis Ferreira from purple spines involves a first mild dissolution of

the $CaCO_3$ mineral phase with dilute acetic acid. Second, an acid-soluble matrix (ASM) and an acid-insoluble matrix (AIM) fractions are separated by centrifugation, both comprising macromolecules such as proteins, polysaccharides, and lipids that are complexed to PHNQs (patent application: PAT 2616615PC00, Albéric *et al.* in preparation). The ASM fraction is further separated by ultrafiltration in ASM > 1kDa and ASM < 1kDa. The ASM > 1kDa fraction is composed of PHNQ-macromolecule complexes, whereas the ASM < 1kDa is composed of free PHNQs that are isolated by ether extraction and further purified from small remaining molecules like peptides. In the case of purple *P. lividus* spines, the ASM<1kDa is mainly composed of spinochrome A (93%) with a small amount of spinochrome B (3%) and C (4%) (*Albéric et al.*, in preparation). This fraction is referred to hereafter as spinochrome A. The process of extracting PHNQs from sea urchins has been detailed in the article by Albéric *et al.* in preparation attached entitled "PHNQ-macromolecule complexes occluded within purple $CaCO_3$-biominerals of *Paracentrotus lividus* sea urchin spines". The manuscript is in progress and reported in Appendix 2. It includes crystalline $CaCO_3$ synthesis by direct precipitation and by vapor diffusion, which I performed in the presence of some PHNQs (Appendix 2 Figures 7 and 8 of the manuscript). Those results are also presented in Chapter 5 (section 5.3).

Mathilda Béarez performed another less delicate extraction from *P. lividus* green and purple spines. This protocol allows for the extraction of larger amounts of PHNQs together with some remaining macromolecules. It consists of a dissolution by HCl 6M and ether extraction. This fraction was used to synthesize the bio-hybrid pigments submitted to textile finishing (Chapter 5, part 5.3).

Finally, pure spinochromes B, C, D, E, and echinochrome A were also extracted by and then obtained from Dr. Elena Vasileva from the Pacific Institute of Bioorganic Chemistry (Vladivostok, Russia) (Hou *et al*., 2018a; Vasileva *et al*., 2021).

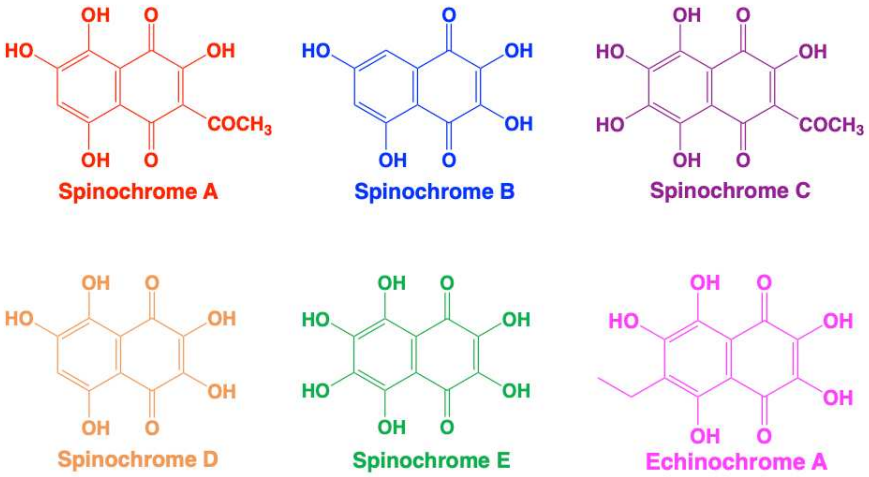

Figure 2.1. The chemical structures of pigments found in the sea urchins: Spinochromes and echinochromes with IUPAC names.

Synthetic naphthoquinones

Naphthazarin (5,8-Dihydroxynaphthalene-1,4-dione), lawsone (2-Hydroxynaphthalene-1,4-dione), and juglone (5-Hydroxynaphthalene-1,4-dione) were purchased from Sigma Aldrich.

As mentioned earlier, naphthoquinones' solubility depends on pH and the solvent. It is especially true for naphthazarin, which was extensively used in this work. Therefore, we measured the different solubilities for naphthazarin according to pH in water and in ethanol (Table 2.1). The solution turns red in an acidic environment and shifts to purple at a basic pH of 11.5, accompanied by a tenfold increase in solubility. In the case of lawsone, the solubility is much higher in water than in juglone and naphthazarin. The solubility of juglone in water is very similar to that of naphthazarin and increases with pH.

Table 2.1. Solubility of naphthazarin in water at different pH and in ethanol:

pH	Solubility	Color	Solubility in ethanol
11.5	2.2 mM	Dark blue	0.63 mM
9.0	0.36 mM	Purple with blue shade	
6	0.18 mM	Pinkish red	

2.2. Chemicals

The reagents utilized in the experimental procedures were purchased from Sigma-Aldrich and Carl Roth and used as received. These included naphthazarin ($C_{10}H_6O_4$), calcium chloride dihydrate ($CaCl_2.2H_2O$), sodium carbonate (Na_2CO_3), ammonium carbonate ($(NH_4)_2CO_3$), sodium hypochlorite (NaOCl) with varying concentrations of active chlorine (ranging from 6% to 14%), sodium hydroxide (NaOH) solution at a concentration of 1M, hydrochloric acid (HCl) at a concentration of 37%, deuterated water (D_2O), absolute ethanol, and 96% ethanol. NaOCl with 12% active chlorine was obtained explicitly from Carl Roth. We utilized water purified using a Millipore Milli-Q® Integral 10 water purification system, guaranteeing the removal of impurities.

2.4. $CaCO_3$ Synthesis

2.4.1. ACC-naphthoquinones synthesis by direct and fast precipitation at pH ~10.2-10.6 or pH 12.5

Stable ACC-naphthoquinone samples were synthesized by fast and direct precipitation following the ACC synthesis used in Zou *et al.,* 2015 where they investigated the impact of particle size on ACC stability. They evidenced that ACC particles with a smaller average size (66 nm) display higher stability against crystallization compared to larger particles (200 nm). As a result, the synthesis conditions highlighted in green in Table 2.2 were chosen for our study, as they produced quite stable ACC particles with an average size of 73 nm ± 28 nm, allowing us to perform the different experiments and characterization of the ACC-naphthoquinone samples described in Section 2.7.

Table 2.2. Summary of Experimental Conditions Zou *et al.,* 2015 (Zou *et al*., 2015)

Approximate particle size	$CaCl_2$ solution		Na_2CO_3 solution		Solution after mixing and before precipitation		
	$CaCl_2$ (M)	Volume (mL)	Na_2CO_3 (mM)	Volume (mL)	$CaCl_2$ (mM)	Na_2CO_3 (mM)	Volume (mL)
200 nm	1	0.25	0.25	49.75	5	5	50
120 nm	1	0.5	0.5	49.5	10	10	50
87 nm	1	1	1	49	20	20	50
73 nm ± 28 nm	1	2	2	48	40	40	50
66 nm	1	5	5	45	100	100	50

Following the Zou *et al.* 2015 procedure, ACC was first synthesized at pH 10.2 to 10.6, depending on naphthoquinone concentrations. Two stock solutions of $CaCl_2.2H_2O$ and Na_2CO_3 were first prepared in ultra-pure Mili-Q water: 1) 212 mg of Na_2CO_3 was dissolved in a 48 mL water solution, resulting in a carbonate concentration of 40 mM and Naphthoquinones were dissolved in Na_2CO_3 solution. 1 M solution of $CaCl_2$ was prepared by dissolving 14.71 g of $CaCl_2.2H_2O$ in 100 mL of water. Subsequently, 2 mL of the 1M $CaCl_2.2H_2O$ solution was added (10 mL/min) to the prepared 48 mL solution of Na_2CO_3 under continuous stirring, resulting in the immediate precipitation of ACC. The precipitate was then filtered after 30 s of $CaCl_2$ addition using a Büchner filtration system with a 5-15 µm pore size sintered filter crucible of 50 mL. For Büchner filtration, Knf® type N860. 3FT.40.18 diaphragm vacuum pump with Pmax of 1.0 bar was used. In order to synthesize calcite, the reaction was left to stir for 48-72 hours, which allowed for ACC's crystallization into calcite+vaterite to calcite only. The filtered product obtained at this stage (30 s), was ACC, which was washed with cold absolute ethanol. The sample was collected in a vial or an Eppendorf and transferred to a desiccator under vacuum (Figure 2.2). ACC was washed with absolute ethanol to quickly remove the excess of water, which promotes crystallization and the excess of pigment loosely bound to the ACC nanoparticles. Figure 2.2 summarizes the different steps of the synthesis.

ACC synthesized at pH 12.5 was also considered as it was shown to crystallize in solution directly into calcite (Tobler *et al*., 2016) in contrast to ACC precipitated at pH 10.5, which first crystallizes into a mixture of calcite and vaterite before fully converting into calcite only. Here,

the pH of the 40 mM Na_2CO_3 solution was increased to pH 12.5 by the addition of 40 mM NaOH before the addition of 2 mL of the 1M $CaCl_2{\cdot}2H_2O$ solution.

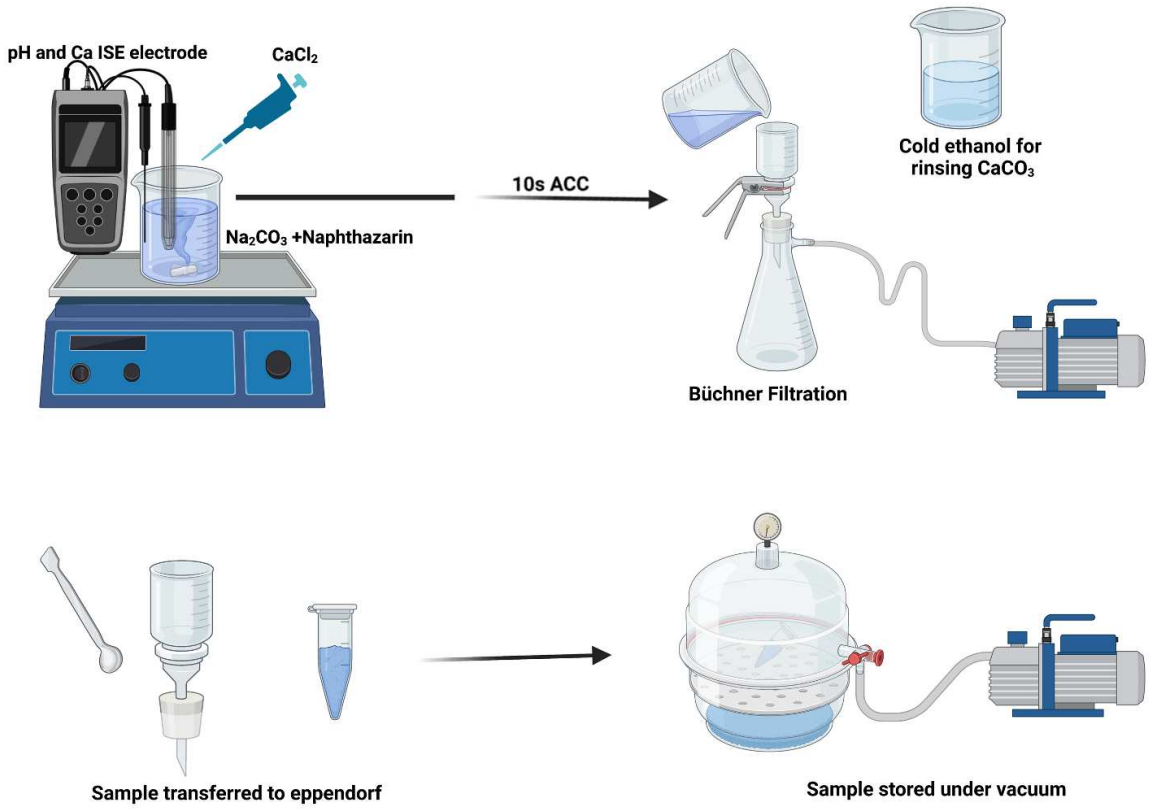

Figure 2.2. Schematic representation of steps involved in the fast direct precipitation synthesis of ACC.

Different concentrations of naphthoquinones (ranging from 0.004 mg/mL to 0.1 mg/mL) were added to the reaction mixture along with Na_2CO_3 before the $CaCl_2{\cdot}2H_2O$ solution was added under stirring. This resulted in the precipitation of $CaCO_3$ with varying colors depending upon the naphthoquinones used. For example, naphthazarin results in shades of blue, from dark blue to periwinkle blue, juglone results in a pinkish orange shade, and echinochrome A in a light orange shade.

2.4.2. ACC-naphthoquinones crystallization into calcite-naphthoquinones

ACC crystallization into calcite was induced in solution and in air by mild-heating to simulate the dissolution-reprecipitation mechanism respectively (Rodriguez-Navarro *et al*., 2014; Zou *et al*., 2015) and the solid-state transformation (Weiner and Addadi, 2011) observed in biominerals. The ACC-naphthoquinone samples' crystallization was induced to investigate the

effect of the different naphthoquinone molecules on ACC crystallization mechanisms and their further incorporation during crystal growth.

2.4.2.1. Thermally-induced crystallization

To thermally induce ACC crystallization, we employed either a Nabertherm oven (20-3000 °C) or a Linkam heating FTIRSP600 stage for *in-situ* measurements (Figure 2.3). The temperature gradually increased at a rate of 5 °C per minute, from 20 to 430 °C. The Linkam stage is equipped with T95 controllers that enable precise temperature control across an extensive temperature range, from below -195°C to 600°C. Furthermore, the Linkam stage is equipped with distinct ports for the circulation of both water and liquid nitrogen, allowing for individual management of cooling rates. This system permits the adjustment of heating and cooling rates, with the capability to increase them to as high as 150° C per minute. This system is provided with the LINK software, which enables us to operate it.

Within the Linkam stage, there is a central opening where we affix a copper plate that possesses a hole in its center, and this central cavity is filled with ACC. The ACC material within the plate is precisely aligned with the central aperture, as depicted in Figure 2.3. This aperture allows the X-ray beam to traverse the sample before being scattered and reaching the detector. This setup facilitates the detailed analysis and the collection of data during the experimental process.

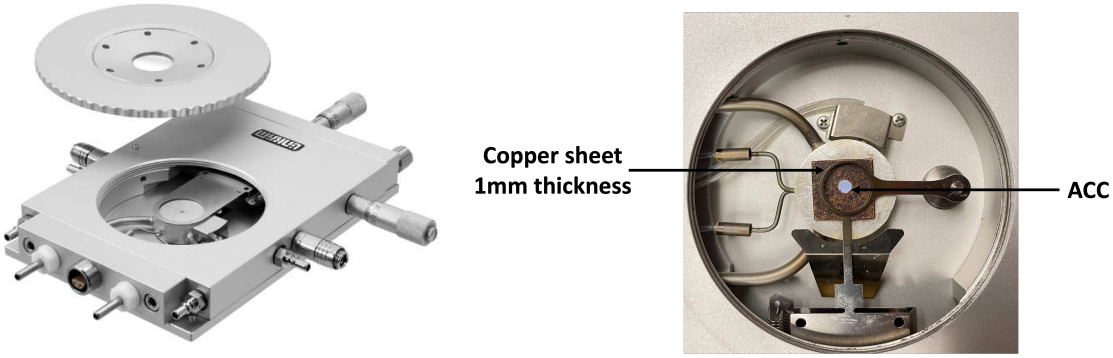

Figure 2.3. FTIRSP600 for vertical mounting in horizontal beam spectrometers at ESRF ID22, incorporating a vertical sample holder to induce ACC crystallization by heating.

2.4.2.2. Crystallization in solution

Water plays a crucial role in the crystallization process of amorphous calcium carbonate (ACC) (Du and Amstad, 2020). ACC crystallization in water at pH 10.2-10.6 was performed by continuously stirring the reaction mixture for 48 to 72 hours, during which ACC crystallizes first into a mixture of calcite and vaterite (~ 2-5 min) that further converts into calcite only. At pH 12.5, the reaction mixture was stirred for 20 minutes for the direct crystallization of ACC into calcite. The reaction mixture was then filtered using a 5-15 μm pore size sintered filter crucible of 50 mL. The powder was then collected and stored under vacuum in a vial.

2.5. $CaCO_3$ synthesis setups

2.5.1. The Metrohm® setup

ACC and its crystallization were synthesized extensively with the Metrohm Titrando setup (Figure 2.4). It allows for the automatic addition of $CaCl_2$ into the Na_2CO_3 solution at specific rates and intervals thanks to motorized pumps (Dosing units). In addition, pH and Ca^{2+} concentration can be monitored *in-situ* during the reaction with a pH electrode and a Ca^{2+} Ion Selective Electrode (ISE) electrode that is controlled with the Tiamo software associated with the setup. The setup includes pH module 867, which is for measuring pH, temperature, mV, Ipol, Upol, and concentration, the pH Module controls standard additions (manual, dosed, and automated dosing). The pH Module is equipped with the most significant bits (MSB) interfaces for connecting stirrers or Dosinos.

Figure 2.5 showcases the pH and [Ca^{2+}] profile obtained during the synthesis of $CaCO_3$. The pH and [Ca^{2+}] profile highlight the different events, *i.e.,* ACC formation (70 s), evolution of ACC (100-390 s), and crystallization of ACC into calcite+vaterite mixture(390-420 s).

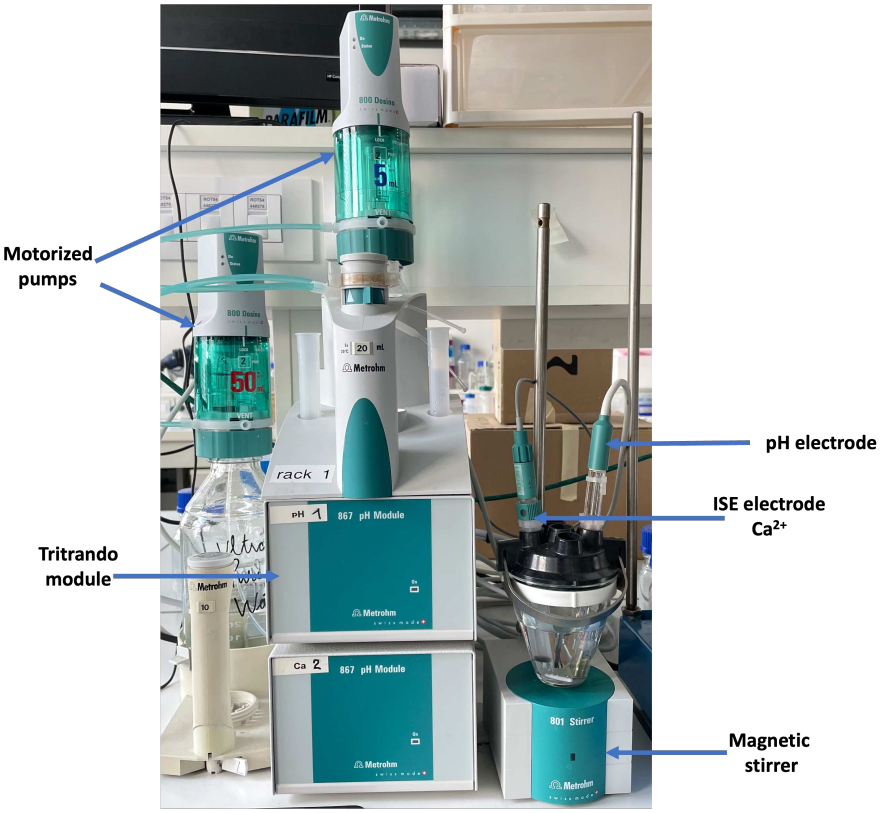

Figure 2.4. A detailed illustration of the metrohm® setup used for *in-situ* pH and [Ca^{2+}] measurement during $CaCO_3$ synthesis**.**

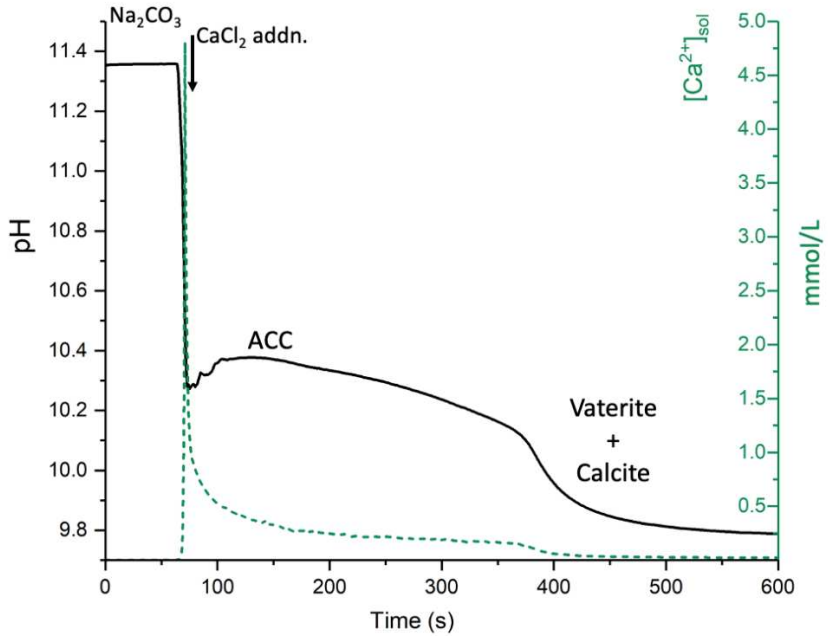

Figure 2.5. pH and [Ca^{2+}] profile obtained during the $CaCO_3$ synthesis highlighting ACC formation and its crystallization.

2.5.1.1. Calibration of the pH and Ca-ISE electrodes

The pH electrode was calibrated using pH 4.01, pH 7.00, and pH 9.21 standard buffers to ensure accurate measurements. The Ca-ISE was calibrated using different Ca^{2+} solutions (0.1 mM, 1 mM, 10 mM, and 50 mM) that were adjusted to pH 10.5-11.0 using 1 M NaOH solution. It is important to note that ion-selective electrode measurements are influenced by ionic strength, temperature, and pH, so the calibration solutions were carefully selected to be as close as possible to the experimental conditions. Before and between each experiment, the electrodes were thoroughly washed with 0.1 M acetic acid, rinsed with double-distilled water, and recalibrated to maintain accuracy.

For all the experiments (calibration and synthesis), [Ca^{2+}] and pH potentiometry curves were recorded by taking measurements every 0.1 or 1 second, depending on the total duration of the experiment. For the $CaCO_3$ synthesis reaction, both the calcium and pH electrodes were initially immersed in the calcium solution. Once the readings for both the calcium potential and pH stabilized (typically after 1 to 5 minutes), the reaction was carried out by adding $CaCl_2$ into Na_2CO_3 solution under a continuous magnetic stirring rate (300 rpm) to initiate the reaction.

2.5.1.2. pH electrode

pH electrodes (Figure 2.6) operate based on the generation of an electrical potential between two liquids with different pH levels. The electrode measures the disparity in H^+ ion activities on either side of the glass membrane, leading to a difference in the number of ion pairs present and an imbalance in surface charge within the hydrated layers. The pH electrode is filled with a neutral solution containing an equal number of H^+ and OH^- ions. When the pH probe is immersed in a solution with a high concentration of H^+ ions, the H^+ ions permeate the glass membrane, resulting in a positive potential on the sensing electrode. Conversely, in an alkaline environment, the H^+ ions move out of the probe, causing an excess of OH^- ions within the probe. The developed potential within the probe is then measured by the pH meter and converted into a pH reading (Bolan and Kandaswamy, 2005).

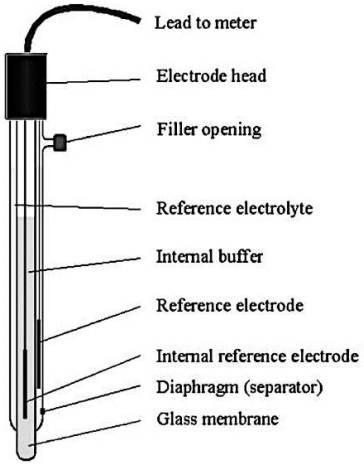

Figure 2.6. Schematic representation of the combined (the measuring electrode and the reference electrode into one unit) pH glass electrode used in the Metrohm® setup.

The pH-dependent potential developed across the membrane is described by the Nernst Equation (2.1), which mathematically relates the potential difference to the pH of the solution being measured.

$$E_{membrane} = E_{inner} - E_{outer} = 0.0592log\left[\frac{\mathcal{A}_{inner}}{\mathcal{A}_{outer}}\right] \quad (2.1)$$

where E_{inner} and E_{outer} are the surface potentials on either side of the membrane, and $\mathcal{A}_{nner}$ and $\mathcal{A}_{outer}$ represent the H^+ activities of the inner and outer solutions, respectively.

2.5.1.3. Calcium ISE electrode

The combined Ion Selective Electrode (ISE) is an electrochemical sensor composed of an internal reference electrode and measuring electrode (Figure 2.7).

ISE electrode has an Ion-Selective Membrane (ISM), which contains a selective ionophore embedded in a polymeric matrix. The ionophore selectively interacts with a specific target ion, allowing the ISE to detect that ion's concentration in the solution specifically. ISM allows only desired ions to go in and out. At equilibrium, no potential difference exists between the electrodes. The detector, which in this case is a potentiometer, measures the potential difference between the internal reference and the internal interface, which is indicative of the ion concentration in the sample solution.

In summary, an ISE is a type of sensor that translates the activity of a specific ion dissolved in a solution into a voltage (or potential) that can be measured in millivolts (mV). The measured electrode potential, E, is related to the activity of calcium ions [A] by the below as follows:

$$E = E_o + 2.303\frac{RT}{nF}\log[A] \quad (2.2)$$

Where E_o = a constant for a given cell, R = the gas constant, T = the temperature in Kelvin, n = the ionic charge.

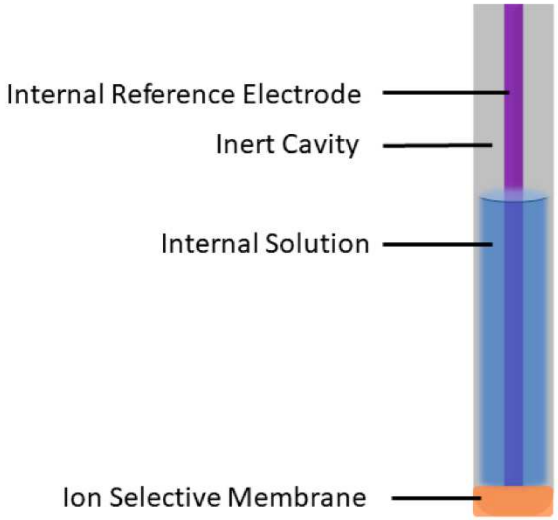

Figure 2.7. Schematic representation of the combined (the measuring electrode and the reference electrode into one unit) polymer membrane electrode (Ca^{2+} Ion selective electrode) used in the Metrohm® setup.

2.5.2. $CaCO_3$ syntheses at or for ESRF beamtime

2.5.2.1. ACC-naphthoquinones synthesis at ID15A

To conduct SAXS/WAXS measurements on ACC-naphthoquinones at the ID15a beamline, the experiments were carried out on-site, thus outside the Metrohm setup. Two beamtimes were performed from 28/01/2022 to 31/01/2022 and from 29/11/2022 to 02/12/2022.

Parameters for the synthesis: pipettes added 2 mL of 1M CaCl2 chloride solution to the reaction mixture (48 mL). The addition time was approximately equivalent to that of metrohm® titrando (10-12 s). The stirring speed was set to 300 rpm. The reaction mixture was

allowed to mix for 30s and then filtered using Büchner filtration. The sample was collected in a vial or Eppendorf and stored under vacuum for 30 minutes before performing measurements.

2.5.2.2. Calcite-naphthoquinone synthesis for ID22

To synthesize more than 50 samples for experiments at ID22 (ESRF) for HR-XRD measurements, multiple syntheses with different concentrations of pigments were performed at the same time. Therefore, these reactions were not carried in the Metrohm® setup but rather on a magnetic stirrer plate with multiple positions (Figure 2.8). Two beamtimes were performed from 29/03/2022 to 02/04/2022 and from 06/03/2023 to 09/03/2023.

Parameters for the synthesis: 2mL of 1M $CaCl_2$ chloride solution was added to the reaction mixture (48 mL) using pipettes. The addition time was approximately equivalent to that of metrohm® titrando (10-12 s). The stirring speed was set to 300 rpm. The pH of the reaction mixture evolved from 11.5 (40 mM Na_2CO_3 solution) to 10.2-10.5 (ACC) to 8.5 (calcite).

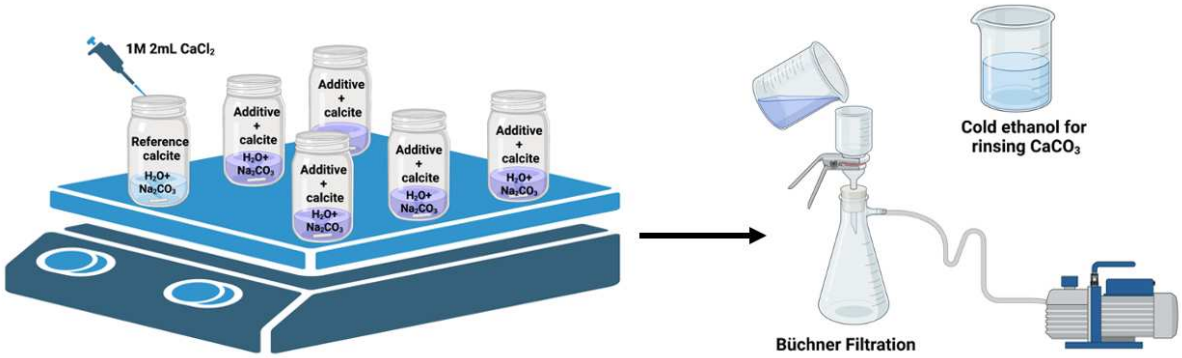

Figure 2.8. Schematic representation of different steps involved in the colored crystalline $CaCO_3$ synthesis by direct precipitation in H_2O.

2.6. $CaCO_3$-naphthoquinone synthesis by vapor diffusion

2.6.1. Mechanism of the reaction

1. Ammonium carbonate ($(NH_4)_2CO_3$) is a solid compound that breaks down upon exposure to heat or water (Figure 2.9). In this case, it degrades by dissolving in water, releasing two significant gases: ammonia (NH_3) and carbon dioxide (CO_2).

2. The vaporized NH_3 and CO_2 then dissolve into the acidic reactive solution, increasing pH as NH_3 reacts with H_2O to produce NH_4^+ and OH^- ions.

3. CO_3^{2-} ions are formed as CO_2 dissolves by reacting with H_2O to produce HCO_3^- and, eventually, CO_3^{2-}. This contributes further to the solution's alkalinity.

An increase in pH is a crucial aspect of the vapor diffusion method because it influences chemical reactions and drives the formation of specific compounds or complexes. This controlled pH environment is essential for the growth of desired crystals and the synthesis of specific compounds with unique properties.

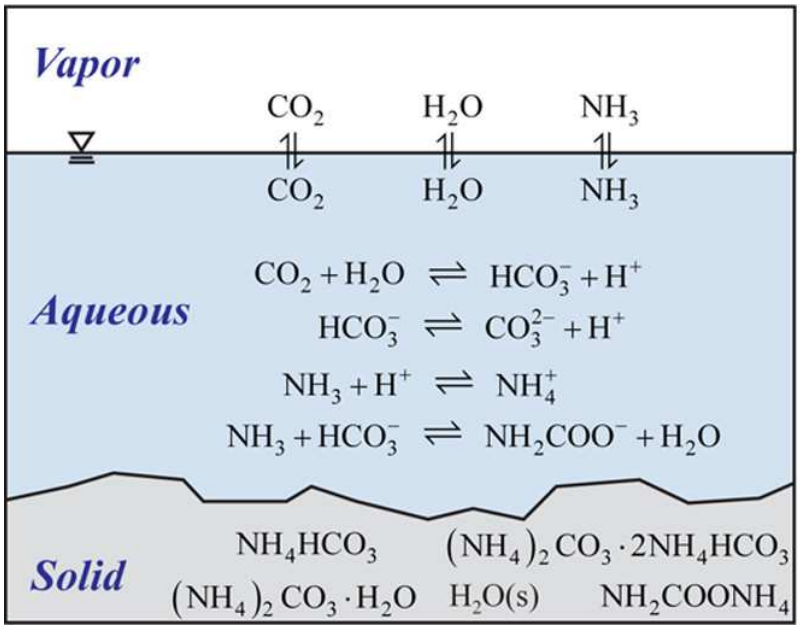

Figure 2.9. Graphical illustration of the reaction mechanism for ammonium carbonate degradation vapor diffusion reaction (image adapted from (Sutter and Mazzotti, 2017)).

2.6.2. ACC-naphthoquinones synthesis in ethanol

Stable ACC nanoparticles were successfully synthesized in ethanol by following a protocol adapted from (Chen *et al*., 2013) (Figure 2.10). Pure ACC and ACC-naphthoquinones samples were synthesized at once in a 5 L glass beaker. For pure ACC, 200 mg of calcium chloride dihydrate ($CaCl_2.2H_2O$) was dissolved in 100 mL absolute ethanol in a glass bottle of 250 mL. Similarly, naphthazarin or lawsone was dissolved along with 200 mg of $CaCl_2.2H_2O$ in 100 mL absolute ethanol in another glass bottle. Both solutions were filtered through a 0.22 µm filter to remove any impurities and ensure a pure reaction mixture.

The prepared solutions were then placed inside the 5 L glass beaker with a separate glass bottle containing 2.5 g of ammonium carbonate ($(NH_4)_2CO_3$). The bottles were covered with parafilm with several holes to allow gas exchange during the reaction (see Figure 2.10a).

Over the course of three days, the reaction took place, resulting in the formation of white ACC nanoparticles suspended in ethanol solution in one bottle, and colored ACC nanoparticles suspended in the second bottle. After the reaction, the white and colored ACC nanoparticle suspensions were centrifuged to separate the nanoparticles from the solvent. The samples were stored under vacuum. Figure 2.10b showcases ACC synthesized in the presence of naphthazarin and lawsone.

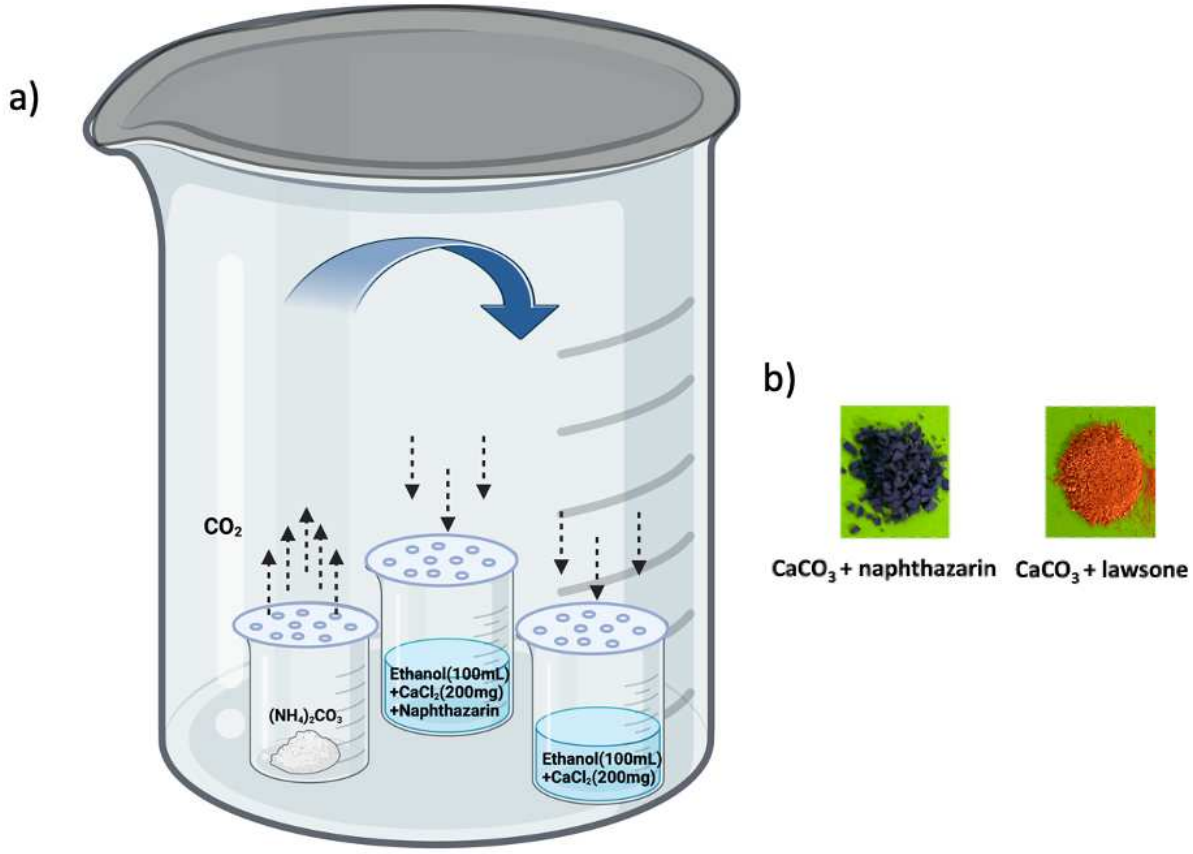

Figure 2.10. a) Schematic representation of ammonium carbonate degradation vapor diffusion synthesis of ACC in the presence of naphthoquinones in ethanol (100 mL), b) colored amorphous $CaCO_3$ synthesized by vapor diffusion method with naphthazarin and lawsone.

2.6.3. Crystalline $CaCO_3$-naphthoquinones synthesis in H_2O

The precipitation of crystalline $CaCO_3$ was achieved using the ammonium carbonate diffusion method by following the procedure of (Albeck *et al*., 1993; Kanold *et al*., 2015). The chemical reaction of this method is very similar to the one described in Section 3.2.1. For this process, 16 multi-well plates were utilized, with each well containing 400 µL of the crystallization solution. Pre-cleaned glass slides were carefully placed at the base of each well to serve as substrates for crystal growth.

To initiate the precipitation, 40 µL of stock solutions of 100 mM $CaCl_2$ in H_2O were added to all the wells. Subsequently, different volumes of naphthoquinone solution were added to each well, varying the concentration of naphthazarin as desired. Finally, the volume in each well was adjusted to 400 µL using either H_2O or 40 mM NaOH in H_2O (40 mM NaOH was used to dissolve naphthazarin concentration >10 µg/mL), depending on the specific experimental requirements. Once the solutions were prepared, the multi-well plate was carefully sealed and placed in a desiccator. Inside the desiccator, a Petri dish containing 2.0 g of solid $(NH_4)_2CO_3$ was placed at the bottom of the desiccator. $(NH_4)_2CO_3$ acted as the source for ammonium carbonate vapor, which diffused into the wells and initiated the precipitation process. The Petri dish was covered with Parafilm or a glass lid that had been punctured with a needle, allowing for controlled diffusion of ammonium carbonate vapor (Figure 2.11).

The crystallization process was typically left to proceed undisturbed, with a duration of 72-96 hours. During this time, calcium carbonate crystals formed on the glass slides supported at the base of each well. After the crystallization period, the glass slides were carefully removed, and the solutions were removed by vacuum cleaning. They were then thoroughly washed with distilled water to remove residual impurities and rinsed with ethanol. Finally, the glass slides were left to dry at room temperature.

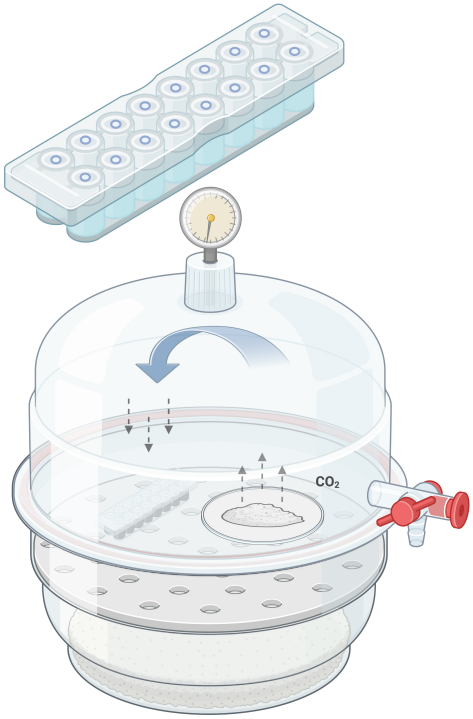

Figure 2.11. Schematic representation of vapor diffusion synthesis of calcite crystals in water (Albeck *et al*., 1993; Kanold *et al*., 2015). Stock solutions used in the synthesis of $CaCl_2.2H_2O$: 100 mM solution, Naphthazarin_NaOH = 200 µg/mL (NaOH concentration = 40 mM), $NaOH/H_2O$ = 40 mM, Naphthazarin_H_2O = 10 µg/mL.

2.7. Analytical techniques

2.7.1. Differential Scanning Calorimetry

2.7.1.1. Technique principle

Differential Scanning Calorimetry (DSC) is a powerful analytical technique used to study the thermal properties of materials. The DSC principle is based on measuring the heat energy required to maintain the sample and a reference sample at the same temperature as they are heated or cooled (Figure 2.12) (Abd-Elghany and Klapötke *et al*., 2018). In this work, we performed DSC measurements to determine the crystallization temperatures of the different ACC-naphthoquinone samples.

Two cells equipped with thermocouples are used to perform DSC measurements along with a programmable furnace, recorder, and gas controller. The thermocouples help quantify the heat

flow associated with the material's phase transitions or reactions (Gill *et al*., 2010). Figure 2.12 illustrates the different phenomena that a sample can undergo when subjected to heat.

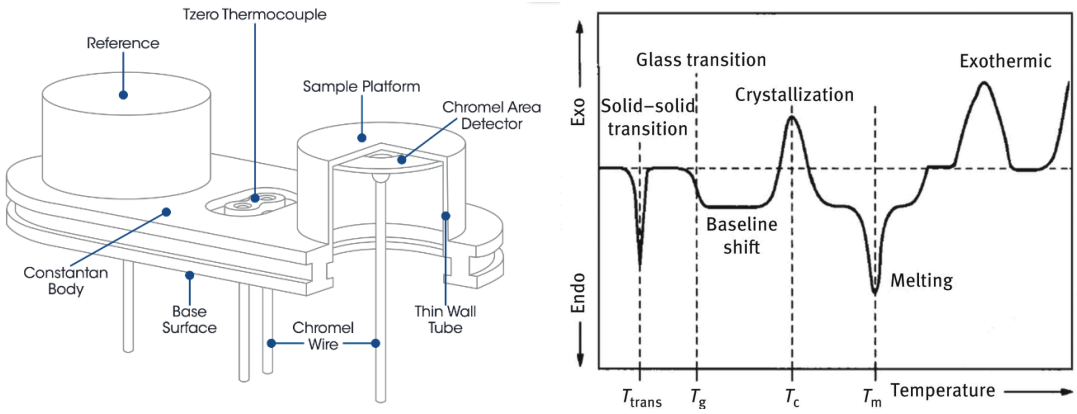

Figure 2.12. DSC instrument illustrated (image adapted for TA brochure) and a graph displaying various phenomena that occur when a material is subjected to heat (Abd-Elghany and Klapötke, 2018).

2.7.1.2. Experimental details and data analysis

DSC measurements were performed on the TA Q20 DSC module with a temperature ramp of 5 °C/min from 20-300 °C and an N_2 flow rate of 50 mL/min. The data was analyzed using the TA universal software provided by the TA company. After analysis from TA universal software, the data was extracted in *.txt* file format and then plotted in OriginPro.

2.7.2. Thermogravimetric analysis

2.7.2.1. Technique principle

Thermogravimetry analysis (TGA) measures the weight changes of a sample as it is heated or cooled under controlled conditions. TGA only provides information about the weight loss, not the identity of the components lost during the measurement. In general, the different weight losses during the measurement can be attributed to the different compounds that are released due to the release of volatile components, decomposition, or oxidation of the samples. Here, we used TGA to determine the amount of H_2O in the ACC-naphthoquinone samples.

2.7.2.2. Experimental details and data analysis

TGA measurements were carried out on the TGA module of Thermo Scientific™ Nicolet™ with a temperature ramp of 5 °C/min from 25 - 400 ºC / 800 ºC in the presence of N_2. The airflow rate was adjusted to 35 mL/min and 50 mL/min. The data was exported using OMNIC software provided by Thermo Scientific™ in .txt format. The data was then analyzed using OriginPro software.

2.7.3. Fourier Transform Infrared Spectroscopy

2.7.3.1. Technique principle

Infrared spectroscopy (IR) is based on the samples' absorption of specific wavelengths of infrared radiation. This occurs due to the selective interaction between the infrared radiation and the covalent bonds present in the sample molecules, leading to changes in the bonds' vibrational energy and, thus, specific absorption patterns (Berna *et al*., 2017). In the case of $CaCO_3$, characteristic bands allow for distinguishing calcite, vaterite and ACC. These bands include the C-O str*etc*hing vibration at approximately 1410-1440 cm^{-1} for calcite, 1480-1490 cm^{-1} for vaterite, and 1400-1500 cm^{-1} for ACC. Additionally, the band at around 700 cm^{-1} indicates the calcite and vaterite polymorph, whereas the presence of a broad band between 2900 and 3700 cm-1 indicates ACC. Table 3 compares the different characteristic bands that allow for the differentiation of the $CaCO_3$ polymorphs.

Table 2.3. Characteristic bands in the IR spectra of ACC, vaterite, and calcite.

ACC (cm^{-1})	Vaterite (cm^{-1})	Calcite (cm^{-1})
3700-2950	1490 and 1420	1805
1650	1083	1410
1474	844	870
1395	744	712
1070		

2.7.3.2. Experimental details and data analysis

To identify the $CaCO_3$ phases obtained, *i.e.,* amorphous (ACC) or crystalline (vaterite and calcite), PerkinElmer Frontier Fourier analyzed samples transform (FT-IR) in attenuated total reflectance (ATR) mode in the 500−4000 cm^{-1} range at a 4 cm^{-1} resolution. The data was

collected using PerkinElmer spectrum software integrated with the IR instrument. The data was exported in .txt format and plotted using OrginPro software.

2.7.4. Raman spectroscopy

2.7.4.1. Technique principle

Raman spectroscopy was used to investigate the presence of pigments in the $CaCO_3$-napththoquinone samples, the CaCO3 crystalline structure, and the inorganic-organic interactions (the effect of incorporated pigment molecules on the vibrational levels). It relies on the principle of inelastic scattering of light by molecules with polarizable vibrational states. When a sample is illuminated with a monochromatic laser, certain molecules in the sample interact with the incident photons and subsequently release scattered photons with either lower energy (Stokes effect) or higher energy (anti-Stokes effect) (Figure 2.13). The difference in energy between the incident and scattered photons corresponds to the vibrational energy levels of the molecules in the sample, providing valuable information about its chemical composition and structure (Bumbrah *et al.*, 2016).

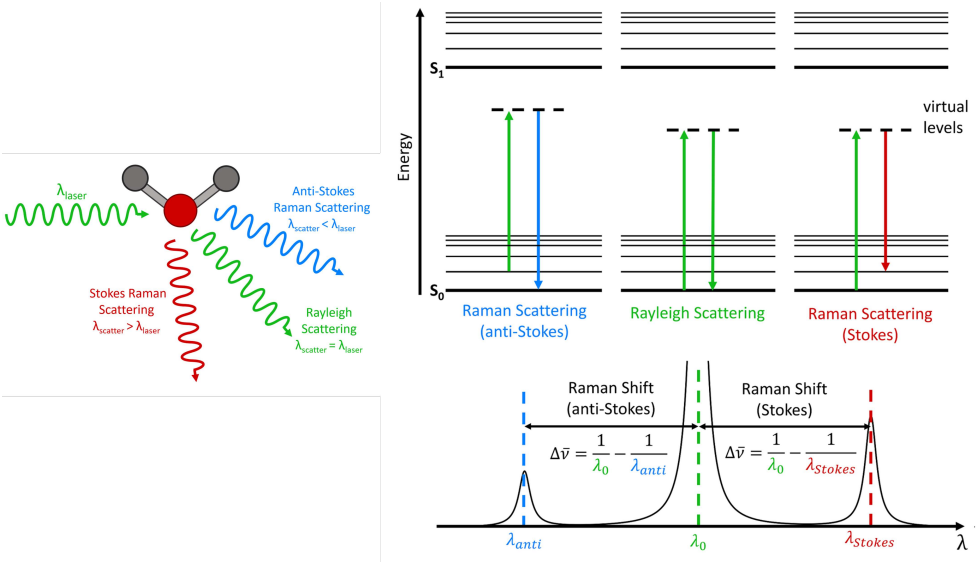

Figure 2.13. Representation of light interaction with a molecule, three scattering processes occur: Rayleigh, Stokes, and anti-Stokes scattering. Each involves incident photons interacting with the molecule, leading to the emission of scattered photons with specific energy changes (image adapted from Edinburgh instruments website).

In the context of $CaCO_3$ (Figure 2.14), Raman spectroscopy plays a crucial role in studying its vibrational modes and identifying different polymorphs. CO_3^{2-} vibrations and lattice modes (Ca-O vibrations) are among the Raman-active modes in calcium carbonate, making them observable in Raman spectra. For instance, in the case of calcite, we can observe ν1 mode at 1086 cm^{-1}: This strong peak corresponds to the symmetric str*etc*hing vibration of the CO_3^{2-} ions in the calcite lattice. ν2 mode at 712 cm^{-1}: This band corresponds to the bending vibration of the CO_3^{2-} ions in the calcite lattice. ν3 mode at 282 cm^{-1}: This peak is associated with the asymmetric str*etc*hing vibration of the CO_3^{2-} ions.

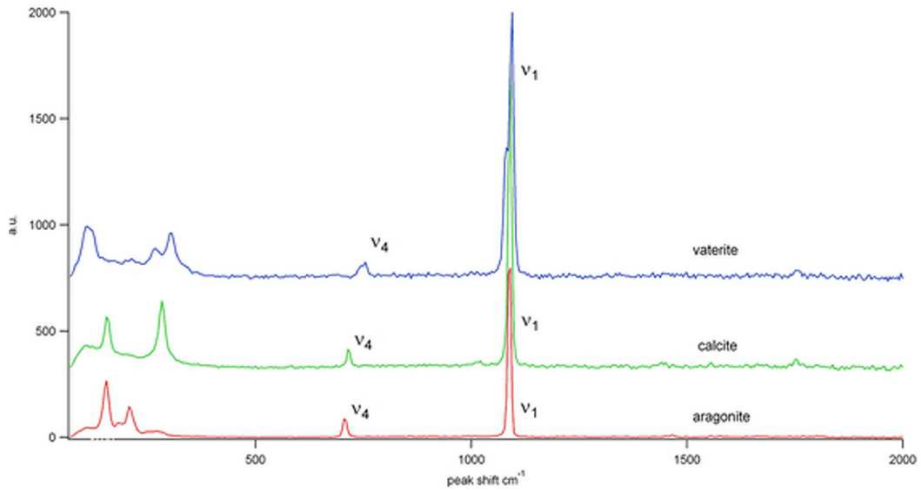

Figure 2.14. Raman spectra of the three $CaCO_3$ polymorphs aragonite, calcite, and vaterite (image adapted from (Nehrke *et al*., 2012)).

2.7.4.2. Experimental details and data analysis

Experiments were performed at the Max Planck Institute for Colloids and Interfaces, Potsdam, Germany, during my 4 month stay (from February 2022 to May 2022) in the framework of a DAAD grant. The spectrometer employed in this study was an Oxford alpha300R Raman imaging microscope equipped with a YAG laser emitting light at a wavelength of 532 nm. The instrument was coupled to Witec project five software for data acquisition and analysis. A charge-coupled device (CCD) detector was utilized to capture the scattered photons. To prevent any potential alteration of the samples, the laser power was used only at 5-50 % of its full capacity. Additionally, the Raman spectra were accumulated multiple times for a set duration to improve signal-to-noise ratios. This approach ensured reliable and precise measurements

while minimizing potential adverse effects on the analyzed samples. Table 2.4 summarizes the experimental parameters of the different mappings performed employing confocal Raman microscopy.

Table 2.4. Experimental parameter for Raman mapping.

Scan (cm^{-1})	Size (µm)	Points	Wavelength (nm)	Integration time (s)
100-3500	50x250	150x250	532	1

2.7.5. UV-visible and UV-visible diffuse reflectance spectroscopies

2.7.5.1. Technique principle

UV-visible spectroscopy is an analytical method that determines the absorption or transmission of discrete wavelengths of UV and visible light by a liquid sample compared to a reference or blank sample (Figure 2.15). The composition of the sample affects this property, providing information on its contents and concentration. Light energy is inversely proportional to its wavelength, meaning that shorter wavelengths carry more energy and vice versa. The promotion of electrons to a higher energy state requires a specific amount of energy, which we can detect as absorption.

Different bonding environments in a substance require different amounts of energy for electron promotion, resulting in different wavelengths of light absorption. Visible light encompasses a spectrum from approximately 380 nm (violet) to 780 nm (red), while UV light has shorter wavelengths down to 100 nm. Hence, UV-visible spectroscopy utilizes light wavelength to locate the specific wavelengths associated with maximum absorbance to identify and analyze various substances.

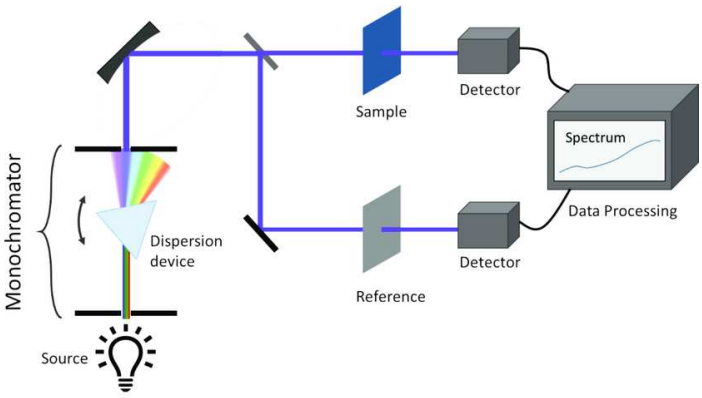

Figure 2.15. Schematic illustration of UV-visible spectrometer.

In order to perform UV-visible diffuse reflectance measurements on powder samples, integrating spheres are needed, which have a spherical inner surface made of light-scattering materials like barium sulfate that have high reflectance. They cause measuring light entering the sphere to scatter uniformly. The aperture for the measurement of light is located on the sphere's surface. To be measured, the sample is placed at this aperture, and the detector is placed at another aperture where it is not directly irradiated by the measurement light (Figure 2.16). Diffused reflectance measurement using an integrating sphere compares the diffused reflectance of a sample to a standard sample (Zerlaut and Anderson, 1981).

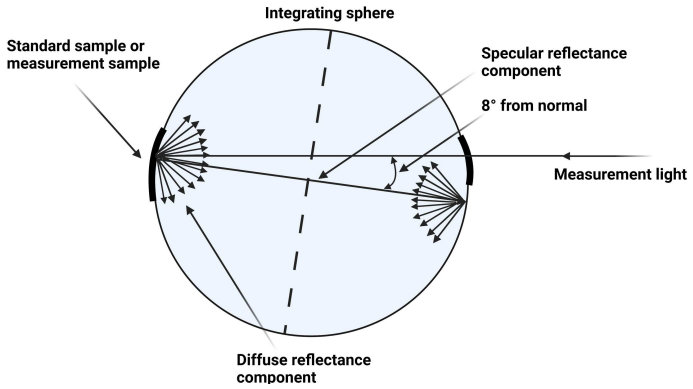

Figure 2.16. Total reflectance measurement using integration sphere.

2.7.5.2. Experimental details and data analysis

The UV-visible spectrometer (CARY 5000-Agilent Technologies) was used in the scan mode in the range of 200-800 nm with a scan speed of 600 nm/s in absorbance mode. The data obtained from UV-vis measurements is plotted using OrginPro software. The absorbance data

values were also subtracted from 1 to obtain the scattered part, which was then normalized. The normalized data was spread on a CIE chromaticity diagram plug-in integrated into the software. The CIE is a coordinate system encompassing all color sensations visible to the human eye. The chromaticity plot allowed for the derivation of RGB coordinates, which were used to assign an exact color to the synthesized colored $CaCO_3$.

2.7.6. X-ray Photoelectron Spectroscopy

2.7.6.1. Technique principle

X-ray Photoelectron Spectroscopy (XPS), also known as Electron Spectroscopy for Chemical Analysis (ESCA), is a powerful technique used to analyze the surface of materials. It provides valuable information about the elemental composition and the chemical and electronic state of the atoms present within the material. XPS is a widely used surface analysis technique that has applications in various scientific and industrial fields.

To perform XPS analysis, a solid surface is exposed to an X-ray beam, which causes electrons within the topmost 1-10 nanometers (nm) of the material to be emitted with varying kinetic energies. These emitted electrons are collected and counted, resulting in the creation of a photoelectron spectrum. The kinetic energies and intensities of the peaks in the spectrum provide valuable information about the elements present on the material's surface and their chemical bonding states (Figure 2.17). The thickness of the surface layer analyzed in XPS is typically defined as being up to three atomic layers thick, approximately 1 nm, for a given material. However, it is essential to consider that in some cases, ultra-thin films may extend up to about 10 nm in thickness, and thin films may range up to around 1 μm in thickness. The specific definitions of these layer types may vary depending on the material's nature, intended use, and specific research or industrial application (Carl *et al*., 2017).

X-ray Photoelectron Spectroscopy is a valuable technique for analyzing delicate or sensitive surfaces without damaging them. It provides valuable insights into the surface chemistry and composition of materials, aiding in understanding various physical and chemical phenomena.

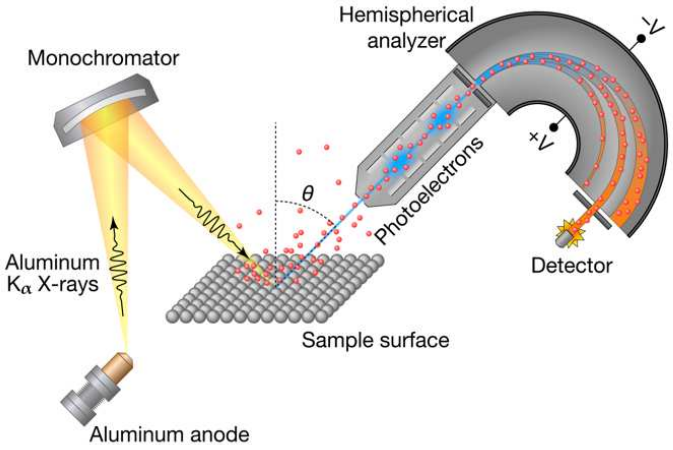

Figure 2.17. Illustration of an XPS instrument to visualize its design and components.

2.7.6.2. Experimental details and data analysis

XPS measurements were performed by Mathieu Fregnaux and analyzed by Anne Vallée at Institut Lavoisier de Versailles, France. XPS surface chemical analyses were performed with a Thermo Electron K-Alpha spectrometer using a monochromatic Al Kα X-ray source with charge compensation. Acquisition parameters were 650 µm spot size, 12 kV primary energy, 6.0 mA emission intensity, constant analyzer energy mode (100 eV), and 0.1 eV energy step size. The Thermo Electron K-alpha spectrometer procedure was used to calibrate the spectrometer. XPS measurement was done using an Ar+ ion source operating at 2 keV, 10 mA beam energy. The sample preparation was performed by suspending the $CaCO_3$ powder in absolute ethanol and spreading it on the sample holder for rapid evaporation of the solvent. Spectra were analyzed using Avantage© software. The data were calibrated on the carbonate peak of the C_{1s}.

2.7.7. Nuclear Magnetic Resonance in solution

2.7.7.1. Technique principle

Nuclear Magnetic Resonance (NMR) spectroscopy relies on the presence of nuclear spins, which can be linked to a combination of a gyroscope and a small magnet. These spins have two possible orientations, α and β, determined by the strength of the magnetic field. The distribution of spins between α and β follows a Boltzmann distribution, resulting in a small population difference.

$$\frac{N_\beta}{N_\alpha} = exp\left(\frac{-\Delta E}{kT}\right) \quad (2.3)$$

where N_β and N_α represent the number of spins one would expect to measure in the spin-up and spin-down configurations, ΔE is the difference in energy between the two states, k is the Boltzmann constant (1.381 x 10^{-23} joules/°K), and T is the absolute temperature in degrees Kelvin.

This limited population difference contributes to the lower sensitivity of NMR spectroscopy. In the absence of an external magnetic field, spins are randomly oriented. However, the spins align along the z-axis (field axis) in a magnetic field, forming a small macroscopic magnet. A radio frequency (RF) pulse is applied to initiate the NMR experiment, causing the spins to rotate into the x- and y-plane, eliminating the z-magnetization (Figure 2.18). The spinning motion of the spins creates an electrical signal in the detection coil, which is captured. The RF pulse initiates the measurement, which is repeated to enhance the quality of the signal. The captured time signal, referred to as the Free Induction Decay (FID), is transformed into a frequency spectrum using the Fourier transform (Keeler *et al*., 2010).

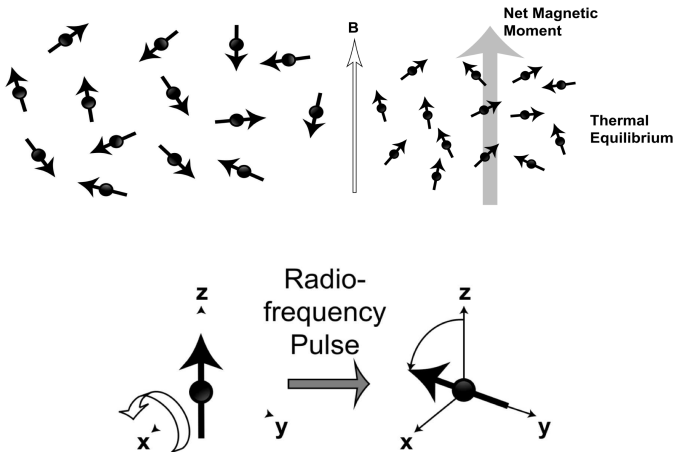

Figure 2.18. Different steps involved in a NMR experiment from magnetic field aligning spins, RF pulse exciting them to xy-plane, returning to equilibrium emitting RF signal revealing molecular properties.

HSQC

The HSQC (Heteronuclear Single Quantum Coherence) experiment in NMR spectroscopy is used to detect proton-carbon single bond correlations. Protons are observed along the F2 (X) axis, while carbons are observed along the F1 (Y) axis. By selectively exciting the protons and observing coherence transfer to the directly bonded carbons, the HSQC spectrum reveals correlations between specific protons covalently bonded to carbon atoms. This technique provides valuable insights into molecular structure, connectivity, and chemical environments, aiding in structural elucidation and compound characterization (Miller *et al*., 2013).

HMBC

In opposition to HSQC, the HMBC (Heteronuclear Multiple Bond Correlation) experiment is used to display ^{1}H and ^{13}C atoms connected through multiple bonds. Analyzing the HMBC spectrum allows identifying quaternary, providing crucial insights into molecular structure and connectivity. It aids in determining the chemical structure and understanding complex molecular arrangements (Miller *et al*., 2013).

2.7.7.2. Experimental details and data analysis

Nuclear Magnetic Resonance (NMR) experiments were conducted using a Bruker Avance III spectrometer equipped with a TCI cryoprobe, operating at a proton (^{1}H) frequency of 500.3 MHz. The NMR spectra were recorded at a temperature of 25°C or 37°C in deuterated water (D_2O). The chemical shifts of hydrogen and carbon-13 were referenced to the 3-(Trimethylsilyl)-1-propanesulfonic acid-d_6 sodium salt (DSS) solvent signal, which was set at δ 4.7 ppm. The data analysis was performed using Bruker Topspin software.

2.7.7.3. Reference sample preparation

Naphthazarin at different pH: to investigate the impact of pH on the peak position of naphthazarin and gain insights into its protonation state, naphthazarin solutions at different pH were prepared by dissolving it in D_2O. The pH of the solution was adjusted using 40 mM NaOH solution in D_2O. NMR measurements were performed on naphthazarin solutions prepared at three different pHs ~11, ~9, ~6. 0.1 mM. DSS solution was used as an internal indicator to suppress the water signal and for the chemical shift standard for NMR experiments (4.7 ppm).

Naphthazarin titration with Ca^{2+} ions at different pH: to investigate the influence of calcium on the peak position of naphthazarin and the effect of Ca^{2+} ions on the oxidation of naphthazarin. Naphthazarin solutions at different pH ~11, ~9, ~6 were prepared according to the method described above. Once the naphthazarin solution was prepared at a particular pH, the 0.1 mM DSS solution was used as an internal indicator to suppress the water signal and for the chemical shift standard for NMR. $CaCl_2$ solution (40 mM) was prepared in D_2O and was added to the NMR tube. Ca^{2+}: naphthazarin of 1:1 was used for all three pH. Additionally, a sample with Ca^{2+}: naphthazarin of 5:1 was also prepared.

2.7.8. Solid-state Nuclear Magnetic Resonance

2.7.8.1. Technique principle

Magic angle spinning (MAS)

MAS (Magic Angle Spinning) is employed to eliminate line-broadening effects caused by anisotropic nuclear spin interactions in the solid state, such as chemical shift anisotropy (CSA) and dipolar coupling. In this technique, the sample is rotated at an angle of 54.74° (θ_R) relative to the applied magnetic field, B_0 (Figure 2.19a) because CSA and dipolar couplings exhibit an angular dependence described by the equation:

$$3cos^2(\theta) - 1 \tag{2.4}$$

The latter averages to zero for θ = 54.74°. In the case of incomplete averaging, the NMR spectrum displays spinning sidebands occurring at frequencies that are multiples of the MAS rate, both sides of the isotropic resonance.

The intensity of spinning sidebands depends on the spinning rate compared to the magnitude of the averaged nuclear spin interaction. Lower MAS rates result in more numerous and more intense spinning sidebands. Hence, MAS enhances resolution and simplifies spectral analysis. To achieve optimal sensitivity and resolution, the spinning rate (ω_r) should be at least three times greater than the largest anisotropy present (Figure 2.19b).

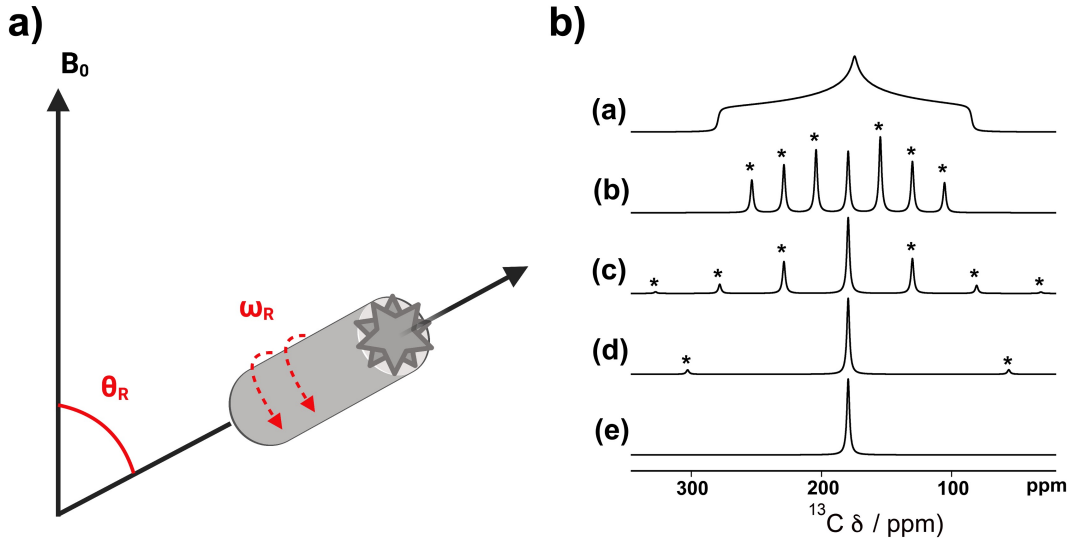

Figure 2.19. a) The sample is positioned at an angle of θ_R, known as the magic angle, with respect to the magnetic field B_0 and rotated around the axis depicted in the figure at a spinning rate of ω_r. The sample is enclosed in a small cylindrical rotor. b) Solid-state ^{13}C NMR spectra of simulated with δ_{iso} = 178 ppm, η_{cs} = 0.9 and Δ_{CS} = 100 ppm at (a) MAS frequency of 0 Hz, static, (b) MAS rate of 1 kHz, (c) MAS rate of 2 kHz, (d) MAS rate of 5 kHz and (e) MAS of 10 kHz. Spinning sidebands are highlighted with an asterisk. The spinning sidebands are separated in multiples of the MAS rate (Bak *et al*., 2000).

Direct acquisition and cross-polarization

In this project, NMR direct acquisition refers to a specific application of ss NMR spectroscopy focused on the direct acquisition of carbon NMR signals from solid samples. In this technique, the NMR instrument generates radiofrequency pulses and magnetic fields to interact with the carbon nuclei directly within the solid material, resulting in measurable NMR signals. In the case of cross-polarization (CP), NMR experiments (Figure 2.20) involve the transfer of polarization from abundant nuclei like ^{1}H, to dilute or rare nuclei like ^{13}C to enhance the signal-to-noise experiments. The matching of the radio-frequency (rf) fields (Hartmann-Hahn condition) was set up properly to ensure an efficient cross-polarization process (Hartmann and Hahn, 1962). The rf fields of the dilute spin (*e.g.,* $\omega_{1C\text{-}13}$) were set equal to that of the abundant spin (*e.g.,* $\omega_{1H\text{-}1}$) by adjusting the power on each of the channels.

$$\omega_I = \omega_S \tag{2.5}$$

$$\gamma_I B_I = \gamma_S B_S \tag{2.6}$$

Where $\omega_{I/S}$ are the nutation frequencies of the spin-locking fields applied to the ^{1}H and $^{13}C/^{15}N$ nuclei. The signal sensitivity of the ^{13}C nuclei can be increased by a factor of $|\gamma_H/\gamma_C|$ *via* CP experiment.

Then, the proton and carbon magnetization precess in the rotating frame at the same rate, allowing for the transfer of the abundant spin polarization to carbon-13. Depending on the samples, the contact time and the recycle delay were set at 0.5-1 ms and 5-15 s, respectively.

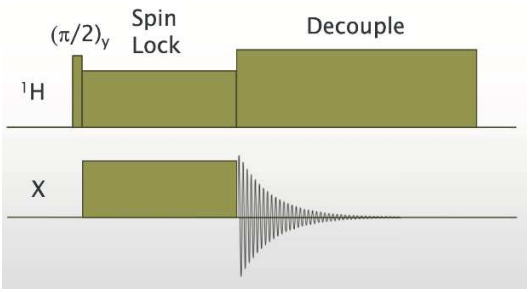

Figure 2.20. Simple CP pulse sequence representing a $\pi/2$ pulse applied on ^{1}H channel, followed by a CP step where magnetization is transferred from ^{1}H to X (^{13}C or ^{15}N spins, for instance) during a contact time t_{CP}. Finally, the signal is acquired on the X channel while decoupling is performed on the proton channel.

2D CP MAS NMR (HETCOR)

The ^{1}H-^{13}C HETCOR technique is a two-dimensional heteronuclear correlation experiment that reveals the correlation between ^{1}H and ^{13}C dipolar coupled spins by showing cross-peaks. The pulse sequence for this experiment begins with a $\pi/2$ pulse on the proton channel, generating a transverse magnetization. Subsequently, during t_1 spin evolution, homonuclear decoupling is applied on the proton channel. The decoupling suppresses the ^{1}H-^{1}H homonuclear dipolar coupling, enabling observation of only the ^{1}H and ^{13}C nuclei in proximity. The CP step is initiated, followed by signal detection. This experiment produces a heteronuclear 2D NMR spectrum that shows ^{13}C nuclei in the direct t_2 dimension and protons in the indirect t_1 dimension.

2.7.8.2. Experimental details and data analysis

NMR experiments were performed on an AV300 Bruker spectrometer operating at 300MHz with Larmor frequency for ν(^{1}H) = 300.29 MHz and ν(^{13}C) = 75.51 MHz. Depending on the experiments, Zirconia rotors of 4 mm diameter were spun at a MAS frequency (νMAS) of 4.5 kHz or 14 kHz. Calibration was carried out using Adamantane (-C=O 37.7 ppm).

^{1}H direct polarization experiments: The ^{1}H 90° pulse length was set to 5.0 µs. The recycle delay (RD) between acquisitions was set to 1-5 s. All spectra were recorded using 4-16 transients.

^{1}H-^{13}C Cross-polarization: The ^{1}H 90° pulse length was set to 3.6 µs with a contact time of 0.5-1ms using a ramp pulse on ^{1}H and square pulse on ^{13}C nuclei. The delay time between scans was set to 0.5 s. SPINAL-64 decoupling sequence was used for ^{1}H in all experiments, and the power varied according to the experiment. All the above parameters vary depending on the sample and the need of the experiment.

^{1}H-^{13}C H*ETC*OR: ^{1}H 90° pulse length was 11.1 µs, followed by refocusing pulses with 6.8 µs length, with further 4 composite pulses at 20.4 µs and one with 6.78 µs. Afterward, the ^{1}H-^{13}C CP step with 1000-2000 µs contact time was performed with a ramp pulse on ^{1}H and a square pulse on ^{13}C nuclei. Followed by auction with 22.6 kHz decoupling on ^{1}H nuclei.

The data analysis was performed using Bruker Topspin software, and spectra were extracted and edited using ssNake and illustrator software.

2.7.8.3. Reference sample preparation

Deprotonated naphthazarin (basic naphthazarin):

To get insight into the molecular state of the naphthazarin in calcite, naphthazarin was precipitated at different pH conditions. The spectra obtained on naphthazarin at different pHs serve as a reference for the naphthazarin within calcite and provide information about the molecular state of the naphthazarin at that pH.

pH adjustment with NaOH

Deprotonated naphthazarin was synthesized by dissolving the 20mg naphthazarin in 50 mL water. The pH of the solution was adjusted using NaOH/HCl to obtain different pH, *i.e.,* pH 9.2, pH 12, and pH 13. The solutions were frozen at -80^{o}C for 1-2 hours and then freeze-dried to obtain a sample denoted "deprotonated naphthazarin_NaOH_pH".

pH adjustment with Na_2CO_3

5mg naphthazarin was dissolved in a solution of 40 mM solution of Na_2CO_3. The pH of the solution was around 11.5. A dark blue colored solution was formed. The solution was frozen at -80^{o}C for 1-2 hours. The dark-colored solution was freeze-dried to obtain the sample denoted "deprotonated naphthazarin_Na_2CO_3" along with recrystallized Na_2CO_3.

2.7.9. X-ray diffraction

2.7.9.1. Technique principle

X-ray diffraction (XRD) is a powerful technique used to study crystalline materials' atomic and molecular structures. We used XRD technique for studying $CaCO_3$ due to its ability to determine the polymorph identification and lattice distortion. It is based on the principle of constructive or destructive interference of monochromatic X-rays with a crystalline sample that has geometrical variations on the scale of the X-ray wavelength. X-rays with energies in the range of 3-8 KeV, corresponding to wavelengths of 0.15-0.4 nm, are commonly employed for X-ray diffraction studies. When a crystal is irradiated with an X-ray beam of a comparable wavelength to its interplanar spacing (denoted by d, the crystal lattice constant), X-ray diffraction occurs (Figure 2.21). This phenomenon involves the constructive interference between elastically scattered X-ray beams at specific angles, denoted by 2θ when Bragg's Law is satisfied:

$$\boldsymbol{n}\lambda = 2\mathrm{d}\sin\theta \tag{2.7}$$

In this equation, n represents the diffraction order, λ is the X-ray wavelength, d is the interplanar spacing, and θ is the diffraction angle. Valuable information about the crystal lattice constants and atomic arrangements can be obtained by varying the angle θ and measuring the intensity of the diffracted X-rays.

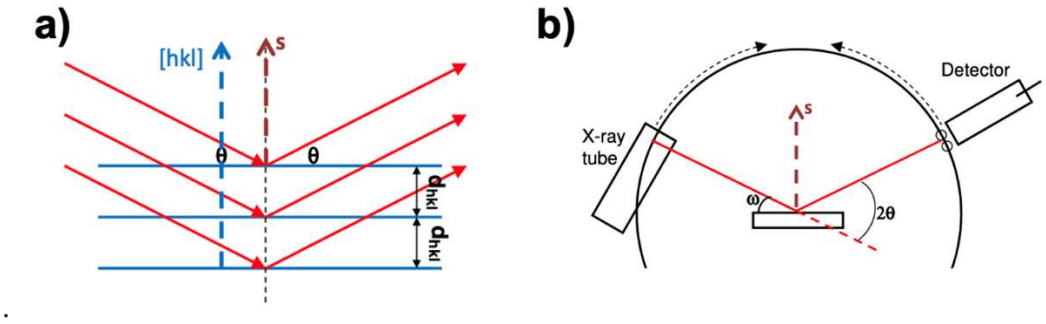

Figure 2.21. a) Schematic illustration of Bragg's law for constructive interference, along with the b) setup of the XRD instrument.

ID22 beamline at ESRF:

We also utilized ESRF beamline ID22 to investigate the influence of organics on the lattice of $CaCO_3$, leveraging ESRF's advantages such as high-resolution analysis, versatile experimental techniques, and tuneable energy and allowing rapid data collection.

The U23 undulator, with a minimum gap of 6 mM and a length of 2 m, produces X-rays in a vacuum at the ID22 beamline (Figure 2.22). A revolver is available to select different undulators, allowing for a wide range of energy from 6 KeV to 80 KeV (2.07Å to 0.15Å) at ID22. In our HR-XRD experiments, a large beam of X-rays was used to illuminate a sufficient volume of the sample to obtain a good statistic (Figure 2.22). The channel cut Si 111 monochromator, which is 300 mM long with a 4 mm distance between the diffracting surfaces, is used to monochromate the beam. The second surface can be adjusted to compensate for changes in the Bragg angle due to changes in heat load. The first block of the monochromator crystal, which experiences the highest heat load, is side-cooled to approximately 105K by copper blocks through which liquid nitrogen flows. The size of the incident beam on the monochromator and the transmitted monochromatic beam to the sample is defined by water-cooled slits, typically in the range of 0.5–1.6 mM (horizontal) by 0.1–1.5 mM (vertical). To reduce preferred orientation effects in crystallographic studies, a spinning capillary mounted on the diffractometer axis is commonly used.

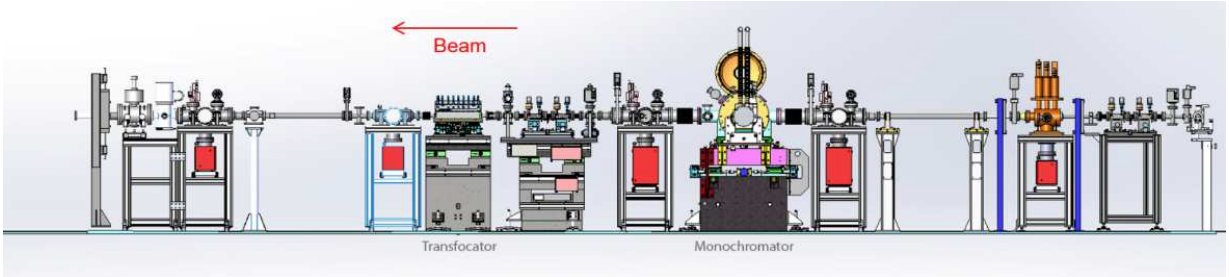

Figure 2.22. The outline of the ID22 optics hutch (image adapted from ESRF website).

2.7.9.2. Experimental details in the lab and data analysis

Powder X-ray diffraction (PXRD) was performed on $CaCO_3$ samples with measurement parameters including 40 kV, 30mA, a 0.010° step size, and a 5−80° 2θ range. performed on Bruker D8 diffractometer, equipped with standard Cu tube (Kα = 1.54 Å). The data was plotted using OriginPro software, and Rietveld refinements were performed using GSAS II software (Toby and Von Dreele, 2013).

2.7.9.3. Experimental details at ID 22 (ESRF, Grenoble) and data analysis

HR-XRD measurements were carried at the ID22 beamline with assistance from beamline scientist Dr. Andy Fitch, ESRF Grenoble. The measurement parameters for this analysis included a 35 keV energy source, a 0.001° step size, and a 0.5−50° 2θ range. X-ray diffraction data were acquired using the flat panel Perkin Elmer XRD 1611CP3 detector, which is suited for total scattering measurements at high energies (https://www.esrf.fr/id22/technical-description). Recorded 2D patterns were processed using 2D powder diffraction data reduction software available for calibration and data integration (A. P. and Hausermann, 1996). *In-situ* heating HR-XRD was carried out using the blower with a heating rate of 5°C/min and ramp cycle from 25-430 °C. The integrated XRD profiles were plotted using OriginPro software. The Rietveld refinement was first carried out at the beamline using a script provided by the ID22 beamline scientist for the TOPAS software.

2.7.9.4. Reference sample preparation

Calcite-naphthazarin was prepared by physical mixing. 199 mg of the previously synthesized calcite was weighed and placed into a mortar to begin the synthesis. Subsequently, 1.0 mg of naphthazarin, known for its vibrant pinkish-purple color, was added to the calcite in the mortar. The two components were then subjected to mechanical mixing using a pestle, ensuring

thorough distribution and incorporation of the pigment into the calcite crystals. The mixing process was performed for 10 minutes, allowing the pigment to be evenly distributed and attached to the calcite particles. As a result of this mixing, the calcite crystals acquired the color of the naphthazarin pigment, giving rise to a light pinkish-purple hue in the final product.

2.7.10. SAXS/WAXS for pair distribution function analysis

2.7.10.1. Technique principle

SAXS/WAXS analysis was performed to study the local structure of the ACC in the presence of naphthoquinones as well as local structural rearrangement during its crystallization. X-rays are scattered from the samples and detected similarly to conventional powder diffraction experiments. However, in order to allow for further pair distribution function (PDF) analysis of the total X-ray scattering intensity, extremely short X-ray wavelengths and wide angular detection ranges are needed to explore a broad range of reciprocal space. The variable Q, representing the scattering vector magnitude, is used to measure positions in the reciprocal space, with the goal of measuring Q values as high as $Q = 30$ Å^{-1} or more.

Pair Distribution Function (PDF) analysis involves several essential steps. It commences with data collection, where X-rays are gathered from the sample. Subsequently, the raw data undergoes corrections to account for background noise, instrumental effects, and absorption. Once the data is refined, the pivotal step is the calculation of F(q) through a Fourier transform. This transforms the data from reciprocal space (q) to reciprocal distance (r). Following this, the transformation to g(r) is conducted, which portrays the real-space distribution of distances between atoms or particles. Analyzing g(r) provides insights into the sample's local ordering, coordination, and interatomic distances.

The obtained PDF represents the distribution of the distance between two points within the scattering particle. The PDF depends on the shape and size of the particle and can be related to the scattering curve through a sine Fourier transform. The analysis of the PDF characterizes the likelihood of locating two atoms at specific inter-atomic distances (Figure 2.23), also known as a distance map, within a solid (Terban and Billinge, 2022).

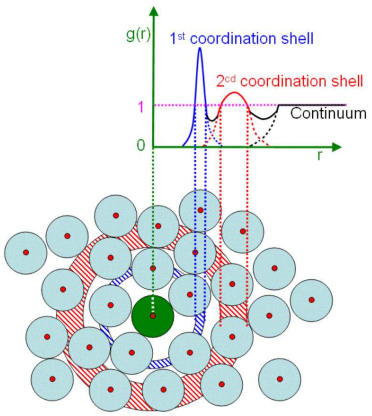

Figure 2.23. Schematic illustration of g(r) dependence on r. The pair distribution function (PDF), also known as the g(r), is a probability density function that gives the number density of atoms at a distance r from an origin atom (image adapted from the Globalsino website).

2.7.10.2. ID15a beamline at ESRF

ID15A is a synchrotron beamline that utilizes high heat load slits to shape the white beam, providing a maximum beam size of 8×6 mm^2. This beamline is designed for a range of experiments, particularly those involving high-energy monochromators and Ge crystal scattering. At the entrance of the experimental hutch, a high-energy monochromator can be mounted, specifically suitable for Ge crystal scattering experiments. The monochromator allows researchers to select and isolate specific X-ray wavelengths, enhancing the precision and accuracy of the experiments.

EH3, another beamline, is equipped with two monochromators: a Double Multilayer Monochromator (DMLM) and a Laue-Laue Monochromator (LLM). These monochromators can be tuned across a broad energy range, from 40 to 140 keV. This wide tunability allows for versatile experiments involving a variety of X-ray energies, catering to diverse research needs.

X-ray focusing at these beamlines is accomplished using 1D Aluminum and Beryllium lenses and transfocators. These optical elements can finely adjust the beam size, allowing researchers to achieve a beam size as small as 10 µm. Such precise focusing is vital for investigations requiring spatial resolution and control over the X-ray beam dimensions.

2.7.10.3. Experimental details and data analysis

PDF analysis has been extensively used to investigate the atomic-scale structure of amorphous materials that exhibit no long-range order. SAXS/WAXS measurements were carried out at ID15A beamline, ESRF Grenoble. *In-situ* heating SAXS measurements were also performed using the linkam stage (FTIRSP600) to control the temperature ramp precisely. X-ray scattering data were acquired using a Pilatus CdTe 2M with 0.5-1s measurement time. Measurements were performed at ID15A beamline, ESRF. Beam energy was set to 60KeV, and beam-size was 0.15*0.15 mm^2 in cross-section. The calibration was performed with aCeO_2 powder standard. The Linkam FTIR600 heating stage temperature was increased from 30°Cto 250-430°C at a rate of 5°C/min. Recorded 2D patterns were processed thanks to Python scripts provided by the beamline scientist to average, mask, and integrate the 2D patterns. For *in-situ* heating measurements 5°C/min heating rate from room temperature to the temperature of crystallization, *i.e*., from 25°C to 250°C-430°C was used. The PDF were calculated with the PDFgetX3 Columbia Technology Ventures) software and plotted using OriginPro software. The differential of the PDF data as a function of temperature (dPDF/dT) was calculated and plotted using a Python script developed by Luca Bertinetti (Center for Biomolecular Biology, Dresden).

2.7.11. Scanning electron microscopy (SEM) and Field Emission Gun-SEM

2.7.11.1. Technique principle

In order to study the effect of naphthoquinones on the calcite morphology and ACC particles size, samples were analyzed using electron microscopy. Scanning Electron Microscopy (SEM) and Field Emission Gun (FEG) Scanning Electron Microscopy (FEG-SEM) follow the same principles, but the electron generation system is different. FEG-SEM utilizes a Field Emission Gun as an electron source (tungsten) instead. In FEGs, an electric potential gradient is applied to emit the electron beam, while SEM employs thermionic emission. Scanning Electron Microscopy (SEM) is a microscopy technique that involves directing a beam of electrons at a specimen to generate a variety of secondary emissions. The X-rays, backscattered electrons, and secondary electrons are collected by detectors and converted into a signal. This signal is then sent to a screen resembling a television screen to produce the final image. SEM-FEG (0.8 nm @15 kV) offers high-resolution surface imaging and can acquire images with a long depth of field compared to SEM (3.0 nm @ 30 kV). FEG-SEM instruments are equipped with

auxiliary detectors for Energy Dispersive Spectroscopy (EDS) and Electron Backscatter Diffraction (EBSD) cameras (Akhtar *et al*., 2018).

2.7.11.2. Experimental details and data analysis

The ACC particles and calcite crystals were imaged by Hitachi SEM and FEG-SEM Hitachi SU-70. FEG-SEM electronic micrographs were obtained by David Montero, CNRS, Sorbonne University. The samples were spread on carbon tape or Si wafer and then coated with a 7 nm Pt layer to reduce the charging of the surface. The samples were examined at an accelerating 2-5 kV voltage under a high vacuum. FIJI software was used to analyze the particle size, and the values obtained were plotted (histogram) using OriginPro software.

2.7.11.3. Sample preparation

In addition, one calcite-naphthazarin sample was obtained by ion sectioning at the Max Planck Institute for Colloids and Interfaces, Potsdam, Germany to reveal the occlusions as well as the microstructures. This process is performed at low temperatures to avoid the degradation of organics as much as possible. The $CaCO_3$ crystals were sandwiched between two copper tapes. The copper tapes enhance the sample's thermal conductivity during the cryo sectioning. However, the sandwiching of crystals between two copper tapes results in gaps. Therefore, the crystals were covered with a layer of copper to maintain high thermal conductivity. Finally, the samples were placed on a sample holder and were cut by an ion beam (Ar) under low-temperature conditions (-60 °C), revealing the inside of the $CaCO_3$ crystals (Figure 2.24).

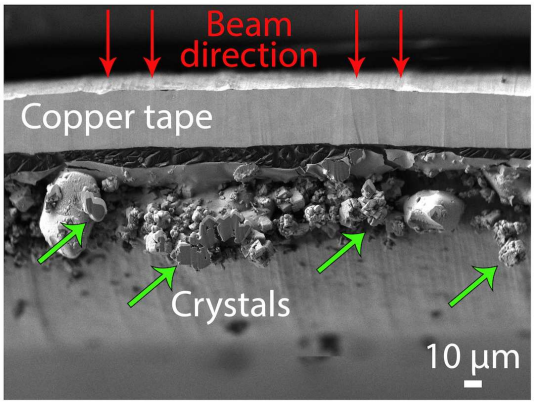

Figure 2.24. SEM micrograph of $CaCO_3$ packed (green arrows) between Cu tape which was cut by ion (Ar) milling at -60 °C.

2.7.12. FIB-SEM

SEM FIB (Scanning Electron Microscopy Focused Ion Beam) was utilized to visualize the presence of naphthazarin within the calcite matrix, offering high-resolution imaging capabilities. Additionally, it facilitated the precise preparation of lamella sections, which is crucial for subsequent analysis using scanning transmission electron microscopy-electron energy loss spectroscopy (STEM-EELS).

2.7.12.1. Technique principle

The Dual-Beam FIB-SEM instrument combines the precision sample modification capabilities of a Focused Ion Beam (FIB) with high-resolution scanning electron microscopy (SEM) imaging, enabling localized sample characterization and fabrication. FIB uses accelerated Gallium ions to selectively remove material from the sample surface in a controlled manner, creating a volume that can be imaged and analyzed in-depth (Figure 2.25).

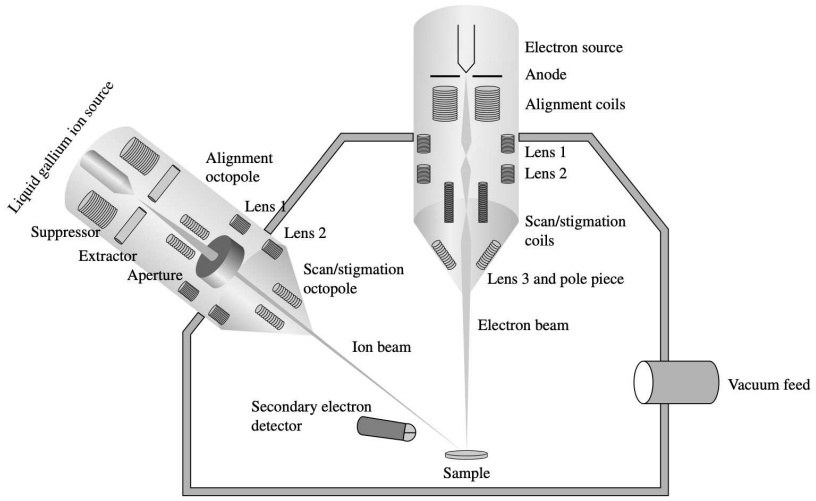

Figure 2.25. Schematic diagram showing the configuration of a two-beam focused ion beam system.

Once removed, the material cannot be restored, and gallium implantation may occur during milling, which should be considered for sensitive materials. FIB's milling capability enables the exposure of in-depth structures that are not visible from the top surface. The instrument's sample stage is also highly flexible, allowing for 360-degree azimuthal rotation and +/- 90-degree tilting, enabling operations in a wide range of geometries (Yao, 2007).

2.7.11.2. Experimental details

The FIB-SEM was performed by Clemens Schmidt at the Max Planck Institute for Colloids and Interfaces, Potsdam, Germany in order to slice and image the samples as well as to obtain FIB-lamella (see below section 2.7.12.3.2.) of one calcite-naphthazarin sample. The Zeiss Crossbeam 540 station was used for FIB-SEM in serial surface mode. Carbon-coated specimens were oriented to align with the longitudinal direction to the beam. A coarse cross-section was initially milled with a 30 nA gallium beam for SEM observations. The exposed surface was fine-polished with a 1-1.5 nA ion beam. Then, the fine-polished block was serially milled using an ion beam of 30 kV. After each slice of the sample was removed, the freshly exposed surface was imaged using SE and electron backscattered diffraction detector (EBSD). The slice thickness was roughly equivalent to the lateral resolution of 2D images, ranging from 6 to 24 nm. The milling and imaging process was fully automated, allowing the simultaneous collection of images.

2.7.12. STEM and STEM-EELS

The STEM and STEM-EELS technique were employed to visualize the presence of naphthazarin associated with the calcite. This advanced imaging method allowed for precise observation at the nanoscale level, revealing the spatial distribution and chemical composition of the samples.

2.7.12.1. Technique principle

STEM utilizes an electron beam that is focused on a very small probe size (< 1 nm) and then scanned across the sample using deflection coils. The resulting image depends on the transmitted electrons, which can form either a bright-field or dark-field STEM image. The most commonly used detector in STEM is an annular detector, which is utilized to create annular dark-field images. By adjusting the intermediate lenses, the camera length in STEM mode can be modified to control the angular range of electrons that fall onto the annular detector (Figure 2.26a). High-angle annular dark-field STEM (HAADF-STEM) imaging collects only those electrons scattered under large angles by the specimen and is sensitive to both thickness and chemical composition. The resulting image is a mass-thickness projection of the crystal being imaged and is not a phase-contrast image like in high-resolution transmission electron microscope (HRTEM) (Tanaka, 2014).

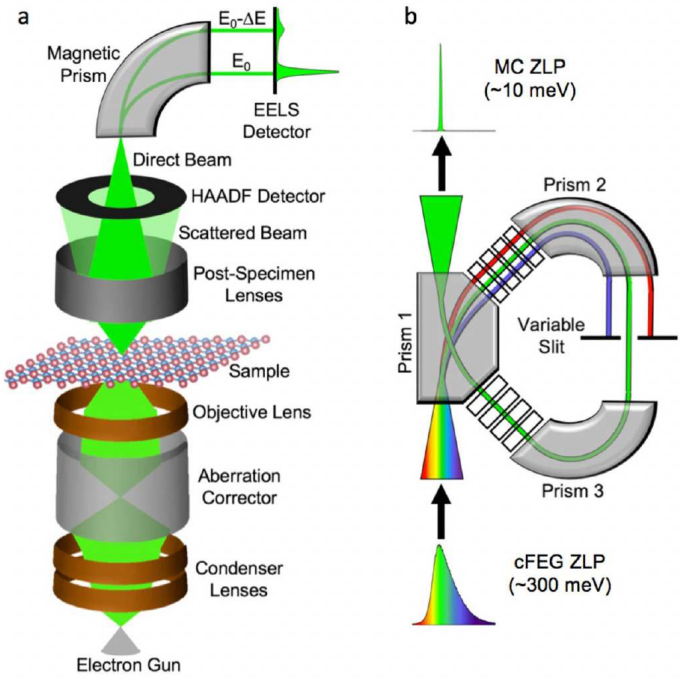

Figure 2.26. Electron energy loss spectroscopy and monochromation are depicted in (a) and (b), respectively. (a) EELS experiment in a scanning transmission electron microscope (STEM), and (b) monochromation process of the electron beam between the electron gun and the condenser lenses (image adapted from (Hachtel *et al.*, 2018)).

The technique of Electron Energy Loss Spectroscopy (EELS) is commonly carried out using STEM. This technique utilizes a focused electron beam that is systematically moved across a sample having a thickness within the 50 nm range. When the beam passes through the sample, some electrons scatter without energy loss (elastic scattering), while others interact with electrons bound to the sample atoms, causing them to lose energy. This process results in atomic electrons being in an excited state, which can de-excite by releasing energy in the form of visible photons, x-rays, or Auger electrons. EELS is a set of methods that assess the variation in the kinetic energy of electrons when they come into contact with a sample. Its purpose is to identify the chemical characteristics of the sample, such as the types and quantities and the chemical state of atoms. It is important to differentiate between low-loss and core-loss excitations in EELS. The latter involves the ejection of electrons, revealing signals associated with atomic ionization edges. These signals provide valuable information about elements' composition and chemical states. On the other hand, the low-loss range in EELS corresponds to excitations of valence electrons. In this range, the energy losses are typically smaller, and

the spectra primarily capture interactions with valence electrons, shedding light on the material's electronic structure and bonding characteristics.

2.7.12.2. Experimental details and data analysis

To analyze the chemical composition of the colored $CaCO_3$, STEM-EELS was performed at LPS Orsay, France, with Marta de Frutos in the framework of METSA experiments. A monochromated CS-corrected Nion Hermes 200-S microscope was used. STEM mode allows for high-resolution imaging and precise elemental analysis. EDX detects X-rays emitted by the sample when it is bombarded with the electron beam. The resulting X-ray signals provide information about the elemental composition of the $CaCO_3$. Core-loss electron energy loss (EEL) spectra were obtained with an energy dispersion of 0.1 eV per channel in the energy range of 280 to 355 eV, covering the characteristic edges of elements of interest C and Ca. The convergence semi-angle was set to 10 mrad, allowing for a sub-nanometer beam size of 0.2 nm. However, the spatial resolution remained fixed at 1-5 nm due to the pixel size. The energy resolution, ΔE, was adjusted by the monochromator slit and estimated to be around 150 meV, determined from the half-width of the zero-loss peak. This peak represents electrons transmitted through the specimen with no energy loss. We applied different electron doses (between 10 and 10000 $e^-/Å^2$) in order to optimize the detection of the naphthazarin. The better contrast was achieved at about 100-200 $e^-/Å^2$. Therefore, for all measurements, the corresponding electron used doses were approximately 100-10^3 200 $e^-/Å^2$.

In EELS experiments, background removal is a crucial step in data analysis as it helps isolate and identify meaningful signals from the atomic ionization edges superimposed on the large signal from the large low-loss signal. The EEL spectroscopy data was enhanced by filtering it through principal component analysis (PCA) in the Hyperspy software suite (http://hyperspy.org/). Specifically, based on existing literature references, the peaks corresponding to the carbonate peak at 290.3 eV and the primary calcium L3-edge peak at 349.3 eV were utilized for energy scale calibration. To further process the data, a power law model was subtracted from each elemental edge to remove the background, which was accomplished using Gatan's Digital Micrograph software (de Frutos *et al*., 2023).

2.7.12.3. Sample preparation

2.7.12.3.1. Ultramicrotomy

1. Calcium carbonate powder was extensively dispersed in absolute ethanol for at least an hour and further dispersed by using a Potter-Elvehjem tissue grinder analog for 10 minutes before resin embedding.

2. Ethanol was progressively replaced by resin (either LR-White or Spurr) following a first incubation into 50% resin (in absolute ethanol) for 10 minutes, three times. Then, incubations with 75% and 100% resin were done similarly.

3. Samples were transferred to micro-molds (8 mm diameter) and kept at 60 ºC until complete resin polymerization. The hardening of resin is not done by cooling but by polymerization.

4. Resin blocks were cut using a microtome Leica (Figure 2.27a) into slices with 50 nm - 60 nm thickness once the resin layer had been removed until the powder was reached.

5. Slices were transferred to Copper holey carbon TEM grids (300x300 meshes) for imaging (Figure 2.27b).

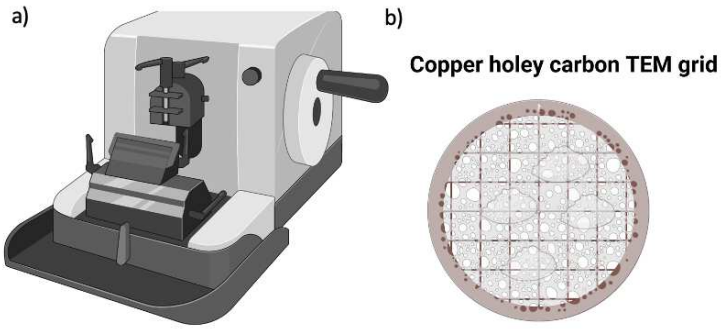

Figure 2.27. Pictorial representation of a) ultramicrotome and b) lamella section of calcite+0.55 mM naphthazarin on copper holey carbon TEM grid.

2.7.12.3.2. FIB lamella

The FIB lamella section for STEM-EELS was prepared at Max Planck instate for colloids and interfaces in Potsdam, Germany, by Clemens Schmidt. A small number of the $CaCO_3$ crystals were placed onto a suitable holder and coated with a protective platinum layer to prevent charging during FIB milling.

The initial milling process was started by inserting the sample holder into the FIB-SEM instrument. The area of interest was located, and initial milling parameters were set, such as ion beam current, acceleration voltage, and milling pattern. The region was exposed to an ion beam to thin down to create a lamella by milling away excess material surrounding the area of interest (Figure 2.28). The samples were polished and thinned down by adjusting the milling parameters to reduce the ion beam current and optimize the milling direction. The progress was monitored using SEM imaging and periodically pausing milling to inspect the lamella thickness. Once the lamella reached the desired thickness(100 nm), final polishing was performed using a low-energy ion beam and/or gas-assisted *etc*hing to achieve a smooth surface (Figure 2.28). Low-energy ion beam cleaning, electron beam cleaning, or a combination of both were used to improve the lamella's quality.

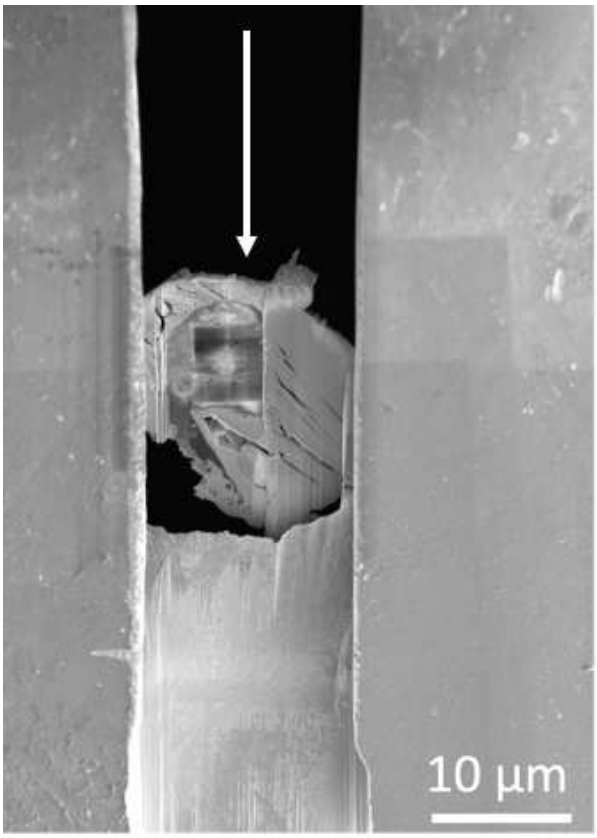

Figure 2.28. $CaCO_3$ +naphthazarin section (white arrow) prepared for STEM-EELS using FIB-SEM.

3

Role of naphthazarin on ACC formation and crystallization

In this chapter, we first explore the impact of naphthazarin in biologically relevant concentrations on the size, composition, and local structure of amorphous calcium carbonate (ACC) nanoparticles as well as on its stability against crystallization in solution and air.

Second, we study the remarkable color transformation of the solution observed from red to blue before ACC precipitation, resulting in a lavender-blue ACC powder, which eventually crystallizes into purple calcite. As already mentioned, naphthazarin is a natural compound structurally similar to polyhydroxy-1,4-naphthoquinones (PHNQs) that change color from red to blue due to successive deprotonations. Interestingly, these color changes occur in a pH range (8.2-10.6) relevant for calcium carbonate formation in mineralizing marine organisms (Land *et al*., 1983; Sevilgen *et al*., 2019). Therefore, by further investigating the role of pH during ACC-naphthazarin co-precipitation and crystallization, we propose possible mechanisms controlling

the coloration of biominerals formed through ACC precursors that lead to stable, vibrant, and diverse colors during biomineralization.

3.1. Effect of naphthazarin on ACC composition, local structure, and nanoparticle size

To validate the amorphous nature of the ACC samples synthesized in the absence or presence of various concentrations of naphthazarin from 0.053 mM to 0.53 mM. we conducted XRD measurements of the samples after 30 s of $CaCl_2$ addition during the direct precipitation method M1. XRD diffractograms of all the ACC samples exhibit no defined Bragg peaks but broad peaks at 32° and 45° indicating the presence of ACC polymorphs (Michel *et al*., 2008)). Figure 3.1 displays the XRD diffractogram acquired for a pure ACC sample synthesized through the direct precipitation method using the Metrohm® setup measured on Bruker D8 (Figure 3.1a) and without using the Metrohm® setup estimated at ESRF ID15A (Figure 3.1b). In Table 3.1, summarizes the names of the samples used in this chapter, along with information about their method of synthesis.

Table 3.1. Sample names and synthesis methods.

S. No.	Sample name	Method of synthesis	Metrohm setup
1	ACC (0-0.55 mM naphthazarin)	Direct precipitation method (M1)	Used
2	ACC (0-0.55 mM naphthazarin)	Direct precipitation method (M2)	Not used
3	Calcite (0-0.55 mM naphthazarin)	Direct precipitation method (M1)	Used
4	Calcite (0-0.55 mM naphthazarin)	Direct precipitation method (M2)	Not used

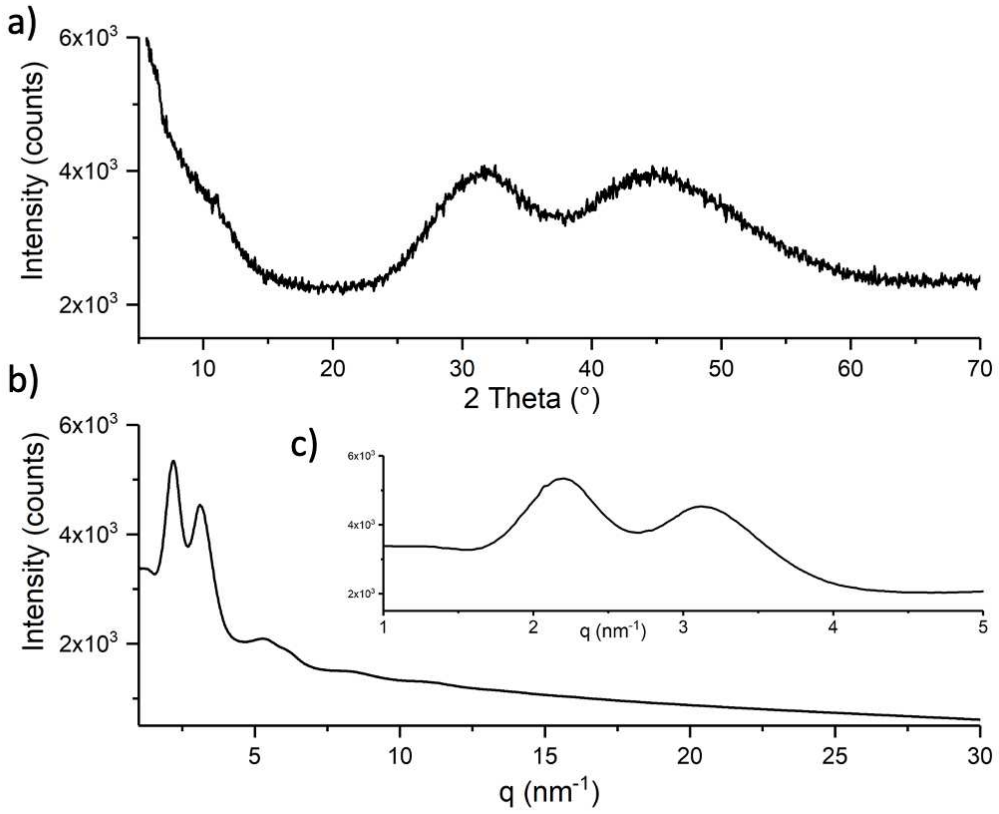

Figure 3.1. XRD diffractogram obtained on ACC synthesized by fast precipitation method on Metrohm® setup (a) and without Metrohm® setup (b). Measurement performed on a) Bruker D8, b) ID15A beamline ESRF, c) zoomed-in view of the diffractogram (b).

Synchrotron radiation source ESRF was preferred for Pair Distribution Function (PDF) analysis over laboratory X-ray diffractometers due to their high intensity, tunable energy range, and rapid data collection and processing. These factors enable more precise and efficient structural analysis of a wide range of samples.

3.1.1. Composition of the ACC-naphthazarin samples

3.1.1.1. H_2O content associated with ACC

Using TGA and DSC measurements, we monitored the removal of water, and the crystallization of ACC, on this basis we quantified the relative weight fractions of water associated with ACC+0.53 mM naphthazarin. The DSC thermograms (Figure 3.2) reveal (i) an endothermic peak occurring within the temperature range of 50-120 °C (hydration enthalpy) and (ii) an exothermic peak at 160 °C for ACC that is shifted at 210 °C for ACC+0.53 mM naphthazarin (crystallization of ACC). These endothermic and exothermic phenomena observed on the DSC

thermogram were then compared with the TGA thermogram in order to distinguish adsorbed from structural water. The thermograms were obtained on ACC, ACC+0.53 mM naphthazarin (Figure 3.2). The relative amounts of adsorbed and structural water lost during the ACC crystallization were extracted from the TGA thermogram plot and summarized in Table 3.2 The weight loss between 50-120 °C and 150-250 °C corresponds to the respective amounts of adsorbed and structural water. It was observed that in the presence of naphthazarin, a slightly higher amount of water is adsorbed on the ACC.

Table 3.2. Presents the quantification of water content associated with ACC.

Sample	**H_2O (wt.%)** (20-100 °C)	**H_2O (wt.%)** (150-250 °C)	**Ca:H_2O** (20-100 °C)	**Ca:H_2O** (150-250 °C)
ACC	12.90 ± 0.2	5.30 ± 0.2	1/0.71	1/0.3
ACC+0.53 mM Naphthazarin	13.85 ± 0.2	5.90 ± 0.2	1/0.77	1/0.33

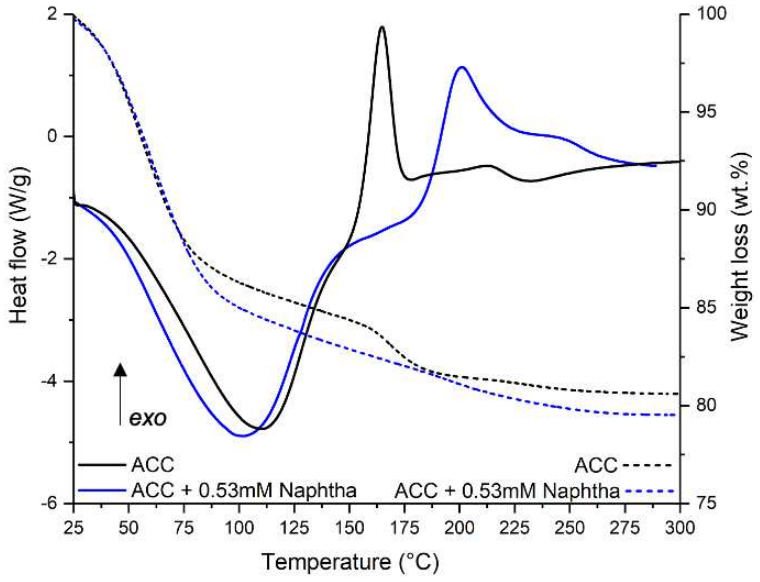

Figure 3.2. TGA thermogram profile for ACC and ACC+0.53 mM naphthazarin overlayed with DSC thermogram for the respective samples.

Overall, naphthazarin facilitates hydration, evident in the increased (~1.0 wt.%) adsorbed water content in ACC+0.53 mM compared to pure ACC. However, TGA reveals small difference (~0.5 wt.%) in the amount of structural water.

3.1.1.2. Naphthazarin content associated with ACC

The amount of naphthazarin associated with ACC in the resulting powder was quantified using UV-visible spectroscopy measurements by first dissolving the ACC+naphthazarin samples with 1M HCl solution that resulted in a clear red-colored solution and second measuring the absorbance of the resulting solution by adjusting the pH to 5.5, at which the calibration curve was obtained.

The calibration curve was obtained as follows: Naphthazarin was dissolved in water at different concentrations ranging from 0.01 to 0.055 mM due to the low solubility of naphthazarin (~0.055 mM) at pH 5.5, which is the obtained pH for all the prepared solutions (Figure 3.3). UV-visible measurements were performed on different concentration of naphthazarin (Figure 3.3a). The UV-vis spectrum for naphthazarin has two bands one at 490 nm and second at 515 nm. To obtain the calibration curve we extracted the absorbance for each concentration at 515 nm. This band was selected because we also observed the maximum absorbance for ACC+naphthazarin samples at around 510-520 nm.

Once the calibration curve was obtained (0-0.055 mM), we then performed the UV-visible measurements on the resulting ACC+0.11 mM naphthazarin and ACC+0.53 mM naphthazarin solutions prepared by dissolving them 1 M HCl solution and then adjusting the pH to 5.5. To get the accurate value of naphthazarin concentration associated with ACC, we must stay within the calibration curve limits. Ideally our samples contain 0.11 mM and 0.53 mM naphthazarin, these concentration values should lie outside the calibration curve limits. In order not to exceed the calibration limits, we decided to dissolve 60 mg of ACC+0.11 mM naphthazarin sample and 20 mg of ACC+0.53 mM naphthazarin in 1M HCl and adjusting the pH to 5.5 while keeping the total volume at 50 mL.

The absorbance spectra were obtained on ACC+0.11 mM naphthazarin and ACC+0.53 mM naphthazarin solution. The absorbance value for each sample at 510 nm were extracted and plotted on the calibration curve, which suggests that the concentration of naphthazarin in ACC+0.11 mM naphthazarin, ACC+0.53 mM naphthazarin was 0.033 mM and 0.051 mM respectively. After this the concentration values were adjusted to 200 mg of ACC (yield of reaction (M1)) to get the exact concentration of naphthazarin associated with ACC. Therefore, the concentration terms for ACC+0.11 mM naphthazarin and ACC+0.53 mM naphthazarin were ~0.11 mM and ~0.51 mM respectively. The quantification of naphthazarin associated with

ACC allowed us to calculate the Ca/naphthazarin molar ratios which are summarized in Table 3.3. UV-vis results indicated that the efficiency of naphthazarin incorporation or association with ACC was approximately 95-100 %.

The association of 95-100 % naphtahzarin with ACC highlights the effeicency of ACC to bind with naphthazarin which opens the door for possible use of $CaCO_3$ synthesis for the treatment of waste water generated by the dyeing industry. In a study conducted by (Zhao and Gao, 2010), they proposed a novel wastewater treatment approach by immobilizing waste anionic dyes (*e.g.*, congo red, CR) and cationic dyes (*e.g.*, methylene blue, MB) by conjugating them to $CaCO_3$. The research demonstrated that the synthesis of $CaCO_3$ in the presence of wastewater containing these (1.8 mM) dyes effectively reduced the color intensity of the solution by 98-99 %. Furthermore, they showcased the potential of reusing the dye-immobilized $CaCO_3$ sludge, as a filler in polymer products, to prevent secondary pollution.

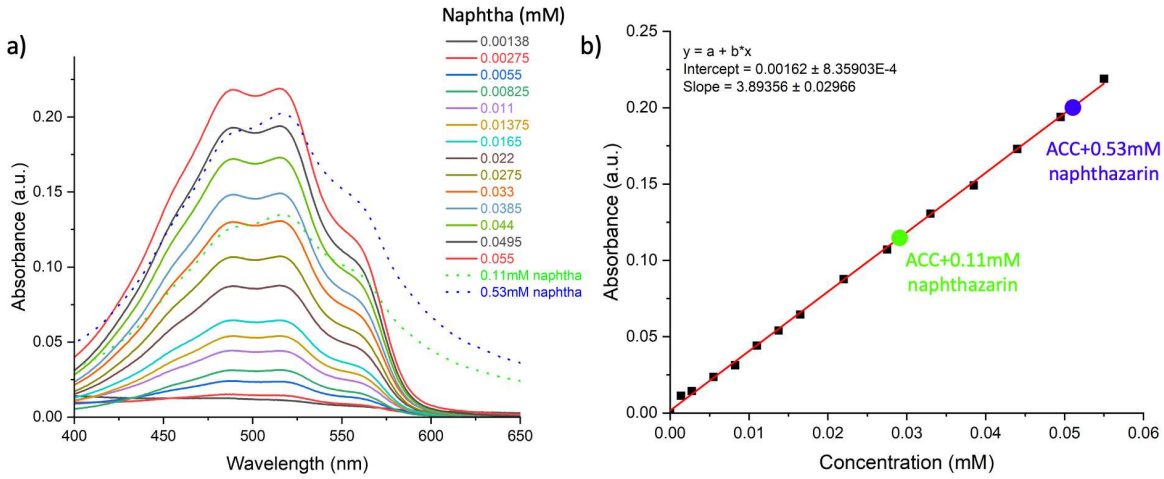

Figure 3.3. a) UV-visible absorbance spectra obtained on different concentration of naphthazarin at pH 5.5. UV-vis spectra solution obtained on solution by dissolving ACC+0.11 mM naphthazarin and ACC+0.53 mM naphthazarin in 1 M HCl at pH 5.5. b) Calibration curve obtained for naphthazarin at pH 5.5 by extracting the absorbance values for each concentration at 510 nm and corresponding absorbance values for ACC+naphthazarin samples.

Table 3.3. Calcium and naphthazarin molar ratio in the samples synthesized by the direct precipitation method (M1).

S. No	Sample	Ca:naphthazarin (Molar ratio)
1	ACC+0.11 mM naphthazarin (M1)	364:1
2	ACC+0.53 mM naphthazarin (M1)	80:1

3.1.1.2. Nanoparticle size and local structure of the ACC-naphthazarin samples

FEG-SEM micrographs obtained on ACC, ACC+0.11 mM and with ACC+0.53 mM naphthazarin revealed the presence of aggregated spherical nanoparticles within the ACC sample (Figure 3.4). The nanoparticles exhibited an average size range of approximately ~140 nm whatever the amount of naphthazarin suggesting particle size distribution is almost the same in the presence and absence of naphthazarin (Figure 3.4d). However, the nanoparticle sizes in our case (~140 nm) markedly deviated from the values reported in the literature, for instance ~70 nm by (Zou *et al*., 2015). This difference can be ascribed to variations in the timing of the filtration process. Specifically, Zou *et al.*, conducted filtration promptly following the precipitation event, while in our experimental approach, we introduced a deliberate delay of 20 to 30 seconds before initiating filtration so that the precipitate formed after addition of $CaCl_2$ was anticipated to be homogeneous in the solution. This contrast in filtration timing underscores the time-sensitive nature of the system as ACC remains in a state of continuous evolution challenging the notion of complete stability during certain periods of its existence. In order to ensure the samples synthesized were repeatable as much as possible we kept the different paraments of the reaction constant such as $CaCl_2$ addition time, mixing time, washing with cold ethanol, stirring rate, drying under vacuum for 30 minutes.

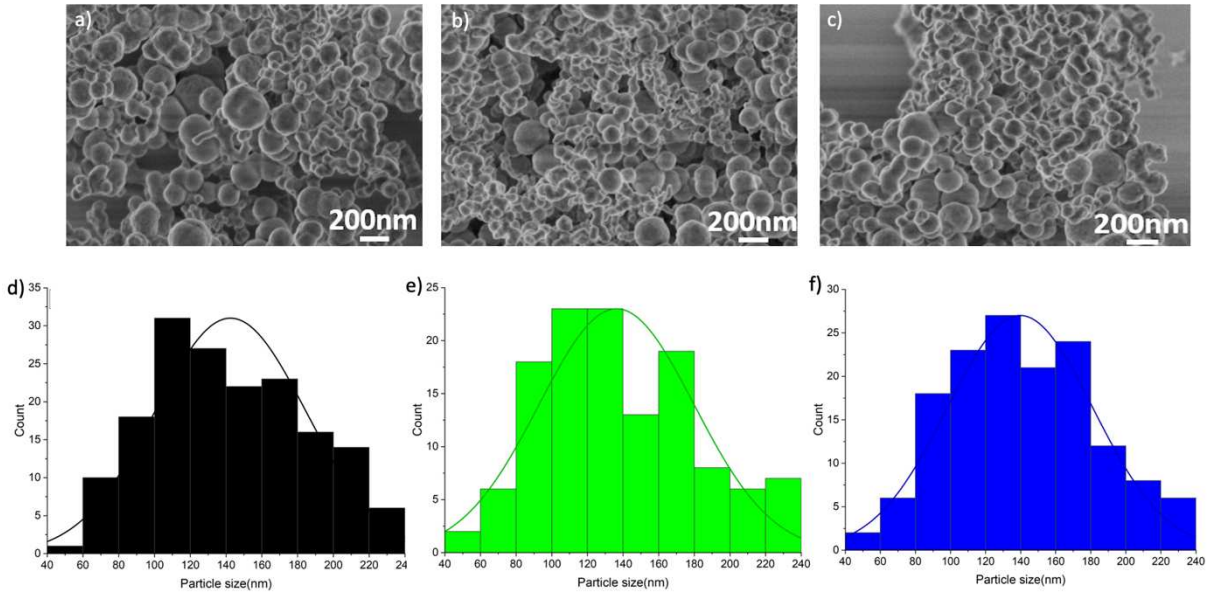

Figure 3.4. FEG-SEM micrographs and size distribution histograms for: a) and d) ACC (averaged size ~142 nm), b) and e) ACC+0.11 mM naphthazarin (averaged size ~138 nm), c) and f) ACC+0.53 mM naphthazarin (averaged size ~137 nm, ~150 particles measured).

To examine the impact of naphthazarin on the local structure of ACC, we conducted SAXS/WAXS measurements and employed Pair Distribution Function (PDF) analysis at the ESRF ID15A beamline. This allowed us to gain insight into how naphthazarin influences the inter-atomic distances within the $CaCO_3$ system. Under room temperature conditions, the ACC PDF profile reveals distinctive short and medium-range order features extending up to 10 Å (Figure 3.5). Notably, the main maxima within these profiles are positioned at approximately 2.4, 2.9, 4.1, and 6.2 Å in agreement with previous reported PDF data (Michel *et al.*, 2008). Each of these maxima corresponds to specific interatomic distances and provides valuable information about the local atomic arrangements within the material. The peak at 2.4 Å primarily represents contributions from Ca-O pairs, indicating the proximity of calcium ions to oxygen ions in the first coordination shell. The 2.9 Å peak relates to O-O pairs, signifying oxygen-oxygen interactions. The 4.1 Å peak predominantly contains contributions from Ca-O and Ca-Ca pairs in the first coordination shell, demonstrating the arrangement of calcium ions relative to each other and their coordination with oxygen ions. The 6.2 Å peak similarly involves Ca-O and Ca-Ca pairs in the second coordination shell, reflecting longer-range structural features. We observed that both ACC and ACC+0.53 mM naphthazarin display similar PDF profiles (Figure 3.5), showcasing the typical short and medium-range order patterns extending up to 10 Å with characteristic positions for the primary maxima. This

suggests that naphthazarin's presence does not significantly alter the short and medium-range structural order of ACC, as indicated by the consistent peak positions and the types of interatomic pairs contributing to these peaks. In a study by (Tobler *et al*., 2014), evidenced the absence of any differences in the local atomic structure of the different ACC precipitates, whether they contained aspartic acid or glycine. The PDFs for all tested ACC samples were found to be identical, and demonstrated a structural coherence within a range of less than 15 Å. This suggests that, at the local atomic level, there were no significant variations in the structure as it might be adsorbed on the surface of the ACC. Interestingly it has been shown that the introduction of Mg^{2+} or polyaspartic acid (pAsp) into ACC results in local structural changes. This alters the local enviro nment around calcium and carbonate ions, affecting their coordination and bonding.This structural transformation is evident in the distinct average coordination number (CN) and radial distance (R) of the first Ca–O coordination shell in Mg-ACC/pAsp-ACC, as revealed through Ca K-edge EXAFS analysis, differing from that of pure ACC (Lam *et al*., 2007). Therefore, in case of naphthazarin it seems that naphthazarin most probably adsorbed on the surface thereby unaffecting the local structure of the ACC.

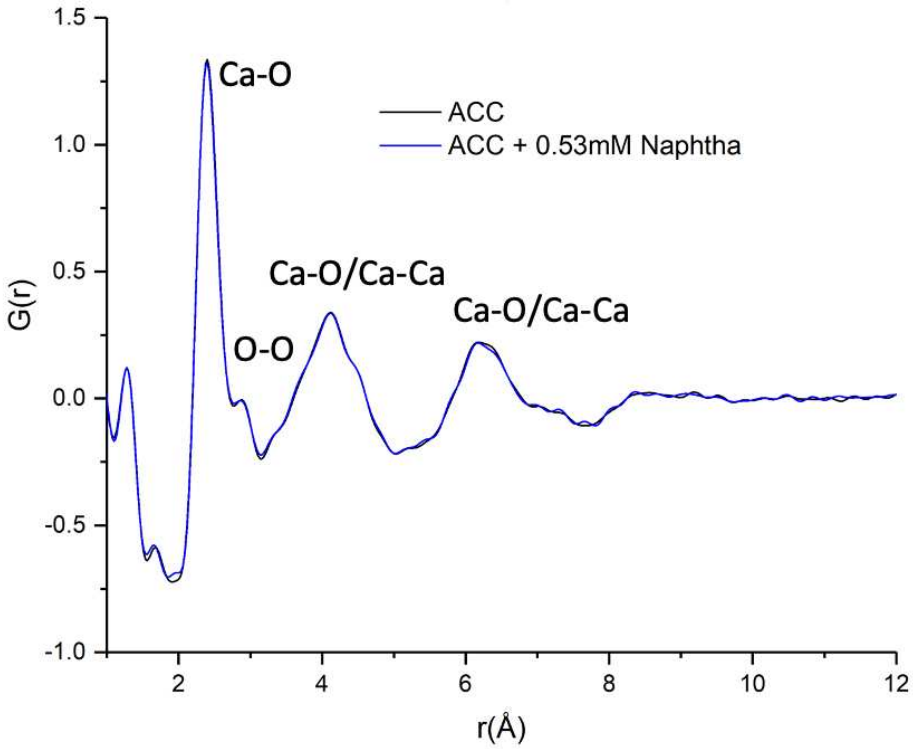

Figure 3.5. PDF profile for ACC and ACC+0.53 mM naphthazarin performed at ESRF ID15A beamline.

3.2. Effect of naphthazarin on ACC stabilization against crystallization

3.2.1. Crystallization in solution

3.2.1.1. In-situ monitoring of pH and free [Ca^{2+}] variations during ACC formation and crystallization in solution

Pure ACC: As seen on Figure 3.6a the addition of $CaCl_2$ solution into the Na_2CO_3 solution resulted in an immediate decrease in pH from ~11.5 to 10.5 and simultaneously an increase in the free [Ca^{2+}]. Immediately after $CaCl_2$ addition the precipitation of ACC starts the free [Ca^{2+}] decreases to 0.5-0.2 mM/L from 2-3 mM/L leading to an increase in pH from ~10.5 to ~10.6 (<100 s). After this, for both pH and free [Ca^{2+}] profile is marked by a small decrease in the slope which corresponds to the stable ACC phase (Figure 3.6a). Then, a noteworthy change occurs during the transformation of ACC into calcite and vaterite (~400 s) (Figure 3.6b), marked by a significant decrease in [Ca^{2+}] concentration (>0.1 mM). This drop in [Ca^{2+}] concentration is a key indicator of the crystallization processes as confirmed by performing XRD measurement on the powder filtered at this stage (~700 s) and which shows the presence of a mixture of calcite and vaterite.

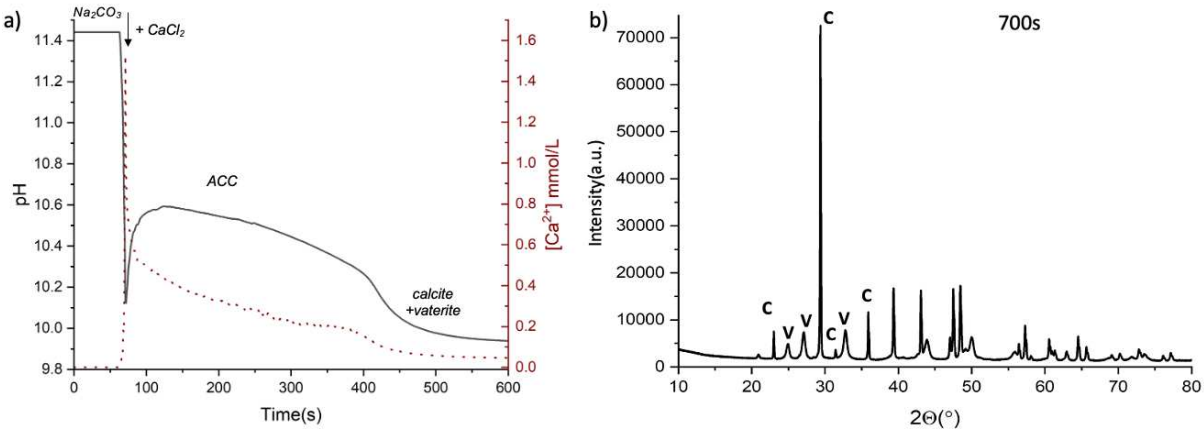

Figure 3.6. a) pH profile and [Ca^{2+}] profile during $CaCO_3$ synthesis, b) XRD diffractogram of ACC obtained by direct precipitation method at 700 s.

ACC+naphthazarin (0.05 to 0.53 mM): As seen in Figure 3.7, upon addition of naphthazarin, the overall line shapes of pH and [Ca^{2+}] evolution curves are similar but the crystallization event is not occurring at the same time. And importantly, the effect of naphthazarin addition does not follow a linear trend. At lower concentrations, (≤0.11 mM) naphthazarin tends to

inhibit the crystallization of ACC into crystalline phases (according to both pH and [Ca^{2+}] curves). This stabilizing effect could be attributed to the molecule's ability to interact with the ACC surface and impede the nucleation and growth of crystal structures. However, it's important to note that beyond the concentration of 0.11 mM, the effectiveness of naphthazarin in preserving ACC stability against crystallization appears to diminish. This decrease in ACC stability against crystallization beyond a certain concentration of naphthazarin could be attributed to aggregation or precipitation: Naphthazarin molecules themselves might start to aggregate or precipitate out of solution at higher concentrations. This aggregation could potentially interfere with their ability to interact with the ACC surfaces, reducing their stabilizing effect. In summary increase in naphthazarin concentration from 0.05 mM to 0.11 mM increases the ACC crystallization time by ~40-50 s and a further increase in naphthazarin concentration from 0.11 mM to 053 mM decreases the ACC crystallization time by ~50 s. Table 3.4 summarizes the ACC crystallization time in presence of different concentration of naphthazarin.

On comparing the effect of naphthazarin on ACC stability against crystallization in solution with other additives such as polyaspartic acid, a direct correlation between the concentration of polyaspartic acid (pAsp) in the solution and the extended stability of ACC against crystallization. (Zou *et al*., 2017) demonstrated that increasing the pAsp from 0.3 wt.% to 6 wt.% the crystallization time increased by 800 s. It's widely acknowledged that pAsp slows ACC's crystallization by binding to the Ca^{2+} ions on crystal surfaces, owing to the attraction between pAsp's negatively charged carboxylic groups, which significantly inhibit the nucleation and growth of crystalline $CaCO_3$. It is worth noting that in their case, they observed a linear trend between ACC stability against crystallization and pAsp concentration *i.e.*, as pAsp concentration increased, ACC stability also increased.

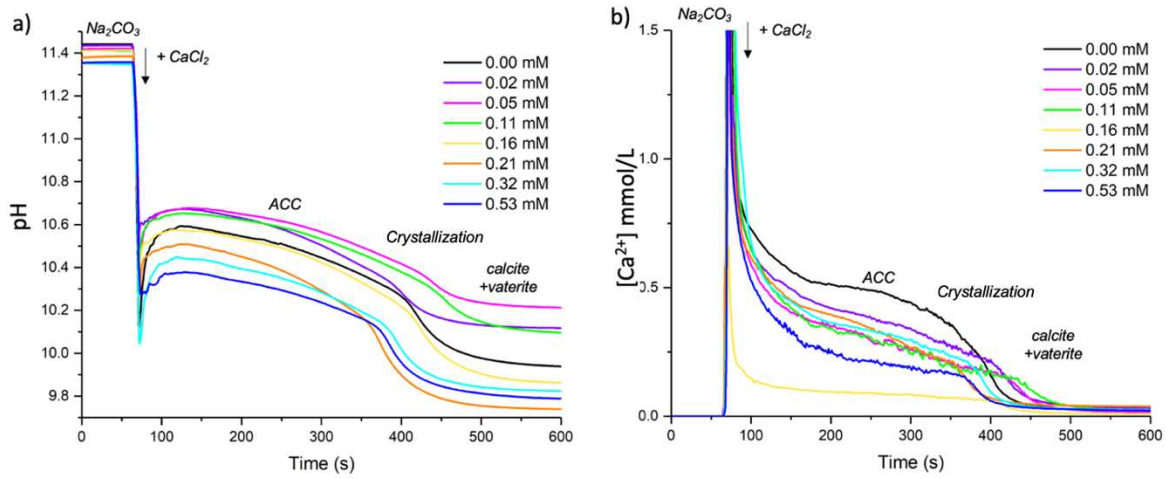

Figure 3.7. a) pH profile for $CaCO_3$ synthesis in the presence of various concentrations of naphthazarin., b) $[Ca^{2+}]$ profile for $CaCO_3$ synthesis in the presence of different concentrations of naphthazarin.

Table 4. ACC crystalline time in the presence of different concentrations of naphthazarin.

S. No.	Sample (M1)	Start of crystallization (s)
1	ACC	400
2	ACC+0.02 mM naphthazarin	395
3	ACC+0.06 mM naphthazarin	440
4	ACC+0.11 mM naphthazarin	440
5	ACC+0.16 mM naphthazarin	405
6	ACC+0.21 mM naphthazarin	357
7	ACC+0.32 mM naphthazarin	380
8	ACC+0.53 mM naphthazarin	360

3.2.1.2. pH variations during the phase transition calcite+vaterite → calcite in solution

To study the latter transition of calcite+vaterite into calcite we monitored the pH profile for 12hrs for $CaCO_3$ and $CaCO_3$ +0.11 mM naphthazarin (Figure 3.8a). We observed that the introduction of naphthazarin exerted a significant delay in the final crystallization (sudden drop in pH after 6 h vs 8 h for ACC and ACC+naphthazarin respectively), in line with earlier observations for the ACC to calcite+vaterite transition. This delay was further substantiated by analyzing XRD diffractograms of the precipitate collected before (700 s and 5 h) and after (8 h for ACC and 10 h for ACC+naphthazarin) the sudden pH transition (Figure 3.8b), revealing

distinct variations in the proportion of calcite and vaterite. Rietveld refinement enabled us to precisely quantify these polymorphic distinctions. Our analysis revealed that ACC primarily transformed into a combination of calcite and vaterite in a ratio of 58:42. Notably, in the case of ACC+0.11 mM naphthazarin, the ratio shifted to 44:56. These findings strongly indicate that the addition of naphthazarin at this concentration promotes the stability of the vaterite polymorph. In a study conducted by (Tobler *et al*., 2016), it was demonstrated that the transition of ACC to calcite is pH-dependent. Specifically, at a lower pH of 10.5, both vaterite and calcite are generated. However, as the pH level rises, the ACC's lifespan is extended, and it undergoes a direct transformation into calcite at pH values exceeding 12.0, without the intermediary formation of vaterite. Our results are consistent with these observations, as we also observe the formation of ACC in a pH range of 10.5-10.6.

After 6 h (Figure 3.8a), a drop in pH from ~9.6 to 9.4 is observed for pure ACC (Figure 3.8a). XRD measurements conducted on samples collected after 5 h and 8 h confirm the full transition into calcite (Figure 3.8b). Indeed, a reduction in the intensity of vaterite peaks after 5 h is observed when compared to the XRD diffractogram captured at 700 s. Subsequently, the XRD diffractogram at 8 h exhibited an absence of vaterite peaks, signifying a complete transformation into calcite as the sole crystalline phase.

Conversely, in the reaction mixture containing 0.11 mM naphthazarin, the transformation from calcite-vaterite to calcite took place around the 8 h mark which is reflected by a drop in pH from ~8.9 to 8.6 (Figure 3.8a). This transformation was also monitored through XRD measurements, conducted after 7 h and 10h (Figure 3.8b). After 7 h, there was a noticeable decrease in the intensity of vaterite peaks when compared to 700 s. In addition, the vaterite peaks remained more pronounced than for pure $CaCO_3$, underscoring the stabilizing effect of naphthazarin on the vaterite polymorph. The XRD diffractogram at 10 h revealed a complete absence of vaterite peaks. These findings further supports the role of naphthazarin in stabilizing the vaterite polymorph and delaying its transformation into calcite.

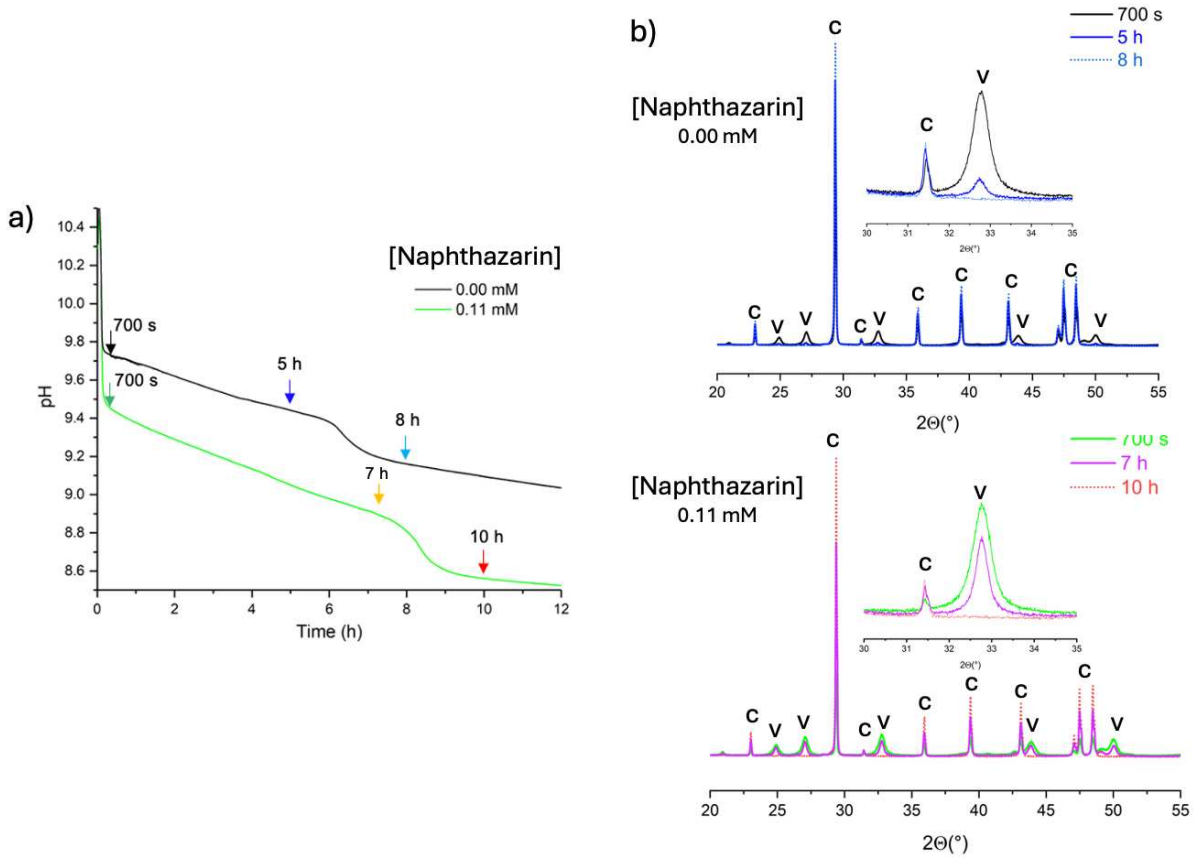

Figure 3.8. a) pH profile of $CaCO_3$ synthesis in the absence and presence of naphthazarin (0.11 mM), illustrating distinct events corresponding to crystallization and sample collection at different time for XRD measurments, b) XRD diffractogram obtained at different time intervals for $CaCO_3$ and $CaCO_3$+0.11 mM naphthazarin.

Following these studies, we have gained insights into the stability of ACC and its crystallization in solution when exposed to naphthazarin, as well as how naphthazarin can influence the selection of polymorphs. Consequently, considering these findings, we opted to run the reaction for 2 days when performed outside the Metrohm® ensuring the complete transformation of the calcite + vaterite mixture into calcite when the naphthazarin concentration exceeds 0.11 mM. Reactions outside the Metrohm® setup were performed for synthesis of large number of samples for ESRF beam time.

We conducted XRD analysis on the powder collected after 700 s and 48 h (Figure 3.9) which confirmed the absence of vaterite peaks in the XRD diffractogram, confirming the transformation into calcite. Specifically, in the presence of 0.11 mM naphthazarin(M2), ACC initially underwent crystallization into a mixture of calcite and vaterite. However, after 48 h,

calcite+vaterite transformed into pure calcite, resembling the synthesis process in the absence of naphthazarin (Figure 3.9).

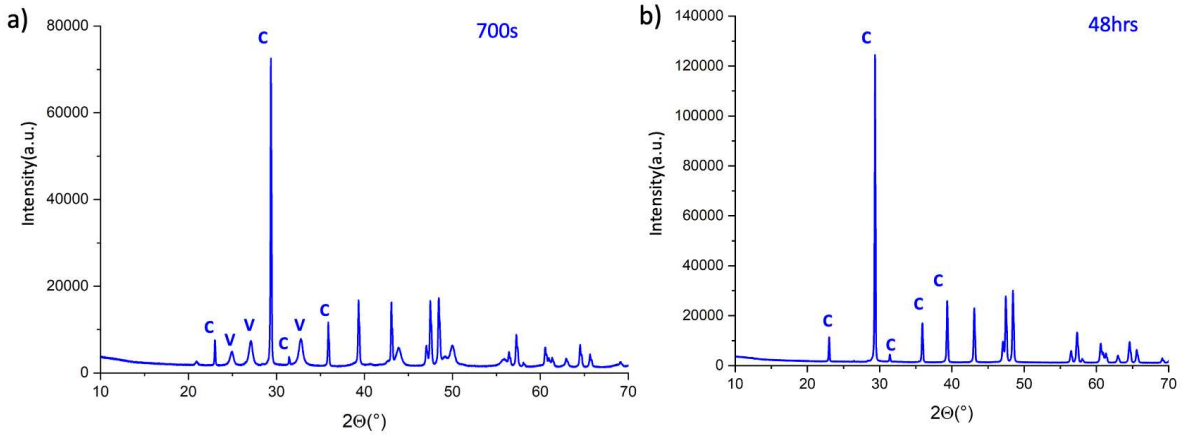

Figure 3.9. XRD diffractograms on $CaCO_3$+0.11 mM naphthazarin filtered at different time intervals of the synthesis (M2), a) 700 s, c) 48 h.

Interestingly, when we increased the concentration of naphthazarin to 0.53 mM (M2), vaterite remained present even after 2 days (Figure 3.10a). To achieve a complete conversion of the vaterite-calcite mixture into calcite only, we allowed the reaction to proceed for an additional 24 h. Subsequent XRD diffractograms obtained on the sample collected after a total of 72 hours confirmed the exclusive presence of the calcite polymorph, as depicted in Figure 3.10b. It is well known that additives can influence vaterite stability. Numerous prior investigations have demonstrated the inhibitory effect of pAsp on the vaterite-to-calcite transformation by impeding either the dissolution of vaterite or the nucleation of calcite (Zou *et al*., 2017). It is commonly proposed that the inhibition of vaterite dissolution is attributed to the adsorption of pAsp onto vaterite. In our case, it is conceivable that naphthazarin may be absorbed onto both ACC and vaterite surfaces, effectively inhibiting their transformation into calcite. Meanwhile, hydroxyl ions within the bulk material further contribute to this stabilization, collectively promoting the retention of the amorphous phase or vaterite and delaying the crystallization into calcite.

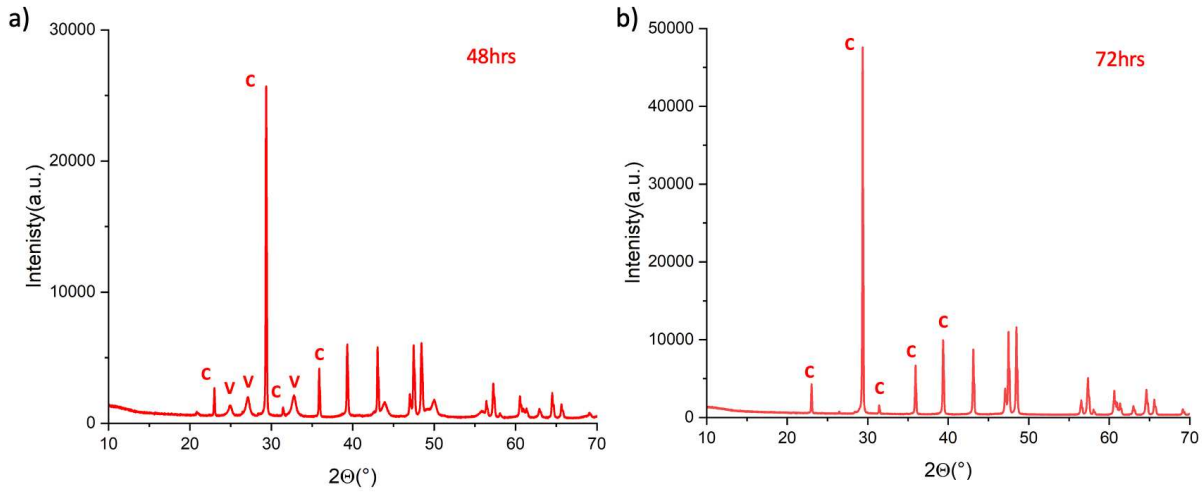

Figure 3.10. XRD diffractograms on $CaCO_3$+0.53 mM naphthazarin filtered at different time intervals of the synthesis(M2), a) 48 h, b) 72 h.

3.2.1.3. Effect of naphthazarin on the morphology of the $CaCO_3$ crystals

SEM observations were conducted on pure $CaCO_3$ obtained at different time intervals (700 s and 18 h) to get insight into morphology (Figures 3.11a and 3.11b). The micrographs depict the coexistence of spherical (vaterite) and rhombohedral (calcite) structures within the $CaCO_3$ samples. The spherical structures exhibit either a porous texture or seem to be composed of smaller particles (Figure 3.11c). However, in stark contrast, observations made at the 18-hour mark reveal a significant difference *i.e.*, at this point, all the spheres have undergone a complete conversion into rhombohedral structures (Figures 3.11d and 3.11e) with notably smoother surfaces (Figure 3.11e).

In the case of $CaCO_3$ in the presence of 0.11 mM naphthazarin (Figure 3.11f), a striking divergence emerges. Spherical and rhombohedral shapes were present at 700 s. Interestingly the rhombohedral structures (Figures 3.11f and 3.11g) observed in the presence of naphthazarin at this time point exhibit a smoother surface compared to the rhombohedral structures (Figures 3.11h and 3.11i) at the 18-hour mark, which appear rougher/with pores. These findings strongly suggest that naphthazarin exerts a significant influence on the morphology and surface characteristics during transformation of calcite+vaterite mixture into calcite. This transformation is accompanied by change in pH and $[Ca^{2+}]$ discussed in section 3.2.1.1, suggesting rearrangement of ions which might be due to dissolution crystallization process.

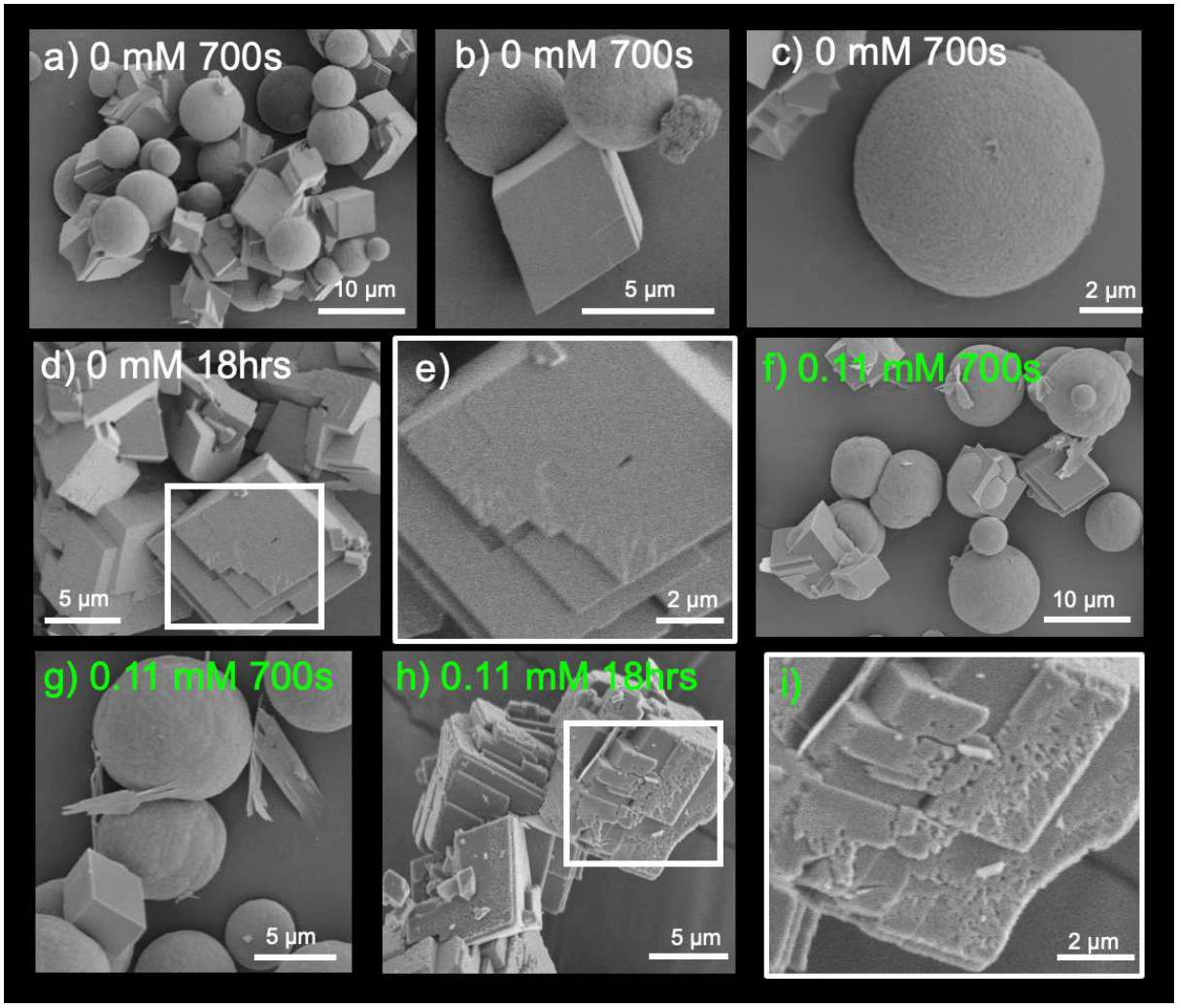

Figure 3.11. SEM micrographs obtained on $CaCO_3$ and $CaCO_3$+0.11 mM naphthazarin at different time intervals showcasing the evolution of crystal morphology over time. Micrograph of $CaCO_3$ a-c) 700 s, d, e) 18 h and $CaCO_3$+0.11 mM naphthazarin f, g) 700 s, h, i) 18 h.

3.2.2. Crystallization in air induced by mild-heating

3.2.2.1. Effect of naphthazarin on ACC crystallization temperature

We conducted a study to assess the effect of naphthazarin on the crystallization temperature of ACC synthesized by M1 through DSC measurements. In the DSC profile of ACC (Figure 3.12), we observed a peak at approximately 100 °C, representing the endothermic process of water loss, and another peak at around 150 °C, signifying the exothermic process of ACC crystallization. The enthalpy of hydration for ACC was determined to be 179.2 J/g, while ACC+0.11 mM naphthazarin (M1) exhibited an enthalpy of 186.7 J/g, and ACC+0.53 mM naphthazarin (M1) showed a higher enthalpy of 242.8 J/g. Notably, the crystallization

temperatures for ACC, ACC+0.11 mM naphthazarin, and ACC+0.53 mM naphthazarin were found to be 152 °C, 160 °C, and 210 °C, respectively, with corresponding enthalpies of crystallization of 29.3 J/g, 36.8 J/g, and 48.38 J/g, respectively. Table 3.5 Summarizes the ACC crystallization temperature, enthalpy of hydration and crystallization.

Table 3.5. DSC thermogram data extracted from DSC thermogram.

S. No.	Sample	Enthalpy of hydration (J/g)	Enthalpy of crystallization (J/g)	ACC crystallization temperature (°C)
1	ACC	179.2	29.3	152
2	ACC+0.11 mM naphthazarin	186.7	36.8	160
3	ACC+0.53 mM naphthazarin	242.8	48.38	210

Comparing the DSC profiles of ACC with those containing varying concentrations of naphthazarin, a clear linear trend emerged (Appendix 1 Figure 1). It became evident that as the naphthazarin concentration increased (0.05 mM to 0.53 mM), the crystallization temperature of ACC also increased (150 °C to 210 °C) (Figure 3.12) suggesting a linear trend with respect to concentration of naphthazarin. This trend indicates that the addition of naphthazarin serves as a stabilizing factor for the ACC phase against crystallization during heating. It has been demonstrated that low-molecular-weight additives (aspartic acid, citrate) can delay the crystallization of ACC particles not in direct contact with bulk water. They achieve this by interacting strongly with water within ACC, which reduces water mobility and raises the energy barrier for dehydration. As a result, these additives enhance ACC's stability against solid-state transformation, requiring higher temperatures to initiate crystallization, all without significantly altering ACC's structure or hydration degree (Tobler *et al*., 2015, 2014).

Another plausible reason behind naphthazarin's role in enhancing the stability of ACC could be its capacity to adsorb water molecules from the surrounding enviro nment, thereby maintaining the ACC below the critical threshold of water content required for crystallization (Radha *et al*., 2010). By effectively reducing the available water for crystallization, naphthazarin contributes to an increase in the ACC's crystallization temperature, making it less prone to spontaneous phase transformation.

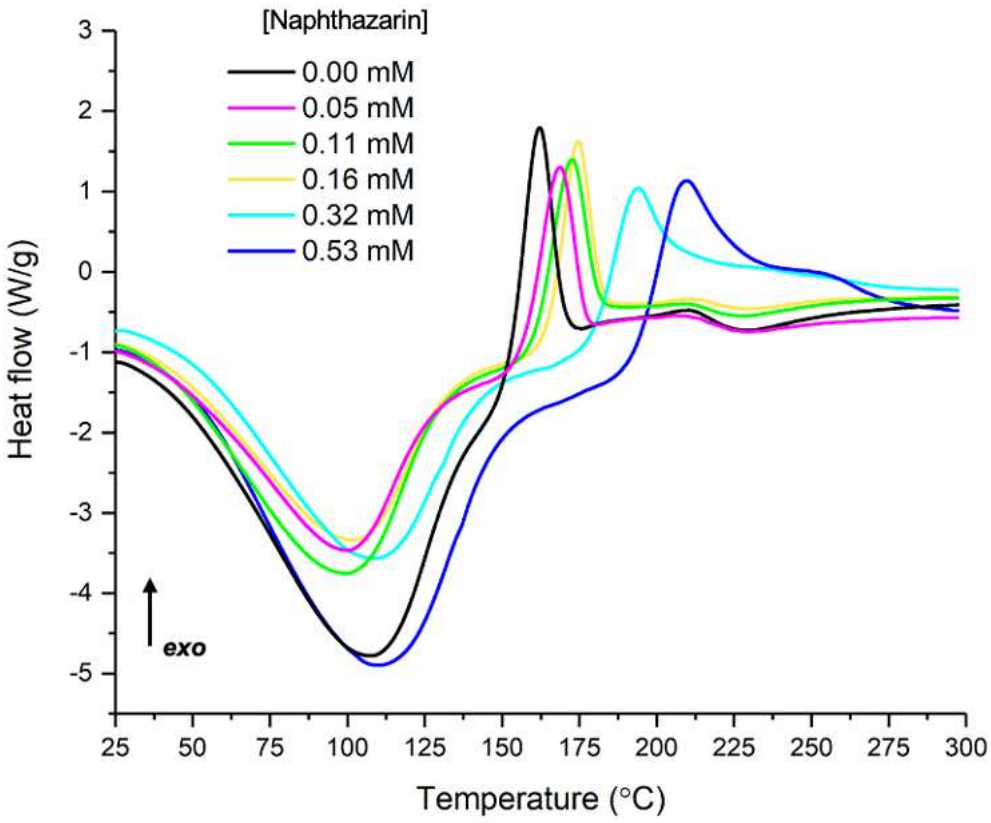

Figure 3.12. DSC thermograms were recorded for ACC samples, including variations with naphthazarin concentrations ranging from 0.05 to 0.53 mM, employing a scanning rate of 5 °C/min within the temperature range of 25 to 300 °C.

3.2.2.2. Morphology

Previous research by (Zou *et al*., 2015) highlighted that the stability of ACC can also be influenced by the size of ACC nanoparticles. Smaller ACC nanoparticles were found to exhibit greater stability in air compared to their larger counterparts. FEG-SEM micrographs (Figures 3.4 and 3.13) were used to assess the impact of naphthazarin on ACC. The average particle size of ACC, ~142 nm, closely matched ACC in the presence of naphthazarin (~138 nm), indicating that naphthazarin does not significantly affect ACC particle size. This suggests that naphthazarin's stabilization of the ACC phase is unlikely due to size effects on ACC nanoparticles, aligning with the findings of the Zou *et al*. study.

Our observations also unveiled an interesting contrast in the transformation of ACC under varying conditions. While ACC dissolution in solution follows a sequence involving calcite and vaterite intermediates before transitioning into calcite, a distinct crystallization mechanism

emerges when ACC is subjected to heating. In the latter case, we witness a direct transformation of ACC into calcite elucidated by *in-situ* heating SAXS measurement (discussed in detail further on; see Figure 3.15), suggesting an entirely different pathway for crystallization. Further examination through FEG-SEM micrographs (Figure 3.13) of heated ACC samples (200°C) reveals a striking divergence in the structure of the resulting calcite compared to its solution-derived counterpart. Notably, the calcite formed through heating does not exhibit a well-defined shape but rather consists of small crystalline nanoparticles (10-100 nn) that fuse, creating expansive structures (100-500 nm) resembling to $CaCO_3$ particle organization in corals. This disparity in crystallization mechanism could be due to differences in the mechanism of crystallization: 1) dissolution-precipitation mechanism in solution, and 2) solid-state crystallization upon heating. We also observed that the in the presence of naphthazarin the nanoparticles that fused together to form expansive structure were smaller. Moreover, the surface of these structure is not smooth and resembles highly porous material, which might be due to dehydration of $CaCO_3$.

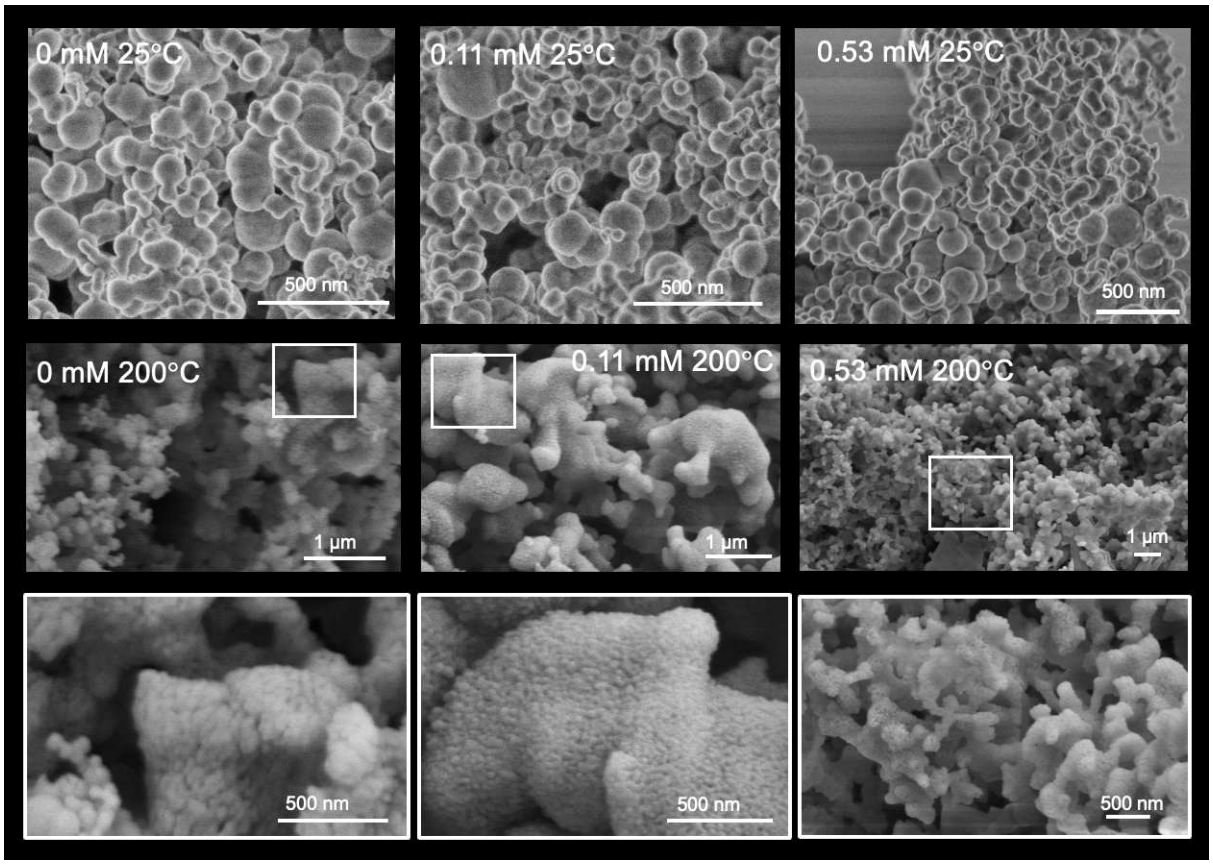

Figure 3.13. FEG-SEM micrographs of ACC, ACC+0.11 mM naphthazarin, and ACC+0.53 mM naphthazarin at 25 °C and 200 °C.

3.2.2.3. Local structure during crystallization

We conducted a heat-assisted crystallization of ACC to replicate the solid-state crystallization process that occurs in biological systems. In this effort to reveal localized structural ordering during the heat-induced ACC crystallization, we generated dPDF/dT maps (Figures 3.14a and 3.14c). dPDF/dT is the rate of change of the Pair Distribution Function with respect to temperature. It provides information, how the local atomic structure within a material evolves as the temperature changes. These maps employ a color scheme where blue signifies a negative change and red indicates a positive change in structural characteristics at corresponding temperature and position.

The most significant alterations in the dPDF/dT maps are associated with the crystallization phase, marked by a sudden upsurge in PDF intensities (Figure 3.14a). This structural reorganization, preceding crystallization (Figure 3.15a), corresponds to the removal of water from the ACC phase. Notably, the onset temperature and duration of ACC crystallization differ among various samples. In the dPDF/dT maps, pure ACC commences crystallization at 140°C and spans a temperature range of 20 °C. However, when 0.11 mM naphthazarin is introduced (Figure 3.14c), the onset temperature for the ACC crystallization event start point remains at 140 °C but extends for over 35 °C. This observation strongly suggests that the addition of naphthazarin indeed influences the crystallization process by prolonging the crystallization events when compared to pure ACC.

Regarding localized structural rearrangements at elevated temperatures (140-200 °C), ACC with naphthazarin exhibits minor distinctions in the degree of short-range order (SRO) rearrangement compared to pure ACC (Figure 3.14b). However, notable differences emerge in the medium-range order (MRO) region, particularly around interatomic distances of 6-7 Å, which corresponds to the second shell of Ca-O/Ca-Ca pairs.

It is worth noting that, even after the heating cycle, the ACC powder remained colored, indicating the continued presence of naphthazarin (as shown in Figure 3.15b). This persistence of color suggests that naphthazarin remains in the system even after the heating process. However, it is difficult to suggest if the naphthazarin present after the heating cycle has modified or degraded.

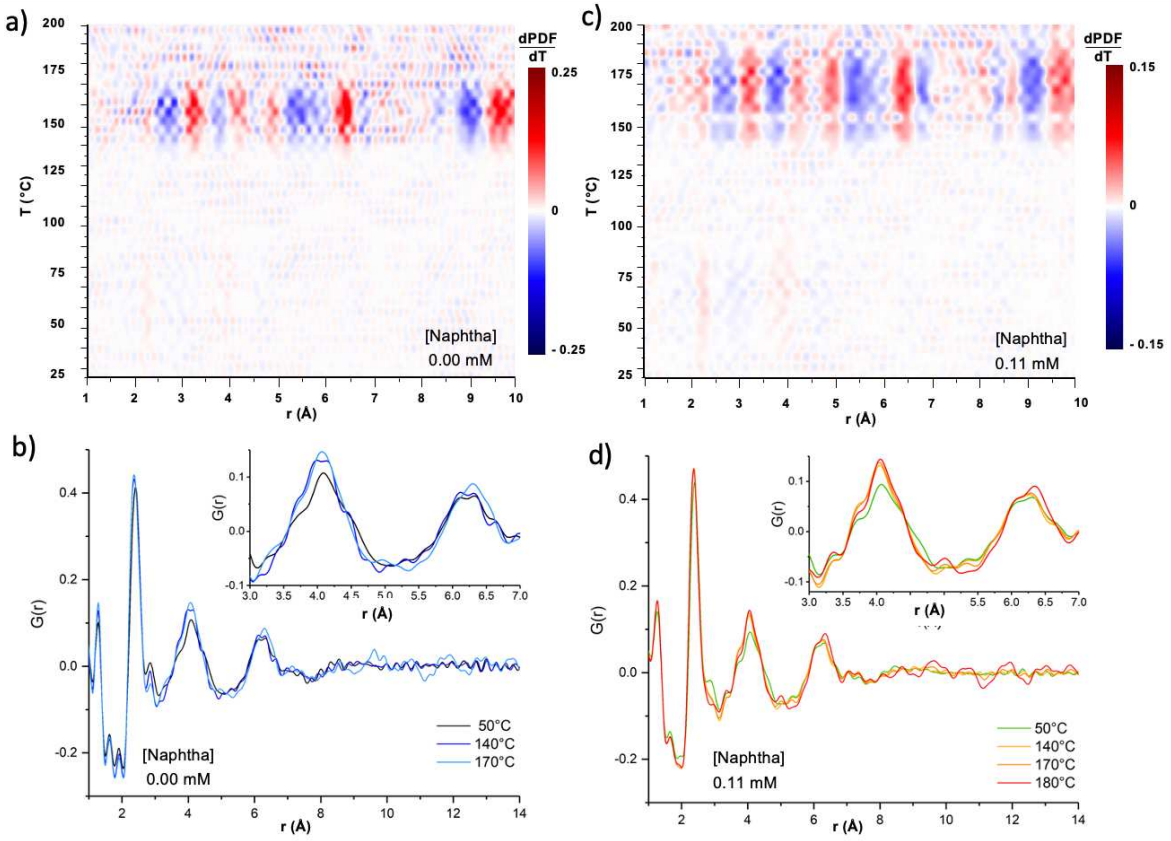

Figure 3.14. Exploring the local structure of ACC and ACC+0.11 mM naphthazarin. (a) dPDF/dT maps and (b) Temperature-dependent PDF profiles of pure ACC, (c) dPDF/dT maps, and (d) Temperature-dependent PDF profiles of ACC+0.11 mM naphthazarin.

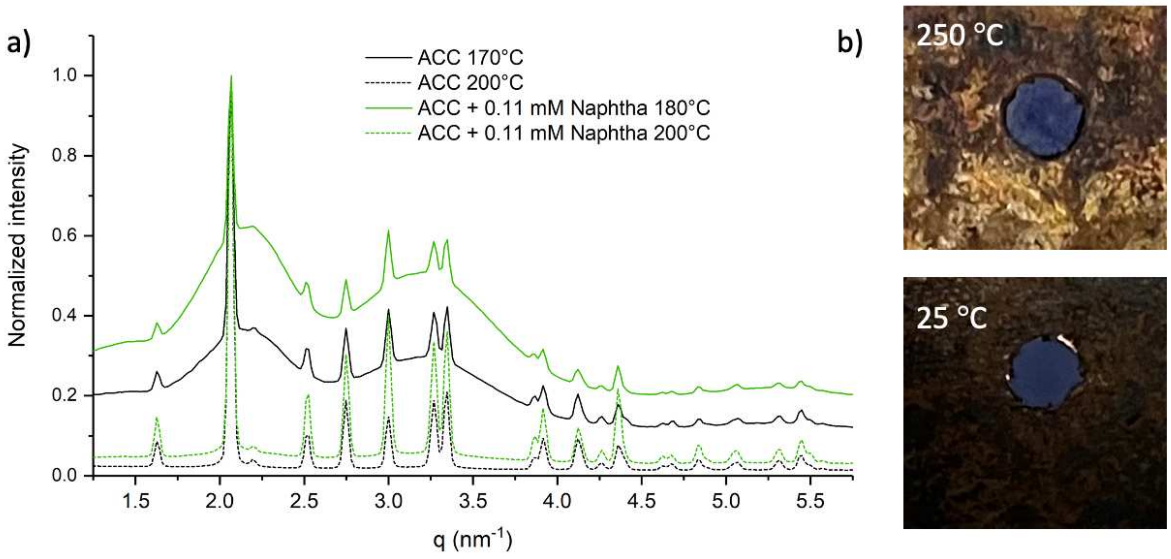

Figure 3.15. a) *In-situ* heating SAXS measurements on ACC and ACC+0.11 mM naphthazarin, b) ACC+0.53 mM naphthazarin at 25 °C and 250 °C (*ex-situ*).

3.3. Color of the ACC-Naphthazarin samples

ACC and ACC-Naphthazarin samples were synthesized using the direct precipitation method. In Figure 3.16, we present a visual depiction of naphthazarin and ACC samples in the presence of varying concentrations of naphthazarin. This illustration offers a comparison of naphthazarin in its natural state, which appears reddish-brown, but also when associated with ACC, where it takes on a lavender-blue hue.

Furthermore, Figure 3.16 also showcases the differences in color of ACC-Naphthazarin samples based on how the image was acquired, 1) by packing the sample in a small well (Figure 16a), and 2) by spreading the sample on a light blue paper surface (Figure 3.16b). This comparison underscores the influence of sample preparation on the observed color, emphasizing that how the sample is arranged can impact the perceived color. Therefore, for a more accurate assessment of color, UV-vis spectroscopy was employed to ensure a precise characterization.

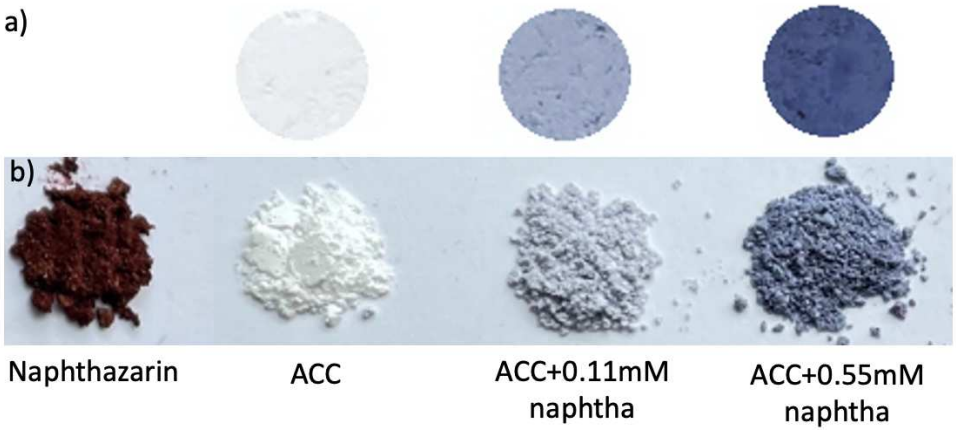

Figure 3.16. ACC synthesized by the direct precipitation method with different naphthazarin concentrations. a) Powder packed in small wells, b) powder spread on paper.

To further study these fluctuations in color, we performed UV-visible diffuse reflectance measurements on naphthazarin, ACC, ACC+0.11 mM naphthazarin, and ACC+0.53 mM naphthazarin.

Visible region: The UV-Vis diffuse reflectance spectra in the visible spectrum (400-800 nm) reveal distinct absorption bands, as shown in Figure 3.17a. Notably, when examining naphthazarin, we observe a significant absorption of light across the entire visible region, with

two pronounced peaks at approximately 550-600 nm and 400-450 nm. This absorption pattern is in agreement with the reddish-brown color of pure naphthazarin. In contrast, the combination of ACC and naphthazarin results in absorption in the 450-650 nm range, with two maximums at around 570 nm and 620 nm, creating a bluish coloration. As the concentration of naphthazarin within ACC increases (0.11 to 0.53 mM), there is a corresponding rise in absorbance, which intensifies the color, leading to a darker appearance. Interestingly we observed that with an increase in naphthazarin concentration (0.11 to 0.53 mM), there was a small change in the relative intensity of the two maxima *i.e.*, 570 nm band intensity in ACC+0.53 nm was almost similar to that of 620 nm.

To quantify these hues exhibited by the ACC-naphthazarin samples and naphthazarin, the x, and y parameters of the CIE 1931 chromaticity diagram were calculated based on the scattered component of the spectra (Figure 3.17a). When the samples containing varying naphthazarin concentrations were represented on the CIE chromaticity diagram (Figure 3.17b), it helped visualize how pigment concentration affects the perceived color of a sample. On the CIE diagram, the ACC lies in the white region, while the naphthazarin lies in the overlapping region of orange and red.

In the case of ACC+naphthazarin samples, as already discussed, the only difference in the UV-vis spectra profile was the difference in the relative intensity of the two maxima in the visible region. Therefore, we normalized the scattered part of the UV-vis diffuse reflectance data with respect to the maxima at 570 nm and then plotted it on the CIE diagram. This gave us insight into the color variation between ACC+0.11 mM naphthazarin and ACC+0.53 mM naphthazarin. ACC+0.11 mM naphthazarin lies in the overlapping region of blue and shade purple resulting in a blue color. Interestingly, we observed that a higher naphthazarin concentration (0.53 mM) pushed the colors toward the region corresponding to the darker hues with a slightly higher contribution from the purple region compared to ACC+0.11 mM naphthazarin (Figure 3.17b). This indicates that subtle variations in the intensity of maxima's in the visible region do contribute towards color variation observed due to an increase in naphthazarin concentration (0.11 to 0.53 mM).

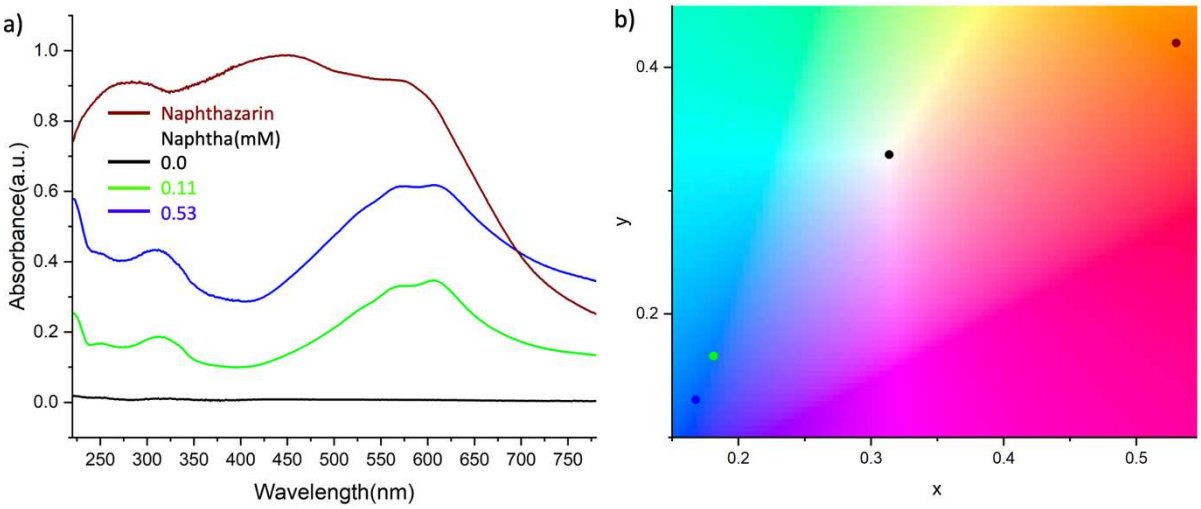

Figure 3.17. a) UV-vis diffuse reflectance on naphthazarin and ACC synthesized by direct precipitation with different naphthazarin concentrations (0.11 mM and 0.53 mM). b) CIE 1931 chromaticity diagram predicting the color of the naphthazarin and ACC+naphthazarin samples.

In a study conducted by (Land *et al*., 1983), the protonation state of naphthazarin in aqueous solution was explored. The findings indicated that naphthazarin predominantly exists in a fully protonated form (NH_2), resulting in a red color, at pH levels below 7.8. Between pH 7.8 and 10.7, naphthazarin takes on singly deprotonated forms (NH^-), leading to a purple color. Beyond pH 10.7, it becomes doubly deprotonated (N^{2-}), resulting in a blue color. These different forms of naphthazarin are associated with distinct UV-vis absorption bands, specifically (NH_2) at 510 nm, (NH^-) at 570 nm, and (N^{2-}) at 610 nm, as depicted in Figure 3.18.

When considering ACC+naphthazarin, the resulting coloration may be attributed to variations in the N^{2-}/NH^- ratio, likely influenced by differences in pH during synthesis. Indeed, for ACC+0.11 mM naphthazarin synthesized at pH 10.6 and ACC+0.53 mM naphthazarin at pH 10.3, (Land *et al*., 1983) study suggests that the color should predominantly originate from naphthazarin being in the NH^- form, resulting in a more pronounced purple hue. However, the observed color in our samples, a lavender-blue shade, does not align with this expectation. We need to emphasize that the transition may not occur precisely at 10.7; instead, it might encompass a narrow range of values, which could result in a lavender-blue color in our particular situation. To get the full picture it is necessary to calibrate the behavior of naphthazarin in our system, particularly in the presence of Na_2CO_3, to understand the precise coloration mechanisms at play.

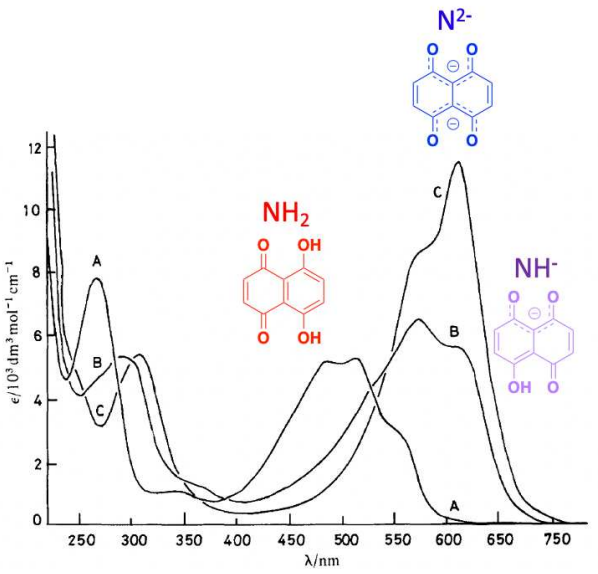

Figure 3.18. Absorption spectra of aqueous solutions of naphthazarin: in A (NH_2): pH 5.8; B (NH^-): pH 9.1; C (N^{2-}): pH 13 (Imaged adapted from (Land *et al*., 1983)).

3.4 Color changes and protonation state of naphthazarin in solution according to pH

3.4.1. pK_a determination in presence of Na_2CO_3

As discussed in section 3.3, naphthazarin in an aqueous solution can exist in the fully protonated form (NH_2) or deprotonated forms *i.e.*, singly deprotonated (NH^-) or doubly deprotonated (N^{2-}) with pK_1, = 7.85 and pK_2, = 10.7 (Land *et al*., 1983). These values were obtained in aqueous solution and pH was modulated with NaOH. To get the complete picture of the behaviour of the naphthazarin molecules in Na_2CO_3 aqueous solution, absorption spectroscopy was performed on a naphthazarin solution prepared at different pH (adjusted with HCl) (Figure 3.19a). The color of the naphthazarin in Na_2CO_3 varies depending upon the pH, the solution is rose-red at mildly acid (~pH 5), blue-violet in dilute alkali (~pH 8.5), deep blue in strong alkali (~pH 11) and neutral pH (Figure 3.19b).

Under acidic conditions (Figure 3.19a), a prominent peak appears at 510 nm, accompanied by local maxima at 570 nm and 630 nm. However, as the solution's pH shifts toward more alkaline values (pH 8.5), the maxima shifts to 570 nm with local maxima at 630 nm. Interestingly, as the pH continues to rise from 8.5 to 10.3, the intensity of the 610 nm peak steadily increases until it matches the intensity of the 570 nm peak. Further pH elevations cause the absorption

maxima to shift to 630 nm and local maxima at 570 nm. The reason behind the redshift with an increase in the extinction coefficient on going from acidic to alkaline is due to successive deprotonation of naphthazarin.

To get precise information on the naphthazarin behavior in Na_2CO_3 pK_a's were calculated from the absorbance spectra of naphthazarin in the presence of Na_2CO_3 at different pH. Experimental absorbances A_{obs}, were fitted to Equation (3.1) (Land *et al*., 1983):

$$A_{obs} = \frac{A_1}{(1+10^{pH-pK_1}+10^{pH-pK_2})} + \frac{A_2}{(1+10^{pH-pK_1}+10^{pH-pK_2})} + \frac{A_3}{(1+10^{pH-pK_1}+10^{pH-pK_2})} \qquad (3.1)$$

where A_1, A_2, and A_3, refer to absorbances attributed to the forms NH_2, NH^- and N^{2-}, respectively, and pK_1 and pK_2 are the pK_a values of NH_2, and NH^-. The pK_1 and pK_2 for naphthazarin were found to be 8.2 and 10.3 respectively (Figure 3.19a) different from the pK_a values reported by Land *et al.,* 1983 (7.85 and 10.7). The reason behind this difference could be: that pK_a of naphthazarin, being an intrinsic property, is not directly changed by Na_2CO_3. However, Na_2CO_3 can indirectly affect naphthazarin's ionization state by altering the solution's pH, solubility, or complex formation. These indirect effects may influence the acid-base behavior of naphthazarin in a particular solution.

The calculated pKa_1 and pKa_2 from Equation 3.1 for naphthazarin were 8.2 and 10.3 respectively. Therefore, naphthazarin exits as singly protonated species (NH^-) at 8.2<pH<10.3 with maxima around 570 nm whereas the doubly deprotonated species (N^{2-}) exits at pH > 10.3 when the maxima is at 630 nm. The ratio between the intensity of the two bands (570 nm and 630 nm) thus corresponds to the protonation state of the naphthazarin (Figure 3.19a) *i.e.*, if the intensity of band at 570 nm is higher than the band at 630 nm it suggests NH^- is the predominant species contributing to the color of the solution and in case of vice versa N^{2-} is the predominant species contributing to the color.

To delve deeper into the naphthazarin color variation due to pH change. The x and y parameters of the CIE 1931 chromaticity diagram were calculated based on the normalized transmittance part of the UV-vis spectra acquired at various pH. Once plotted on the CIE diagram (Figure 19c), the x and y parameters reveal the colors of the solutions according to pH. A striking transition in color from orange-red hue to blue is reported on the diagram as the pH shifted from acidic to basic conditions. This transition fits with the colors perceived by the human eye reported in Figure 3.19b), indicating that the NH^-/N^{2-} ratios can indeed be used to describe the

observed colors. This shift in coloration highlights the influence of pH on the optical properties of the solution and underscores its significance as a key determinant in color changes within the studied system.

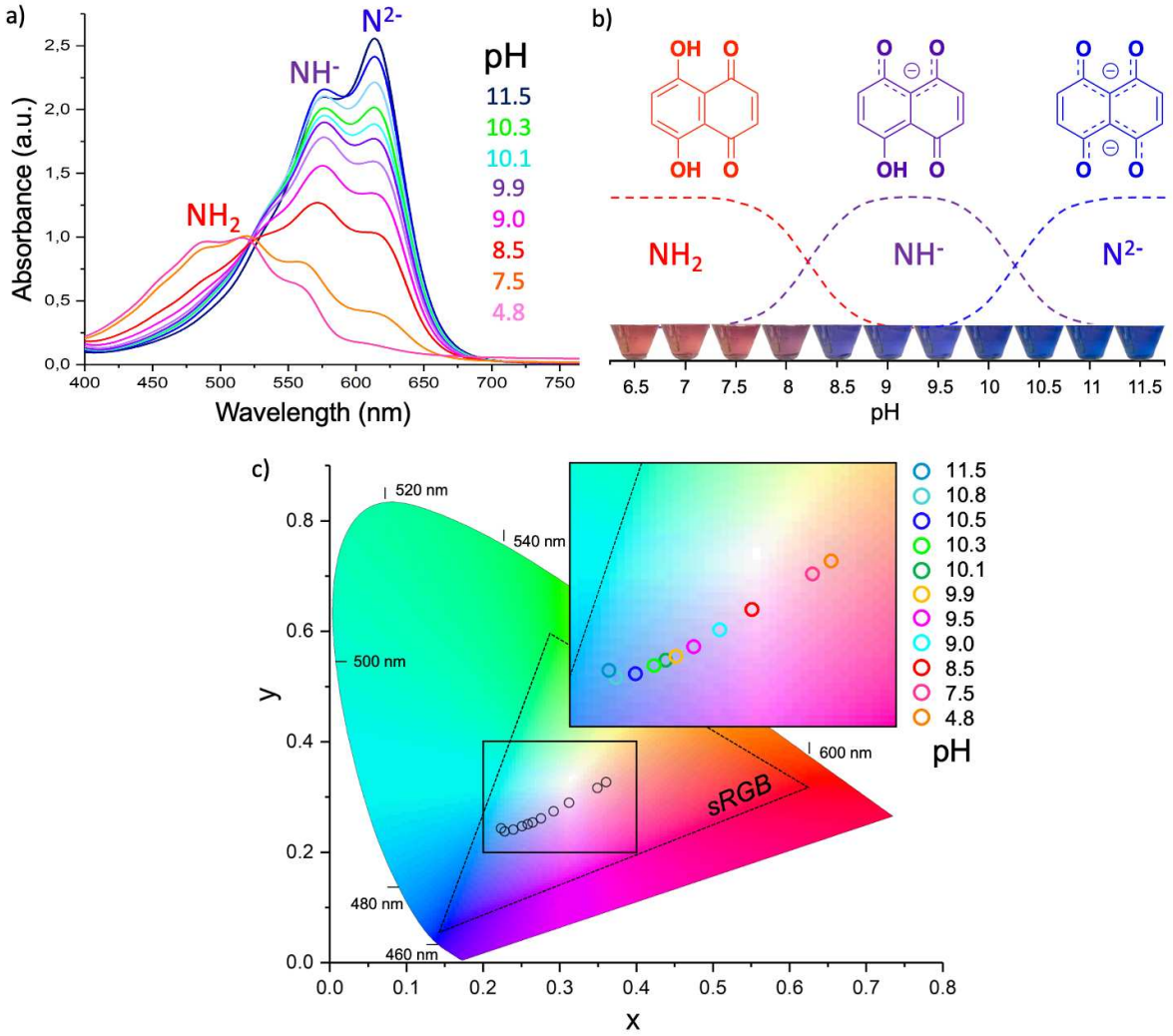

Figure 3.19. a) UV-vis spectra on naphthazarin in the presence of Na_2CO_3 (40 mM) at different pH. pH is regulated by the addition of HCl and b) respective color variation range according to pH with the speciation diagram displayed for $NH_2/NH^-/N^{2-}$. c) CIE 1931 chromaticity diagram predicting the color of the naphthazarin at each pH as perceived by human eyes.

3.4.2. Effect of Ca^{2+} on naphthazarin pK_a and oxidation

In our experimental system, the alteration in coloration is not solely governed by pH levels but might also be linked with the $[Ca^{2+}]$ throughout the $CaCO_3$ synthesis process *via* direct

precipitation. Figure 3.20a effectively illustrates the interplay between pH and [Ca^{2+}] at different stages of the reaction.

To investigate the influence of Ca^{2+} on the pK_a values of naphthazarin during the formation and crystallization of ACC, we first chose a modulate the pH with NaOH (Figure 3.20a) for our study. This decision was based on the fact that NaOH does not induce the precipitation of $CaCO_3$.

To study the impact of Ca^{2+} on the naphthazarin oxidation, our approach involved conducting time-dependent *in-situ* UV-vis measurements (Figure 3.20b) at a pH of 10.5, and [Ca^{2+}] of ~2 mM which corresponds to conditions where ACC starts to precipitate (70-350 s) as depicted in Figure 20a. Initially, we observed that at pH 10.5, naphthazarin existed as a mixture of NH^- and N^{2-} forms. However, upon the addition of 2 mM [Ca^{2+}], the profile of naphthazarin changed notably. The introduction of Ca^{2+} caused naphthazarin to primarily exist in the N^{2-} form suggesting a shift in the pK_a values to lower values. UV-vis spectra obtained at various time points also indicated that this transition was accompanied by the oxidation of naphthazarin, as evidenced by the decreasing absorbance intensity over time (Figure 3.20b).

As previously discussed, the presence of Ca^{2+} ions initially shifts the pK_a values of naphthazarin to lower levels. This occurs predominantly at the onset of the reaction when Ca^{2+} concentration is relatively high (0.5 mM-2 mM). However, as the reaction progresses and Ca^{2+} is gradually consumed (Ca^{2+} reduced to <0.2 mM), the pK_a values of naphthazarin return to their original values. Consequently, the likelihood of naphthazarin undergoing oxidation in our experimental setup appears to be quite low, offering valuable insights into the stability of naphthazarin under the studied conditions.

These findings suggest that the color changes observed during the ACC synthesis and its subsequent crystallization into different polymorphs are jointly influenced by pH and to some extent by [Ca^{2+}]. These factors impact the protonation state of naphthazarin, which in turn governs its coloration in the solution. To gain precise insights into naphthazarin's behavior in the presence of [Ca^{2+}], we calculated the pK_a values from its absorbance spectra under different pH conditions. The experimental absorbances (A_{obs}) were fitted to Equation 3.1, revealing pK_1 and pK_2 values for naphthazarin as 9.4 and 7.5, respectively in presence of 2 mM Ca^{2+} (as illustrated in Figure 3.20c).

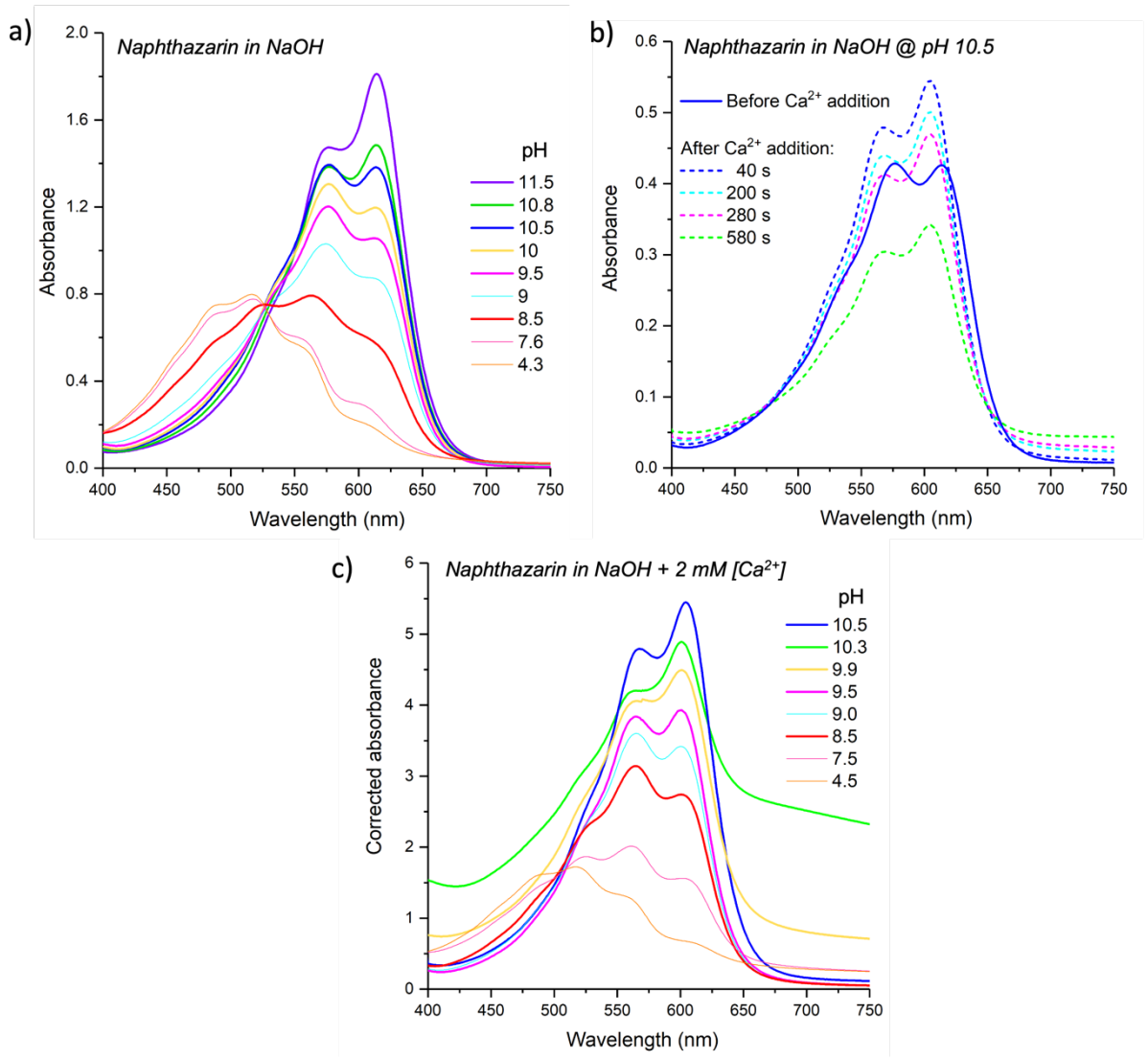

Figure 3.20. UV-vis absorbance spectra under varying conditions: a) Naphthazarin in a NaOH solution at different pH levels, b) Naphthazarin in a NaOH solution at pH 10.5 with the addition of 2 mM Ca^{2+}, c) Naphthazarin at different pH levels modulated by NaOH in the presence of 2 mM Ca^{2+}.

3.5. Color changes during ACC formation and crystallization in solution and in air

3.5.1. Color changes of the filtrate during ACC formation and crystallization

Ex-situ UV-vis measurements on the filtrate of the reaction were performed to gain a comprehensive understanding of the color changes and the molecular state of the naphthazarin during ACC formation and crystallization in the presence of 0.53 mM naphthazarin (M1)

(Figure 3.21b). Surprisingly, at a pH of 10.3, which occurs just after the addition of $CaCl_2$, naphthazarin predominantly existed in a N^{2-} form. As the reaction progressed and reached a plateau at a pH of 10.4, naphthazarin exhibited a mixture of N^{2-} and NH^- forms. Subsequently, at pH 10.0 (midway through the ACC to vaterite+calcite conversion), naphthazarin still appeared as a blend of NH^- and N^{2-} forms. However, at 500 s, corresponding to a pH of 9.8 (full ACC to vaterite+calcite conversion), naphthazarin primarily existed in the NH^- form, which persisted until the conclusion of the reaction at a pH of 8.6. As discussed in section 4.2, the results demonstrate the apparent influence of Ca^{2+} ions on the protonation state of naphthazarin. At 10.4, naphthazarin should theoretically exist as a mixture of both NH^- and N^{2-} states. However, the presence of Ca^{2+} shifted the equilibrium predominantly towards the N^{2-} form. Table 3.6 summarizes the color changes that happen during the ACC formation as well as its crystallization into a mixture of vaterite and calcite.

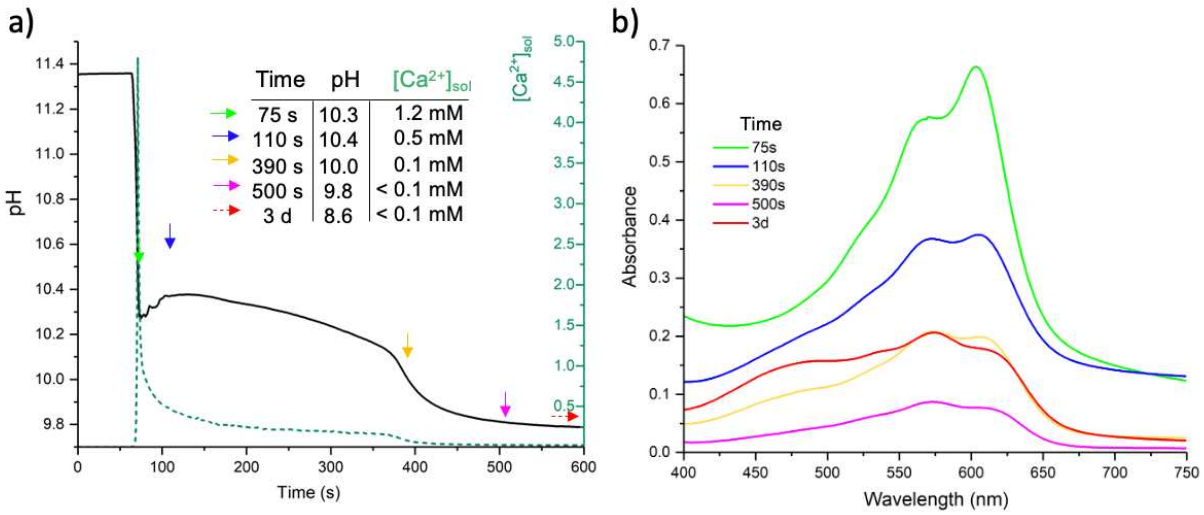

Figure 3.21. a) pH profile and [Ca^{2+}] profile for ACC+0.53 mM naphthazarin, illustrates the different time intervals at which the titrants were collected, b) corresponding *ex-situ* UV-vis measurement on filtrate (Filtrate collected at different time period of the synthesis).

Table 3.6. Color changes in solution during ACC+0.53 mM formation and crystallization into crystalline polymorphs.

pH	Naphthazarin form	Color of the filtrate
11.4 (before $CaCl_2$ addition)	N^{2-}	Dark blue
10.1-10.3 (ACC precipitation starts)	N^{2-} and NH^-	Blue with purple shade
10.4-10.6 (ACC stable)	N^{2-} and NH^-	Blue with purple shade
10.0 (ACC to calcite+vaterite crystallization starts)	N^{2-} and NH^-(predominant)	Purple with blue shade
9.8 (ACC to calcite+vaterite crystallization ends)	N^{2-} and NH^-(predominant)	Purple with blue shade
8.6 (full calcite conversion)	NH^-(predominant) and NH_2	Purple

This section warrants an explicit clarification that the UV-vis spectrum under examination is associated with the filtrate rather than the solid substance. The sequence of measurements conducted here holds significant importance as it aids in elucidating the coloration of the eventual solid product. To expound further, these measurements yield valuable insights into the potential molecular species of naphthazarin coexisting with $CaCO_3$ at various junctures in the synthesis process. For instance, when the solution exhibits a blue color during the ACC filtration stage, it signifies that the prevailing molecular species within the solution at that specific point is likely N^{2-}. This observation, in turn, provides critical information that helps explain the blue coloration exhibited by the ACC as the predominant species influencing its coloration.

3.5.2. Color of the naphthazarin-calcite powder after ACC crystallization

3.5.2.1. ACC crystallized in solution

UV-vis diffuse reflectance spectroscopy was employed to gain insights into both the coloration and molecular state of naphthazarin within the ACC (M1) as well as calcite powder synthesized in the presence of naphthazarin. UV-vis spectra of ACC+0.11 mM naphthazarin depicts that naphthazarin likely exists in a combination of two molecular species: NH^- and N^{2-}, with the latter being the predominant form (Figure 3.22a). We extended our investigation to compare

ACC+0.11 mM naphthazarin (M1), ACC+0.53 mM naphthazarin (M1) with calcite+0.11 mM naphthazarin (M2) and calcite+0.53 mM naphthazarin (M2) (Figure 3.22a). In the case of calcite samples, we observed a broad band in the visible region spanning from 450 to 650 nm with a maximum at around 610 nm and local maxima at about 520 nm. This spectral feature strongly suggests that naphthazarin exists as a combination of NH_2 (520 nm), NH^- (570 nm), and N^{2-} (620 nm) molecular species within the calcite with dominant contribution from N^{2-} and NH^- towards the color. In the case of ACC+0.11 mM samples, we observed local maxima at around 570 nm and maxima at 620 nm, suggesting the significant contribution to the colour of ACC was from N^{2-} species. Interestingly, for ACC+0.53 mM naphthazarin, the peaks at 570 nm and 620 nm were almost equivalent in intensity, suggesting the contribution of both species. These also correlate well with the fact that ACC+0.11 mM naphthazarin synthesized at pH 10.6 and ACC+0.11 mM naphthazarin at pH 10.3 and 10.3 being the pKa_2 of naphthazarin at which the N^{2-} and NH^- contribution towards color is equivalent.

To get more insights into the color difference of ACC+naphthazarin and calcite+naphthazarin, we translated the scattered portion of the UV-vis diffuse reflectance data into a CIE diagram after normalizing, as illustrated in Figure 3.22b. The ACC+0.11 mM naphthazarin lies in the lighter blue-purple region and calcite+0.11 mM naphthazarin in comparison lies in darker region. With increase in naphthazarin concentration we observe that ACC+0.53 mM naphthazarin lays on the darker blue region and a similar trend was followed in case of calcite+0.53 mM naphthazarin. Intriguingly, in the case of calcite samples we observe that they lie more towards the purple region in comparison to ACC samples (Figure 3.22b), echoing the alteration in molecular composition of naphthazarin within the calcite and ACC. This observation further emphasizes the influence that naphthazarin species exert on the coloration within $CaCO_3$ and their dependence on pH.

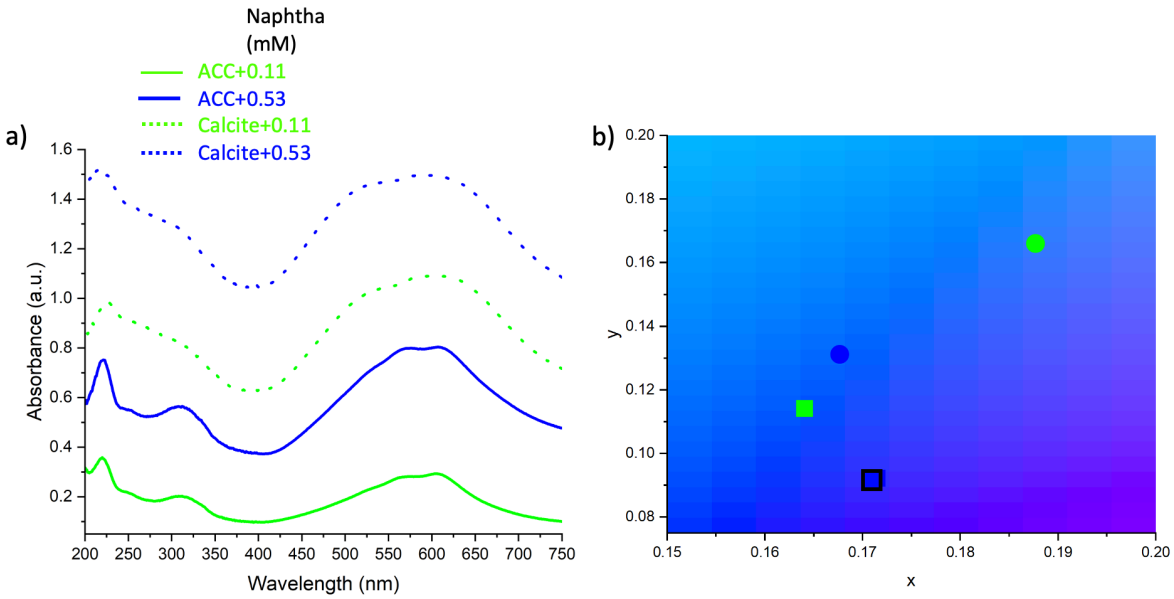

Figure 3.22. a) UV-Vis diffused reflectance on ACC+0.11 mM naphthazarin and calcite+0.11 mM naphthazarin, b) scattered part of UV-vis reflectance data mapped on CIE 1931.

3.5.2.2. ACC crystallized in air induced by heating

Ex-situ heating UV-Vis diffused reflectance measurements revealed the color changes that ACC undergoes during its crystallization induced by heating (5 °C/min) in a Nabertherm furnace (Figure 3.23a). At room temperature, it is evident that naphthazarin in ACC exists in a mixture of NH^- and N^{2-} species. As the temperature increases up to 200 °C, there is a noticeable rise in the contribution of the N^{2-} species. However, as the temperature continues to climb to 300 °C, the contribution of N^{2-} starts to decrease. Interestingly, at this point, the sample exhibits a similar contribution from both NH^- and N^{2-} species as observed in the ACC+naphthazarin sample at room temperature. This phenomenon could be due to the decomposition of naphthazarin adsorbed on the surface of ACC at 300 °C. When the temperature reaches 400 °C, a significant transformation occurs. The naphthazarin adsorbed on the surface undergoes complete degradation, resulting in the absence of distinct peaks corresponding to different naphthazarin species. Instead, a single peak emerges, which is likely originating from the naphthazarin that has become incorporated within the calcite matrix. These findings align closely with the UV-vis data when plotted on the CIE color map (Figure 3.23b), providing a compelling correlation. The CIE chromaticity mapping reveals that ACC exhibits a less pronounced blue hue at room temperature compared to when it is at 200 °C. This color shift is in harmony with the predominance of the N^{2-} contribution at 200 °C. As the temperature

continues to rise (300 °C), the N^{2-} contribution gradually diminishes, causing the ACC to exhibit a lighter shade. Finally, at 400 °C, when most of the naphthazarin was degraded, the sample's position on the RGB color map closely approaches the white region. This progression on the color map illustrates the changes in ACC coloration as a function of temperature and the evolution of different naphthazarin species within the material. Table 3.7 provides detailed information on how the color of the ACC evolves throughout the crystallization process.

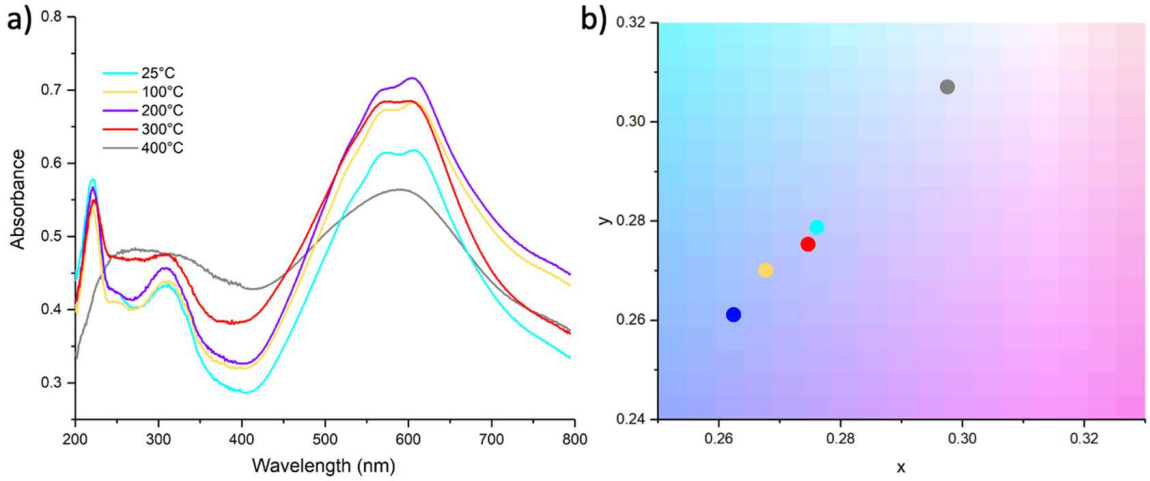

Figure 3.23. a) *ex-situ* UV-vis diffuse reflectance on ACC+ 0.53 mM naphthazarin at different temperatures, and b) scattered part of UV-vis reflectance data mapped on CIE 1931.

Table 3.7. Color changes during ACC crystallization into crystalline polymorph induced by heating in Nabertherm furnace (5°C/min):

Temperature (°C)	**Naphthazarin form**	**Color**
25	N^{2-} and NH^{-}	Purplish blue
100	N^{2-}(predominant) and NH^{-}	Blue with purple shade
200 (crystallization)	N^{2-}(predominant) and NH^{-}	Blue with purple shade
300	N^{2-} and NH^{-}	Purple with blue shade
400	Single broad band	Light purple with a pink shade

3.6. Molecular state of naphthazarin within calcite

3.6.1. Surface composition of naphthazarin-ACC powder

Utilizing XPS, we conducted an investigation of the surface composition of naphthazarin and ACC+naphthazarin particles within the top 10-20 nm of a sample. Figure 3.24 showcases high-resolution XPS spectra focusing on the C1s energy levels, while the corresponding surface atomic ratios are presented in Table 3.8. In Figure 3.24a, the deconvoluted spectra of naphthazarin revealed three main peaks at 284.6±0.1, 286.2±0.1, and 287.1±0.1 eV, which can be attributed to the carbon atoms in the aromatic ring or amorphous carbon, -C-OH and -C=O, respectively (Stipp and Hochella, 1991). The deconvoluted spectra of ACC (Figure 3.24b) reveal three distinct peaks. The first peak, located at approximately 284.6±0.1eV, may arise from either surface contamination or the presence of amorphous carbon. The second small peak, found at around 286.4±0.1 eV, is attributed to the possible contamination, and the third peak, found at around 290.1±0.1 eV, is attributed to the CO_3^{2-} (Tobler *et al*., 2015). For ACC C 1s:Ca 2p and O 1S:C 2P ratio was found to be 1.3 and 2.89 respectively, which is in close correlation with the theoretical ratio of 1 and 3.

In the case of ACC+0.53 mM naphthazarin, the deconvoluted spectra (Figure 3.24c) revealed four main peaks at 284.6±0.1, 286.2±0.1, 287.1±0.1, and 290.1±0.1 eV corresponding to amorphous carbon (contamination/degradation of sample by beam) or carbon atoms in the aromatic ring, -C-OH, -C=O and CO_3^{2-} respectively (Stipp and Hochella, 1991). Interestingly, in ACC+0.53 naphthazarin we observed a relative higher contribution from -C-OH with respect to -C=O was evident (Figure 3.24c), suggesting the protonation of naphthazarin. The ratios summarized in Table 3.8 support the presence of naphthazarin on the ACC surface, as the C1s:Ca2p ratio significantly increased from 1.3 in pure ACC to 2.13 in ACC+0.53 mM naphthazarin, alongside a concurrent increase in the O 1S:Ca 2p ratio (2.89 to 3.13). These findings collectively indicate the presence of naphthazarin and informs on its chemical state, shedding light on the surface composition and molecular configuration within the analyzed particles.

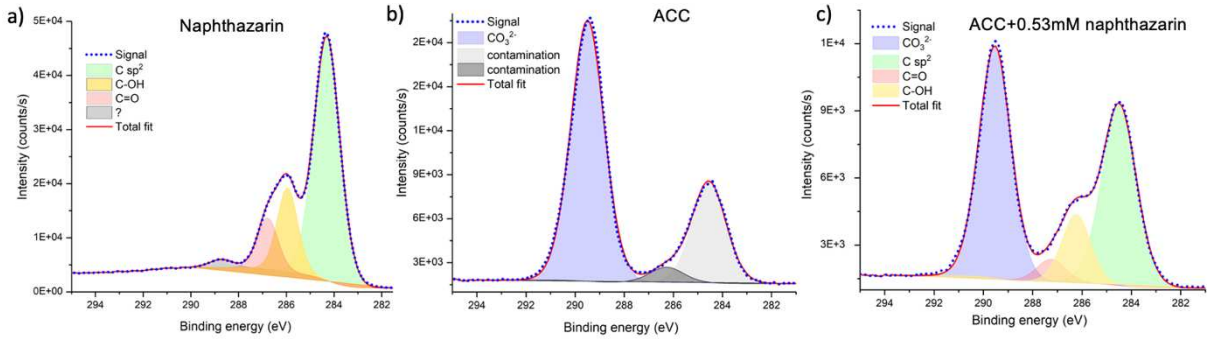

Figure 3.24. XPS spectra focusing on the C1s energy levels obtained on a) naphthazarin, b) ACC and c) ACC+0.53 mM naphthazarin.

Table 3.8. Atomic ratios calculated from XPS data.

Sample	C 1s: Ca 2p	O 1s:Ca 2p
ACC	1.3	2.9
ACC+0.53 mM Naphthazarin	2.1	3.1

3.6.2. Chemical nature of naphthazarin associated with $CaCO_3$

To gain more insight into the chemical nature of naphthazarin within our system, solid-state NMR (ss NMR) measurements were conducted. Initially, ^{1}H to ^{13}C cross-polarization (CP) NMR was performed on pure naphthazarin (used as received from the supplier Sigma Aldrich®) (Figure 3.25a). In this analysis, three chemically distinct carbon enviro nments are evidenced through three distinct peaks at 112, 137 and 173 ppm. On comparing the spectra values with the literature, naphthazarin is in polymorph A form (Olivieri *et al*., 1990). These three distinct resonances are explained by the fast proton exchange between the hydroxyl and keto groups increasing the molecule symmetry and leading to only three magnetically inequivalent carbons. Thus, the resonance assig nment is the following:

- ¥ Resonance at 112 ppm corresponds to quaternary sp^2 carbons (9, 10)
- ¥ Resonance at 134 ppm corresponds to protonated sp^2 carbons =C-H (2, 3, 6, 7)
- ¥ Resonance at 173 ppm corresponds to oxidized sp^2 carbons C-O (1, 4, 5, 8)

To investigate how the pigments interact with calcite, ^{13}C ss NMR was performed on the calcite sample supplemented with 0.53 mM naphthazarin (Figure 3.25b). In the ss NMR spectra, a

characteristic peak for carbonate appeared at 168 ppm, originating from hydrated and disordered $CaCO_3$ domains (also evidenced on the pure calcite sample). Interestingly, naphthazarin resonances undergo strong modifications upon association with calcite. Carbons 9, 10 resonance is significantly shifted downfield from 112 to 117 ppm. Similarly, carbons 2, 3, 6, 7 resonance is now broad and composite and shifted downfield from 134 ppm to 137 ppm. Moreover, a significant change is also observed for carbons 1, 4, 5, 8 resonances for which a strong downfield shift is observed from 173 ppm to 180 ppm together with the appearance of another peak at 170 ppm as a shoulder on the left side of the carbonate peak. At this stage a definitive assig nment cannot be proposed as the 180 ppm and 170 ppm resonances could arise from (i) naphthazarin through the splitting of the carbons 1,4,5,8, resonance into two resonances due to the quench of the fast exchange between the hydroxyl and keto group (180 ppm: C=O and 170 ppm: -C-OH), or induced by the deprotonation of the OH group (180 ppm: C=O and 170 ppm; -C-O^-). Or (ii) the 170 ppm peak could come from a new form of hydrated carbonate induced by the presence of naphthazarin carbons 1,4,5,8, with naphthazarin being doubly protonated in fast exchange or doubly deprotonated in fast exchange.

However, the strong modification of the ^{13}C- NMR spectrum of naphthazarin reflects the change in its molecular enviro nment along with its incorporation within calcite.

Two possible explanations can account for the aforementioned changes. Firstly, it is plausible that the naphthazarin molecules within the calcite system are in a rigid state, hindering or preventing the exchange between the hydroxyl and keto groups from taking place. (Shiau *et al*., 1980) suggested that the structure of crystalline naphthazarin is dynamically disordered and at room temperature involves a fast tautomeric equilibrium between different forms of naphthazarin. At a lowered temperature of -160 ºC, they observed for naphthazarin that spectral lines assigned to carbon 9,10 remain unchanged, however, the other lines assigned to other carbons split into two (in particular carbons 1, 4, 5, 8) indicating that lowering of temperature leads to freezing of the dynamic exchange process (Figure 3.26). Secondly, the naphthazarin molecules incorporated within the calcite system may have undergone deprotonation due to the pH of the synthesis conditions, leading to the generation of more chemically distinct carbon atoms and resulting in the splitting of peaks in the spectra.

In the case of ACC and ACC+0.53 mM naphthazarin, cross-polarization ^{13}C NMR spectra revealed (Figure 3.25b), that a characteristic broad peak for carbonate appeared at 167 ppm, originating from hydrated and disordered $CaCO_3$ domains. Unfortunately, we barely observed

naphthazarin peak maybe due to the dynamics of the system although the amount of naphthazarin was similar in ACC and calcite samples. However, and very interestingly, we identified the peak corresponding to naphthazarin carbons 2, 3, 6, and 7, positioned at the same chemical shift (137 ppm) as for the calcite+naphthazarin sample suggesting the same molecular state of naphthazarin into ACC and calcite *i.e*. deprotonated naphthazarin.

Deprotonated naphthazarin

To gain insight into the molecular configuration of naphthazarin within the ACC and calcite matrix, we conducted ^{1}H-^{13}C CP NMR measurements of naphthazarin under varying pH conditions (Figure 3.25a). Naphthazarin samples were prepared at different pH by dissolving the naphthazarin in NaOH solution and then freeze drying. When examining the NMR spectrum of naphthazarin at pH 13, three ^{13}C resonances are still observed indicating the same number of magnetically inequivalent carbons than for pure naphthazarin. However, a notable downfield shift of the three ^{13}C resonances is observed (180, 137, 117 ppm). Moreover, a significant broadening of the resonances is evidenced (in particular for carbons 1, 4, 5, and 8) that could be linked to the potential degradation of naphthazarin at high pH. But very interestingly, the position of the resonances of quaternary sp^2 carbons (9, 10) and protonated sp^2 carbons (2, 3, 6, 7) matches with those of naphthazarin in calcite. Only quaternary oxidized carbons (1, 4, 5, and 8) do not match (maybe due to the potential degradation of naphthazarin, which may contribute to both the broadening of the signals and the different position at this high pH level).

Conversely, when examining naphthazarin at intermediate pH (pH 9), we observed a different pattern. The peaks corresponding to positions 1, 4, 5, 8 exhibited clear splitting corresponding to fully protonated and doubly deprotonated form. Similarly, the peak corresponding to positions 2, 3, 6, 7 of naphthazarin also split into separate peaks.

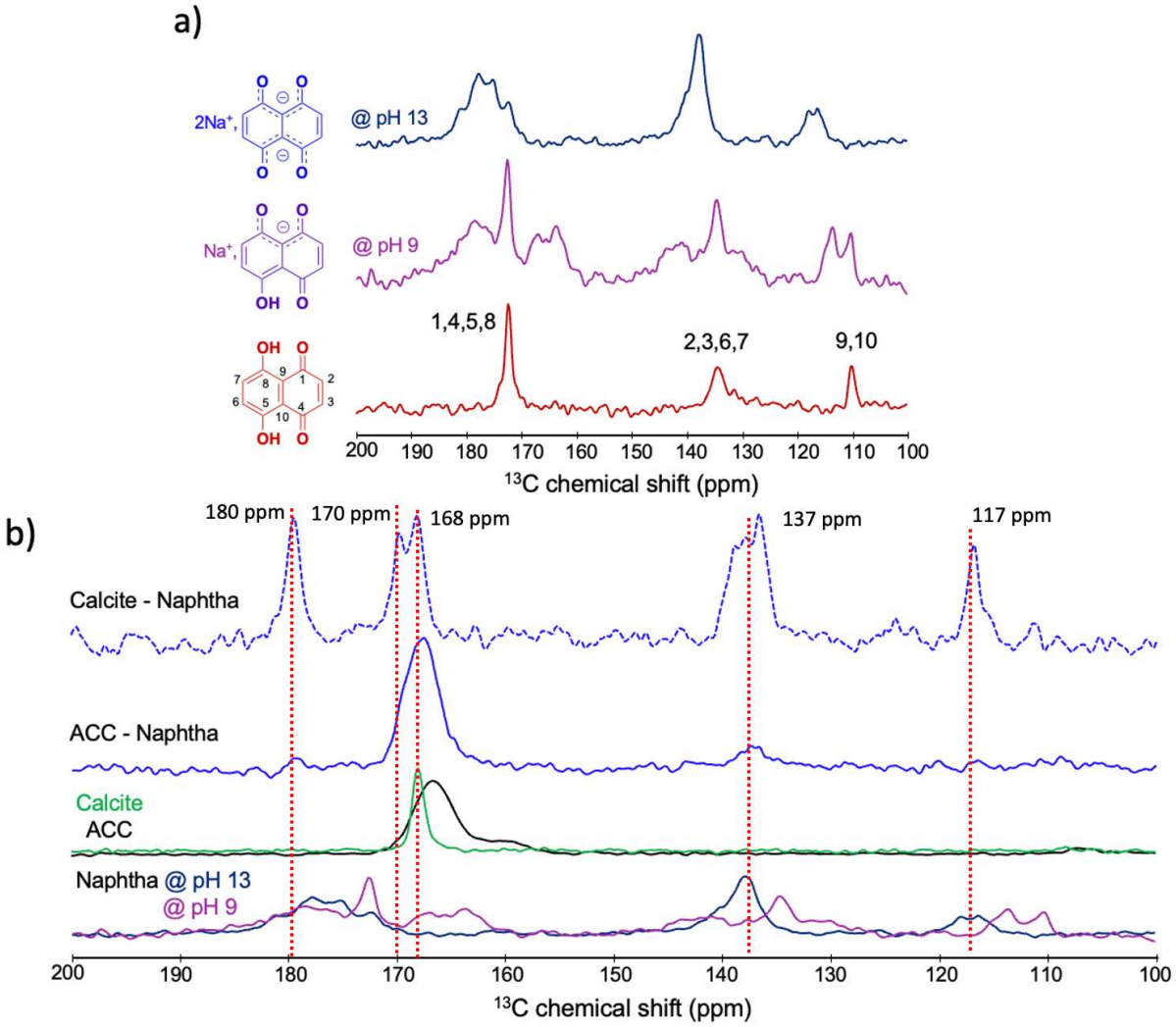

Figure 3.25. a) cross-polarization ^{13}C NMR on naphthazarin, naphthazarin at pH 9, and naphthazarin at pH 13, b) cross-polarization ^{13}C NMR on calcite, calcite+0.53 mM naphthazarin, ACC, ACC+0.53 mM naphthazarin and naphthazarin at pH 9, 13.

To further understand the protonation-deprotonation phenomenon in naphthazarin, we conducted solution-state NMR experiments using D_2O as the solvent (Figure 3.27). These experiments revealed a clear trend: as the pD increased, the signals corresponding to non-exchangeable protons of naphthazarin shifted up field, transitioning from 7.2 to 6.89 ppm. This shift is strongly correlated with the deprotonation of naphthazarin, as increased pD results in the observed-up field shift. Importantly, these protons stay magnetically equivalent.

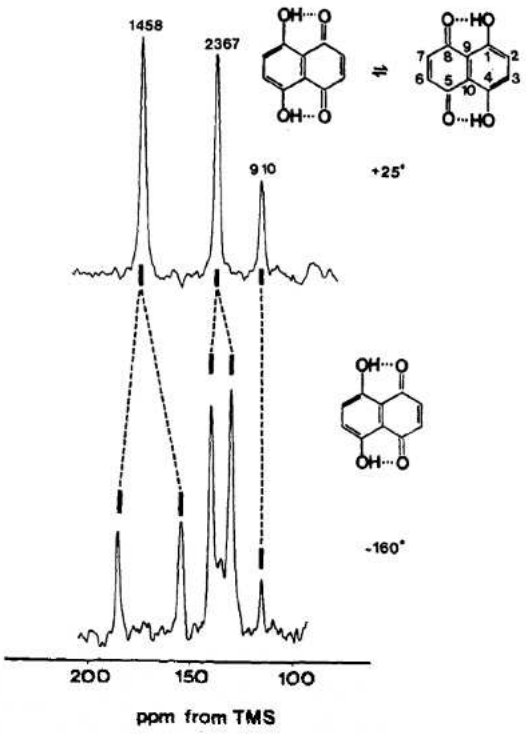

Figure 3.26. ^{13}C CPMAS NMR spectra of solid naphthazarin (600 scans, 30-Hz line broadening, contact time 1ms, and recycle time 3 s): upper spectrum, 25 °C; lower spectrum, -160 °C (Image adapted from (Shiau *et al.*, 1980)).

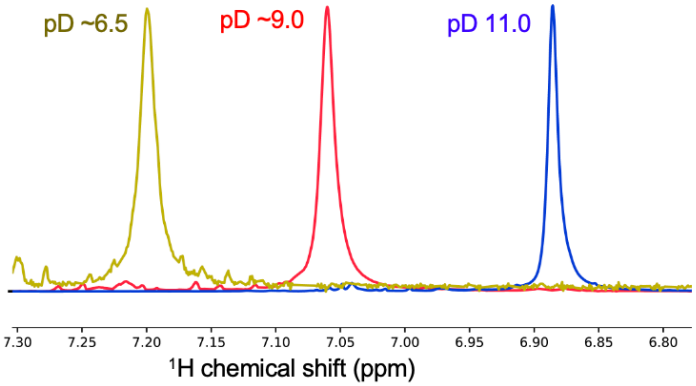

Figure 3.27. Solution state NMR on naphthazarin in D_2O water at different pH with sodium trimethylsilylpropanesulfonate (DSS) as an internal reference and chemical shift standard for proton NMR spectroscopy of aqueous solutions.

Additionally, HMBC experiments were recorded to gain insight into the evolution of quaternary carbons position (in particular carbons 1,4, 5, 8) by unveiling correlations between the carbonyl carbons and protons (Figure 3.28). Interestingly, as pD increased, the signal from the carbonyl carbon moved downfield, in agreement with the observations from the ss NMR. In case of solution NMR we observed the downfield shift in the carbonyl carbon signal from ~175.8 to ~178 ppm with increase in pD. This trend is very similar to that observed in ss NMR where the downfield shift with respect to pH was from 173 to 180 ppm.

We also studied how Ca^{2+}ions can affect the NMR spectra peak positions of the naphthazarin which provides insight into the interaction between naphthazarin and Ca^{2+}. The addition of Ca^{2+} in a 1:1 molar ratio with respect to naphthazarin, the ^{1}H NMR spectra showed minimal change in terms of chemical shifts (6.83-7.22 ppm), compared to the absence of Ca^{2+} (6.89-7.2 ppm). This indicates that Ca^{2+} does not significantly affect the protonation state of naphthazarin (Figure 3.29). However, it's noteworthy that in case of an excess of Ca^{2+} (1:5 molar ratio) at pH 11 we observed precipitation of naphthazarin, suggesting an interaction between the two species. In our reaction system, the competition between carbonate ions and Ca^{2+} ions resulted in the consumption of Ca^{2+}, preventing their excess accumulation, which ultimately avoids the precipitation of naphthazarin. These findings also showcase that Ca^{2+} has a limited effect on the protonation state of the naphthazarin.

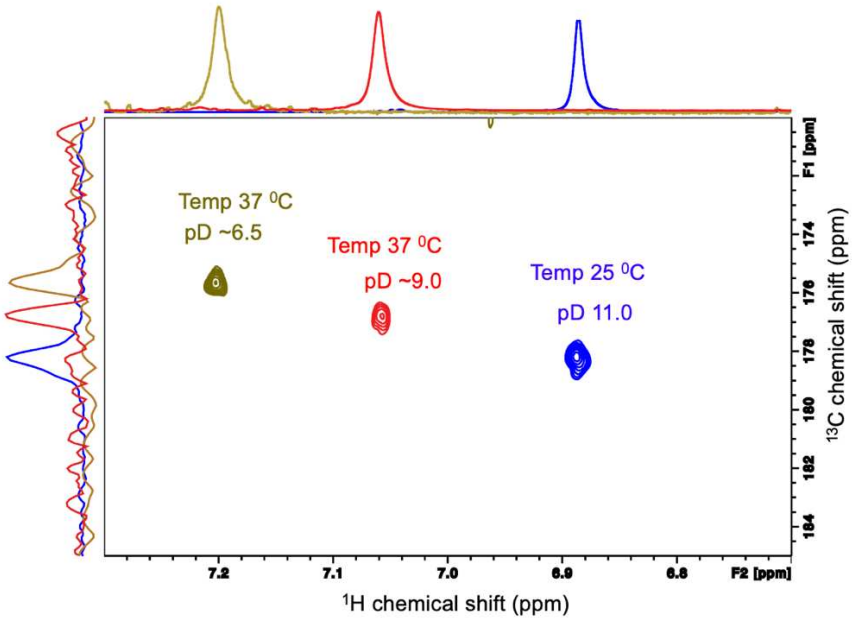

Figure 3.28. $^{1}H\{^{13}C\}$ HMBC NMR spectra of naphthazarin (carbonyl region) in D_2O with DSS as an internal reference at different pD.

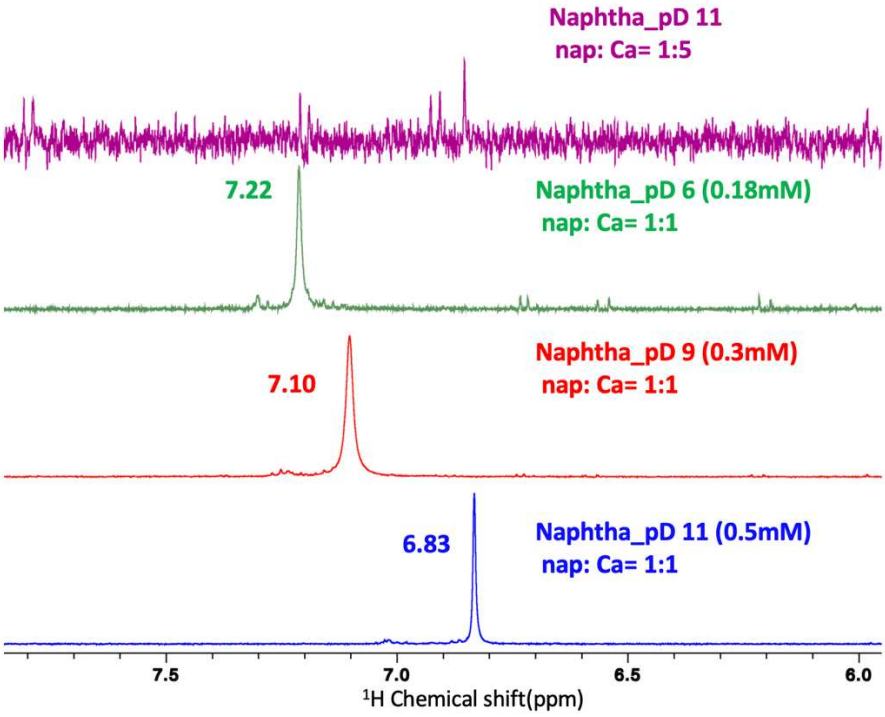

Figure 3.29. Solution state ^{1}H NMR spectra of naphthazarin with various amount of Ca^{2+} in D_2O with DSS as an internal reference at different pD.

In conclusion, our extensive investigation into the interaction of naphthazarin with calcite and ACC, conducted through a combination of solid-state NMR and solution-state NMR experiments, has yielded significant insights into the chemical dynamics of naphthazarin within these systems.

One of the key observations from our study was that the chemical enviro nment of naphthazarin within ACC and calcite differed significantly from the fully protonated form, as indicated by the shift in resonance peaks towards higher field values. These findings align with the outcomes of our solution-state NMR experiments where we explored naphthazarin's behaviour under varying pH conditions. The downfield shifts in the resonance peaks of naphthazarin within calcite and ACC suggest a deprotonated molecular state within these materials.

However, it's worth noting that our investigation also revealed intriguing peak splitting of C-O in the calcite+naphthazarin system. While we have yet to definitively assign the origins of these split peaks, further studies will be essential to unravel the exact molecular state of naphthazarin within this specific context. These split peaks hold valuable information regarding the complex

interplay between naphthazarin and the crystalline structure of calcite, and they warrant additional research to provide a more detailed and precise understanding of this interaction.

The implications of these findings extend to the biomineral pigmentation and color stability, particularly in the context of bio-inspired hybrid pigment coloration applications.

In-vivo Insights: Understanding the interaction between these pigments and ACC offers insights into sea urchin biomineral pigmentation. Sea urchins exhibit a remarkable range of colors in their mineralized tissues, particularly in their spines, from green to purple, sometimes within a single spine. Our research uncovered an intriguing color transformation: red transitioning to blue during ACC precipitation, resulting in lavender-blue ACC powder that eventually crystallizes into purple calcite. This phenomenon resembles the behavior of polyhydroxy-1,4-naphthoquinones (PHNQs), natural compounds that shift from red to blue as they undergo successive deprotonations, highlighting the possible role of pH and [Ca^{2+}] in biomineral coloration. In essence our results offer insights into the mechanisms underpinning the vibrant coloration observed in biominerals formed through ACC precursors.

Bio-inspired hybrid pigments: Beyond the natural world, these results have implications for bio-inspired coloration applications. By understanding how pigments interact with ACC and calcite, it becomes possible to synthesize hybrid pigments with different colors and shades. Such pigments can be used in a wide range of applications, from vibrant coloration in textiles (discussed in chapter 5) and paints to advanced materials in technology and art.

Color stability and durability: By taking inspiration from the sea urchin spines that showcases different and intense color that are stable against harsh conditions. We synthesized hybrid pigments that are photostable as well as quite thermally resistant to degradation. This has implications in industries such as fashion, where long-lasting and enviro nmentally friendly dyes and coloration methods are highly sought after (Presented in chapter 5).

4

Multiscale investigation of the naphthazarin- calcite interactions

Sea urchin spines are remarkable examples of nature's ability to form cm-long convoluted biominerals with durable colors. They exhibit a wide range of colors due to the presence of polyhydroxylated naphthoquinone molecules (PHNQ) that are shielded from the external enviro nment by being incorporated within the calcite structures. This encapsulation protects the pigment molecules from potential degradation due to external factors like UV radiation or mechanical abrasion.

Taking inspiration from sea urchin spines, we synthesized calcite crystals in the presence of different concentrations of naphthazarin (0.11 and 0.53 mM) using the direct precipitation and the vapor diffusion method described in detail in Chapter 2 (section 2.5 and 2.6). In Chapter 4, our investigation sought to understand the processes by which naphthazarin molecules interact or become occluded within the calcite crystals during ACC crystallization induced in solution or in air. Furthermore, we shed light onto the organic-inorganic interactions between

naphthazarin and calcite at the surface and in the bulk of the hybrid pigments from the micron to the atomic scale. This *in-vitro* thorough study may provide valuable insights into the process through which sea urchins create enduring, vibrantly colored calcite structures.

Table 4.1: Presents a variety of methods employed to synthesize crystalline $CaCO_3$ studied in this chapter.

Parameters	**Method (M2)**	**Method (M3)**	**Method (M4)**	**Method (M5)**
Synthesis method	Direct precipitation method	Direct precipitation method	Direct precipitation method	Vapor diffusion method
Reactants	40 mM $CaCO_3$ synthesis: $CaCl_2$ (1M) into Na_2CO_3	40 mM $CaCO_3$ synthesis: 40 mM NaOH $CaCl_2$ (1M) into Na_2CO_3	40 mM $CaCO_3$ synthesis: $CaCl_2$ (1M) into Na_2CO_3	$CaCl_2$ + NaOH (0 or 40 mM) $(NH_4)_2CO_3$ degradation
Experimental conditions	Solvent: H_2O Initial pH: 11.5 Final pH: 8.5 Time: 48-72 h	Solvent: H_2O Initial pH: 12.6 Final pH: 12.55 Time: 5 h	Solvent: H_2O Initial pH: 11.5 Final pH: 10.5 Time: 30s Heating at 200, 250 400 ºC for 1 h	Solvent: H_2O Initial pH: 6.0 Final pH: 8.5-9.0 Time: 48-72 h
$CaCO_3$ polymorphs	ACC to Vaterite+Calcite to Calcite	ACC to Calcite	ACC to Calcite	ACC to Calcite
Method of crystallization	Crystallization induced in solution	Crystallization induced in solution	Crystallization induced by heating	Crystallization induced in solution

Method 3: The advantage of this synthesis is that it leads to the direct crystallization of ACC into calcite. However, the pH 12.6 at which this reaction takes place can lead to the degradation

of naphthazarin which makes this synthesis route difficult to handle and manipulate due to the degradation of pigments as color of the naphthazarin solution brown after few hours.

4.1. Color quantification and color stability at the surface and within the calcite crystals

4.1.2. Color of the calcite-naphthazarin single crystals

The general color of the ACC/calcite-naphthazarin powders obtained by direct precipitation (M1) has been previously assessed by UV-visible diffuse reflectance measurements in Chapter 3 (Section 3.3 and 3.5). Here, using optical microscopy we present an attempt of visualizing the color of/within the calcite single crystals obtained by M2 and by the vapor diffusion route (M5).

We employed the capabilities of a light microscope for a more in-depth analysis of calcite+(0.11 - 0.53 mM) naphthazarin, which confirmed the presence of a distinct color associated with the calcite crystals already with 0.11 mM naphthazarin (Figure 4.1 a-d). We observe that at 0.11 mM concentration of naphthazarin the calcite crystals appear to have a cyan color and at 0.53 mM crystals acquired blue color. The color transitions from cyan to light blue to dark blue at different concentrations could be driven by a mix of structural and pigmented coloration.

Cyan, observed at low concentrations, likely results from structural color, with microstructures of a size tuned to interact with cyan wavelengths (490-520 nm). Dark blue, prominent at high concentrations (0.53 mM), could be primarily due to pigmented color as indeed naphthazarin has blue color in alkaline medium which correlated well as the pH of the synthesis of calcite+naphthazarin sample falls within the same range.

Furthermore, alongside the colored calcite crystals, we have observed the development of dark blue needle-like structures arranged radially in a rosette pattern (as shown in Figure 4.1d), which can be notably abundant in certain samples. The needles are likely due to the crystallization of pure naphthazarin at basic pH. (Figure 4.1c). Indeed, naphthazarin polymorph A was shown to crystallize into needles in C_6F_6, by slow evaporation of solvent (Herbstein *et al*., 1985).

These needles are assigned to the recrystallization of pure naphthazarin at basic pH as it was already shown that polymorph A and C of naphthazarin can exhibit needles shape (Herbstein *et al*., 1985; Olivieri *et al*., 1990). Indeed, naphthazarin can exist in three crystalline forms (A, B and C) with different crystal shapes (needles, plates, or prisms). However, the needles of naphthazarin A crystals were reported to be dark green in color (Herbstein *et al*., 1985). Therefore, we here form Naphthazarin A and the color difference observed in our case is due to the alkaline pH of the solution as it discussed in Chapter 3, where naphthazarin solutions exhibit blue color in alkaline medium.

In calcite+naphthazarin crystals by vapor diffusion (M5), we observed purple color (Figure 4.1e) in calcite crystals which suggests that this coloration may be attributed to the incorporation of pigments. However, the difference in color between calcite+0.53 mM and calcite synthesized by vapor diffusion could potentially arise from variations in the synthesis conditions or could be linked to differences in the crystal structure of the calcite crystals.

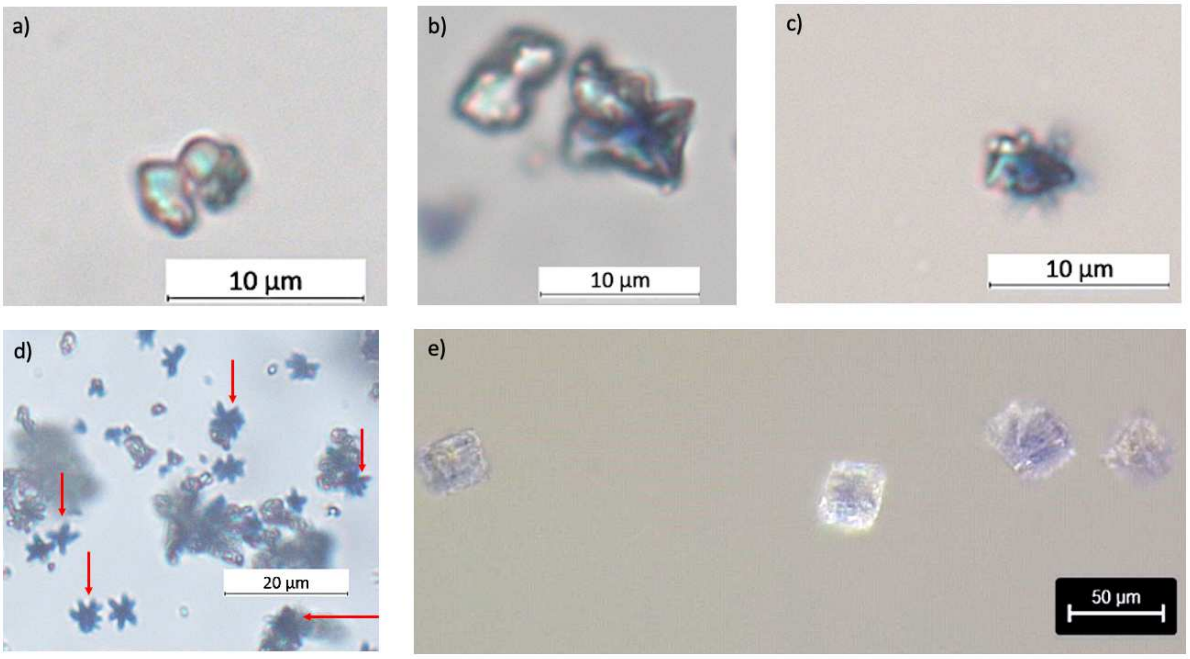

Figure 4.1. a) Calcite+0.11 mM naphthazarin, b-d) calcite+0.53 mM naphthazarin observed under a confocal microscope, e) calcite+naphthazarin (360 µg/mL (0.36 mM)) crystals synthesized by vapour diffusion method.

4.1.2. Color quantification of the naphthazarin-calcite powders obtained *via* different routes and with various naphthazarin concentrations

Color quantification of the calcite-naphthazarin sample obtained by M1 with 0.11 mM naphthazarin is reported in Chapter 3 (Section 3). Briefly, in Na_2CO_3 solution, we showed that naphthazarin's color changes from rose-red at pH 6 to blue-violet at pH 8.5-10.0 and to deep blue at pH 10.3-11.5 which are due to electronic transitions in the different protonated forms, NH_2, NH^- and N^{2-} forms. The observed color of the calcite-naphthazarin powders could be also related to the proportion of the different forms of naphthazarin, which have been associated with/incorporated into $CaCO_3$ at different stages of the synthesis.

Here, we additionally study the effect of increasing naphthazarin concentration up to 0.53 mM on the final color of the hybrid pigments obtained by M2. In particular, we compare the naphthazarin-calcite samples obtained by M2, *i.e.,* co-precipitation of $CaCO_3$ together with naphthazarin versus a physical mixing obtained by manual grinding of pure calcite with 0.5wt% of naphthazarin (Figure 4.2a i-iv).

With an increase in naphthazarin concentration (0.11 to 0.53 mM) darker blue color are visually observed via M2 (Figures 4.2a iii and iv), whereas in a case of physical mixing resulted in a pinkish purple colour (Figure 4.2a ii).

According to UV-visible diffuse reflectance measurements, we observe absorption bands for all samples in the 450-700 nm wavelength range. For calcite+0.11 mM naphthazarin and calcite+0.53 mM naphthazarin display very similar spectra with a broad band at 600 nm and another at 530 nm, which strongly suggests the presence of N^{2-} and NH^- forms within the examined sample (Figure 4.2b). The contribution of N^{2-} species is higher compared to NH^- in both cases. However, we do observed a small difference in the relative intensities of these two bands for calcite+0.53 mM and calcite+0.11 mM naphthazarin samples. It seems that in calcite+0.53 naphthazarin the relative contribution of NH^- is higher compared to calcite+0.11 mM naphthazarin. This difference might be due to the difference in the pH at the end of reaction *i.e.,* calcite+0.53 mM naphthazarin pH is 8.5-8.6 and calcite+0.11 mM naphthazarin pH is 8.8-8.9.

Additionally, we observe have absorbance contribution at around 500 nm. This specific wavelength suggests the presence of the NH_2 form, which contributes to the overall spectral

profile. Therefore, our findings point to a clear dominance of NH^- and N^{2-} forms in the calcite-naphthazarin (0.11 and 0.53 mM). In the case of sample calcite-naphthazarin prepared by physical mixing (PM), we observe that the spectral profile is different from the calcite-naphthazarin samples (M2) as well from naphthazarin. The differences in the peak positions suggest that the whole spectrum is shifted to lower wavelengths when compared to calcite +naphthazarin (M2) and to higher wavelengths in comparison to naphthazarin. This results in the maximum contribution due to (570 nm) NH^- and (520 nm) NH_2, resulting in a purplish-pink color (Figure 4.2b). The physical mixing of naphthazarin and calcite seems to have modified the nature of the naphthazarin as well as changed color from reddish brown to pinkish purple indicating interaction between the two species.

To quantify these hues exhibited by the calcite-naphthazarin (M2) samples, calcite-naphthazarin (PM) and naphthazarin, the x, and y parameters of the CIE 1931 chromaticity diagram were calculated based on the scattered component of the spectra (Figure 4.2c). When the samples containing varying naphthazarin concentrations were represented on the CIE chromaticity diagram (Figures 4.2c and 4.2d), it helped visualize how pigment concentration affects the perceived color of a sample. On the CIE diagram, calcite lies in the white region, while naphthazarin lies in the overlapping region of orange and red.

In the case of calcite+0.11 mM naphthazarin samples, as discussed above, the only difference in the UV-vis spectra profile was the difference in the relative intensity of the two maxima in the visible region. Therefore, we normalized the scattered part of the UV-vis diffuse reflectance data with respect to the maxima at 530 nm and then mapped onto the CIE diagram. This gave us insight into the color variation between calcite+0.11 mM naphthazarin, calcite+0.53 mM naphthazarin, calcite+naphthazarin (PM). Calcite+0.11 mM naphthazarin lies in the overlapping region of blue and purple shades resulting in a blue color. Interestingly, we observed that a higher naphthazarin concentration (0.53 mM) pushed the colors toward the region corresponding to the darker hues with a slightly higher contribution from the purple as well as blue region as compared to ACC+0.11 mM naphthazarin (Figure 4.2d). This indicates that subtle variations in the intensity of maxima in the visible region do contribute towards observed color variation due to an increase in naphthazarin concentration (0.11 to 0.53 mM). When examining samples synthesized through physical mixing, we notice that they occupy a color spectrum range between pink and orange. This observation contrasts with the original naphthazarin sample, which resides in the orange region. This consistency aligns with our

earlier findings, demonstrating that the process of physically mixing indeed alters the characteristics of naphthazarin due to its interaction with calcite.

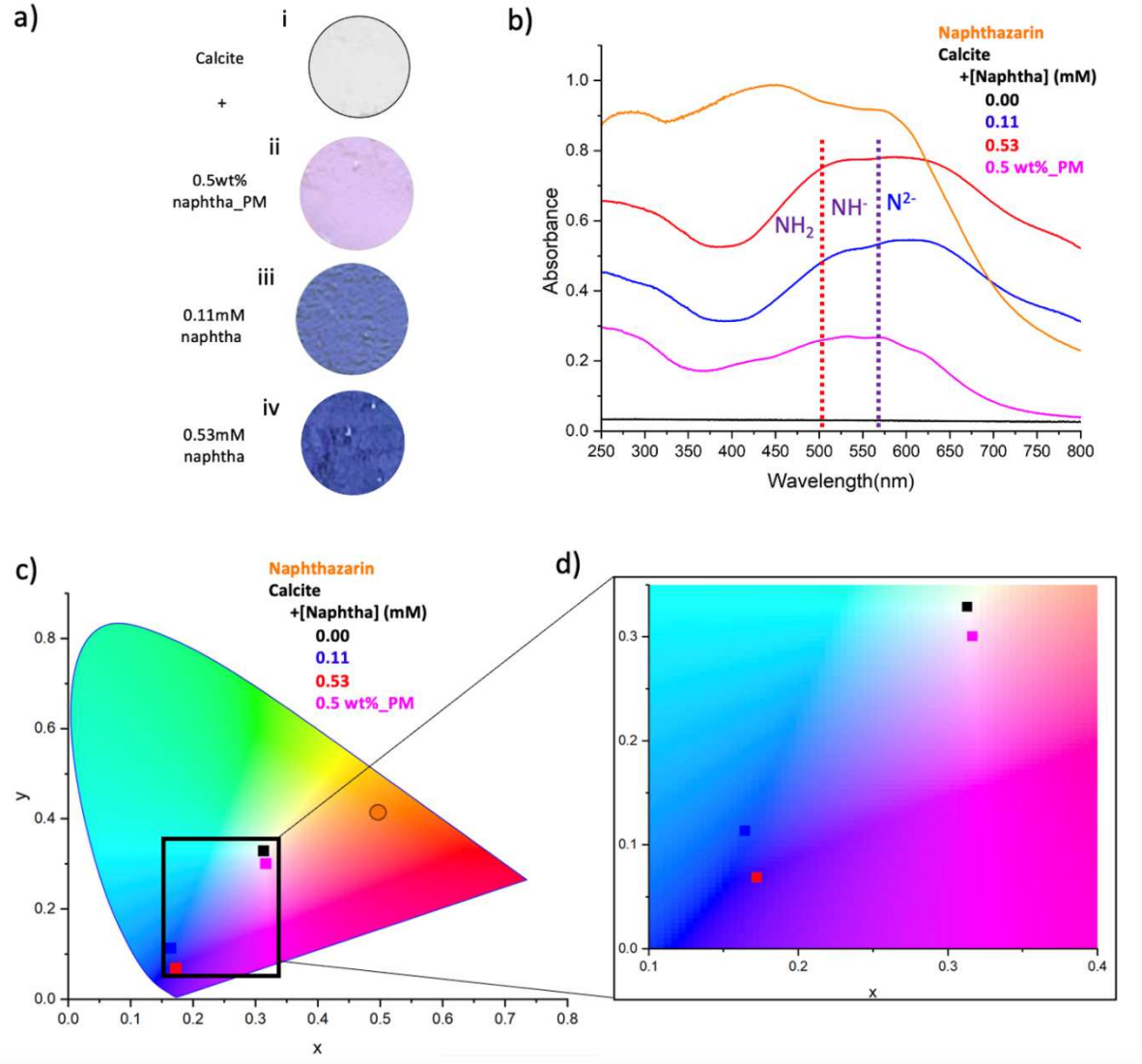

Figure 4.2. Calcite synthesized by direct precipitation in water method (M1), i) calcite, ii) calcite+0.5 wt% naphtha_PM (physical mixing), iii) calcite+0.11 mM naphtha, iv) calcite+0.53 mM naphtha, b) UV-visible diffuse reflectance spectra of calcite samples prepared with varying naphthazarin concentrations (M2) and physical mixing. To aid in visual comparison, c) CIE 1931 diagram corresponding scattered part of the UV-visible diffuse reflectance spectrum of calcite samples, d) zoomed region of CIE diagram.

4.1.3. Color stability of the calcite-naphthazarin powders

4.1.3.1 Thermal stability

In order to study the thermal stability of the hybrid pigments, we first measured the stability of pure naphthazarin by DSC measurements, which revealed that it melts at 225 °C and starts to degrade at 244 °C (Figure 4.3a).

To analyze the stability of the hybrid pigment (calcite+0.11 mM naphthazarin synthesized by M2), we conducted *in-situ* heating colorimetric experiments from 25 to 500 °C in the presence of air at 5 °C/min. Figure 4.3b showcases the colorimetric data for 25, 200, 400 and 500 °C. We observe the broad absorbance band between 400-700 nm. This band corelates well with the UV-vis diffuse reflectance data discussed in section 4.1.2. However, it can be seen that it is difficult to distinguish different bands in 400-700 region which provided information about the different forms of naphthazarin. This could be due to the low sensitivity of the technique or it could be due to the angle at which the optical fibre was placed above the sample which might not allow for all the reflected light to be collected by the optical fibre. However, with increase in temperature from 25 to 400 °C we did not observe significant change in the spectral profile of calcite+0.11 mM naphthazarin (M2), which is stark contrast to the images acquired on calcite+0.11 mM naphthazarin (M2) sample *ex-situ* heating. Figure 4.3c highlights the color changes upon heating of sample from purple blue color (25 °C) to a color with pink shade (200 °C and 400 °C). This color change strongly suggests a reaction to the heightened thermal conditions, which can be attributed to either the removal of adsorbed water or structural water molecules (Figure 4.3c). At 500 °C, the absorbance band vanishes indicating the degradation of naphthazarin associated with calcite+0.11 mM naphthazarin resulting in a white color (Figures 4.3b and 4.3c).

To delve deeper into the color changes during heating, the colorimetric data was graphically represented on the CIE 1931 chromaticity diagram a two-dimensional color space (Figure 4.3d). By representing the data in the CIE color space, we gathered information about the stability as well as the color changes during the heating of the calcite+0.11 mM naphthazarin sample. However, due to absence of distinct bands in the 400-800 nm region, CIE map only provided accurate information regarding the intensity of the color with respect to temperature. Notably, we observed alteration in color at 200 °C, shifting from darker blue and purple to a lighter purple blue. When the calcite+0.11 mM naphthazarin sample was exposed to 400 °C,

the color became lighter and acquired lighter blue and purple shade, and with further increase in temperature to 500 °C the pigment degraded completely, resulting in a color close to white

These findings strongly suggest that the hybrid pigments exhibit an exceptional level of stability against heating, particularly when compared to naphthazarin, which starts to degrade at a significantly lower temperature of 244 °C.

When we examine the stability of calcite+0.11 mM naphthazarin in contrast to that of sea urchin spines, a fascinating insight emerges. It has been observed that upon subjecting the purple spines to heat, a distinct color transition is observed as shown in Figure 4.3f. At around 170 °C, the once vibrant purple hue transforms into a more subdued purple-brown shade. This alteration points to the degradation of organics present within the calcite structures of the spines. It's important to emphasize that the nature of the organics within the spines is inherently diverse, encompassing pigments and various other organic compounds. As the temperature continues to rise, the color of the spines further evolves. At approximately 220 °C, the transformation is even more pronounced, with the color shifting to a complete brown hue. Finally, at a temperature of 400 °C, the spines attain a white color, signalling the comprehensive degradation of most of the organic constituents (Figure 4.3f) (Albéric *et al*. 2018).

Overall, our findings emphasize the stability of these hybrid pigments within a range of room temperature to high-temperature (25-400 °C) conditions.

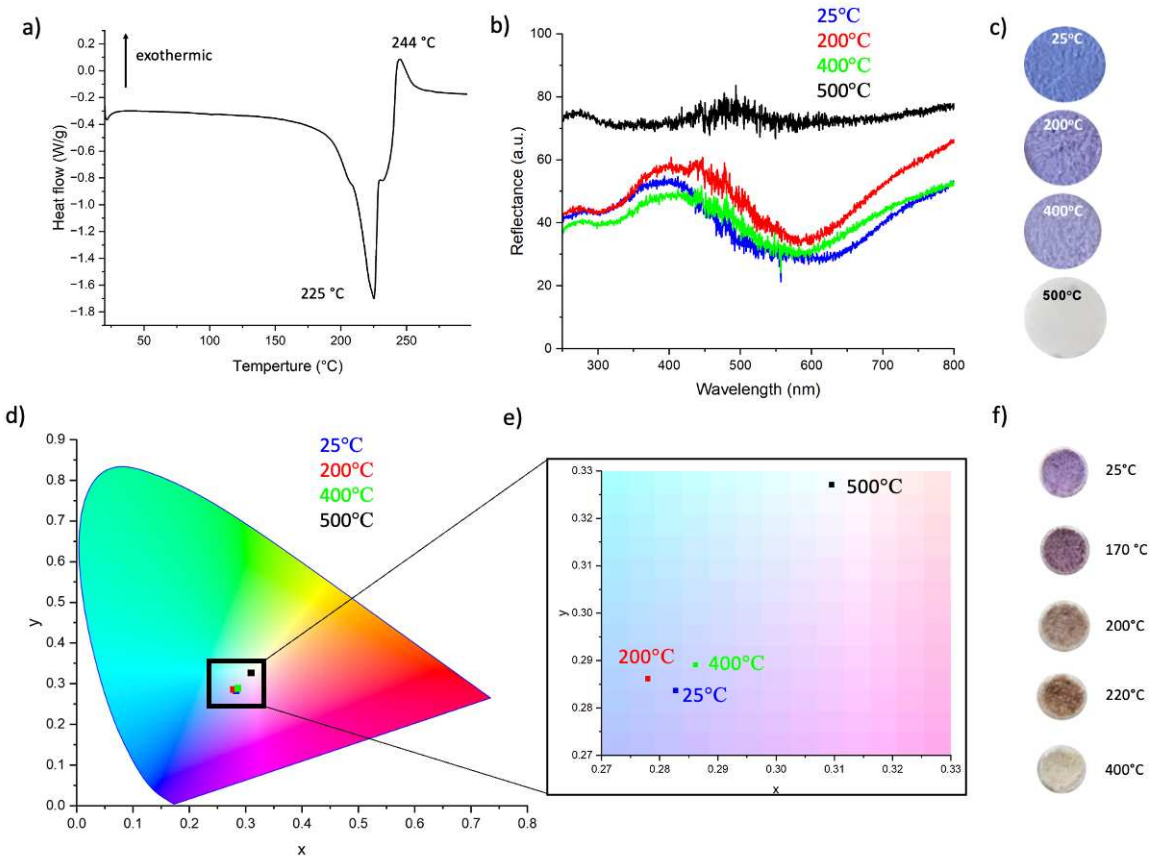

Figure 4.3. a) DSC thermogram on naphthazarin (20-300 °C at 5 °C/min) displaying melting point at 225 °C and degradation at 244 °C, b) *In-situ* heating (5 °C/min) colorimetric measurements on calcite+0.11 mM naphthazarin (M2) at different temperature (25 °C, 200 °C, 400 °C, 500 °C), c) Images acquired on calcite+0.11 mM naphthazarin (M2) sample heated for 1 hr at different temperatures (25 °C, 200 °C, 200 °C, 500 °C) and allowed to cool to RT, d, e) CIE 1931 diagram of the *in-situ* colorimetric measurement on calcite+0.11 mM naphthazarin synthesized by direct precipitation (M2), f) images acquired by Marie Albéric on purple sea urchin spine powder after heating at different temperatures.

4.1.3.2. Chemical stability

The chemical stability of the colors was assessed by oxidative treatments with NaOCl (Marzec *et al*., 2018) at different initial concentrations of naphthazarin (0.11 mM and 0.53 mM) for different times from 2 to 24 h. NaOCl was considered because it is widely used to remove efficiently the inter-crystalline organic tissues of biominerals (Penkmann, 2008). In the case of sea urchin spines, it was shown that the color resists intensive bleaching up to NaOCl 12 % for

48 h (Figure 4.4). This is confirmed by UV-vis diffuse reflectance measurements conducted on bleached purple spine powder samples by Marie Albéric (Figure 4.4).

We observed that bleaching with 1% NaOCl for 2 h of the different samples resulted in the complete degradation of naphthazarin in the case of the physical mixture of calcite with 0.5 wt% naphthazarin (Figure 4.5a ii), whereas only a reduction in intensity of color of the M2 calcite-naphthazarin samples (0.11 and 0.53 mM) (Figures 4.5a, iii and iv) was observed while the hue remained intact (Figure 4.5a, iii and iv).

We obtained similar results when bleaching was done for 24 h suggesting that naphthazarin is quite protected by the mineral phase. The concentration of NaOCl also did not impact the degradation of naphthazarin as we did not observe significant color changes for samples bleached with 1, 5 and 12 % NaOCl.

The quantitative analyses by UV-visible diffuse reflectance measurements of the different samples confirm these visual observations. Indeed, the UV-visible spectra profile of bleached (calcite+0.11 mM naphthazarin, calcite+0.53 mM naphthazarin and physical mixing sample) were different. For calcite+0.11 mM naphthazarin bleached we observed only decrease in the overall absorbance but no change in overall spectral profile.

In case of calcite+0.53 mM naphthazarin bleached along with decrease in the absorbance we observe spectral changes as global maxima shifted to approximately 580 nm from 620-630 nm and also the relative intensity of the band with maxima around 510 nm is different when compared to unbleached counterparts. This suggests that NH^- species is contributing more towards color in calcite+0.53 mM bleached sample when compared to unbleached samples. It is worth considering that as naphthazarin degrades relatively in higher amount in comparison to calcite+0.11 mM naphthazarin bleached, particularly in the case of calcite+0.53 mM naphthazarin, the degraded naphthazarin may be the N^{2-} form as the band at 620 nm diminishes (Figure 4.5a).

To gain better understanding of the color changes of bleached samples, the scattered part of the UV-vis diffused reflectance was mapped on the CIE 1931 diagram. On the CIE diagram, calcite-naphthazarin (PM) bleached lies in region close to white and calcite+0.11 mM naphthazarin bleached lies in lighter purple blue region. For bleached samples, we observed a decrease in the intensity of the color as it lies in the white region. For Calcite+0.53 mM

naphthazarin, we observed that bleached counterpart had lighter compared to calcite+0.11 mM naphthazarin (bleached).

Overall, these results show that most of the naphthazarin is adsorbed on the surface of the calcite (Physical mixing as well as (M2)). However, bleaching did not completely degrade the color in case of samples obtained by M2 suggesting incorporated naphthazarin was well protected.

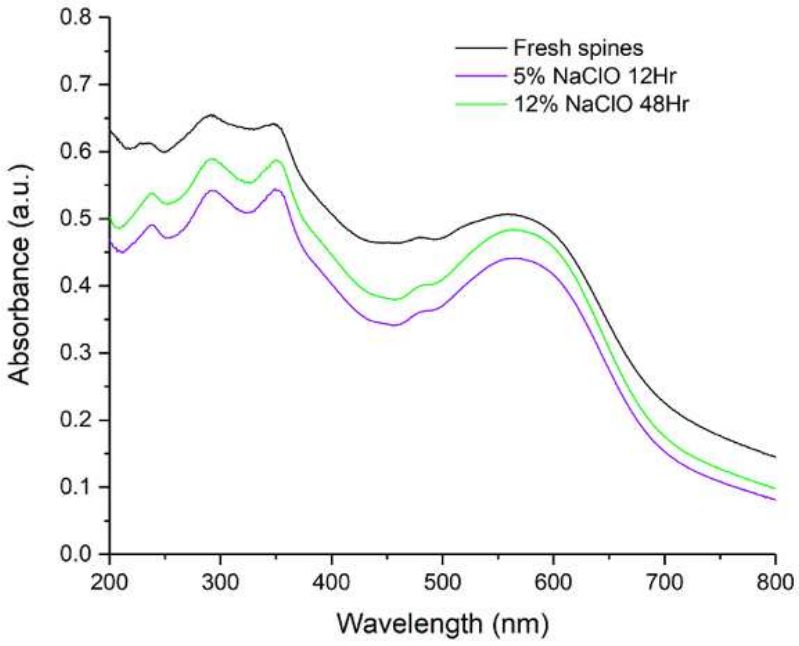

Figure 4.4. The UV-Vis diffuse reflectance spectrum of purple sea urchin spine powder: fresh spines powder, bleached spine powder with 5% NaOCl for 12h, and bleached spines powder with 12 % NaOCl for 48h.

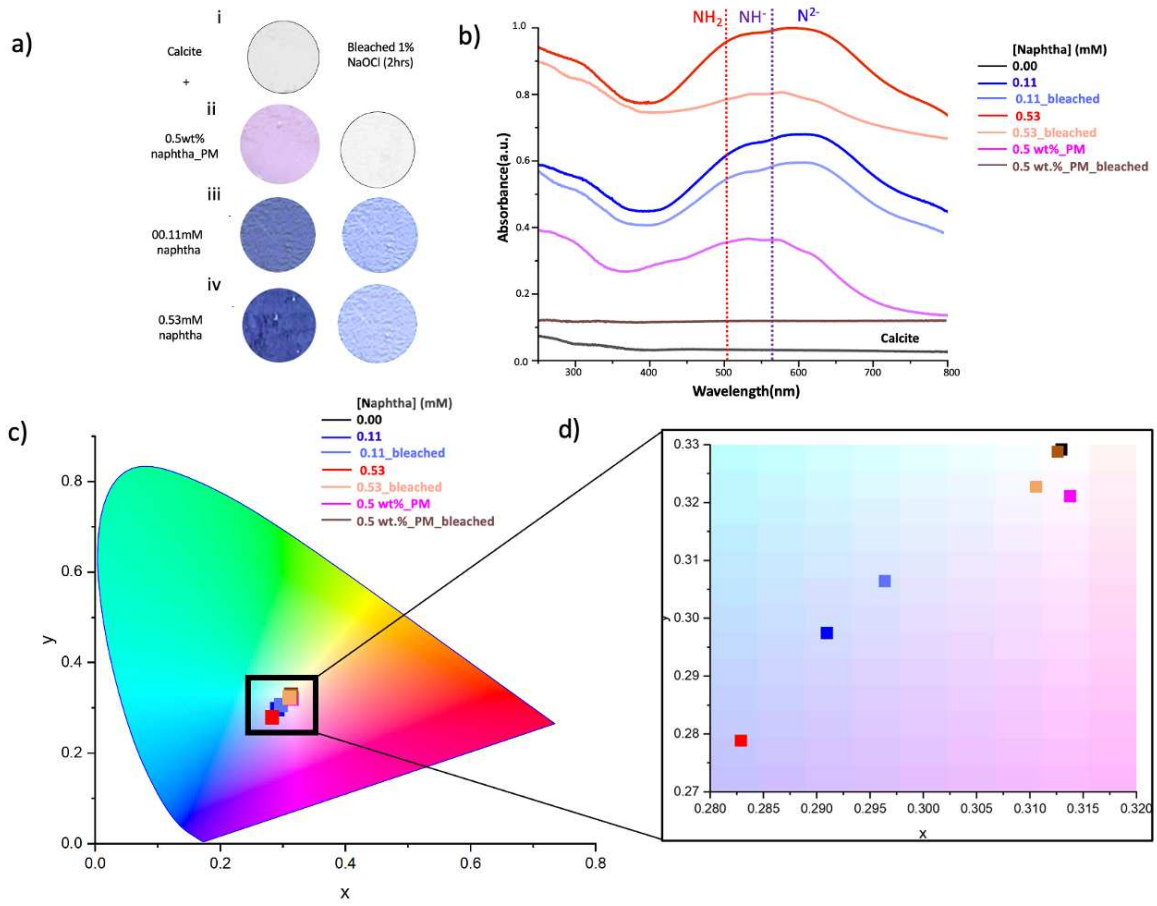

Figure 4.5. a) UV-visible diffuse reflectance spectra of calcite samples prepared with varying naphthazarin concentrations using precipitation (M2), physical mixing, and post-bleaching methods. To aid in visual comparison, b) spectrum have been vertically shifted along the y-axis to facilitate the comparison of their profiles. c) CIE 1931 diagram corresponding scattered part of the UV-Vis diffused reflectance spectrum of calcite samples prepared with different concentrations of naphthazarin, d) zoomed of CIE 1931 diagram of calcite samples prepared with different concentrations of naphthazarin.

4.1.4. Naphthazarin at the surface and occluded within the calcite crystals

4.1.4.1. Surface analyses

In order to study the presence of naphthazarin on the $CaCO_3$ crystals XPS measurement and Raman spectroscopy techniques were used. In contrast to UV-visible diffuse reflectance measurements, which allow to probe the samples up to few microns in depth, while XPS (1 nm-1 µm) and Raman spectroscopy (20-50 µm) provide atomic-level surface characterization (Clarà Saracho *et al.*, 2020).

Figure 4.6 showcases high-resolution XPS spectra of the C1s, Ca2p and O1s energy levels of naphthazarin, calcite+naphthazarin (0.22 mM and 0.53 mM) (M2) and bleached calcite+0.11 mM naphthazarin while the corresponding surface atomic ratios are presented in Table 4.2.

As reported in Chapter 3, the deconvolution of the C1s spectra of naphthazarin revealed three main peaks at 284.6±0.1 eV, 286.2±0.1 eV, and 287.1±0.1 eV, which can be attributed to the carbon atoms in the aromatic ring or amorphous carbon, -C-OH and -C=O, respectively (Le Guillou *et al*., 2018) (Figure 4.6a). In the O 1s region, we detect signals corresponding to the presence of a carbonyl group (-C=O) at an energy level of 531 eV (Figure 4.6c) and signals associated with the hydroxyl functional group (-C-OH) at a slightly higher energy level of 532.4 eV (Figure 4.6c).

In the carbon region for calcite, we observe an amorphous carbon or contamination signal at 284.2±0.1 eV and 289.2±0.1 eV corresponding to CO_3^{2-} (Tobler *et al*., 2015). For calcite-naphthazarin (Figure 4.6a), we observe an additional signal in the 286-287 eV range, due to the presence of organic carbon signal. This organic signal might be coming from the presence of C-OH, -C=C- of the naphthazarin (Stipp and Hochella, 1991).

In the calcium region, the Ca 2p doublet with the Ca $2p_{3/2}$ contribution at a binding energy of 346.6±0.2 eV is also detected (Figure 4.6b), which allow one to calculate Ca/C ratio. In addition, distinctive signals originating from specific chemical groups within the compound in the oxygen region are detected for calcite-naphthazarin sample. Specifically, we detect signals corresponding to the presence of a -C=O at an energy level of 531 eV and signals associated with the -C-OH at a slightly higher energy level of 532.4 eV were absent (Figure 4.6c). The measurement performed on crystalline $CaCO_3$ with different naphthazarin concentrations shows that with an increase in naphthazarin concentration from 0.22 mM to 0.53 mM the C/Ca and O/Ca ratio increases indicating naphthazarin concentration on the surface increases (Table 4.2).

For calcite-naphthazarin samples, we have only a C=O signal in the oxygen region and it might be due to the following reasons: 1) naphthazarin concentration might be low, and -C=O signal was from carbonates, 2) the -C=O signal was due to naphthazarin, which means -C-OH signal is absent suggesting the naphthazarin might be in deprotonated form. These XPS results provided information about binding energies and thus atomic compositions of $CaCO_3$ as summarized in Table 4.2.

Finally, in the case of the bleached sample, no organic carbon signal was observed and the C/Ca and O/Ca ratios are very close to that of calcite without naphthazarin, suggesting that most of naphthazarin was removed after bleaching (Table 4.2). The small difference in the C/Ca and O/Ca ratios can be attributed to the smaller organics units generated from degradations of naphthazarin that might be still associated with the calcite

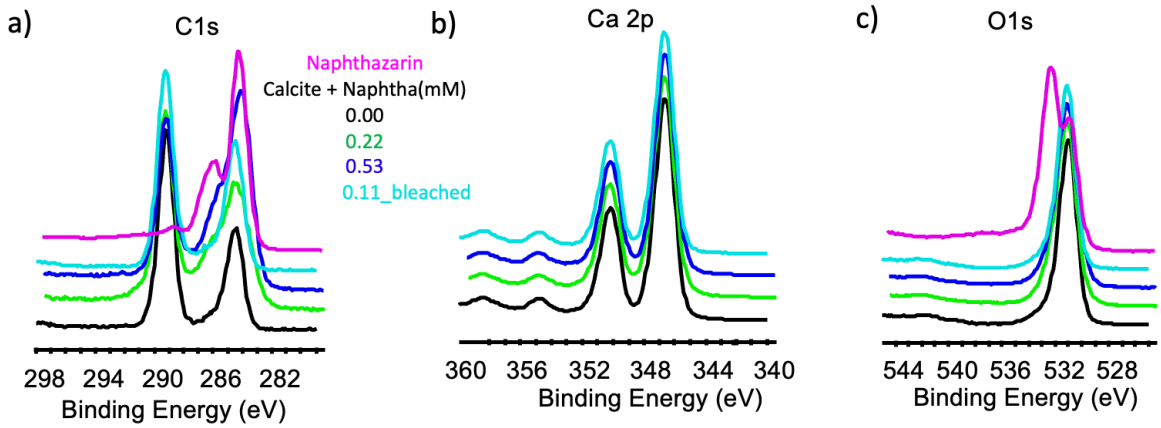

Figure 4.6. XPS analysis of naphthazarin, calcite, and calcite+naphthazarin samples. a) Carbon region (C 1s), b) calcium region (Ca 2p), c) oxygen region (O 1s).

Table 4.2. Summary of the different C/Ca and O/Ca ratios measured in pure calcite and in the different calcite-naphthazarin samples (0.22 mM, 0.53 mM and 0.11 mM).

Naphthazarin concentration (mM)	C/Ca ratios	O/Ca ratios
0.0	1.47	2.61
0.22	2.9	2.99
0.53	2.96	3.38
0.11_ Bleached	1.76	2.69

Raman mapping analysis was used to get insights into the spatial distribution of naphthazarin at the surface of the calcite+0.53 mM naphthazarin (M2) sample (Figures 4.7a and 4.7b). Each pixel in the map represents a 1 µm x 1 µm area of the sample's surface, and the Raman spectra are recorded at each of these points and contain all the data points from 100-3500 cm^{-1}. The average Raman spectra of the 2D map revealed characteristic features of calcite, including the symmetric str*etc*hing vibration mode (v1) at 1084 cm^{-1} and the asymmetric str*etc*hing vibration

mode (ν3) at 282 cm^{-1} of the CO_3^{2-} ions. Other bands attributed to naphthazarin are detected. In particular, distinctive peaks, the -O-H in-plane bending vibrations around 1240 cm^{-1} , str*etc*hing vibrations or in plane bending vibrations for C-H/C-C at 1410 and 1374 cm^{-1} are observed (Zahedi Tabrizi *et al*., 2004). These findings provide compelling evidence confirming the presence of naphthazarin on the surface of the $CaCO_3$ crystals.

Once we analyzed, the average Raman map and we selected the distinct spectral bands for 1084 cm^{-1} for calcite and 1240 cm^{-1} for naphthazarin which allowed us to plot the 2D map with blue for calcite and red for naphthazarin (Figure 4.7c). Analyzing this color-coded map allowed us to visually discern the locations where calcite and naphthazarin were present, thus providing insight into their spatial arrangement. It suggests that naphthazarin is not distributed uniformly with some region crystals having higher concentration of naphthazarin than others. This also highlights that the naphthazarin might not be adsorbed even on all the crystals as some regions on the 2D shows no presence of naphthazarin.

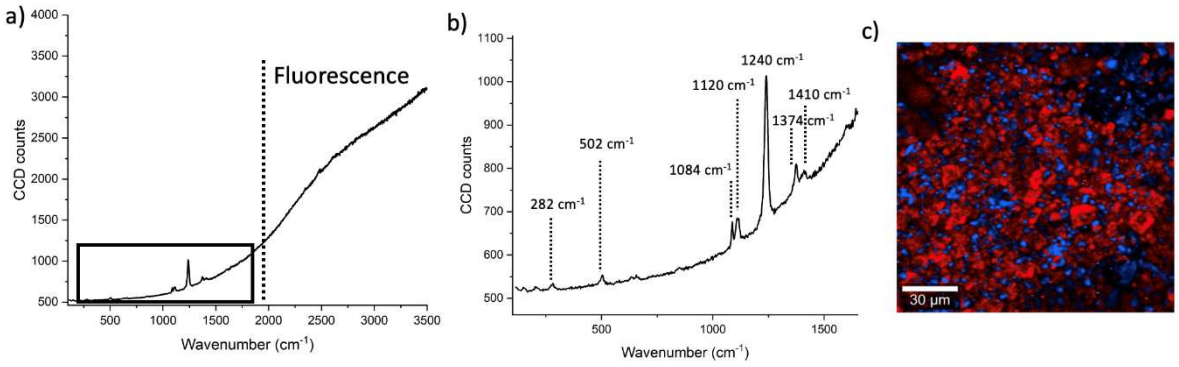

Figure 4.7. a) Raman Spectrum of calcite+0.53 mM naphthazarin powder with a step size of 1µm using red laser (532 nm) b) Zoomed spectrum (a) Spectra of calcite+0.53 mM naphthazarin c) Raman map extracted from the Raman spectrum obtained on calcite+0.53 mM naphthazarin powder packed with a step size of 1 µm. The red color corresponds to $CaCO_3$ and the blue color shows naphthazarin distribution.

4.1.4.2. Quantification of naphthazarin associated with calcite: adsorbed versus occluded

The total amount of naphthazarin associated with calcite and the amount only incorporated into calcite were quantified using UV-vis spectroscopy measurements of the calcite+0.11 mM naphthazarin and calcite+0.53 mM naphthazarin samples synthesized by M2.

The amount of naphthazarin associated with calcite in the resulting powder was quantified using UV-visible spectroscopy measurements by first dissolving the calcite+naphthazarin samples with 1 M HCl solution that results in a clear red-colored solution and second measuring the absorbance of the resulting solution by adjusting the pH to 5.5, at which the calibration curve is obtained.

The calibration curve was obtained as follows: Naphthazarin was dissolved in water at different concentrations ranging from 0.01 to 0.055 mM at pH 5.5, which is the obtained pH for all the prepared solutions (Figure 4.8). UV-visible measurements were performed on different concentration of naphthazarin (Figure 4.8a).

Once the calibrations curve was obtained, we then performed the UV-visible measurements on the resulting calcite+0.11 mM naphthazarin and calcite+0.53 mM naphthazarin as well as bleached samples solutions prepared by dissolving them in 1 M HCl solution and then adjusting the pH to 5.5. To get the accurate value of naphthazarin concentration associated with ACC, we must stay within the calibration curve limits. Ideally our samples contain 0.11 mM and 0.53 mM naphthazarin, these concentration values should lie outside the calibration curve limits. In order not to exceed the calibration limits, we decided to dissolve 50mg of calcite+0.11 mM naphthazarin sample, 20 mg of calcite+0.53 mM naphthazarin, 100mg of calcite+0.11 mM naphthazarin bleached, 50mg of calcite+0.53 mM naphthazarin bleached in 1 M HCl and adjusting the pH to 5.5 while keeping the total volume at 50 mL.

The absorbance spectra were obtained on calcite+0.11 mM naphthazarin, calcite+0.53 mM naphthazarin as well as on bleached samples solution. The absorbance value for each sample at 510 nm were extracted and plotted on the calibration curve, which suggests that the concentration of naphthazarin in calcite+0.11 mM naphthazarin, calcite+0.53 mM naphthazarin, calcite+0.11 mM naphthazarin bleached and calcite+0.53 mM naphthazarin bleached was 0.026 mM, 0.048 mM, 0.006 mM and 0.008 mM respectively. After this the concentration values were adjusted to 200 mg of calcite (yield of the reaction (M2)) to get the exact concentration of naphthazarin associated with calcite. Therefore, the concentration terms for calcite+0.11 mM naphthazarin and calcite+0.53 mM naphthazarin were ~0.1 mM and ~0.48 mM respectively and for bleached counterparts 0.11 mM and 0.53 mM were 0.012 mM and 0.032 mM respectively UV-vis results indicated that the efficiency of naphthazarin incorporation or association with ACC was approximately 90-95 %. However, in case of bleached samples the incorporation percentage of naphthazarin was approximately 5-10 %.

Overall, these results indicate that a relatively low concentration of naphthazarin is incorporated within the $CaCO_3$ crystals, while the majority of the naphthazarin appears to be adsorbed on the surface of the $CaCO_3$ crystals.

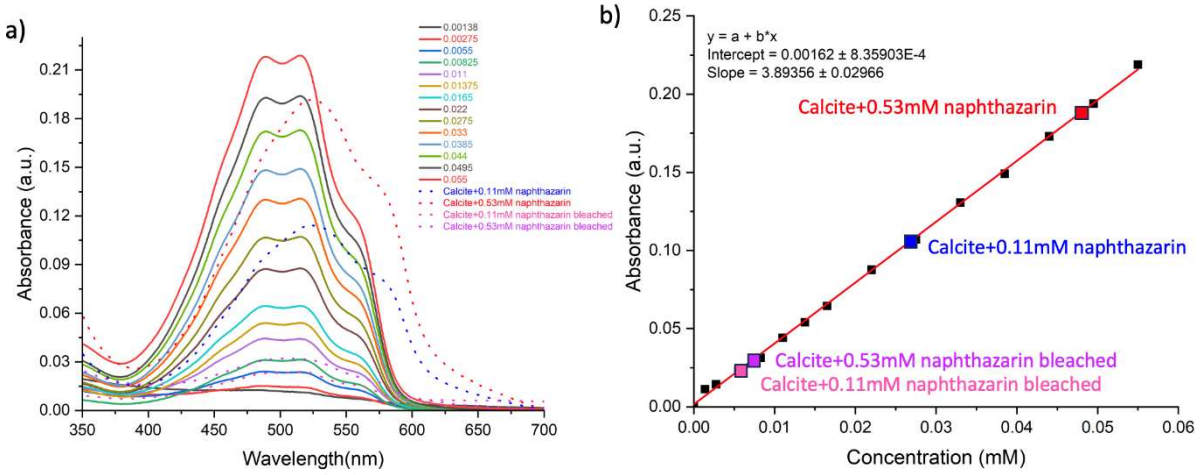

Figure 4.8. a) UV-visible absorbance spectra obtained on different concentration of naphthazarin at pH 5.5. UV-vis spectra solution obtained on solution by dissolving calcite+0.11 mM naphthazarin, calcite+0.53 mM naphthazarin and bleached counterparts in 1M HCl at pH 5.5. b) Calibration curve obtained for naphthazarin at pH 5.5 by extracting the absorbance values for each concentration at 510 nm and corresponding absorbance values for calcite+naphthazarin samples.

NaOCl is strong oxidising agent that leads to the complete degradation of organics. Finally, we made sure that the NaOCl treatment (1 %, 24 h) had no discernible effect on either the crystal shapes nor the surface characteristics of pure $CaCO_3$ samples (Figure 4.9), which suggest that the incorporated naphthazarin within the calcite-naphthazarin crystals should be still intact.

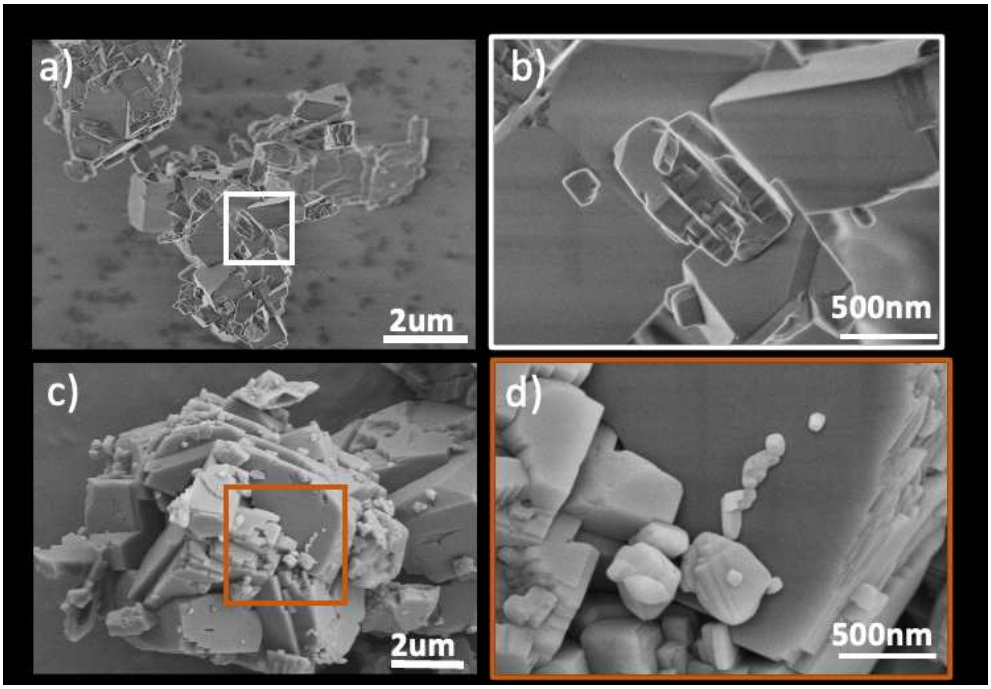

Figure 4.9. SEM-FEG micrographs: a, b) calcite, c, d) calcite bleached (1 % NaOCl, 24 h).

4.2. Local naphthazarin-calcite interactions from micro- to the nano-scale

4.2.1. Qualitative evaluation of naphthazarin-calcite interactions

In our investigation of the interaction between naphthazarin and calcite, we conducted experiments involving the suspending and stirring of calcite+naphthazarin (M2) in water and ethanol for 2 h. Our observations were compared with those of ACC+naphthazarin (M1) and calcite+naphthazarin physical mixing. For calcite+naphthazarin and ACC+ naphthazarin sample we did not observe leaching out of pigment into the water or ethanol but we do observe leaching of pigment into water and ethanol for calcite+naphthazarin physical mixing. These finding indicate that naphthazarin definitely exhibits stronger interactions when coprecipitated with $CaCO_3$ in comparison to physical mixing. However, at this stage we cannot confirm the true nature of interactions, but we can just speculate that the interactions might be strong electrostatic interactions with the $CaCO_3$ matrix.

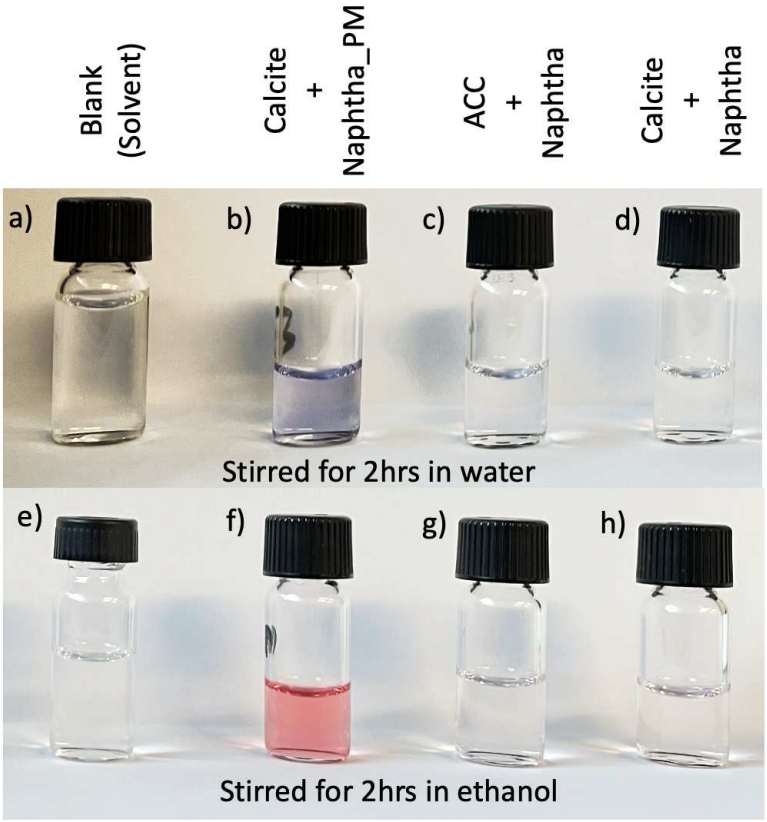

Figure 4.10. Images of filtrate obtained after powdered samples were suspended in water (b-d) and ethanol (f-h). a) Water, b) calcite + naphthazarin (1 wt.%) (PM), c) ACC+ (0.11 mM) naphthazarin, d) calcite + (0.11 mM) naphthazarin, e) ethanol, f) calcite+ naphthazarin (1 wt.%) (PM), g) ACC+ (0.11 mM) naphthazarin, h) calcite+ (0.11 mM) naphthazarin.

As discussed in section 4.1.4.2. that most of the naphthazarin is adsorbed on the surface of calcite rather than being incorporated. UV-vis diffuse reflectance spectra analysis of bleached ACC+0.53 mM naphthazarin provided insights into the incorporation of naphthazarin within ACC (Figure 4.11). We observed that bleaching completely degraded he naphthazarin as no absorbance band was observed in the visible region suggests that naphthazarin likely resides on the surface of the ACC. However it known that ACC can be porous in nature (Sun *et al*., 2020), therefore it is possible that naphthazarin could be present everywhere within the ACC matrix.

Similarly, it has been observed that bleaching of the regenerating part of the sea urchin spine where the ACC polymorph is present at the surface of already crystalline calcite, leads to discoloration indicating that pigments might not be well protected when associated with the ACC matrix as compared to the calcite matrix.

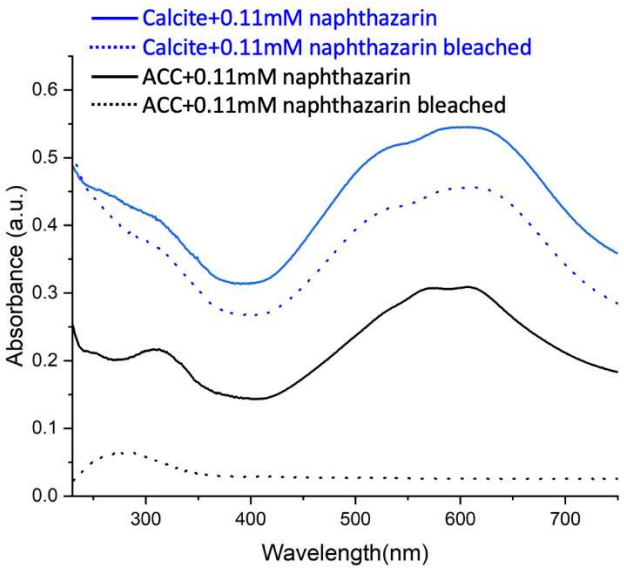

Figure 4.11. a) UV-vis reflectance spectra on ACC+ 0.53 mM naphthazarin and ACC+ 0.53 mM naphthazarin bleached (1 % NaOCl 2 h).

4.2.2. Effect of naphthazarin on calcite crystals morphology and surface

To investigate the impact of naphthazarin on the morphology and the surface of calcite, we employed FEG-SEM imaging to examine the samples synthesized by M5 (vapor diffusion method), M2 (direct precipitation method at pH 10.5) and M3 (at pH12.5) as well as by M4 (ACC formation at pH 10.5 and crystallization induced by heating).

4.2.2.1. Calcite-naphthazarin crystals obtained by vapor diffusion M5

Vapor diffusion (M5) is a well-established and commonly employed technique for investigating the influence of organics on crystal morphologies. SEM micrographs obtained on calcite crystals with naphthazarin concentrations starting from 10 µg/mL show noticeable alteration in their morphology (Figure 4.12). The crystals display an elongation in their overall shape. Despite this change in crystal morphology, the crystal surfaces remained largely unaffected, which could be attributed to the relatively low concentration of naphthazarin.

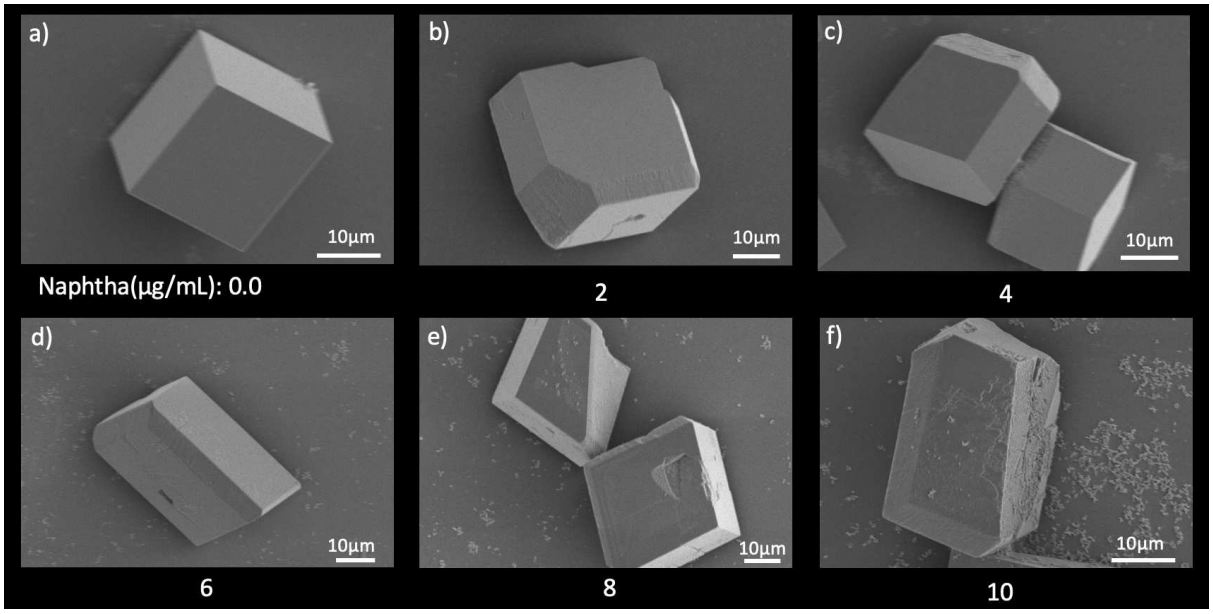

Figure 4.12. SEM micrographs were obtained on single crystal assay by vapor diffusion synthesis with varying concentrations of naphthazarin. a) calcite, b) calcite+naphthazarin (2 µg/mL), c) calcite+naphthazarin (4 µg/mL), d) calcite+naphthazarin (6 µg/mL), e) calcite+naphthazarin (8 µg/mL), f) calcite+naphthazarin(10 µg/mL).

To explore the impact of higher concentrations of naphthazarin on the morphology and surface of the calcite crystals, the initial pH of the $CaCl_2$ solution had to be increased in order to increase naphthazarin solubility. An initial solution of naphthazarin (83 µg/mL) was first prepared in the presence of 2 mM NaOH and second diluted by 3, 2 and 1.4 times, which resulted in 25, 42 and 58 µg/mL of naphthazarin together with 13, 20 and 28 mM NaOH, respectively. Figure 4.13, display the SEM-FEG micrographs obtained for these three concentrations. we can observe that with increase in concentration of naphthazarin lead to the change in morphology. At 25 µg/mL we evidence the elongation and development of new edges (110) (Jimenez-Lopez *et al*., 2003), at 42 µg/mL the calcite exhibited structure resembling of stacked non non-aligned crystals, a phenomenon observed (Aizenberg *et al*., 2002) when growing synthetic calcite crystals epitaxially on the spicule surfaces were misaligned in the a,b-plane. With further increase in naphthazarin concentration to 58 µg/mL, we observed the elongation crystal which can be can be correlated with a study by (Aizenberg *et al*., 1997). In this study, they showed that calcite crystals grown in the presence of macromolecules extracted from sea urchins by vapor diffusion cause morphological modifications and anisotropic textural changes in the grown crystals. Notably, the calcite crystals exhibited well-developed stepped faces slightly oblique to the c- axis and perpendicular to the a-axis.

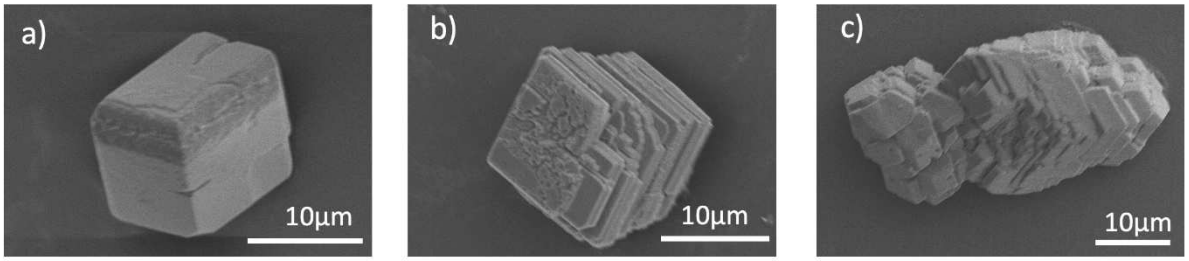

Figure 4.13. SEM micrographs obtained on calcite-naphthazarin with different concentration, a) 25, b) 42, c) 58 µg/mL together with 13, 20 and 28 mM NaOH respectively (~pH 12.5).

The presence of NaOH in the solution cannot be ignored as it has been shown that pH variation can influence the crystal morphology (Tobler *et al*., 2016). Therefore, additional vapor diffusion $CaCO_3$ syntheses were performed in the presence of NaOH concentration of 40 mM (pH 12.5) for pure calcite and calcite+naphthazarin. SEM micrographs revealed the presence of individual calcite crystal (Figures 4.14a and 4.14e), aggregates of calcite crystals (Figures 4.14b and 4.15f) and another polymorph of $CaCO_3$ (Figures 4.14d and 4.14h) in the form rosette mostly likely vaterite (Trushina *et al*., 2014). At this pH, aggregates of calcite crystals are observed, this phenomenon of fused calcite crystals is well documented for calcite synthesis at pH 12.5 (Tobler *et al*., 2016). The additional $CaCO_3$ polymorph ratio with respect to calcite was quite low as we observed very few of these structures. The addition of naphthazarin (concentration 40 µg/mL) did not lead to an elongation of the crystals as observed before in the absence or low NaOH concentration but in a drastic alteration of the surface in the form of pitss (Figures 4.14e-g). This effect is studied in detail below for the precipitation method at pH 10.5 to 8.5.

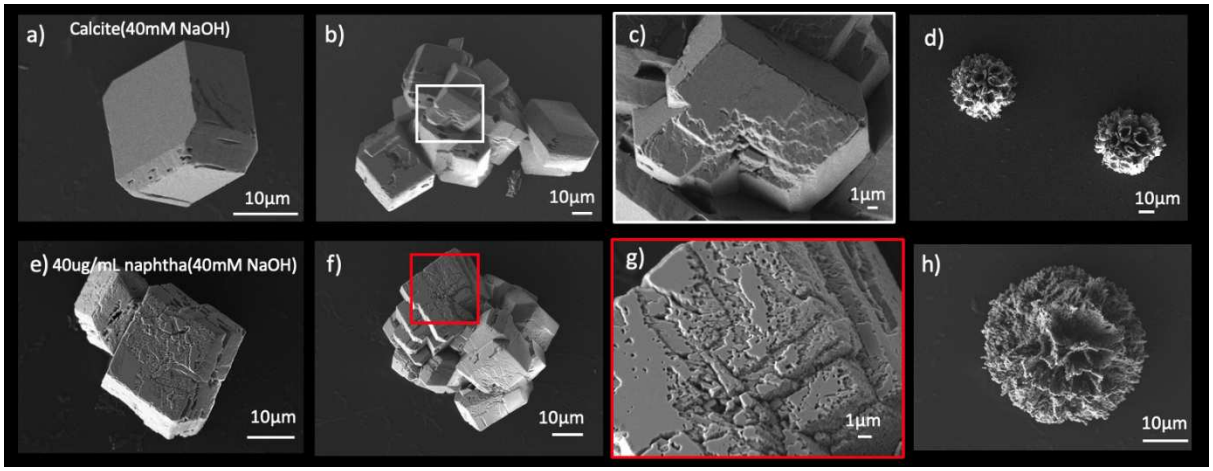

Figure 4.14. SEM micrographs were obtained on single crystal assay by vapor diffusion synthesis with 40 µg/mL naphthazarin in the presence of 40 mM NaOH. In the absence of naphthazarin a) single crystal, b) fused crystals, c) zoomed in on (b), d) different $CaCO_3$ polymorph. In the presence of naphthazarin e) single crystal, f) fused crystals, g) zoomed in on (f), h) different $CaCO_3$ polymorph.

4.2.2.2. Calcite-naphthazarin crystals obtained by direct precipitation M2 and M3

In Chapter 3, we observed that the surface defects were absent when SEM micrographs were obtained on samples filtered at 700 s (vaterite and calcite mixture) (see chapter 3, section 3.2.1.3). However, surface defects were present for samples obtained at 18 h. This observation indicated the significance of kinetics or the potential role of organic compounds in introducing defects during the transformation of calcite/vaterite mixture into calcite. Given that kinetics can play role in the modification of crystal surface, we therefore investigated the effect of naphthazarin on the calcite after synthesis was performed (2-3 days) (outside metrohm). We also analyzed the calcite obtained by heating of ACC (M4). This synthesis method was explored to follow the solid-state transformation of ACC into calcite. This crystallization routeway mimics the solid-state crystallization of ACC into calcite as observed in sea urchins.

The SEM-FEG micrographs on calcite in Figure 4.15a reveal the regular rhombohedral shape (euhedral calcite crystals) and smooth surface of the calcite crystals. The synthesis results in the broken edges of some calcite crystals due to stirring which exposes the inner morphology. The broken edges provided insights into the crystal formation mechanism i.e., it might be due to the attachment of small calcite blocks i.e. Kossel's model of a growing crystal surface (Mullin, 2001).The SEM-FEG micrographs of calcite+naphthazarin samples synthesized by

direct precipitation (M2) with different concentrations of naphthazarin (0.025-0.53 mM) revealed notable alterations in the surface of the calcite crystals (Figure 4.15). One of the prominent changes at 0.025 mM observed is the heightened roughness of the crystal surfaces although the shape of the crystal remained unchanged (Figure 4.15b). As the concentration of naphthazarin was increased to 0.53 mM, the shape of the crystals became distorted along with formation of edges as observed for vapor diffusion synthesis (Section 4.2.2.1) (Figures 4.15c-f). The roughness resembles pits with geometric shapes such as rhombohedral-shaped holes (Figure 4.15f). These surface irregularities can serve as indicators of two distinct phenomena: 1) Organic inclusions: some crystal holes or pores may stem from trapped organic inclusions, like pigment molecules, within the crystal during their formation Over time, as the crystal continues to form, these organic inclusions can create voids or openings on the crystal's surface (Page *et al*., 2008). 2) Calcite-shaped holes: alternatively, holes may form due to specific growth conditions, affecting certain crystal facets and leading to rhombohedral crystal-shaped holes (Orme *et al*., 2001).

The rhombohedral holes on the surface of the calcite can also be related to the concentration of naphthazarin, as only a relatively low concentration of naphthazarin resides within the crystal and the majority of naphthazarin seems to be adsorbed or bound to the surface of the $CaCO_3$ crystals. Moreover, the naphthazarin concentration incorporated values obtained for unbleached samples are very similar to that of ACC (discussed in Chapter 3). However, for bleached ACC and calcite samples, the values are very different suggesting that whatever gets incorporated or absorbed at the ACC stage does not get fully incorporated within the calcite. In our case, naphthazarin is associated with calcite, primarily through surface adsorption, with smaller concentrations being incorporated into the bulk.

Another hypothesis for the low concentration of naphthazarin to get incorporated could be due to π-π stacking of the naphthazarin molecules. The π-π stacking phenomenon involves attractive interactions between adjacent aromatic rings in molecules like naphthazarin. Its planar, aromatic structure enables these interactions. During $CaCO_3$ formation or crystallization, π-π stacking can prevent naphthazarin from integrating into the crystal lattice.

This interference can be attributed to the relatively stronger π-π stacking forces compared to the interactions between naphthazarin and the $CaCO_3$ lattice. As a result, naphthazarin molecules may prefer to stack together or adhere to the crystal surface rather than integrating into the $CaCO_3$ structure.

We also observed that for naphthazarin concentration 0.22 mM or higher (0.53 mM) leads to the crystallization of naphthazarin as a rosette of needles which can be seen in (Figure 4.16d-f) as already observed by light microscopy (see Figure 4.1 Section 4. 1.1). SEM micrographs revealed that they resemble more to flat rosette of fibres than to true needles. By performing EDX measurements on the needles, we observe higher carbon signal and very low calcium sigmal which indicates naphthazarin reprecipitate as needles. This precipitation of naphthazarin from the reaction mixture does corelate well with the hypothesis that at higher concentration naphthazarin might aggregate and hence hinder its ability to interact with $CaCO_3$ hence it destabilizes the ACC phase against crystallization.

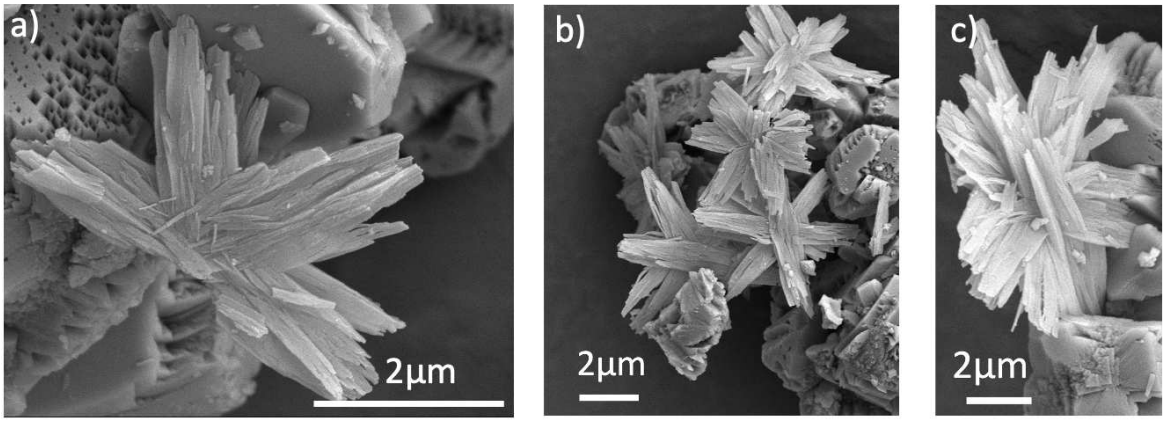

Figure 4.16. SEM micrographs obtained on calcite+0.53 mM naphthazarin(M2) showcasing the precipitated naphthazarin.

Our analysis of heated ACC samples at 200°C using SEM revealed a distinct contrast in the resulting calcite structure compared to its solution-derived counterpart in chapter 3. The heated calcite lacked a defined shape and comprised small crystalline nanoparticles (10-100 nm) that merged to form extensive structures (100-500 nm), reminiscent of $CaCO_3$ particle organization in corals (Figure 4.17). Interestingly when we examined the ACC samples heated to 400°C we observed that pure ACC structure remained unaffected however in presence of naphthazarin (0.11 and 0.53 mM) the ACC structure looked smooth instead of aggregation of small crystalline nanoparticles. These results indicate that heating of ACC at high temperature (400 °C) could result in the degradation of the naphthazarin which could result in contraction of ACC and hence smooth structure. However, at this stage we do not have a proper explanation for this phenomenon.

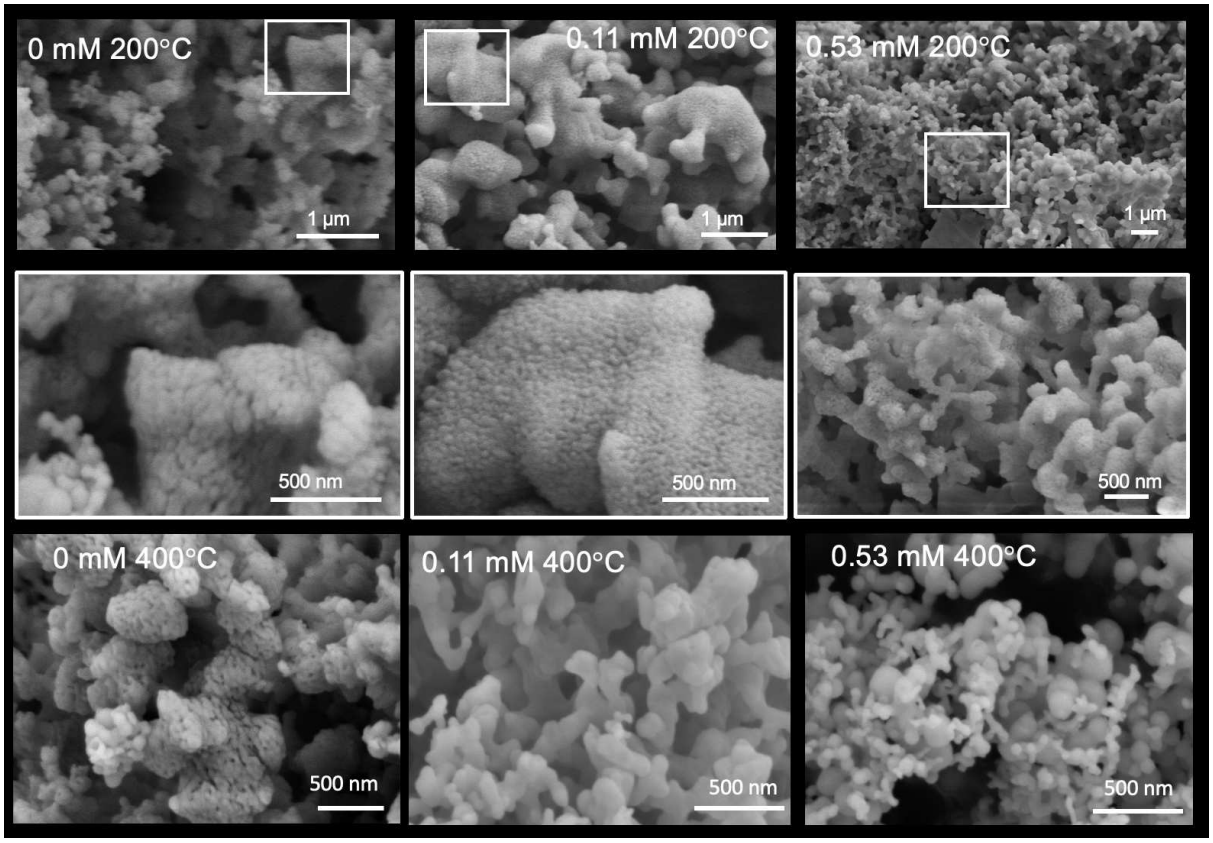

Figure 4.17. FEG-SEM micrographs of ACC, ACC+0.11 mM naphthazarin, and ACC+0.53 mM naphthazarin at 200 °C, Zoomed of micrographs obtained on samples heated at 200 °C, and 400 °C.

4.2.2.3. Calcite-naphthazarin crystals obtained by direct precipitation M3

We also explored how high pH and naphthazarin concentration can affect the calcite morphology by synthesizing calcite at pH 12.5 (M3). Indeed, it was show that at pH >12.0 the lifetime of ACC increases and it directly converts into calcite (Tobler *et al*., 2016) without the formation of vaterite as an intermediate as opposed to syntheses at pH <12. Figure 4.18, illustrates the pH profile during the $CaCO_3$ synthesized at pH 12.5 and the corresponding XRD diffractograms obtained on $CaCO_3$ filtered at 270 s and 570 s confirming the direct crystallization of ACC into calcite. The pH profile of this synthesis is quite different from the ACC synthesis at pH 10.5. Here, we observe an increase in pH upon ACC crystallization into calcite which opposite of synthesis at 10.5. It's important to note that in this context, the distinct increase in pH, indicates a fundamentally different system due to the presence of hydroxide ions (OH^-). This increase pH might also be linked to the decrease in the Ca^{2+} in the solution.

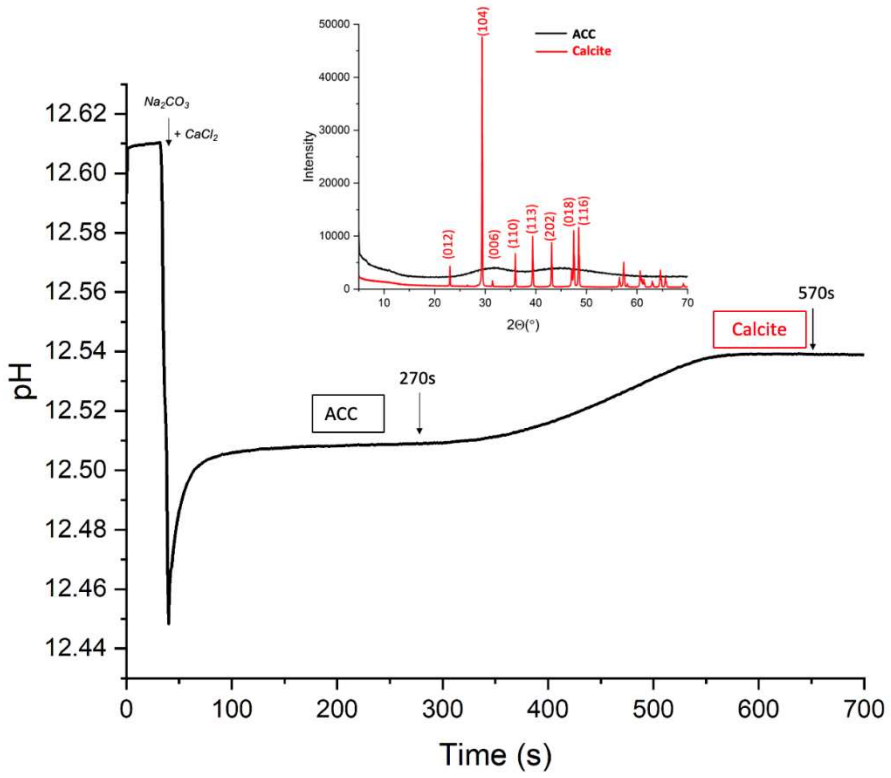

Figure 4.18. pH profile for the synthesis of $CaCO_3$ at pH 12.5 and XRD diffractograms obtained on $CaCO_3$ powder obtained a different time intervals, 270 s and 570 s.

Similarly, to fused crystals obtained by vapor diffusion at high pH (12.5), all crystals formed by M3 form aggregates, they appear to cluster into floral structures (Figures 4.19a and 4.19b). This distinct morphology indicates that the highly alkaline pH enviro nment had a significant influence on the crystal's growth pattern. In addition, the introduction of naphthazarin (0.11 mM and 0.53 mM) promoted the decrease in size of the individual crystals from 500 nm to 200-300 nm (Figures 4.19c-f). Notably, while naphthazarin played a role in modulating the size of these small, fused crystals, the surface characteristics of the calcite crystals remained unaltered. This phenomenon hints at the rapid kinetics of the synthesis process, where changes in crystal morphology take precedence over surface modifications.

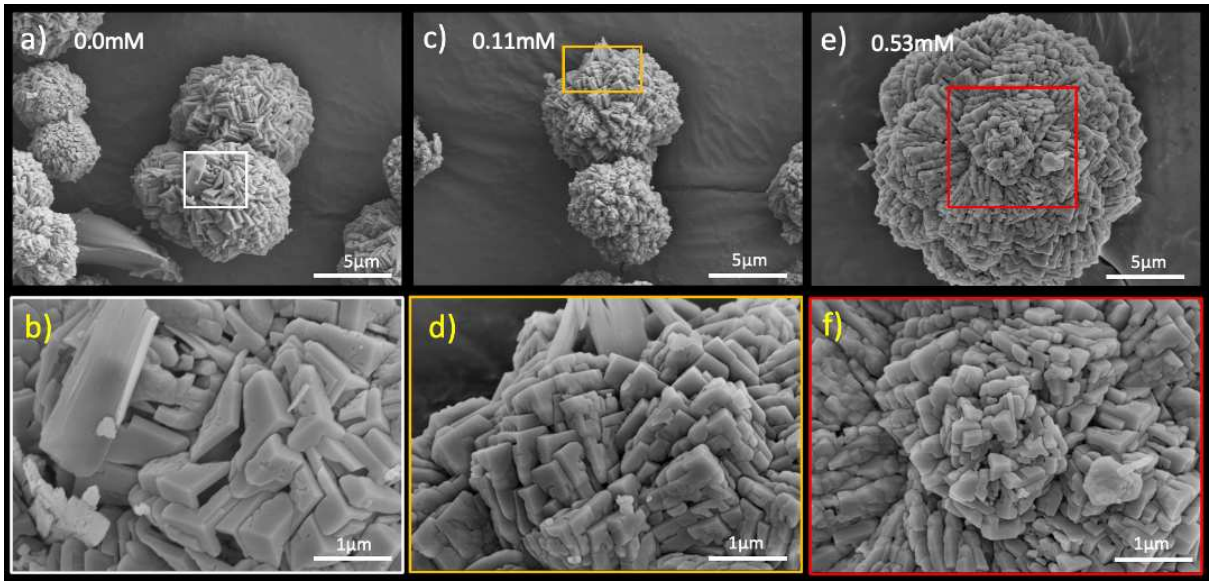

Figure 4.19. SEM micrographs on calcite synthesis at pH 12.5. a) Calcite, c) calcite+0.11 mM naphthazarin, e) calcite+0.53 mM naphthazarin. Zoomed region b) calcite, d) calcite+0.11 mM naphthazarin, f) calcite+0.53 mM naphthazarin.

Overall, these results on the crystal shape and morphology show that naphthazarin can have different effect depending on the concentration but also on the pH and the mode of the synthesis. Low concentrations of naphthazarin (10 µg/mL) modified the shape of the calcite crystals formed by vapor diffusion whereas higher concentration (40 mM) are needed to modify the surface of calcite obtained by M5. In calcite synthesized by M2 we observed the opposite trend as low concentration of naphthazarin (0.025 mM) modified the surface of the crystals without effecting the shape of the crystals and high concentration (0.53 mM) was required to induce changes in the surface as well as shape of the crystals. In case synthesis methods where direct crystallization ACC into calcite happens *i.e.,* 1) crystallization induced by heating, 2) synthesized at 12.5. In both cases the structure obtained will be quite different however one common factor was that the calcite structure was formed of smaller crystallites fused together. In former case we observed that the calcite structure was formed of small nano crystallites (200 °C) in the presence and absence of naphthazarin. However, at 400 °C we observe that presence of naphthazarin make the structure smooth compared to pure ACC. In the latter we observe that the presence of naphthazarin effects the size of the crystallites fused together. These results highlight the fact that the morphology of the calcite depends on various factor that change during the course of synthesis, such as kinetics, pH change, concentration of the organics, interaction between organics and Ca^{2+} ions.

Drawing parallels to previous investigations, such as those conducted by (Aizenberg *et al*., 1997; Berman *et al*., 1988), who scrutinized sea urchin macromolecules (1-10 μg/mL) via vapor diffusion synthesis, and the work of (Zou *et al*., 2020), who explored Poly(Aspartic acid) (pAsp) (1.5 wt%) through direct precipitation synthesis, we can infer that naphthazarin, might assume a multifaceted function during calcite growth. In particular, naphthazarin could potentially be adsorbed primarily on the surface of the calcite crystals, while also becoming occluded within the crystal. This dual interaction could lead to a combined effect on the surface and shape of the calcite crystals. The adsorption on the surface might hinder calcite nucleation, as seen in the case of pAsp, while the occlusion within the crystal lattice could lead to deformation, similar to the sea urchin macromolecules.

4.2.3. Spatial distribution of naphthazarin within the calcite crystals

To inspect the naphthazarin presence within the calcite crystals, different techniques and methods were employed. STEM analysis was performed on 60 nm lamella sections of calcite+0.53 mM naphthazarin_bleached prepared by ultramicrotomy. The analysis revealed distinct contrast patterns, with naphthazarin appearing as light contrast and calcite as dark contrast. This contrast discrepancy is due to variations in the electron density of these materials. Naphthazarin, with its lower electron density, appears as a lighter area, whereas calcite, having higher electron density, results in a darker contrast in the imaging. (Figure 4.20). This observation suggests that naphthazarin has been occluded or trapped within the calcite. These findings align with the research conducted by (Page *et al*., 2008) investigating the inclusion of organic entities (PEO-$(RGD)_5$) inside calcite, where they provided evidence of rhombohedral pores with sizes reaching up to 50 nm. Interestingly, these dimensions were slightly smaller on average than the hydrodynamic radius of the PEO-$(RGD)_5$ aggregates. In our case, we observed pore sizes ranging from 1 to 5 nm (arrows in Figure 4.20c), which could potentially be attributed to the aggregation of naphthazarin as naphthazarin is a few Angstroms.

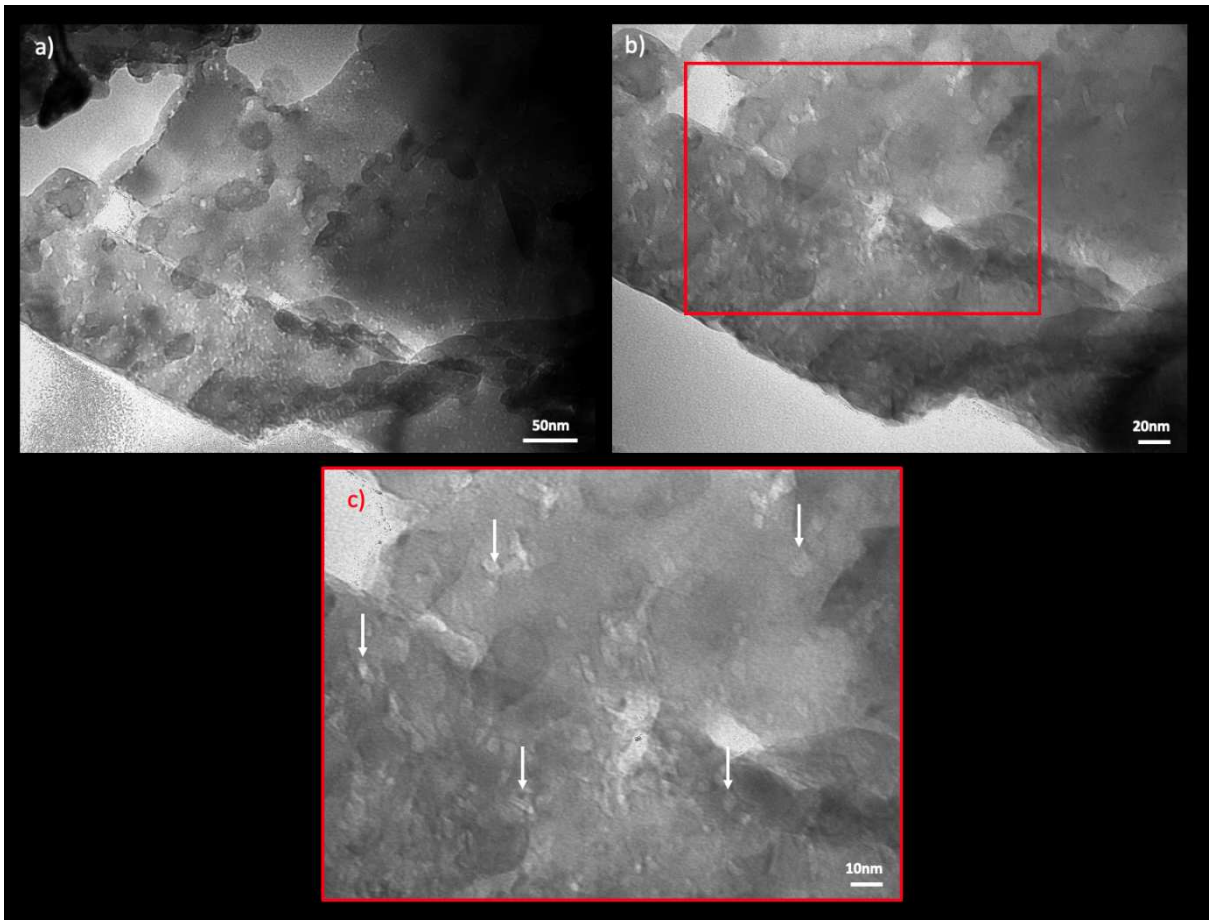

Figure 4.20. STEM analysis on sample Calcite+0.53 mM naphtha bleached for 2 h with 10% NaOCl observed on 60 nm sections. Arrows on micrograph (c) indicate lighter contrast due to the presence of naphthazarin.

FIB-SEM analysis allowed us to investigate the presence of naphthazarin occlusion within the calcite. This analysis was performed to achieve two goals: 1) to check for the organic occlusions within the calcite crystals, and 2) to have FIB lamella of 50-70 nm thickness for STEM-EELS analysis. FIB and ultramicrotomy yield different calcite sections due to the cutting methods. FIB uses an ion beam, offering precision and clean cut, while ultramicrotomy employs a blade, posing challenges with brittle calcite, often resulting in crystal breakage or uneven layers. The SEM micrographs from the FIB section (Figures 4.21a and 4.21b) revealed the presence of small pores (20-100 nm) within the calcite crystals. Importantly, some of these pores exhibited indications of being filled (Figures 4.21c and 4.21d), which could potentially be naphthazarin or artifacts generated during FIB lamella preparation. This observation

suggests that naphthazarin may be incorporated into the calcite matrix, occupying these void spaces and filling them partially or completely.

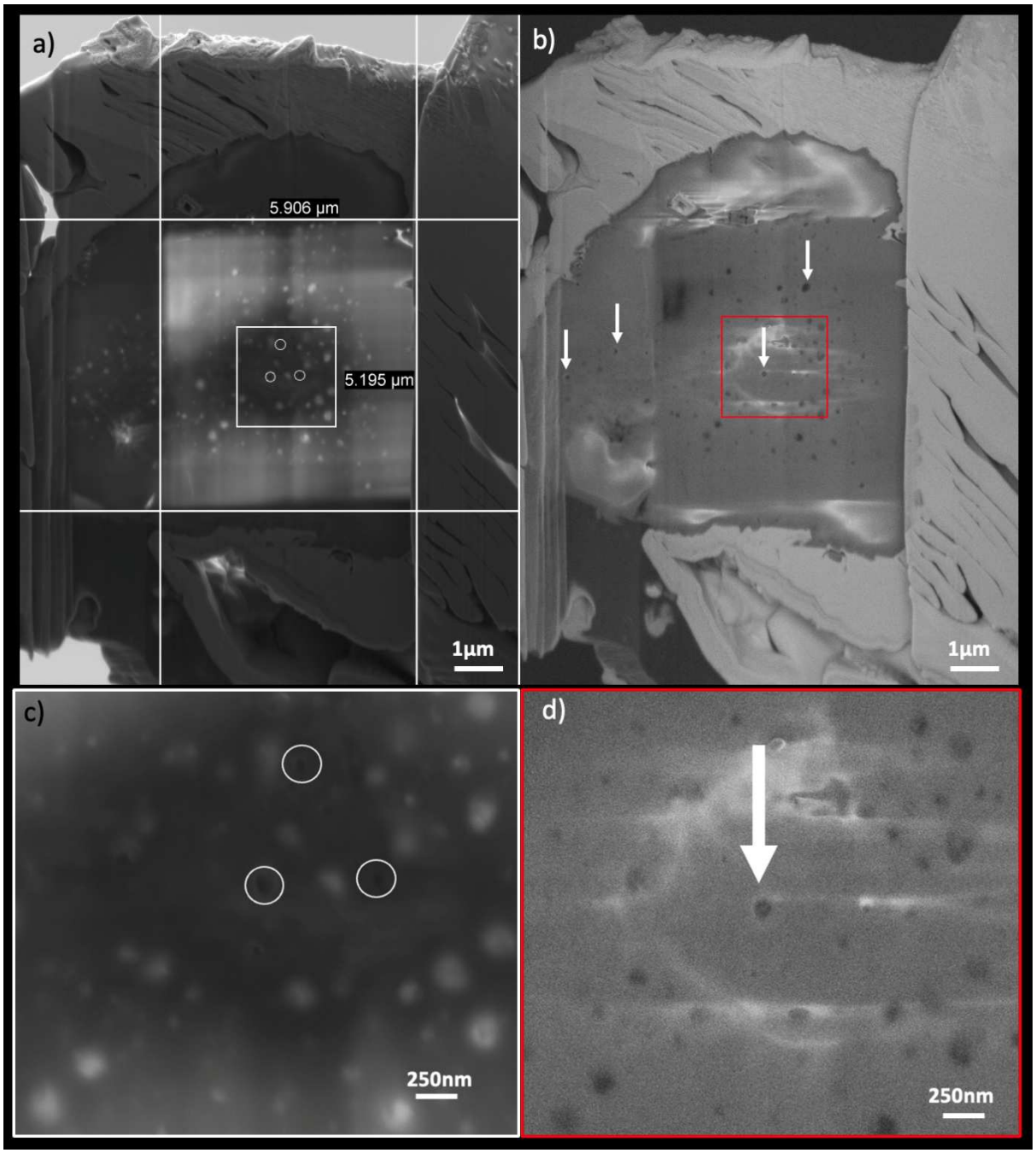

Figure 4.21. SEM micrographs of the FIB lamella section of calcite+0.53 mM naphthazarin of 60-70 nm thickness a), c) SE detector, b), d) ESB detector. c) and d) are zoomed-in views of an area on micrograph (a) and micrograph (c) respectively.

To confirm the pores indeed contained naphthazarin STEM-EELS analysis was first performed on lamella sections used for STEM analysis. This analytical technique, STEM-EELS, allowed

for precise examination at the nanoscale. By probing the interaction of high-energy electrons with the sample, STEM-EELS enabled the identification and characterization of organic compounds within the calcite matrix (de Frutos *et al*., 2023).

Firstly, STEM-EELS measurement was performed on naphthazarin to gather information about the reference (organic in calcite), and the dose-effect (Appendix 1 Table 1) was studied to reveal the degradation dose and peak evolution. This preliminary study aims to optimize the detection of naphthazarin. In the carbon region at a low dose of 10-100 e/Å^2 (Figure 4.22a), an amorphous carbon peak at ~285.1 eV, and three other small peaks in the region between 286 eV and 289 eV were observed for naphthazarin. The later peaks correspond to the organic carbon, which is due to naphthazarin, and the former peak corresponds to either carbon grid or organic decomposed into amorphous carbon under electron beam irradiation. With an increase in the dose to which naphthazarin is exposed, the carbon peaks generated by the naphthazarin evolve. As the dose was increased to 700 e/Å^2 the intensity of the 287.5 eV peak increased This peak is associated with the production of carbon monoxide by the degradation of naphthazarin under the electron beam. Further increase in dose led to a decrease in the intensity of organic peaks generated. The decrease in the intensity of peaks corresponds to the degradation of naphthazarin into amorphous carbon. Similarly, it was observed that in the oxygen region (Figure 4.22b), the increase in dose led to a decrease in the signal from the organic oxygen signal generated by naphthazarin at 541 eV and an increase in the signal generated by carbon monoxide located at 533.1 eV.

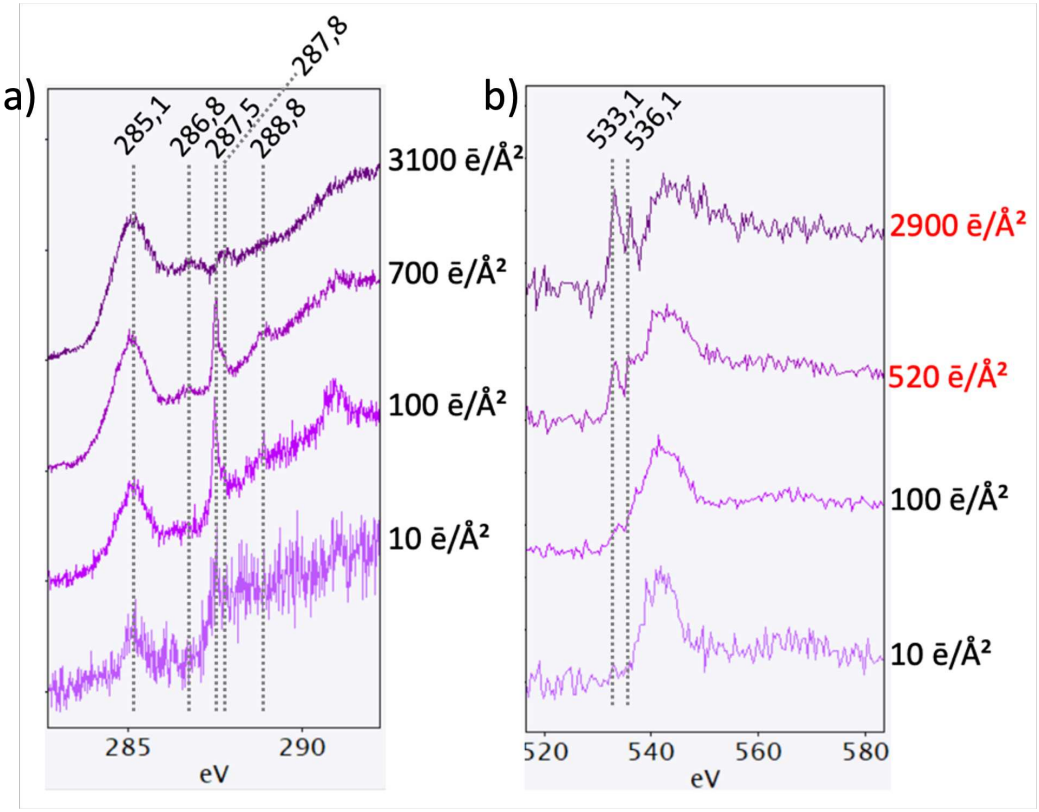

Figure 4.22. Effect of dose on naphthazarin a) peaks of naphthazarin generated in carbon region (C Kedge), b) peaks of naphthazarin generated in oxygen region (O K edge).

On calcite+0.53 mM naphthazarin specimens, at a very low dose of 10 e/Å^2, only signals from calcium (around 350 eV) and carbonate carbon (290 eV) were observed. The absence of a naphthazarin signal could be attributed to the low concentration of naphthazarin in the calcite sample. Increasing the dose to approximately 400 e/Å^2 resulted in the detection of an organic signal from naphthazarin. However, at this dose, the observed organic carbon signal originated from degraded organic matter. Unfortunately, the results obtained from the experiments conducted on sections of calcite+0.53 mM naphthazarin suggested that naphthazarin may have leached out during the sample preparation and settled onto the entire grid (Figure 4.23). Consequently, the presence of organic signals throughout the grid made it challenging to determine the exact distribution of naphthazarin in the calcite+0.53 mM naphthazarin.

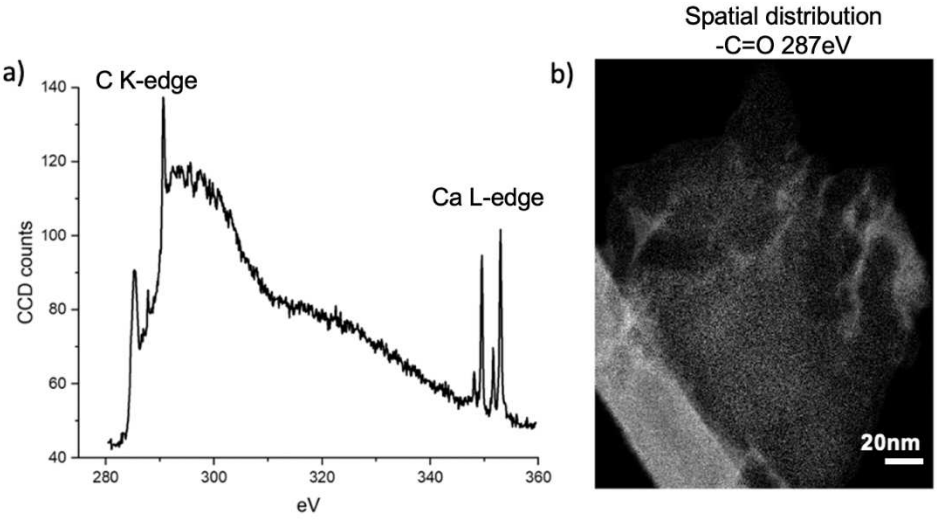

Figure 4.23. a) EELS signal on the thin part of the lamella section and b) the map of organic carbon of naphthazarin corresponding to 287 eV peak in the STEM-EELS spectra.

STEM-EELS analysis was also performed on a FIB lamella of calcite+0.53 mM naphthazarin to avoid the artifacts that could arise from sample preparation. STEM-EELS analysis performed on FIB lamella shed light on the presence of organic components within the calcite matrix. In the carbon region for calcite+0.53 mM naphthazarin, we observe an amorphous carbon signal at 285 eV and an organic carbon signal between 286-287 eV. This organic signal might be coming from the presence of C-OH, -C=C- of the naphthazarin. The carbonates are associated with the 290 eV peak and the Ca 2p doublet at a binding energy of 349 eV and 353 eV (Figure 4.24).

Our findings (Figures 4.24 and 4.25) revealed intriguing insights into the distribution of naphthazarin within the sample. It became evident that naphthazarin was indeed present throughout the sample, indicating its successful incorporation into the calcite (Figure 4.25). However, a noteworthy observation was the non-uniformity in signal intensity across different regions of the sample. This non-uniform distribution of naphthazarin within the calcite crystal has significant implications, suggesting potential aggregation of naphthazarin in some regions which could be due to variations in the degree of interaction between the organic compound and the mineral phase (Figure 4.24)

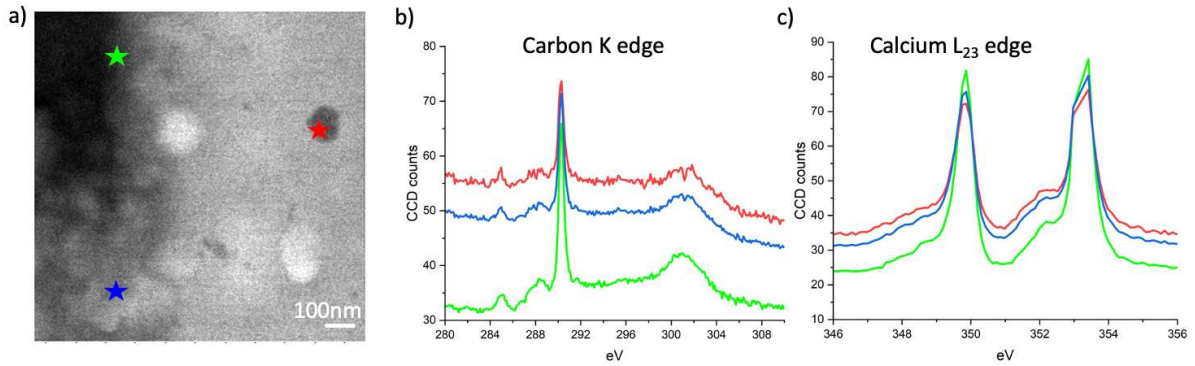

Figure 4.24. (a) HAADF image on FIB lamella of calcite+0.53 mM naphthazarin. (b) EELS spectrum in the energy range corresponding to the carbon K-edge for the different positions indicated by stars in (a). Three peaks were detected at about 285, 287.4, and 290.3 eV, associated with the presence of organic species (285 and 287.4 eV) and carbonate (290.3eV) respectively. (c) Spectra of the calcium L_{23}-edge for the same positions show two main peaks at 349.3 eV and 352.6 eV.

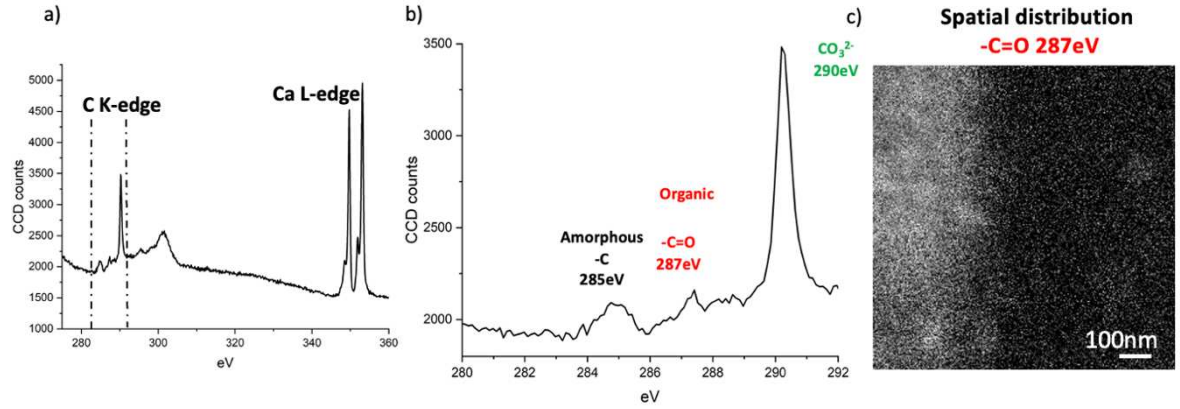

Figure 4.25. a) EELS signal on the FIB lamella of calcite+0.53 mM naphthazarin, b) zoomed spectra in the carbon region, c) the map of organic carbon of naphthazarin corresponding to 287eV peak in the STEM-EELS spectra.

4.3. Bulk naphthazarin-calcite interactions from the molecular to the atomic level

4.3.1. Molecular proximities between naphthazarin and calcite

The use of 2D ss NMR spectroscopy can offer insight into the local chemical enviro nment and molecular interactions between calcite and naphthazarin. Hence, 2D ^{1}H-^{13}C HECTOR spectra (recorded with ^{1}H homonuclear decoupling) were acquired to investigate the molecular proximities within the calcite-naphthazarin sample.

First, pure naphthazarin powder was investigated as a reference sample. The corresponding 2D ^{1}H-^{13}C HECTOR spectrum (Figure 4.26) reveals mainly intramolecular proximities within naphthazarin molecules as the 2D spectrum displays correlation resonances between all carbon moieties of the molecule (C-O at 173 ppm, =C-H at 134 ppm and quaternary carbons at 110 ppm) with two main proton resonances corresponding to =C-H (at $\delta(^{1}H)$ = 6.2 ppm; according to ^{1}H liquid state NMR, Chapter 3) and C-OH (at $\delta(^{1}H)$ = 11 ppm).

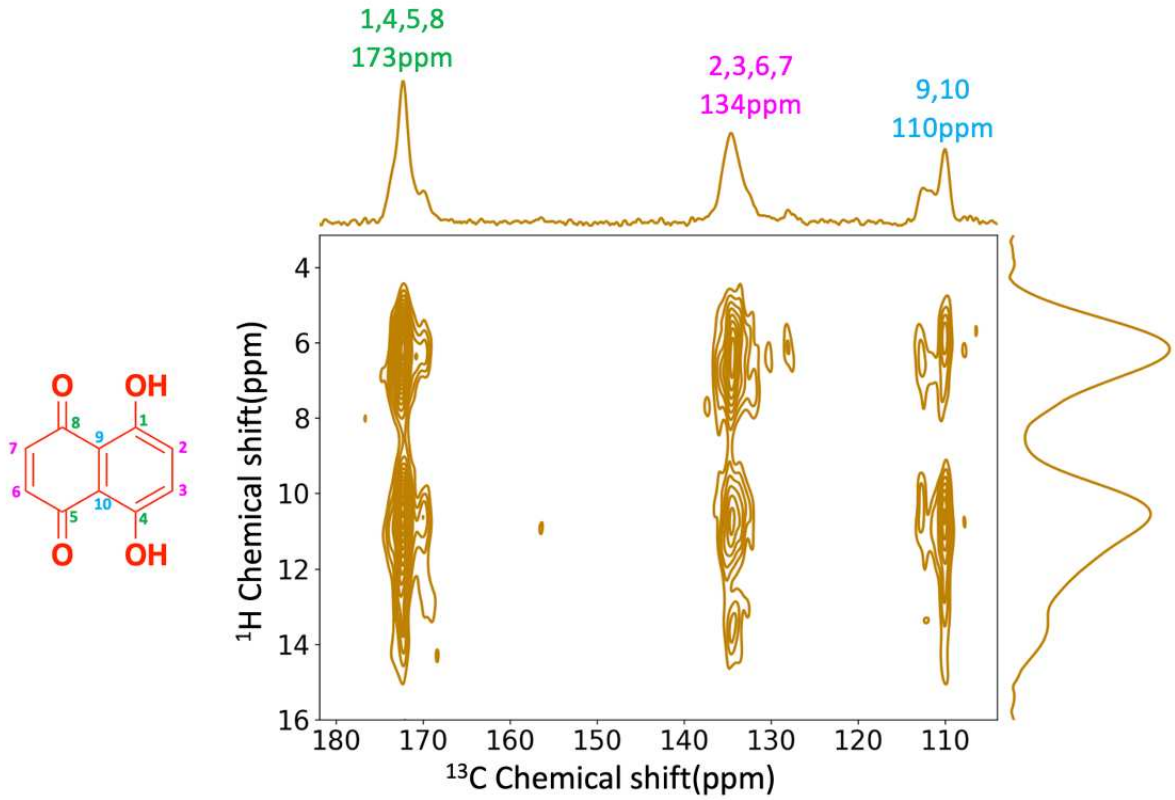

Figure 4.26. 2D ^{1}H-^{13}C H*ETC*OR spectrum of naphthazarin (contact time = 1 ms).

The 2D ^{1}H-^{13}C H*ETC*OR spectrum of calcite+0.53 mM naphthazarin is shown in Figure 4.27 displaying two main proton resonances coming from naphthazarin at $\delta(^{1}H)$ = 5.3 ppm and calcite at $\delta(^{1}H)$ = 7 ppm (at this stage the shift of the =C-H position compared to pure naphthazarin could be due to a different chemical enviro nment of naphthazarin within or adsorbed on calcite). Several important features can be highlighted:

- The two ^{13}C resonances in the carbonyl region at 178 and 170 ppm are belonging to naphthazarin indicating unambiguously that the latter does not correspond to carbonates.
- The -OH proton resonance from naphthazarin is now absent in the 2D indicating that the molecule is in a deprotonated form.
- Disordered carbonates from calcite at 168 ppm are also correlating with protons from naphthazarin.

In more detail, the carbonates in a disordered enviro nment display a main correlation with protons around 7 ppm that probably arises from structural water. But importantly, these disordered carbonates display also a correlation with protons from naphthazarin indicating a close proximity between the molecule and disordered/hydrated region of calcite.

The fact that naphthazarin in under a deprotonated form in the sample highlights the impact of the synthesis conditions, and the high pH in particular, on its final molecular state. This observation is in agreement with ^{13}C NMR data discussed in Chapter 3.

Finally, the 178 and 170 ppm resonances seem to arise from a splitting of the carbonyl resonance however the origin of two peaks and their respective positions are still unknown. The origin of 178 and 170 ppm peaks might be due to the deprotonation of naphthazarin resulting in the generation of chemically different carbonyl carbon atoms

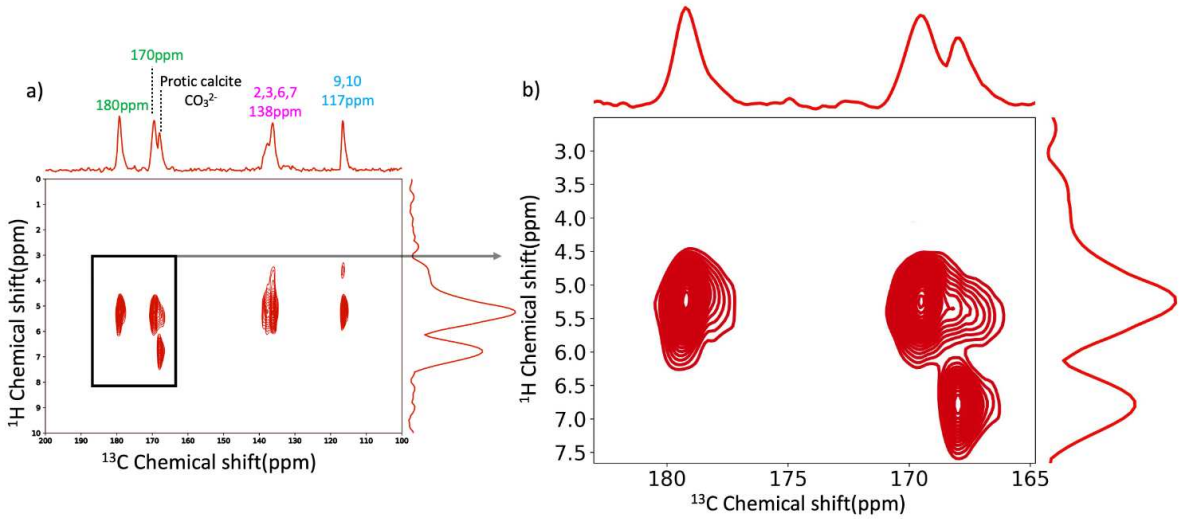

Figure 4.27. a) 2D ^{1}H-^{13}C H*ETC*OR spectrum of calcite+0.53 mM naphthazarin (contact time = 2s), b) zoom highlighting the carbonyl and carbonate region.

To get further understanding of the impact of the pH on the molecular state of naphthazarin, a 2D ^{1}H-^{13}C HETCOR spectrum (Figure 4.28a) has been recorded on naphthazarin at pH 13 (this naphthazarin sample was prepared by dissolving the molecule in aqueous solution at pH 13, then the sample was freeze dried). One single proton resonance corresponding to =C-H at $\delta(^1H)$ = 7 ppm is evidenced in agreement with the alkaline pH that is inducing the deprotonation of naphthazarin. However, alkaline pH is also inducing a significant broadening of the ^{13}C resonances, in particular for C-O and =C-H, due to multiple ^{13}C sites correlating with slightly different proton resonances (Figure 4.28 zoomed region). This observation could be linked to a partial degradation of naphthazarin at high pH that might also happen for the calcite+0.53 mM naphthazarin sample.

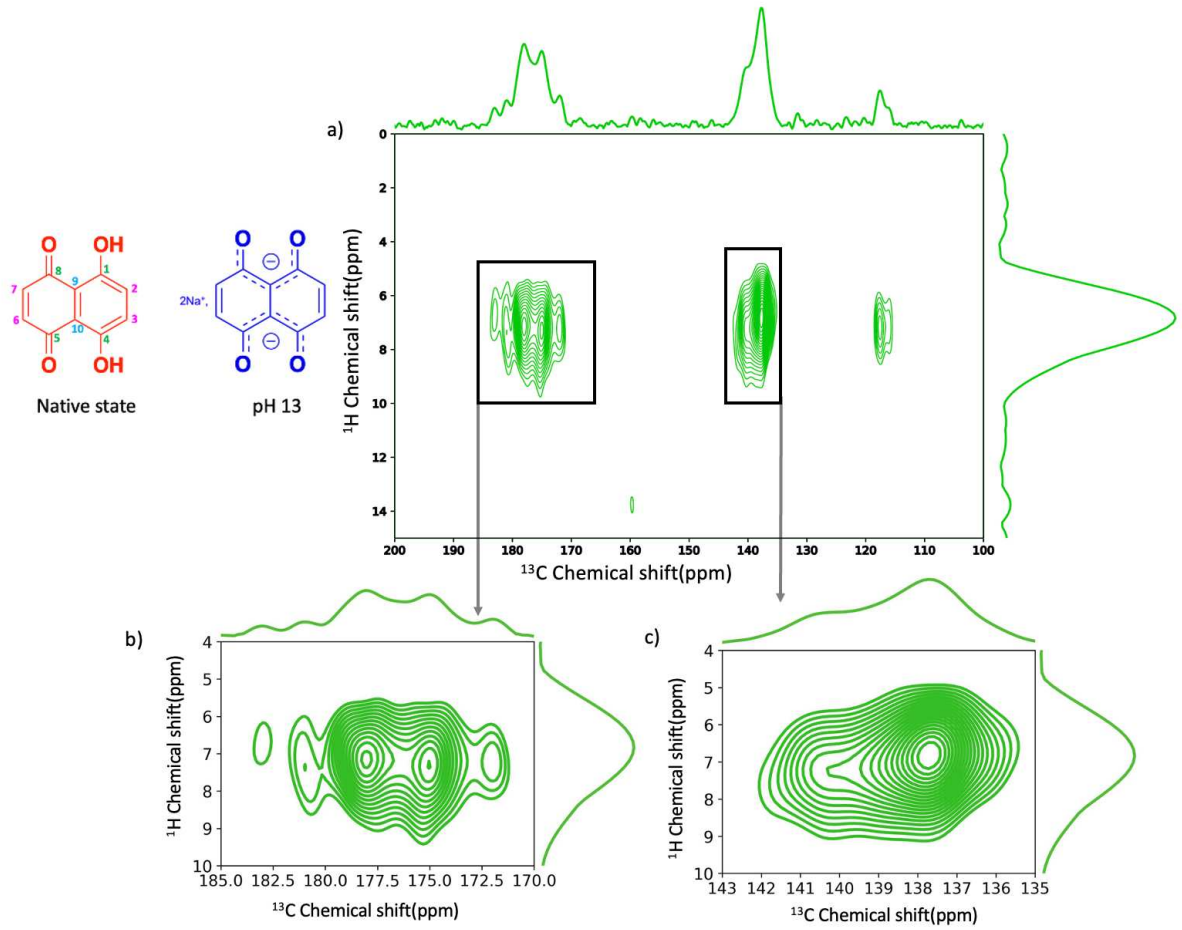

Figure 4.28. a) 2D ^{1}H-^{13}C H*ETC*OR spectrum of naphthazarin at pH 13 (contact time = 1 ms), b) zoom of the =C-H region, c) zoom of the carbonyl region.

As a conclusion, the molecular state of naphthazarin in calcite (and ACC) is strongly impacted by the synthesis condition and alkaline pH in particular. As a result, naphthazarin seems to be present in the deprotonated form in $CaCO_3$ even a partial degradation of naphthazarin into smaller organic units cannot be excluded.

4.3.2. Calcite lattice distortions in calcite-naphthazarin crystals

HR-XRD measurements combined with Rietveld refinement analysis were employed to investigate the possible impact of naphthazarin incorporation in calcite on the crystal lattice parameters, and thus lattice distortions. As discussed earlier, 0.025-0.055 mM of naphthazarin gets incorporated in calcite crystals obtained by M2 when synthesis is performed in the presence of 0.55 mM naphthazarin and possibly in the form of aggregates (nano-inclusions) as evidenced by STEM analysis. By comparing the diffractograms of various samples, including

calcite, calcite+0.11 mM naphthazarin, and calcite+0.53 mM naphthazarin, specific peaks, such as (104), (006), and (110), were meticulously examined with the specific aim of assessing how the naphthazarin impact the c and a parameters of the calcite unit cell (Figure 4.29).

Surprisingly, the introduction of naphthazarin into the calcite crystals did not cause any significant peak shifts. Through Rietveld refinement (Appendix 1 Table 2), a-, and c- lattice parameters were extracted and lattice distortions, $\Delta c/c$ were calculated with respect to synthetic pure calcite. The results revealed that the lattice distortion in the c-axis direction ($\Delta c/c$ = 0.0017) was negligible in comparison to the one found in sea urchin spines (0.04-0.05%) (Albéric *et al*., 2018) and mollusks (0.2 %) (Pokroy *et al*., 2006), or even in synthetic calcite samples synthesized in the presence of amino acids (0.01-0.15 %) via vapour diffusion synthesis and hydrothermal synthesis. (Borukhin *et al*., 2012).

Nonetheless, the introduction of naphthazarin into the system did result in the small broadening of the diffraction peaks. However most broadening of peaks was observed for samples prepared by physical mixing and in case of calcite-naphthazarin samples it does not follow any linear trend with respect to naphthazarin concentration. We observed higher broadening for calcite+0.11 mM naphthazarin in comparison to calcite+0.53 mM naphthazarin. Moreover, the broadening phenomena were not homogenous for all peaks. This broadening phenomenon can typically be ascribed to two primary factors: the reduction in the size of coherently scattering crystalline blocks and an increase in microstrain fluctuations (Pokroy *et al*., 2006). These alterations can be linked to several underlying causes. Firstly, the presence of naphthazarin might induce a reduction in the size of amorphous calcium carbonate (ACC) particles, consequently affecting the coherence of crystalline domains. Secondly, the mild annealing treatments applied during the experiment could lead to the degradation of intra-crystalline organic macromolecules, further contributing to the observed broadening of diffraction peaks (Zou *et al*., 2020). The broadening effect was the highest in samples prepared by physical mixing, it might be due to the grinding of calcite particles to smaller sizes. (Lang *et al*., 2020) observed the absence of lattice distortion when calcite was synthesised in presence of glucose (0.15 M) by hydrothermal synthesis. They postulated that the absence of lattice distortion might be due to the absence of acidic groups in glucose.

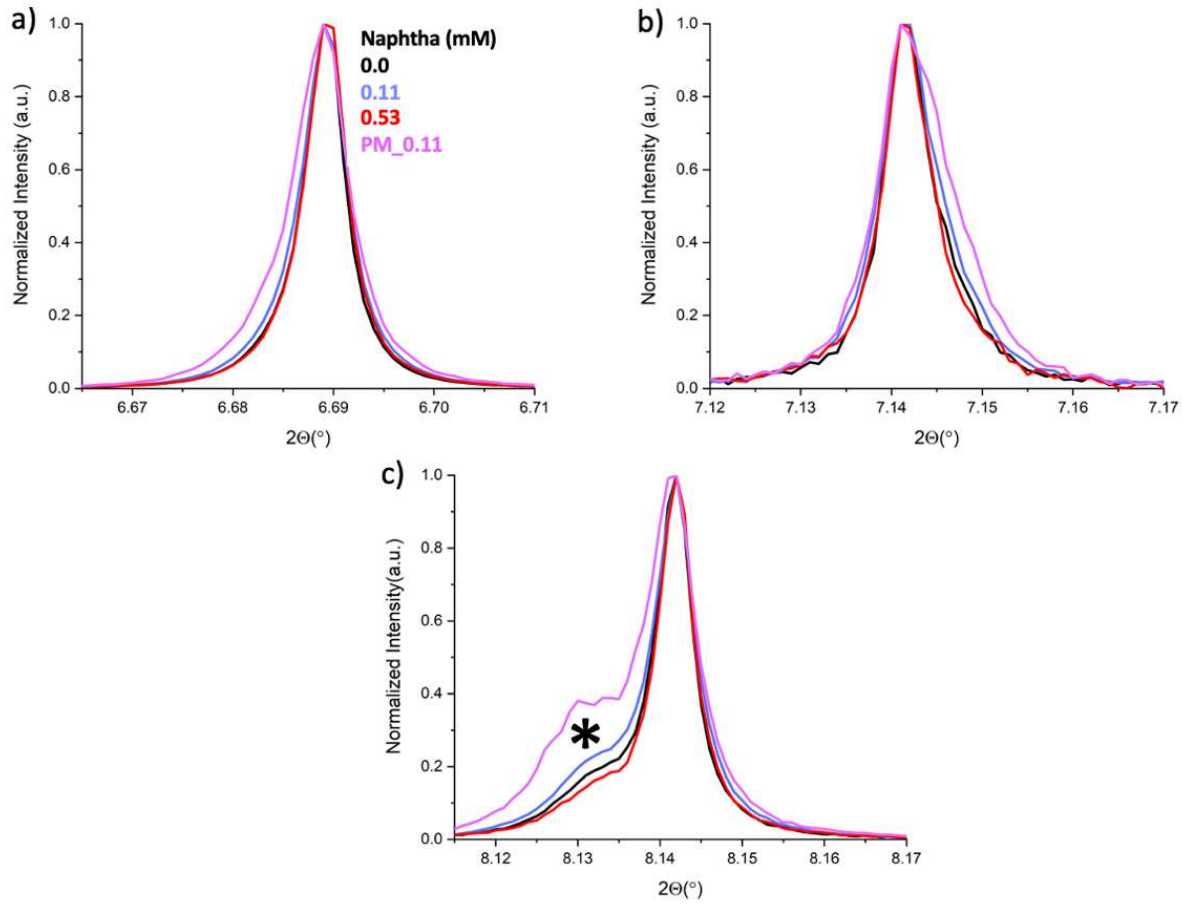

Figure 4.29. HR-XRD diffractograms with normalized intensity for colored calcite synthesized at pH 11.4. a) (104) peak, b) (006) peak, c) (110) peak.

The investigation of naphthazarin incorporation and its effects on the calcite crystal lattice was extended through *in-situ* heating HR-XRD experiments (Figure 4.30). Surprisingly, the presence of naphthazarin did not induce significant lattice distortions even during the destruction of organics within the lattice. Typically, the introduction of organics in the lattice causes distortions, and upon their degradation, the lattice returns to its relaxed state, offering insights into their presence and impact on lattice distortion. However, in this case, the calcite lattice remained unaffected by the presence of organics suggesting that the naphthazarin might be located within the crystal structure of calcite without significantly affecting the arrangement of calcium and carbonate ions in the crystal lattice. We do observe the broadening of (006) and (110) peaks as temperature increased to 200 °C which could be either due to macrostrains within the lattice as in the case of *ex-situ* 400 °C the broadening decreases in comparison to 200 °C (Figure 4.30). A point worth noting is the absence of lattice distortions, could also be

attributed to a relatively low concentration of naphthazarin within calcite as it is expected that only 5-10 % of naphthazarin of the total gets incorporated within calcite.

Similarly, XRD diffractograms obtained on calcite obtained by heating the ACC to 400 ºC (Figure 4.31) revealed that the solid-state transformation of ACC in the presence of naphthazarin to calcite does not result in lattice distortion suggesting the in case of naphthazarin irrespective of solid-state crystallization or dissolution/precipitation crystallization naphthazarin does not significantly affect the lattice structure.

Interestingly, during the analysis, an additional peak was observed alongside the (110) peak (Figures 4.29c and 4.30b), indicating the potential existence of another phase or differently shaped calcite within the system. Remarkably, this extra peak was found even in the pure calcite samples, raising questions about its origin. During *in-situ* measurements, it was observed that at 200 °C, the additional peak associated with the (110) peak vanished, suggesting the possibility of phase conversion to calcite or the complete transformation of differently shaped crystals into rhombohedral calcite or it could be due to the presence of different sizes or different shapes of crystals and upon heating they disappear forming rhombohedral calcite.

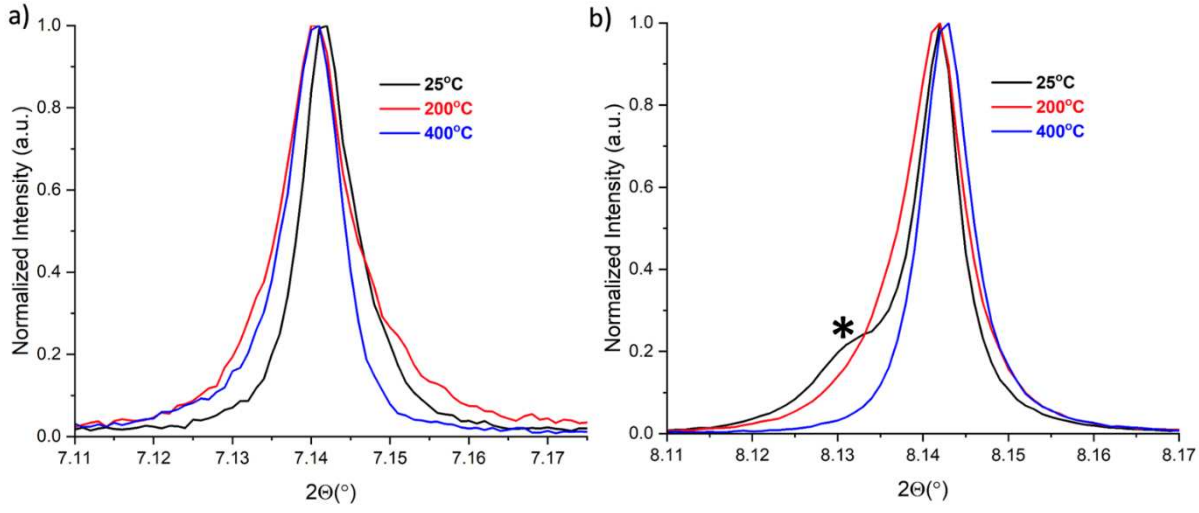

Figure 4.30. *In-situ* heating HR-XRD diffractogram with normalized intensity, a) (006) peak, b) (110) peak for calcite+0.11 mM naphtha at 25 ºC, 200 ºC, and *ex-situ* 400 ºC.

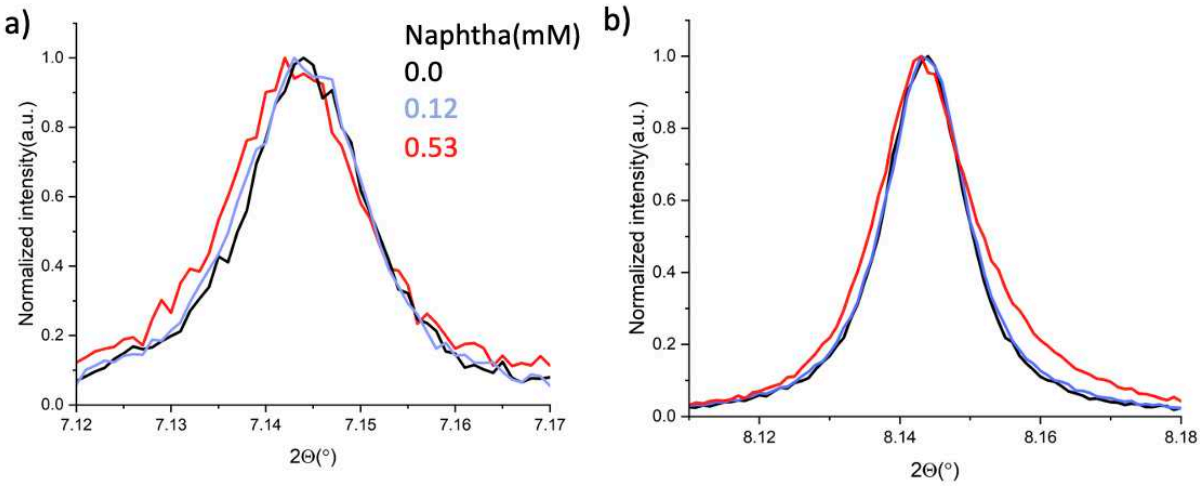

Figure 4.31. *Ex-situ* heating HR-XRD diffractogram with normalized intensity, a) (006) peak, b) (110) peak for different concentrations of naphthazarin

To further investigate the additional peak associated with the (110) peak due to the presence of different sizes of crystal SEM observations were performed on calcite-naphthazarin heated to 400 ºC. The SEM micrographs (Figure 4.32) revealed that the heating did not affect the small crystals, confirming that the additional peak associated with (110) was not because of the crystal size.

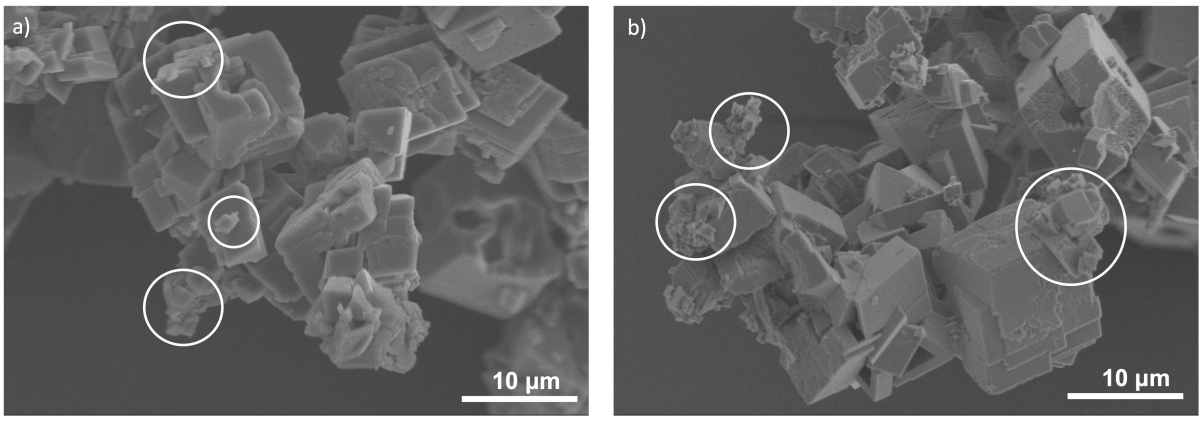

Figure 4.32. SEM micrographs on a) calcite at room temperature, b) calcite annealed at 400 ºC.

Interestingly we did observe the presence of another phase similar to ACC during the STEM-EELS analysis performed on lamella sections prepared by FIB-SEM (Figure 4.33). In Figure 4.33, in the Ca $L_{2,3}$-edge spectrum, we can observe four well-defined peaks (blue spectra) that correspond to the crystal field splitting of the L_2 and L_3 lines confirming the presence of calcite.

In contrast, we notice two distinctive peaks along with two accompanying shoulders (red spectrum) suggesting the presence of ACC (Albéric *et al*., 2019). The presence of an amorphous phase evidenced by STEM-EELS analysis could provide an explanation for the presence of an additional peak associated with the (110), which upon heating converts to the crystalline phase resulting in the disappearance of the peak.

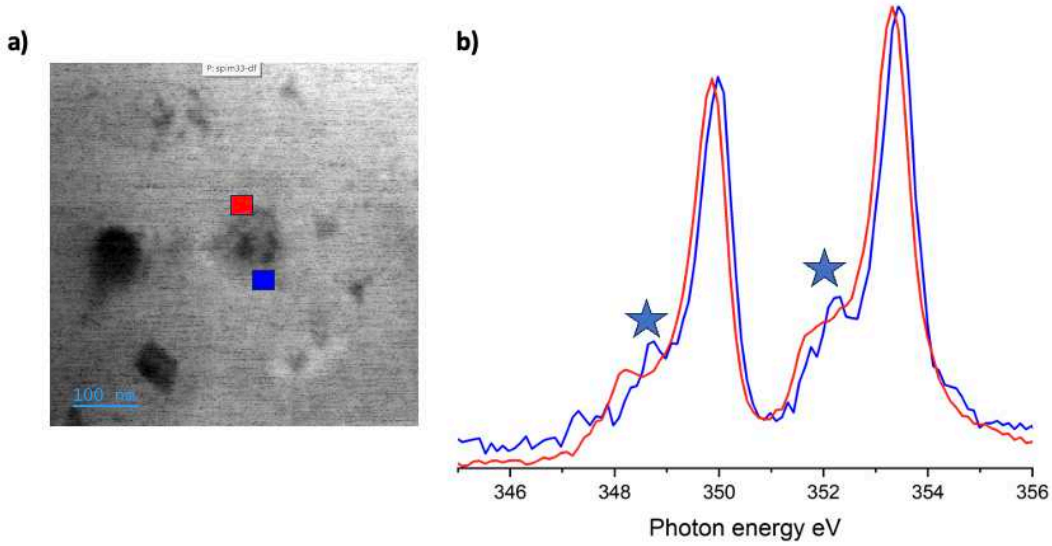

Figure 4.33. STEM-EELS analysis on FIB lamella of calcite+0.53 mM naphthazarin, a) HAADF image, b) Ca L-edge region.

It has also been evidenced by (Borukhin *et al*., 2012) that the method of synthesis can affect the lattice distortion induced by the additives. As a result, we performed the synthesis of calcite in the presence of amino acids (glycine and aspartic acid) with a concentration similar to that of naphthazarin. The HR-XRD diffractograms of various samples, including calcite, calcite+0.11 mM aspartic acid/glycine, and calcite+0.53 mM aspartic acid/glycine, revealed that even amino acids did not introduce lattice distortions (Figures 4.34a and 4.34b). These findings were further supported by performing *ex-situ* heating experiments on calcite+0.11 mM aspartic acid. The results revealed that the degradation of organics by heating the samples did not result in significant lattice distortion (Figure 4.34c). An additional peak was observed alongside the (110) peak similar to that observed in calcite and calcite-naphthazarin. At 200 °C, the additional peak associated with the (110) peak vanished which aligned with the previous findings (Figure 4.34d).

For the absence of significant lattice distortions in our case, we also have to take into consideration that the concentration of amino acids used by (Borukhin *et al*., 2012) was many folds higher than we used in our synthesis. These findings suggest that the absence of lattice distortion could either be due to the method of synthesis (direct precipitation M2) or due to the very low concentration range for additives used during the synthesis of crystalline $CaCO_3$.

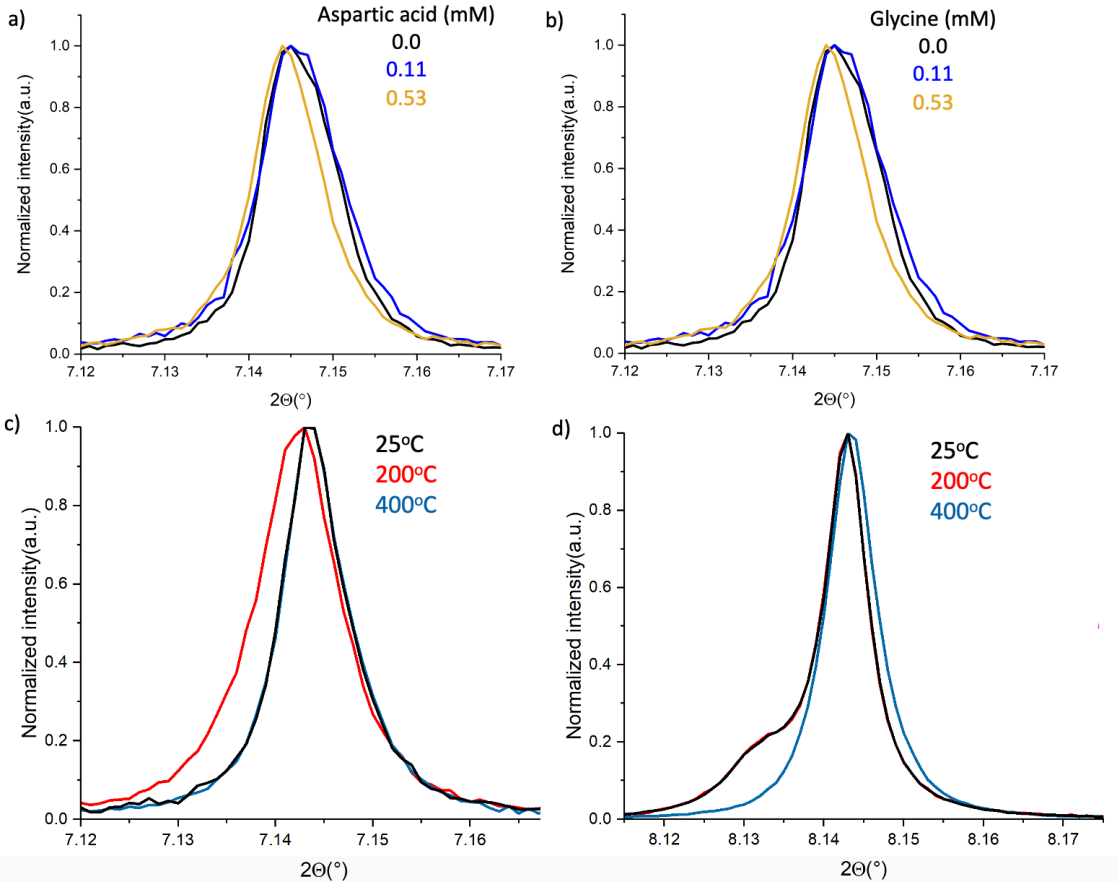

Figure 4.34. HR-XRD diffractogram ((006) peak) with normalized intensity for calcite synthesized in the presence of a) aspartic acid, and b) glycine. *Ex-situ* heating HR-XRD diffractogram with normalized intensity for calcite synthesized in the presence of 0.11 mM aspartic acid, c) ((006) peak, d) (110 peaks)).

In summary, HR-XRD analysis combined with Rietveld refinement provided valuable insights into the effect of naphthazarin incorporation on the crystal lattice parameters of the investigated samples. The absence of peak shifts, minimal lattice distortion, and broadening of peaks were observed. *In-situ* heating experiments further confirmed the absence of significant lattice distortions induced by naphthazarin. Additionally, the presence of an additional peak hinted at the possibility of another phase or differently shaped calcite within the system. Further

investigations, including *in-situ* heating experiments, shed light on small lattice distortions induced by the presence of pigments, indicating potential phase transformations within the calcite crystals.

Raman spectroscopy technique was also used to confirm that naphthazarin was residing within a calcite lattice structure. It provides information about the vibrational modes and chemical bonds present in a material, making it ideal for detecting subtle alterations caused by pigment incorporation. Thus, by looking at carbonate-associated bands, we can gain insights into the structural changes and interactions occurring within the crystal lattice. The Raman spectrum of calcite (Figure 4.35) revealed several characteristic peaks associated with its crystal structure;

- ν1 mode at 1086 cm^{-1}: This strong peak corresponds to the symmetric stretching vibration of the CO_3^{2-} ions in the calcite lattice.
- ν2 mode at 712 cm^{-1}: This band corresponds to the bending vibration of the CO_3^{2-} ions in the calcite lattice.
- ν3 mode at 282 cm^{-1}: This peak is associated with the asymmetric stretching vibration of the CO_3^{2-} ions.

We observed shifts in Raman spectra peaks (ν1 mode) in the case of calcite+0.11 mM naphthazarin to lower wavenumber from 1086 to 1084 cm^{-1} (Figure 4.35b), indicating expansion of calcite lattice upon occlusion of naphthazarin. Crystal lattice expansion results in lower-frequency (redshift) Raman bands due to longer bond lengths and weaker bonds. Conversely, lattice contraction leads to higher-frequency (blueshift) Raman bands, reflecting shorter bond lengths and stronger bonds. These results suggested that naphthazarin induces modifications in the crystal symmetry or chemical environment around it.

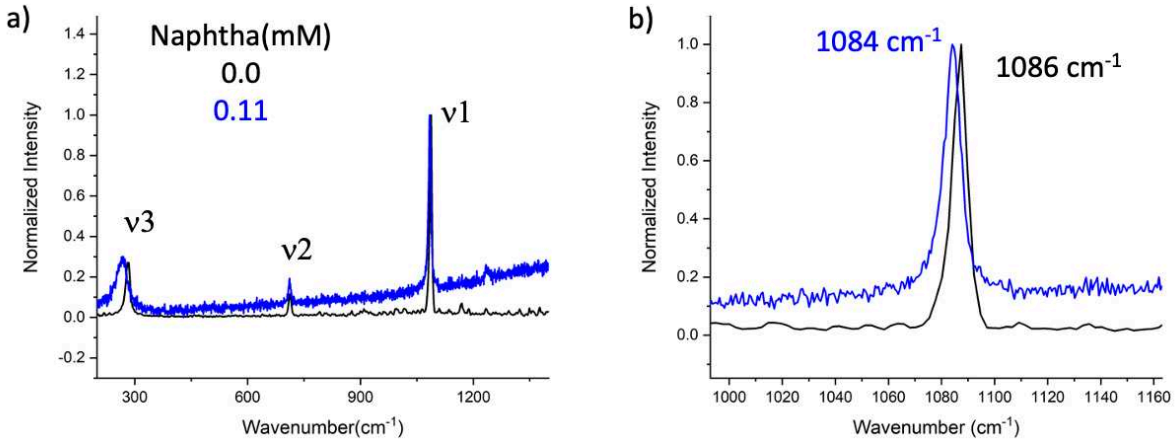

Figure 4.35. a) Raman spectra on calcite (black color) and calcite+0.11 mM naphthazarin (blue color), b) zoom of the ν1 mode region.

However, we also evidenced through experiments conducted by varying the laser power which revealed that these shifts in the Raman peaks could be primarily attributed to the absorption of energy by the organic naphthazarin molecules. With an increase in laser power, the ν1 mode peak shifted to a lower wavenumber (Figure 4.36), suggesting the absorption of energy by organic molecules. This absorption of energy induces changes in the lattice vibrations and, subsequently, the Raman spectra. In the calcite sample, this pattern did not hold, as an increase in laser power did not influence the peak position, as the peak remained stable at 1086 cm^{-1} even when the power reached 20 mW (Figure 4.36). These studies revealed that naphthazarin might be occluded within the calcite without affecting the lattice of the crystal.

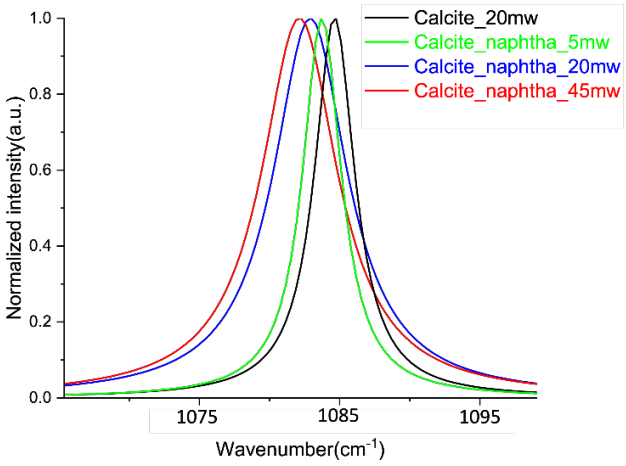

Figure 4.36. Raman spectra in the ν1 mode region of calcite with varying laser power.

Our observations established a direct correlation between naphthazarin concentration and resulting calcite color, with higher concentrations yielding darker hues. The naphthazarin-calcite hybrid system showed remarkable stability and retained colour up to 400 ºC. Naphthazarin also influenced crystal shape, leading to elongated structures. Predominantly naphthazarin was surface-bound, around 5-10 % of naphthazarin incorporated into calcite depending upon the initial concentration of naphthazarin in reaction mixture. The presence of naphthazarin on the surface causes irregularities and rhombohedral crystal-shaped voids. The effect of naphthazarin on calcite morphology varied with synthesis route, solvent, concentration, and pH. STEM-EELS analysis showed non-uniform naphthazarin distribution

within calcite, and NMR suggested the presence of a deprotonated naphthazarin form. Interestingly, incorporation did not significantly distort the lattice, possibly due to low concentration. Figure 4.37 provides a overview of the key findings outlined in Chapter 4.

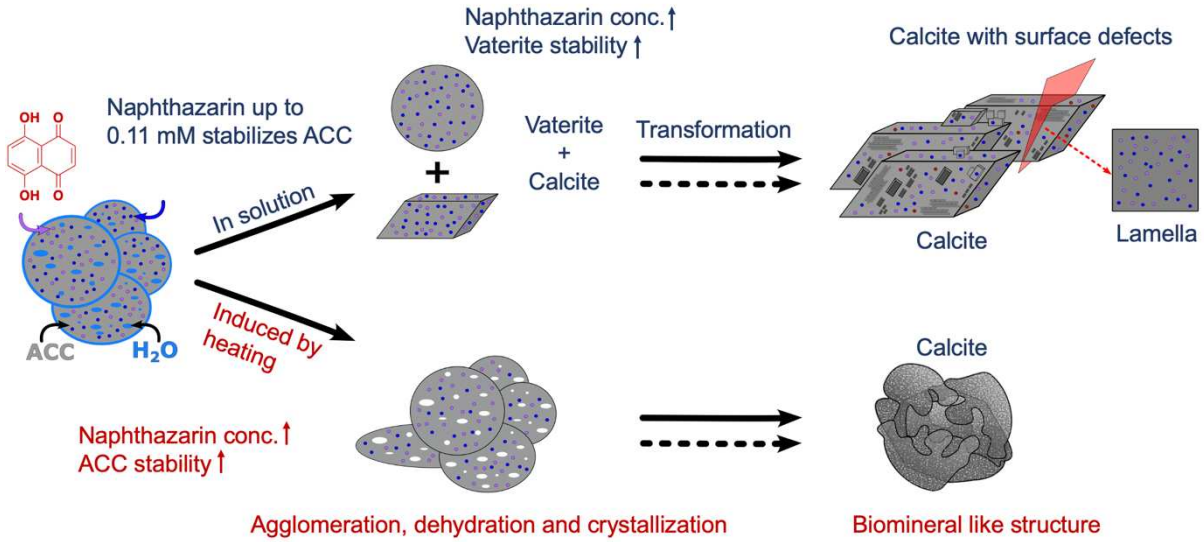

Figure 4.37. Proposed scheme summarizing the $CaCO_3$ formation, crystallization (in solution vs in air by heating), effect of naphthazrin on polymorph stability, morphology and naphthazarin association with $CaCO_3$ of naphthazarin.

5

$CaCO_3$-naphthoquinone biohybrid pigments

In order to further understand the importance of (poly)hydroxylated-naphthoquinones in biomineralization in sea urchins and develop biohybrid pigments for coloration applications, this chapter considers two more commercially available natural naphthoquinones as well as naphthazarin: lawsone and juglone and six biogenic extracted PHNQs from sea urchins (Figure 5.1). The variety of these compounds, in particular in terms of their -OH group's number and position allow us to study the impact of these molecular structures on the color, the structure, and the morphology of ACC nanoparticles as well as of calcite crystals. From this study, we can for example propose some possible explanation why some PHNQ molecules are preferentially incorporated into sea urchin skeletons over others while all being synthesized in the red spherule cells. Additionally, we investigate how the conditions of synthesis (solvent and kinetics) of a reaction can play a pivotal role in the incorporation and interaction of some

pigments within the ACC matrix and thus the intensity of the final color of the hybrid pigments. Finally, this chapter also introduces the initial exploration of naphthazarin, PHNQs, and biohybrid pigments in the context of dyeing various types of textile fibers.

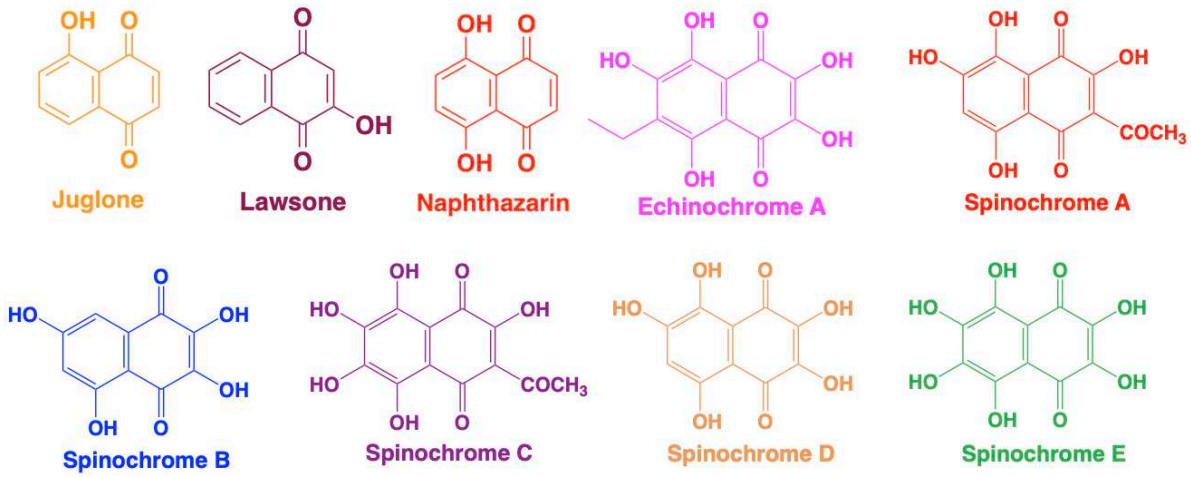

Figure 5.1. Different naphthoquinone molecules studied in this chapter.

5.1. CaCO$_3$-lawsone/-juglone hybrid pigments

5.1.1. Halochromic properties of lawsone and juglone

We explored the other commercially available naphthoquinones to get insight if the structure of the molecule can have an effect on ACC formation as well as crystallization in calcite. Additionally, lawsone and juglone are halochromic dye similar to naphthazarin but exhibit different colors which provides potential for differently colored biohybrid pigments.

Lawsone and juglone exhibit an array of colors in response to changes in pH (Figure 5.2). In particular, lawsone gives rise to intense orange colors in aqueous solutions at pH > 5 whereas at around pH 4, light orange shades are observed and at pH 3, a yellow color is obtained (Figure 5.2). Similarly, to naphthazarin color changes (Chapter 3, section 3.4), this shift in color is attributed to different protonation states (refer to Figure 1.24). However, here one protonated form (lawsone+) is in addition observed at pH <3. Around pH 4 the neutral (lawsone) form is the main one present whereas at pH > 5 it is the deprotonated form (lawsone$^-$) (Hashem *et al.*, 2000).

Juglone, on the other hand, presents a beetroot red color at pH > 9.5 whereas at around pH 9, it changes to red, at pH 8.5 it adopts an orange tint and at pH < 6, it is yellow (Figure 5.2). We attributed these color changes to different protonation states as well: for pH < 7, juglone exists mainly in its protonated form (juglone +), for 7<pH<8 it remains in its a neutral form (juglone). and for pH > 9 it is deprotonated (Hashem *et al*., 2000).

The study of these color changes according to pH is therefore due to the protonation and deprotonation processes of lawsone and juglone which provides valuable insights into how these compounds may further interact with Ca^{2+} and CO_3^{2-} ions in solution and therefore impact ACC and calcite color, composition and structure as compared to naphthazarin.

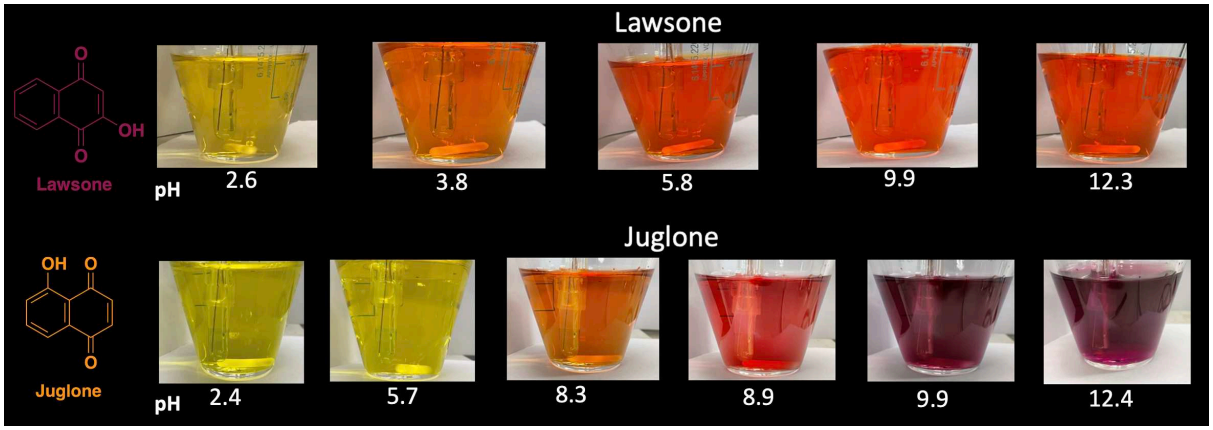

Figure 5.2. The color changes observed in lawsone and juglone within an aqueous enviro nment in response to varying pH levels.

5.1.2. Effect of lawsone and juglone on ACC stability

5.1.2.1. Crystallization in solution

To investigate how lawsone and juglone influence the stability of ACC against crystallization in solution, we conducted experiments akin to those discussed in Chapter 3, Section 3.2.1. pH profiles during ACC formation and subsequent crystallization in the presence of these two pigments were thus measured (Figure 5.3). The addition of 0.11 mM of both pigments did not significantly delay (20-30 s) the crystallization of ACC when compared to that of 0.11 mM naphthazarin which delayed the ACC crystallization by around 50 s (Figure 5.3c). This limited stabilizing effect of lawsone and juglone as compared to naphthazarin could be attributed to the different molecule's ability to impede nucleation, interact with ACC and promote the

growth of the crystalline structures. The reason behind this effect could be due to the superior complexation of Ca^{2+} ions by naphthoquinones with two ortho -OH groups, in contrast to those with just one -OH group as seen in compounds like lawsone and juglone, is attributed to their enhanced chelating ability, and the favorable geometric arrangement created by the two -OH groups. These factors collectively make naphthazarin with two ortho -OH groups more effective at binding and complexing Ca^{2+} ions as discussed in in Chapter 3, NMR section 3.6.2, that Ca^{2+} can precipitate naphthazarin at pH 11. Remarkably, the positioning of the -OH group in either lawsone or juglone had no discernible impact on the stabilization of ACC against crystallization.

In addition, the pH profiles of ACC crystallization in the presence of 0.11 mM and 0.22 mM of lawsone and juglone are respectively very similar (Figures 5.3a and 5.3b), suggesting that an increase in the concentration of these two pigments, did not enhance further ACC stability against crystallization in solution. This contrasts with the effect reported for naphthazarin, which shows a decrease in stability by 30-40 s with increasing concentration beyond 0.11 mM (Figure 5.3c). This decrease in ACC stability against crystallization beyond a certain concentration of naphthazarin could be attributed to, aggregation or precipitation: Naphthazarin molecules themselves might start to aggregate or precipitate out of solution at higher concentrations. This aggregation could potentially interfere with their ability to interact with the ACC surfaces, reducing their stabilizing effect. As lawsone and juglone possibly exhibit weaker interactions with Ca^{2+} ions when compared to naphthazarin, it is plausible that the aggregation or precipitation of lawsone or juglone does not disrupt the stabilizing effect.

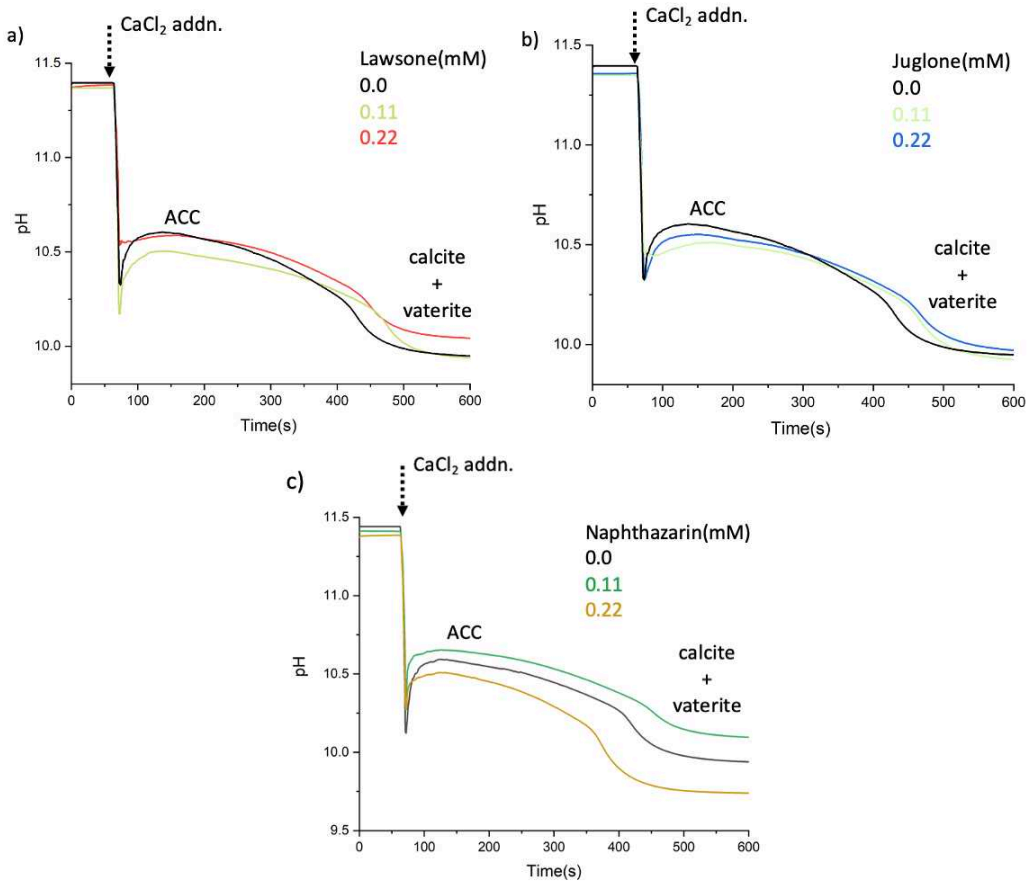

Figure 5.3. pH profile for ACC synthesis and crystallization in the presence of 0.11 and 0.22 mM concentrations of a) lawsone b) juglone, and c) naphthazarin.

5.1.2.1. Crystallization in air induced by heating

By comparing the DSC profiles of pure ACC with those containing varying concentrations of lawsone and juglone, we investigated the influence of the later on ACC crystallization temperature (Figure 5.4). The addition of 0.11 mM pigment leads to an increase in ACC crystallization temperature from 160 °C to 175 °C (Figures 5.4a and 5.4b). However, no further increase in ACC stability is detected for higher concentration (0.22 mM) (Figures 4a and 4b). Similar trend has been observed in case of naphthazarin where addition of 0.022 mM naphthazarin leads to increase in the ACC crystallization temperature by 10-15 °C (Figure 5.4c). However, we observe that further increase in concentration (0.53 mM) of juglone or lawsone did not increase the ACC crystallization temperature which is in stark contrast when compared to naphthazarin(0.53 mM), where ACC crystallization increase by 50 °C. This indicates that neither lawsone nor juglone stabilize significantly ACC against crystallization

induced by heating. Possibly, these two molecules do not interact with ACC or do not have a discernible impact on the mobility of water molecules associated with ACC.

In the case of lawsone and juglone we observe similar trends whereas in naphthazarin different trends in stability of ACC against crystallization in solution and by heating are observed. The similarity in stability trend for lawsone and juglone could be the limited interaction within solution which results in their inability to affect the stability of ACC. The limited interaction might also contribute towards less binding or associated of lawsone and juglone with ACC, which ultimately results in the inability to influence the ACC stability against crystallization induced by heating. Naphthazarin does interact with ACC therefore gets associated with ACC in larger concentration compared to lawsone and juglone and hence we observe a linear trend in ACC stability against crystallization induced by heating.

PDF measurements conducted on ACC (M1) synthesized in the presence of lawsone and juglone revealed that the short and medium-range structural order of ACC remained unaltered (Appendix 1 Figure 2). These findings are consistent with the impact of naphthazarin on ACC's local structure. This suggests that even though lawsone and juglone exhibit a lower affinity for $CaCO_3$ compared to naphthazarin, any limited association they have with ACC likely involves surface adsorption, thereby leaving the local structure of ACC unaffected.

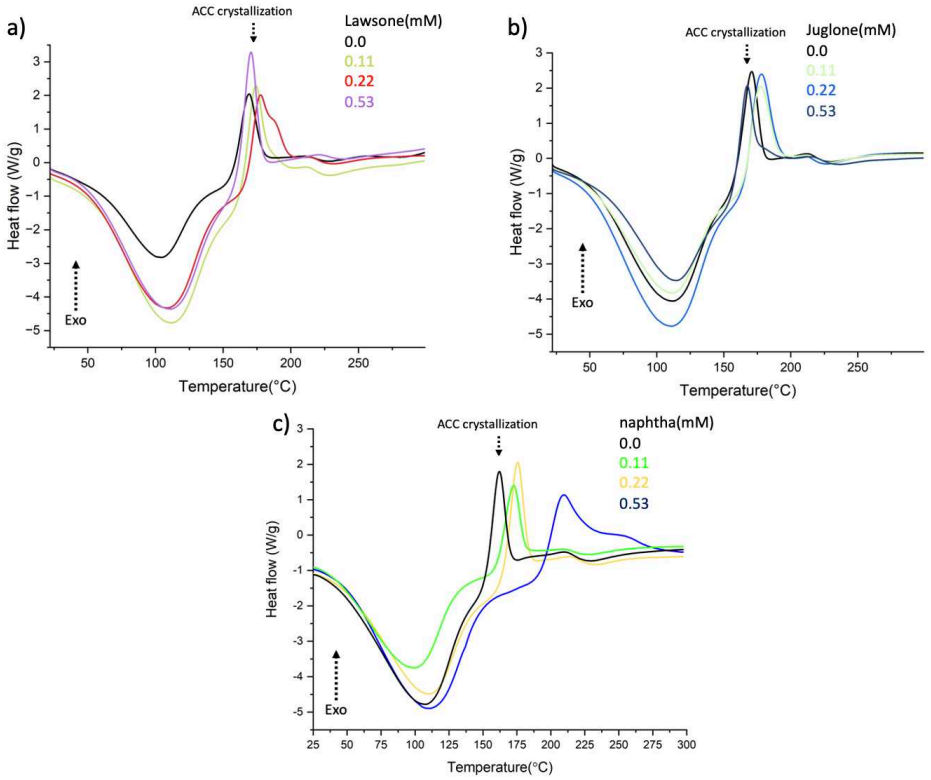

Figure 5.4. DSC thermograms of ACC and ACC synthesized in the presence in the presence of 0.11, 0.22 and 0.53 mM concentrations of a) lawsone, b) juglone, c) naphthazarin.

5.1.3. Calcite-lawsone/-juglone hybrid pigments

Calcite hybrid pigments were synthesized through direct precipitation outside the Metrohm® setup. Their morphology, surface properties, calcite lattice distortions, and color were analyzed using SEM, SEM-FEG, HR-XRD, and UV-visible spectroscopy respectively. Although neither of these two pigments seem to play a significant role on ACC crystallization, they might interact differently with calcite crystals.

5.1.3.1. Effect of lawsone and juglone on calcite crystal morphology and surface

The electron micrographs in Figure 5.5 revealed alterations in the shape and surface of the calcite crystals when synthesized (M2) in the presence of lawsone and juglone. The shape of the crystal is unaffected upon addition of 0.11 mM lawsone. One of the prominent changes observed is the presence of crystals with large defects in the middle with increase in lawsone concentration to 0.22 mM (Figures 5.5c and 5.5d). In case of juglone (0.04 mM) we observe that calcite crystals shape changed with appearance of multiple edges along with the appearance of pits and kinks on the surface. At 0.06 mM and 0.11 mM concentration of juglone

the surface of calcite crystal exhibited rhombohedral shaped pits along with hole in the crystals which might be due incomplete formation of crystal (Figure 5.5 f-h).

The observation of a defect, represented by a large void or incomplete formation in the crystal's center (as depicted in Figure 5.5d) suggests that the introduction of lawsone may facilitate the growth of calcite crystals through a spiral growth mechanism. This phenomenon is noteworthy, as the synthesized calcite crystals appear larger than 1µm, a characteristic that, as indicated by the findings of by (Darkins *et al*., 2022), tends to favor spiral growth over 2D nucleation. This prevalence of spiral growth can be attributed to the relatively slow diffusion rates within the boundary layer, resulting in a diminished surface supersaturation that aligns with the spiral growth mechanism (Darkins *et al*., 2022). Notably, the presence of certain additives, such as aspartic acid and Congo red have been found to have the potential to modify the predominant mechanism, either by inhibiting spiral growth or actively promoting 2D nucleation (Darkins *et al*., 2022).

In the case of juglone, the calcite growth may also follow a spiral-like mechanism similar to that observed in the presence of lawsone (Figure 55.d, e, and f). This calcite growth mechanism is quite different to one observed in presence of naphthazarin where it might be due due to Ca^{2+} and CO_3^{2-} growth units binding to kink sites at step edges.

However, the surface of the calcite crystals is differently affected depending on the pigments considered. For lawsone, the surface is not significantly affected as compared to naphthazarin (Chapter 4, section 4.2.2.2) and juglone. For the latter, the roughness of the calcite crystal surfaces is largely affected, a phenomenon that became more pronounced with increasing concentration of juglone from 0.04 mM to 0.11 mM (Figure 5.5).

Additionally, the micrographs reveal the presence of holes or pores on the crystal surfaces which were also observed in the case of naphthazarin. These surface irregularities can be attributed to two distinct phenomena explained in Chapter 4. Firstly, some crystal holes or pores may result from the entrapment of organic inclusions, such as pigment molecules, during the crystal's formation (Figures 5.5e-h). As the crystal continues to grow, these organic inclusions can generate voids or openings on the crystal's surface (Page *et al*., 2008). Secondly, holes may also form due to specific growth conditions, impacting certain crystal facets and giving rise to rhombohedral crystal-shaped voids (Orme *et al*., 2001).

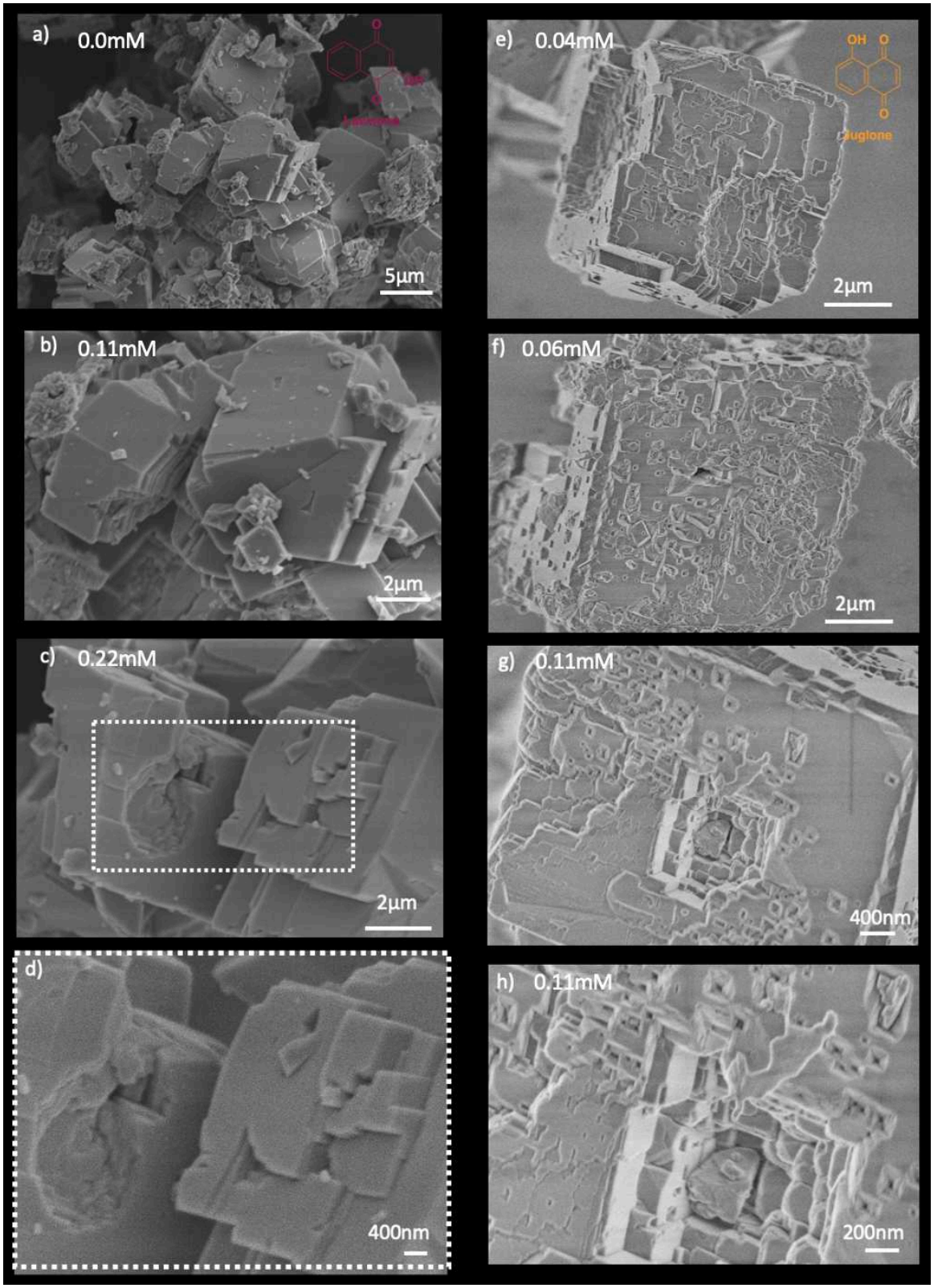

Figure 5.5. SEM micrograph calcite+ lawsone synthesized by direct precipitation method. a) and b) calcite+0.11 mM lawsone, c-e) calcite+0.22 mM lawsone. SEM-FEG micrograph of calcite crystals synthesized in the presence of juglone with different concentrations: e) 0.04 mM, f) 0.06 mM, and g, h) 0.11 mM.

5.1.3.2. Effect of lawsone and juglone on the crystal structure

The different organic-inorganic interactions revealed at the micro-scale between lawsone and juglone were further studied at the atomic level.

Figure 5.6a and 5.6c showcases the reflection (006) of the diffractograms of pure calcite and calcite synthesized in the presence of juglone or lawsone at 0.01, 0.11, and 0.22 mM. The introduction of lawsone and juglone into the calcite crystals did not cause any significant peak shifts. In addition, after Rietveld refinement (Appendix 1 Table 2) and calculation of calcite lattice distortion along the c-axis direction with respect to pure calcite, $\Delta c/c$, was calculated to be $< 0.01\%$ for both pigment molecules and all concentrations. This finding contrasts with other biogenic calcite structures like sea urchin spines (Albéric *et al*., 2018b) and mollusks (Pokroy *et al*., 2006), as already discussed in the case of naphthazarin (Chapter 4, part 4.3.2). The possible reasons behind the absence of lattice distortion could be: 1) low amount of pigment molecules getting incorporated within the calcite lattice or 2) the particular molecular structure of the pigment molecules that incorporate within calcite coherently without creating any lattice mismatch.

Degradation of organics potentially incorporated into calcite lattice is very well known to lead to c-axis relaxation and thus lattice distortions decrease (Albéric *et al*., 2018b). *In-situ* heating HR-XRD experiments (Figures 5.6b and 5.6d) were then conducted as well up to 400 °C. After correction of the intrinsic calcite thermal expansion, no lattice relaxation was measured neither for juglone nor lawsone for 0.11 mM at 400°C

Interestingly we do observe small broadening in (006) peak upon heating (Figure 5.6b and 5.6d) similar to that of calcite+naphthazarin. These broadening could be due to the increase in the microstrains which could be caused by organic molecules that might be incorporated within the calcite structure as they produce inhomogeneous deformation fields on a nanometer scale that are detected by X-rays (Boaz Pokroy *et al*., 2006). These alterations in microstrain can be linked to several underlying causes. Firstly, the presence of juglone or lawsone might induce a reduction in the size of crystallites, consequently affecting the coherence of crystalline domains. Secondly, the annealing treatments applied could lead to the degradation of intra-crystalline organic macromolecules, further contributing to the observed broadening of diffraction peaks.

The subtle lattice distortion in the c-axis direction in the studied calcite samples suggests that the mechanisms and factors influencing the crystal lattice in this context may differ from those governing the formation of other biogenic or synthetic calcite structures.

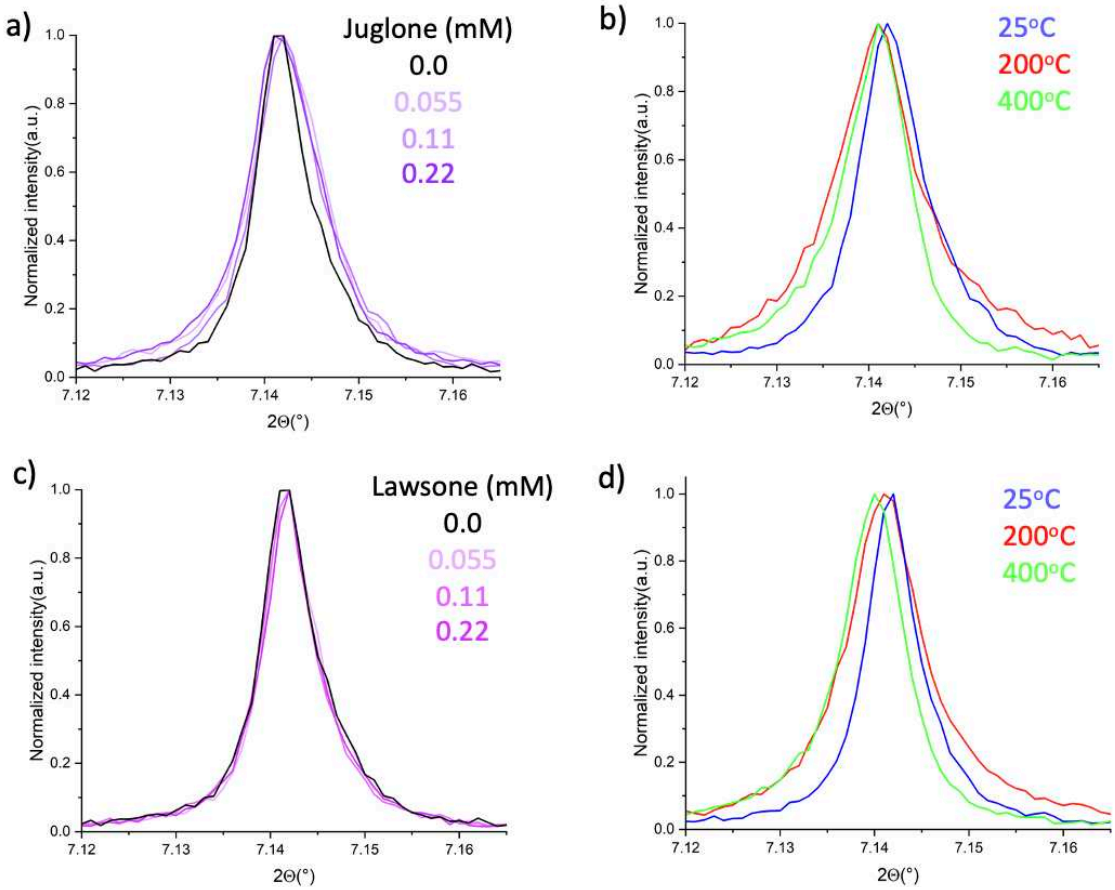

Figure 5.6. (006) reflection peak of the HR-XRD diffractograms with normalized intensity for calcite synthesized in the presence of a) juglone with concentrations from 0.055 to 0.22 mM at 25°C, b) 0.11 mM juglone at 25 °C, 200 °C and 400 °C, c) lawsone with concentrations from 0.055 to 0.22 mM at 25 °C and d) 0.11 mM lawsone at 25 °C, 200 °C and 400 °C.

5.1.3.3. Color of the calcite-lawsone/-juglone hybrid pigments

All the calcite-lawsone hybrid pigments were very light even for 0.22 mM concentrations whereas the calcite-juglone pigments presented more intense yellow-orange colors (Figure 5.7) that where further quantified by UV-visible spectroscopy (Figure 5.8).

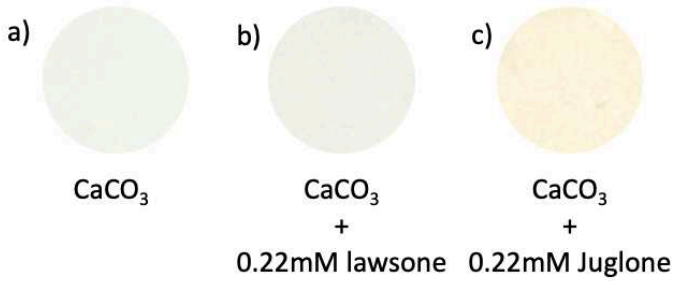

Figure 5.7. Images of calcite synthesised in presence of 0.22 mM lawone and 0.22 mM juglone.

To further quantify the color of the different samples, UV-visible diffuse reflectance measurements were performed (Figure 5.8).

Visible region: The UV-visible diffused reflectance spectra of calcite-juglone in the visible region (400-800 nm) reveal several different notable absorption bands (Figure 5.8a). The absorption of visible light at this wavelength contributes to the observed color of the compound. Calcite+0.22 mM juglone absorbs at around 550-400 nm, resulting in a yellow orange coloration. We observed that with increase in juglone concentration the absorbance increased implying darker shade.

CIE-1931 Chromaticity diagram: We further evaluated the color of the calcite-juglone by depicting the portion of unabsorbed or scattered light from the diffused reflectance UV-Vis on the CIE 1931 chromaticity diagram. Calcite+ 0.011 mM juglone (Figure 5.8b) samples occupy an overlapping area with shades of light pink and light-yellow resulting in a lightly yellowish-orange shade. Increasing juglone concentration (0.11 mM) leads to an increase in the intensity of the color which tends to push the colors towards the region corresponding to darker color.

The pH of the reaction is very similar to that of calcite+naphthazarin synthesis. Therefore the pH at the end of the reaction should be around ~8.5, as shown in Figure 5.1, juglone exhibit organish red color which is different from the color imparted to the calcite. We also observed that during the synthesis the juglone does not undergo ideal color changes but rather turns light brown which might be due to degradation of juglone and hence the color imparted is different from orangish red. It has been shown that half-life of juglone drastically decreases in basic medium to hours from several days when in acidic medium (Wright *et al*., 2007).

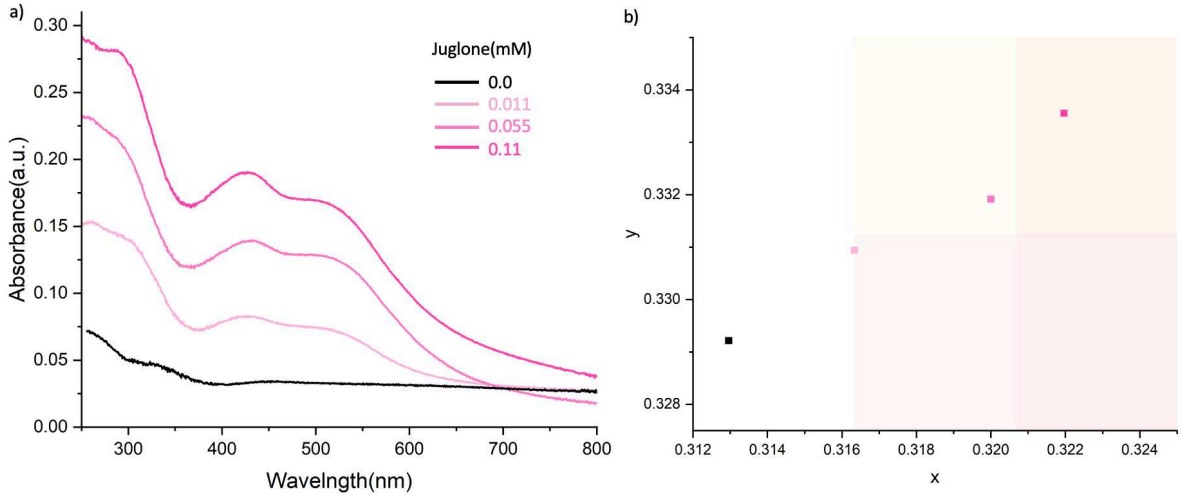

Figure 5.8. a) The UV-Vis diffused reflectance spectrum of calcite samples prepared in the presence of different concentrations of juglone, b) CIE 1931 diagram corresponding scattered part of the UV-Vis diffused reflectance spectrum of calcite samples prepared in the presence of different concentrations of juglone.

5.2. ACC-lawsone/-naphthazarin hybrid pigments formed in ethanol

The exploration of vapor diffusion synthesis for ACC synthesis in ethanol was driven by the issue encountered in the direct precipitation method in aqueous solutions:
1) increased solubility of naphthazarin in ethanol from 0.055 mM to 0.63 mM in water, and
2) uncolored calcite-lawsone hybrid pigments despite the intense orange color of the precipitation media.

5.2.1. Color of the ACC-lawsone/-naphthazarin hybrid pigments

Interestingly, the synthesis of ACC through vapor diffusion in ethanol in the presence of lawsone give rise to intense coloration for similar concentrations (0.33 mM) as the one used during direct precipitation (Figure 5.9). This marked difference in coloration between the two synthesis methods suggests the critical influence of kinetics, solvent of the reaction and pH change during the course of reaction in the incorporation of lawsone into the ACC polymorph.

The reason behind this phenomenon may lie in the distinct mechanisms and rates of ACC formation in these two solvents. When ACC is directly precipitated in water, the rapid and uncontrolled nature of the process may not allow sufficient time for lawsone to be effectively

incorporated into the ACC structure, resulting in minimal coloration. In contrast, the vapor diffusion method in ethanol provides a slower and more controlled environment, allowing lawsone to be either incorporated within the ACC matrix or adsorbed on the ACC matrix, leading to the striking coloration observed. This observation highlights the significance of reaction kinetics along with solvent (ethanol) during ACC formation in determining the extent of lawsone in the resulting ACC.

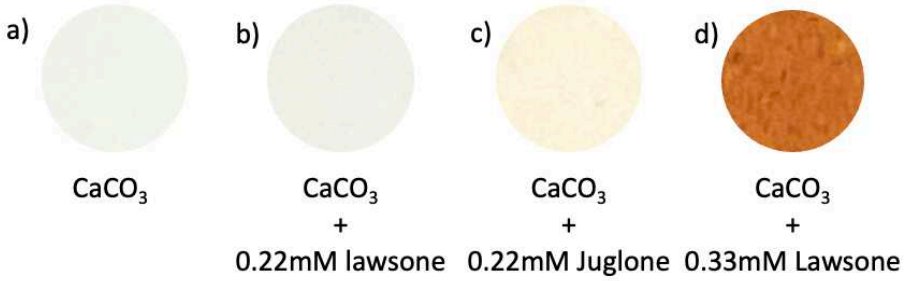

Figure 5.9. ACC synthesized by direct precipitation method, a) , b) ACC+0.22 mM lawsone, c) ACC+0.22 mM juglone, d) ACC synthesized by vapor diffusion method in the presence of 0.22 mM lawsone.

5.2.2. ACC stability, particle size and local structure

Differential Thermal Analysis (DTA) thermogram of pure ACC shows an endothermic peak at around 80-90 ºC indicating the loss of bound water or ethanol, and an exothermic peak at around 310 ºC likely due to ACC crystallization (Figure 5.10). This ACC crystallization temperature is substantially higher than the one of ACC synthesized by direct precipitation in water (160 ºC) indicating enhanced stability depending upon the method of synthesis.

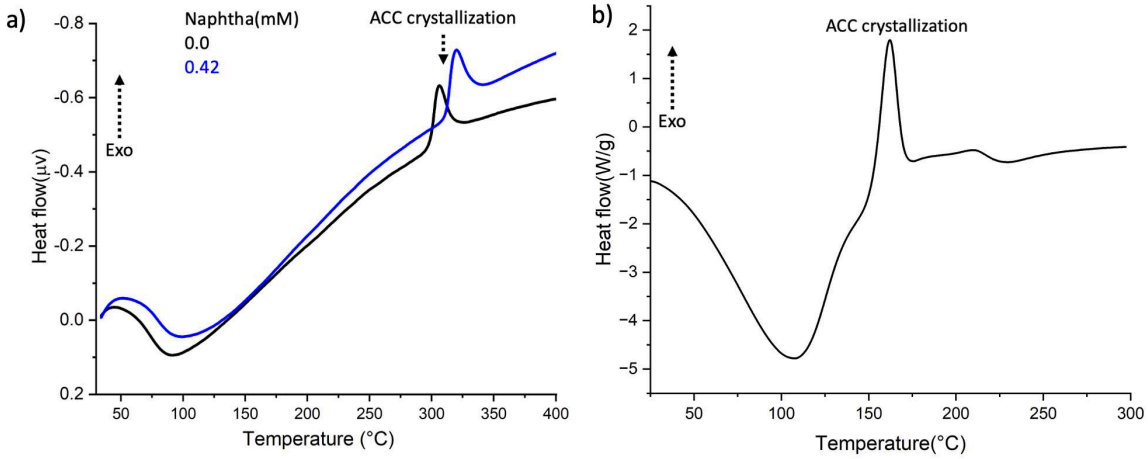

Figure 5.10. a) Differential thermal analysis of ACC synthesized by vapor diffusion in ethanol in the absence (0 mM) and presence (0.42 mM) of naphthazarin, and b) DSC thermogram of pure ACC synthesized by direct precipitation M1.

This higher stability of ACC synthesized in ethanol by the vapor diffusion method can be attributed to a couple of key factors. One plausible explanation is the likelihood of achieving complete dehydration during the synthesis process, which sets it apart from ACC formed by direct precipitation in water. It is believed that the stability of ACC was achieved through the addition of ammonia and ethanol *i.e.,* NH_3 presence in the coordination sphere around the calcium ions may prevent their reorganization into one of the stable crystalline phases. Conversely, ethanol impedes the dissolution of ACC, thereby hindering the solution-mediated phase transition from ACC to vaterite or calcite (Lee *et al*., 2005). The absence of water molecules within the ACC structure plays a pivotal role in bolstering its stability by restricting the mobility of ions within the ACC, causing a significant reduction in the structural rearrangement needed for crystallization is significantly hindered, thus more stable (Du *et al*., 2018; Zou *et al*., 2015).

Another contributing factor could be the relatively small size of the ACC particles produced in ethanol. FEG-SEM micrographs unveiled that the average particle size of ACC nanoparticles is 90-95 nm (Figure 5.11) notably smaller than their counterparts synthesised through direct precipitation synthesis (average size of 140 nm; Chapter 3). Smaller particles often exhibit greater stability due to their increased surface energy and reduced susceptibility to crystal nucleation (Zou *et al*.). The smaller size restricts the formation of crystal nuclei, allowing to maintain its amorphous structure for an extended period (Nudelman *et al*., 2010).

In essence, the heightened stability of ACC synthesized by vapor diffusion in ethanol may be a result of both the absence of water molecules and the small size of the particles, which collectively contribute to the preservation of its amorphous state.

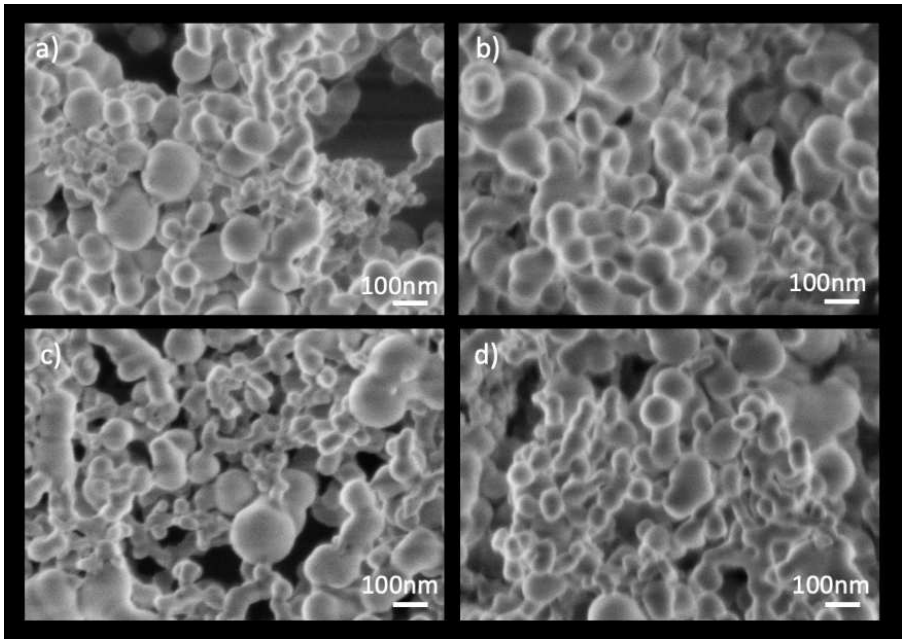

Figure 5.11. FEG-SEM micrographs obtained on ACC synthesized by vapor diffusion synthesis in ethanol, a) and b) ACC, c) and d) ACC+0.42 mM naphthazarin.

By comparing the DTA profiles of pure ACC with one containing 0.44 mM naphthazarin, we observed a slight increase in the ACC crystallization temperature from 310 to 320 ºC (Figure 5.10a). However, this increase in crystallization temperature when compared to ACC with similar naphthazarin concentration synthesized by direct precipitation in water (150 to 210 ºC) is significantly smaller. The lower amount of water bound to ACC may be the reason for the limited impact of naphthazarin on its stability. This stands in contrast to the situation when ACC is synthesized through direct precipitation in an aqueous medium, where naphthazarin exhibits a more pronounced influence on stability. This disparity in behavior can also be attributed to the distinct chemical and structural characteristics of ACC formed under these differing conditions.

5.3. Calcite-PHNQs hybrid pigments

5.3.1. Color of the calcite-PHNQ hybrid pigments

Figure 5.12, display photographs of purple sea urchin spine powder and the calcite-spinochromes (0.22 mM) samples synthesized by direct precipitation (outside the Methrom set up). Calcite-spinochrome A bears resemblance to the color of the sea urchin spines powder. Spinochrome B imparts light yellow color and spinochrome E almost white color.

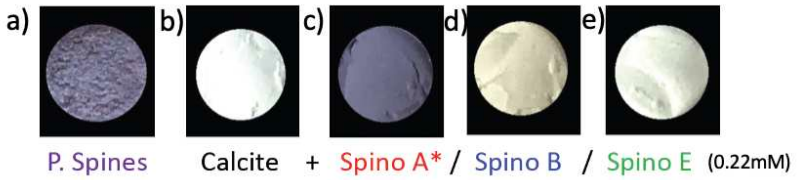

Figure 5.12. Purple spines powder and calcite-Spinochromes (0.22 mM) synthesized by fast direct precipitation (without Metrohm® setup).

To further quantify the color of the different samples, UV-visible diffuse reflectance measurements were performed (Figure 5.13).

Visible region: The UV-visible diffuse reflectance spectra of calcite-PHNQs (spinochrome A, B, D, E, and echinochrome A) and spines in the visible region (400-800 nm) reveal several different notable absorption bands (Figure 5.13a). The absorption of visible light at this wavelength contributes to the observed color of the compound. For instance, calcite-echinochrome A absorbs at around 500-550 nm, resulting in a yellow coloration. Similarly, calcite-spinochrome A and spines absorb in the range of 550-650 nm resulting in a purple color. However, absorbance bands for other pigments (spinochrome B, D, E) were absent in the visible region, which correlated well with the white/light yellow color of the samples.

UV region: The analysis of the UV region provides valuable insights into the electronic structure and molecular properties of the different samples (Figure 5.13a). All samples display absorption bands between 250 and 370 nm, representing π-π* transitions. We observe similar spectra profiles for calcite-spinochrome A sample and spine powder suggesting that the color might be due to the same molecules. However, for all other pigment molecules, the profile is different which provides insight into the role of substituents on the π-π* transitions.

CIE-1931 Chromaticity diagram: We further evaluated the color of the calcite-PHNQs and spines by depicting the portion of unabsorbed or scattered light from the diffuse reflectance UV-Vis on the CIE 1931 chromaticity diagram (Figure 5.13b). Calcite-spinochrome E appears in the white region on the CIE diagram very similar to that of calcite, while the powder spines occupy an overlapping area encompassing shades of purple, green, and orange. This overlap becomes more pronounced for calcite-spinochrome A, intensifying the color and shifting it towards darker hues towards blue, and green regions. Calcite+spinochrome B/echinochrome A occupies an overlapping area with shades of pink and yellow, resulting in a yellowish-orange

shade. This phenomenon is pronounced for calcite-spinochrome D shifting it towards darker yellow hues representation on the CIE 1931 diagram.

These findings underscore the intriguing phenomenon that different pigments interact distinctively within calcite, yielding a diverse range of hues. Some pigments seem to have a stronger tendency to bond with calcite, resulting in the creation of richer and more intense hues, while others do not exhibit this interaction. This observation suggests that the molecular structure and specific functional groups of these pigments might play a pivotal role in their interaction with calcite. Interestingly, the UV-Vis profiles of both the spines and calcite+spinochrome A exhibited remarkable similarity. This observation strongly suggests that spinochrome A could potentially serve as the primary contributor to the distinctive coloration observed in the purple sea urchin spines. Moreover, it raises the intriguing possibility that these molecular characteristics could also influence the crystallization pathway, influencing not only the coloration but also the overall structure and properties of the resulting calcite crystals.

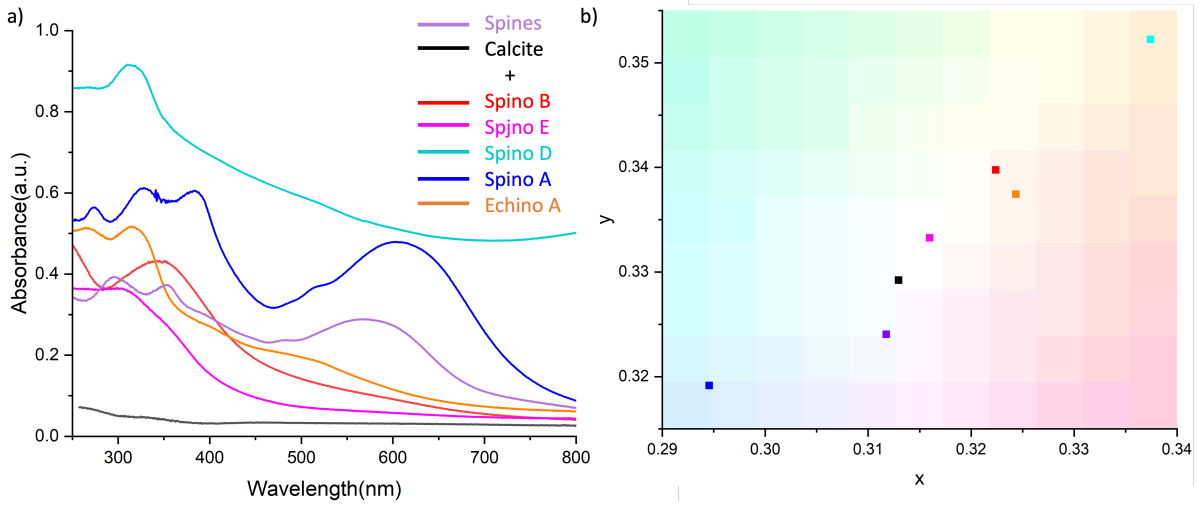

Figure 5.13. a) The UV-Vis diffused reflectance spectrum of calcite samples prepared in the presence of different pigments with 0.22 mM concentration, b) CIE 1931 diagram corresponding scattered parts of the UV-Vis diffuse reflectance spectrum of calcite samples prepared in the presence of different pigment molecules with 0.22 mM concentration.

5.3.2. Effect of PHNQs on $CaCO_3$ polymorph conversion

Similarly, to $CaCO_3$-naphthzarin samples (Chapters 3 and 4) synthesized by direct precipitation (M2) in water, $CaCO_3$-spinochrome samples are formed via ACC that further crystallized into a mixture of calcite and vaterite before to fully converting to calcite only. Here, we report that spinochrome A, B and E at a concentration of 0.14, 0.18 and 0.16 mM respectively, impact differently the conversion from calcite/vaterite to calcite (Figure 5.14). Indeed, for 2 days of synthesis for all samples, only calcite is detected in $CaCO_3$-spinochrome B whereas vaterite is still present in $CaCO_3$-spinochrome A and $CaCO_3$-spinochrome E. This finding suggests that spinochrome A and spinochrome E impact the crystallization process, specifically delaying the complete transformation of the vaterite/calcite mixture into calcite. The delay in the transformation seems to be even more significant for spinochrome A. The differences in the ability to stabilise vaterite phase might be due to structural differences between the molecules. Spinochrome A might interact better with vaterite phase compared to other molecules thus inhibiting the conversion of vaterite to calcite.

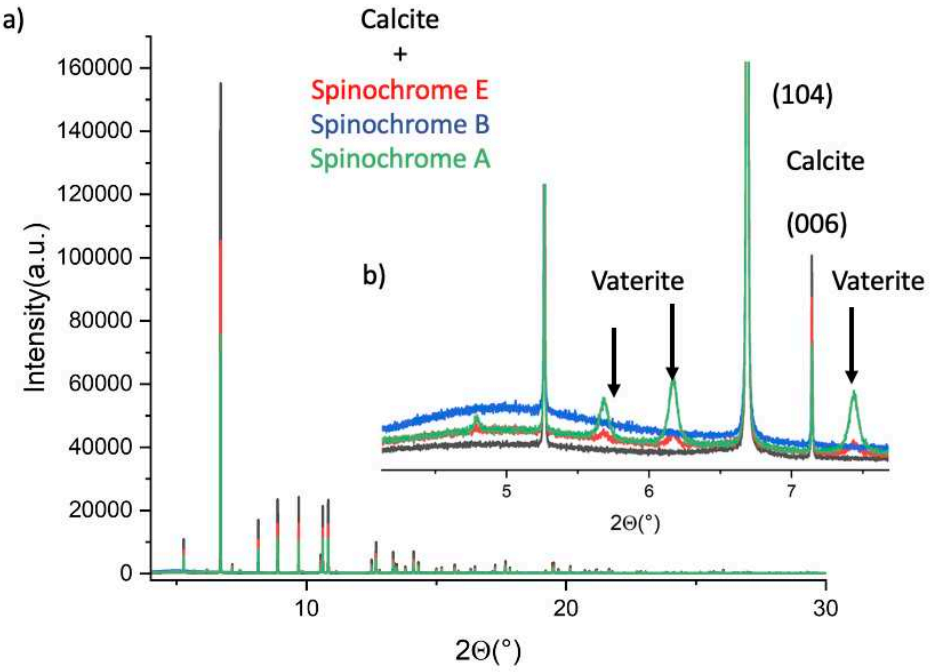

Figure 5.14. a) HR-XRD diffractogram for calcite synthesized in the presence of spinochrome E (0.16 mM), spinochrome B (0.18 mM), spinochrome A(0.14 mM) by direct precipitation for 2 days and b) zoomed section of diffractogram showing the characteristic peaks of calcite and vaterite.

5.3.3. Effect of PHNQs on calcite crystal morphology and surface

5.3.3.1. Vapor diffusion

Single crystal synthesis by vapor diffusion in the presence of spinochromes A, B, and E, reveal notable differences in their effects on crystal morphology (Figure 5.15). The synthesis was performed in the presence of 1.6µg /mL NaOH and the spinochrome concentration was varied from 0 to 100 µg/mL. The rationale behind the use of NaOH was to dissolve a concentration higher than 10 µg/mL of PHNQs in the reaction mixture. SEM-FEG micrographs in Figure 5.15a show the likely presence of calcite along with likely vaterite in the control well. The calcite exhibited two morphologies: 1) aggregates of euhedral calcite crystals, and 2) single crystals with holes/wells on the surface. The first morphology could be an effect of pH on the calcite growth as discussed in Chapter 4, as synthesis at pH>12 leads to the formation of a rosette-like spherical structure. The second morphology could be the incomplete formation of calcite crystals leading to the presence of a hole/well in the middle of crystals. The presence of

vaterite (cauliflower-like structures may result from the reaggregation of the spheroids of vaterite) may result from concentration gradients introduced during the vapor diffusion method. These gradients involve variations in ammonia concentration, pH, and the ratio of CO_3^{2-} to Ca^{2+} ions, which change both with depth within the solution and over time. (Liu *et al*., 2016) observed that calcite crystals tended to nucleate and grow in either the upper regions of the aqueous solution, while vaterite crystals exhibited a preference for lower areas as well.

Among spinochromes, spinochrome E exhibited the most significant alterations of the crystal morphology when introduced at a concentration of 25 µg/mL (Figure 5.15e) leading to the elongation of the crystals along the c-axis (104). It has been shown that organics extracted from sea urchins can influence calcite morphology at very low concentration(5 µg/mL) (Kanold *et al*., 2015). This effect became even more pronounced at 100 µg/mL (Figure 5.15g). In contrast, spinochrome B displayed the least pronounced influence on crystal morphology among the three spinochromes studied (Figure 5.15b). The elongation of the crystal structure was observed for spinochrome A only at a concentration higher than 25 µg/mL, *i.e.,* at 100 µg/mL (Figures 15d, g, j). Crystals were elongated and this phenomenon was common for all spinochromes.

The calcite crystals in the presence of 100 µg/mL spinochrome A and E might be made of small crystals of various shapes and sizes aggregated together, resulting in elongated structures (Figure 5.15d, g). The morphological changes observed during the calcite growth in the presence of spinochrome can be correlated with a study by (Aizenberg *et al*., 1997). In this study, they showed that calcite crystals grown in the presence of macromolecules (1-10 µg/mL) extracted from sea urchins by vapor diffusion cause morphological modifications and anisotropic textural changes in the grown crystals. This correlation between macromolecule adsorption and crystal defects suggests that protein adsorption and occlusion play a role in both the observed morphological modifications and anisotropic textural changes. Notably, the calcite crystals exhibited well-developed stepped faces slightly oblique to the c- axis and perpendicular to the a-axis. Similar studies by (Volkmer *et al*., 2004) using acidic peptides, have revealed specific interaction with distinct crystal faces of calcite, resulting in the development of stepped diamond-shaped (012) crystal faces in addition to the prismatic (110) faces. This is observed when the peptides are present during the crystallization of $CaCO_3$. The orientation of carbonate ions on these faces is favorable for their interaction with acidic macromolecules containing aspartic acid or glutamic acid residues. The diversity in how

spinochrome A, B, and E differently affect crystal morphology and thus growth is still under investigation but is surely in relation to specific interactions between the side groups of these molecules and the Ca^{2+} and CO_3^{2-} ions. Indeed, all three spinochromes (A, B, and E) feature hydroxyl groups capable of forming hydrogen bonds with Ca^{2+} ions. The degree of interaction with CO_3^{2-} ions may be influenced by the number and arrangement of hydroxyl groups, with spinochrome B and E, characterized by a greater abundance of hydroxyl groups, possibly exhibiting an enhanced propensity for CO_3^{2-} interaction as respect to the other spinochromes. In terms of acidity, spinochrome E is likely the most acidic among the three due to the presence of multiple hydroxyl groups that readily donate protons (H^+) in alkaline aqueous solutions contributing to stronger interaction with Ca^{2+}. This might explain why spinochrome E has a more pronounced influence on morphology compared to spinochromes A and B.

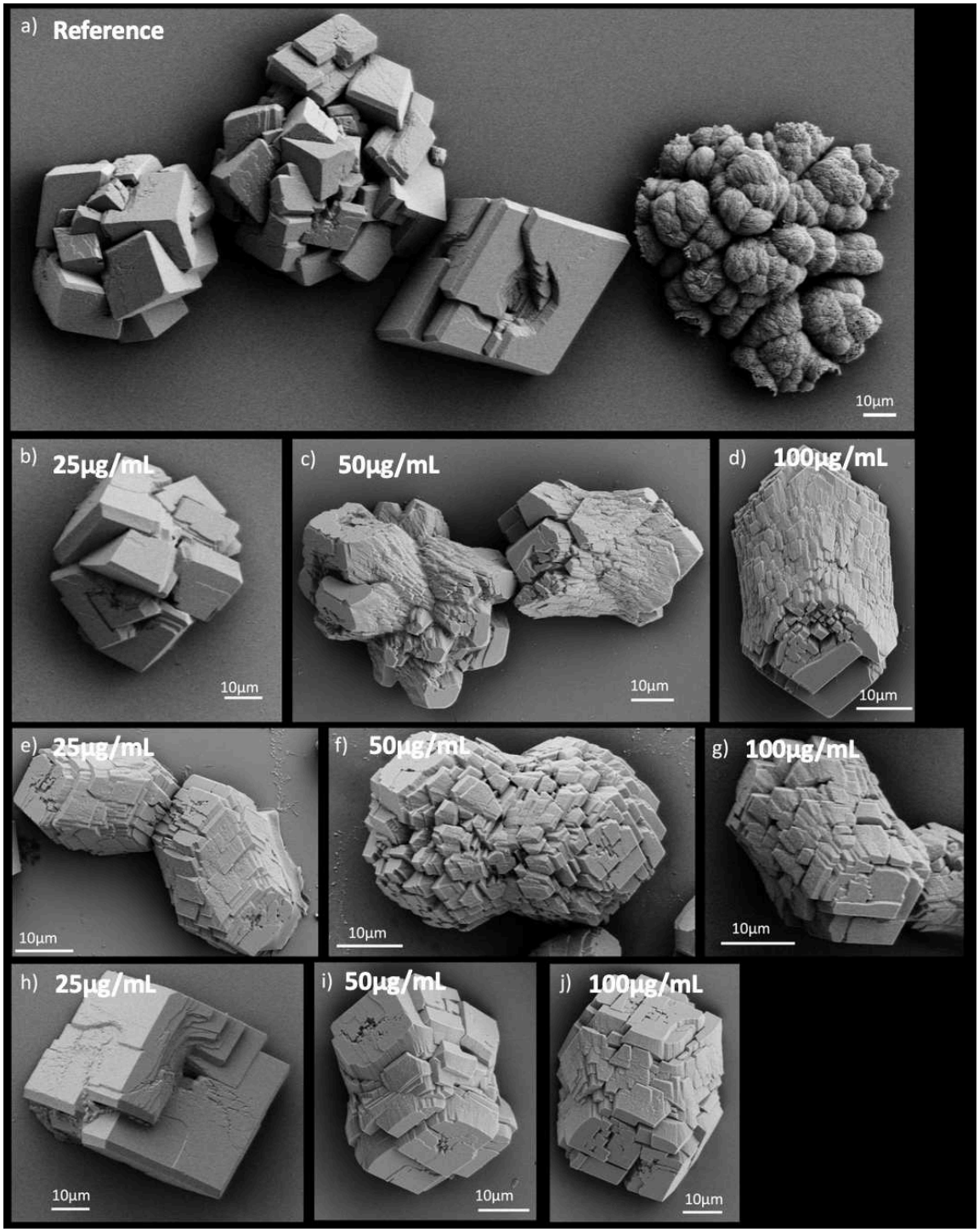

Figure 5.15. Electronic micrographs on calcite crystals synthesized by slow vapor diffusion method in the presence of different spinochromes. a) control, b) 25 µg/mL, c) 100 µg/mL, d) 100 µg/mL in presence of spinochrome A, e) 25 µg/mL, f) 100 µg/mL, g) 100 µg/mL in presence of spinochrome E, h) 25 µg/mL, i) 100 µg/mL, j) 100 µg/mL in presence of spinochrome B.

5.3.3.2. Direct precipitation

The SEM micrographs presented in Figure 5.16 illustrate alteration in the shape *i.e.*, elongation of these crystals when echinochrome A was introduced into the system at 40 µg/mL (0.14 mM) (Figure 5.16a). In contrast to the typical rhombohedral structure that is commonly associated with crystalline calcite, the presence of echinochrome A resulted in the formation of calcite crystals with notably distorted shapes (anhedral calcite form). This phenomenon of shape change from euhedral calcite to anhedral calcite form on the addition of organics is well-known. and already discussed above. Similarly, but to a smaller extend, SEM micrographs in Figure 5.16e showcased that the addition of spinochrome A also induces changes in crystal morphology at 40 µg/mL (0.14 mM). However, for the same concentrations of spinochrome B, the deviation from the typical rhombohedral shape of calcite crystals is small. These deformations, which may be attributed to the specific binding or inhibitory effects of PHNQs on certain crystal facets, suggest that spinochrome A and echinochrome A influence more the growth and development of the calcite crystals than spinochrome B.

Observations of the samples at higher magnification reveal different aspects of the crystal surface according to PHNQs. Spinochrome A did not seem to affect the crystal surface. However, in the presence of Echinochrome A, crystal surfaces show the presence of holes at the crystal surfaces (red arrows), and it seems that crystals might have been formed from aggregation or deposition of elongated crystals (Figure 5.16b). Some of the pores may be associated with organic inclusions within the crystal structure similar to the phenomenon observed in the case of juglone. When spinochrome B was introduced, a significant increase in the roughness/pores of the crystal surfaces was observed (Figures 5.16c and 5.16d). This increase in pores on the surface suggests that spinochrome B interacts with the growing crystal surfaces, resulting in a texture comparable to that of porous crystals.

The diversity of morphology and surface of the crystals indicate different interactions between PHNQ and calcite during crystal growth. The disparity in response altering calcite morphology of different pigment molecules might be due to the difference in the substituent groups which affects their ability to interact with Ca^{2+} ions and thus the morphology. On comparing these results with calcite-naphthazarin (M2) we can clearly see the possible role of substituents as for similar concentration naphthazarin induced much less morphological distortions

The specific mechanisms behind these alterations caused would require further investigation but likely involve interactions between these organic compounds and the growing calcite crystals at the molecular level.

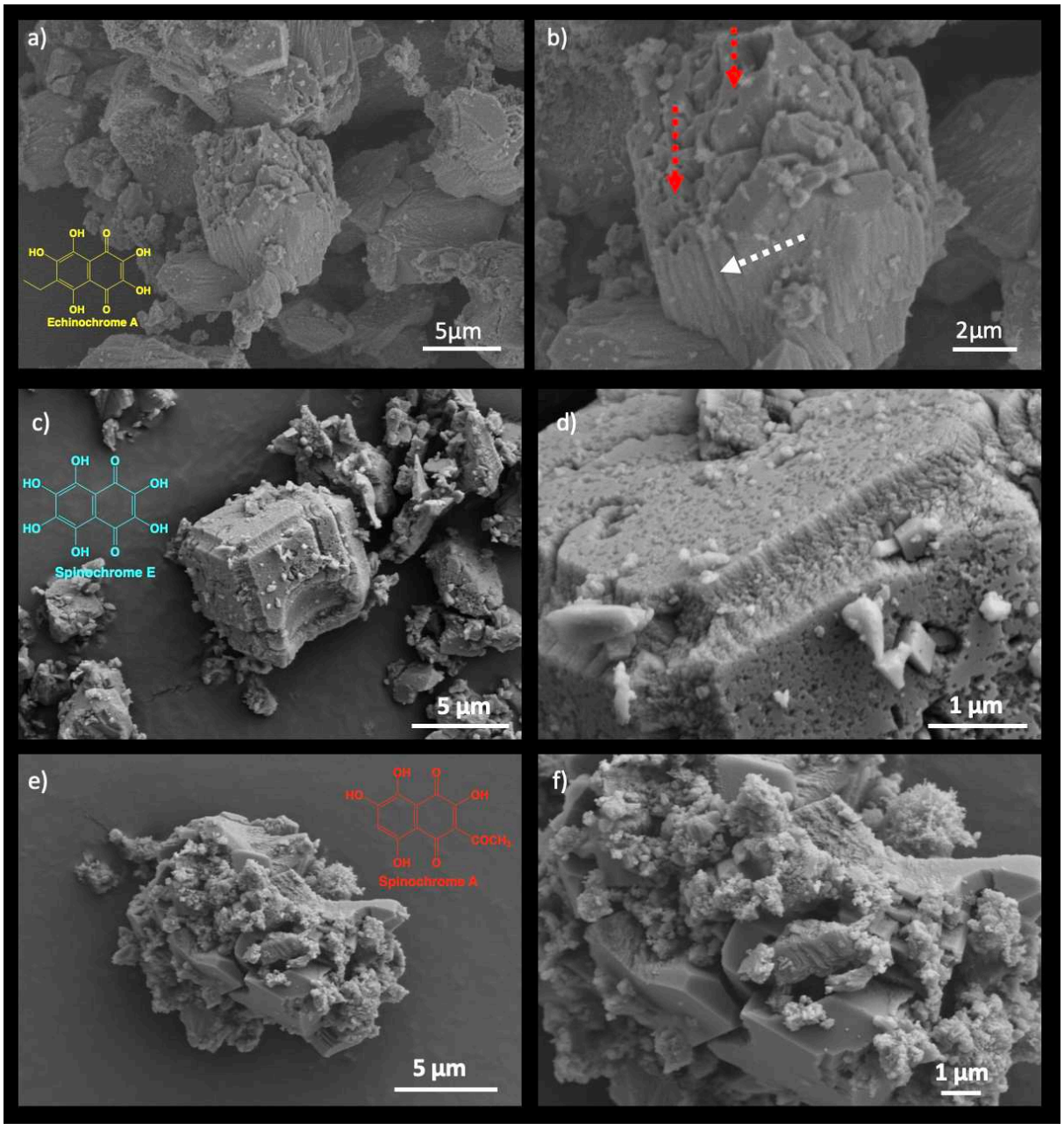

Figure 5.16. a)-b) SEM micrograph obtained on calcite +0.14 mM (40 µg/mL) echinochrome A synthesized by direct precipitation method. The arrow drawn on the micrograph suggests that the crystal may result from an aggregation of elongated crystals resembling needles. c) calcite +0.14 mM (40 µg/mL) spinochrome B, d) zoomed-in view on micrograph c, e) calcite+0.14 mM (40 µg/mL) spinochrome A, f) zoomed-in view on micrograph e.

5.3.4. Effect of PHNQs on calcite lattice distortions

The diffractograms obtained on calcite synthesized in the presence of PHNQs such as echinochrome A, spinochrome E, spinochrome B, spinochrome D, and spinochrome A by direct precipitation synthesis, unveil intriguing insights into the impact of these pigments on the crystal lattice structure (Figure 5.17). The introduction of PHNQ molecules into the calcite crystals leads to a peak shift to lower 2 theta values suggesting elongation of the crystal lattices. Through Rietveld refinement, lattice parameters were extracted and the lattice distortion in the c-axis direction calculated and expressed as Δc/c. We observed that Δc/c varies depending on the PHNQ molecule and its concentration: echinochrome A (0.01-0.02%), spinochrome E (0.01-0.03%), spinochrome B (0.01-0.03%), spinochrome D (0.01-0.02%), and spinochrome A (<0.01%). Although these lattice distortion values are quite small compared to lattice distortion in sea urchins spines (0.04-0.05%) (Albéric *et al.*, 2018b), this difference might be due to the presence of other macromolecules in the sea urchins spines. However, it is evident that incorporation of PHNQs results in larger lattice distortion compared to naphthazarin, juglone or lawsone, further suggesting the role substituents might play at molecular level interaction.

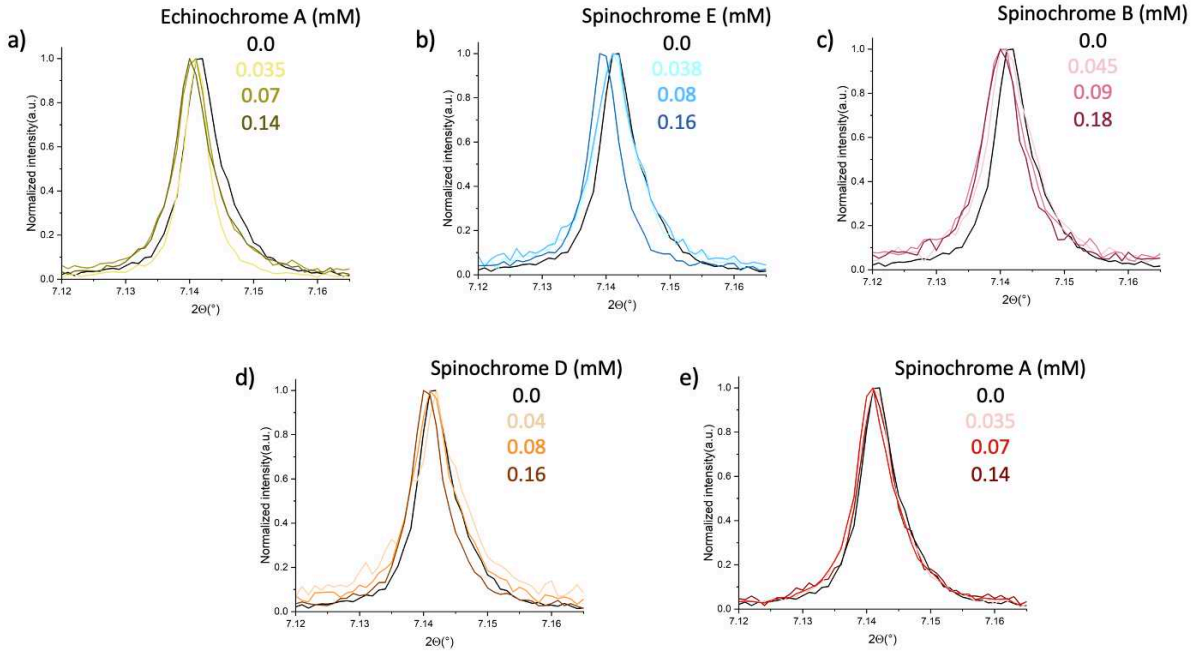

Figure 5.17. (006) reflection peak of the HR-XRD diffractograms with normalized intensity for calcite synthesized in the presence of a) echinochrome A, b) spinochrome E, c) spinochrome B, d) spinochrome D, and e) spinochrome A with concentration from 0.035 to 0.18 mM.

PHNQs incorporation within calcite was further investigated through *in-situ* heating HR-XRD experiments up to 400 °C in order to degrade PHNQs and lead to possible lattice relaxation. HR-XRD diffractograms after correction of calcite thermal expansion are presented in Figure 5.18 for calcite synthesized in the presence of spinochrome B (0.11 mM) (Figure 5.18a), echinochrome A (0.11 mM) (Figure 5.18b) and spinochrome A (0.11 mM) (Figure 5.18c). However, apart from peak broadening, no lattice relaxation was measured. In our case the $\Delta c/c$ after annealing was negative. Moreover, the broadening phenomena were not homogenous for the pigments. We observed the maximum broadening in the presence of spinochrome B in comparison to spinochrome A and echinochrome A. These broadening as discussed in Section 5.1.3.2 of this Chapter, could be due to the increase in the microstrains which could be caused by organic molecules that might be incorporated within the calcite structure as they produce inhomogeneous deformation fields on a nanometer scale that can be detected by X-rays (Boaz Pokroy *et al*., 2006). However, calcite-spinochrome B data seems noisy for spinochrome A at 200°C. Therefore, experiments should be repeated in order to get reliable data.

In summary, Spinochrome A appears to exhibits a unique interaction with calcite compared to Spinochromes B and E. It hinders the transformation into calcite with minimal impact on atomic structure and morphology, particularly in vapor diffusion synthesis. This distinction may explain its preference for incorporation into *Paracentrotus lividus* sea urchin spines, influencing their coloration and structure. This observation underscores the significance of molecular-level interactions in the intricate processes governing biomineralization.

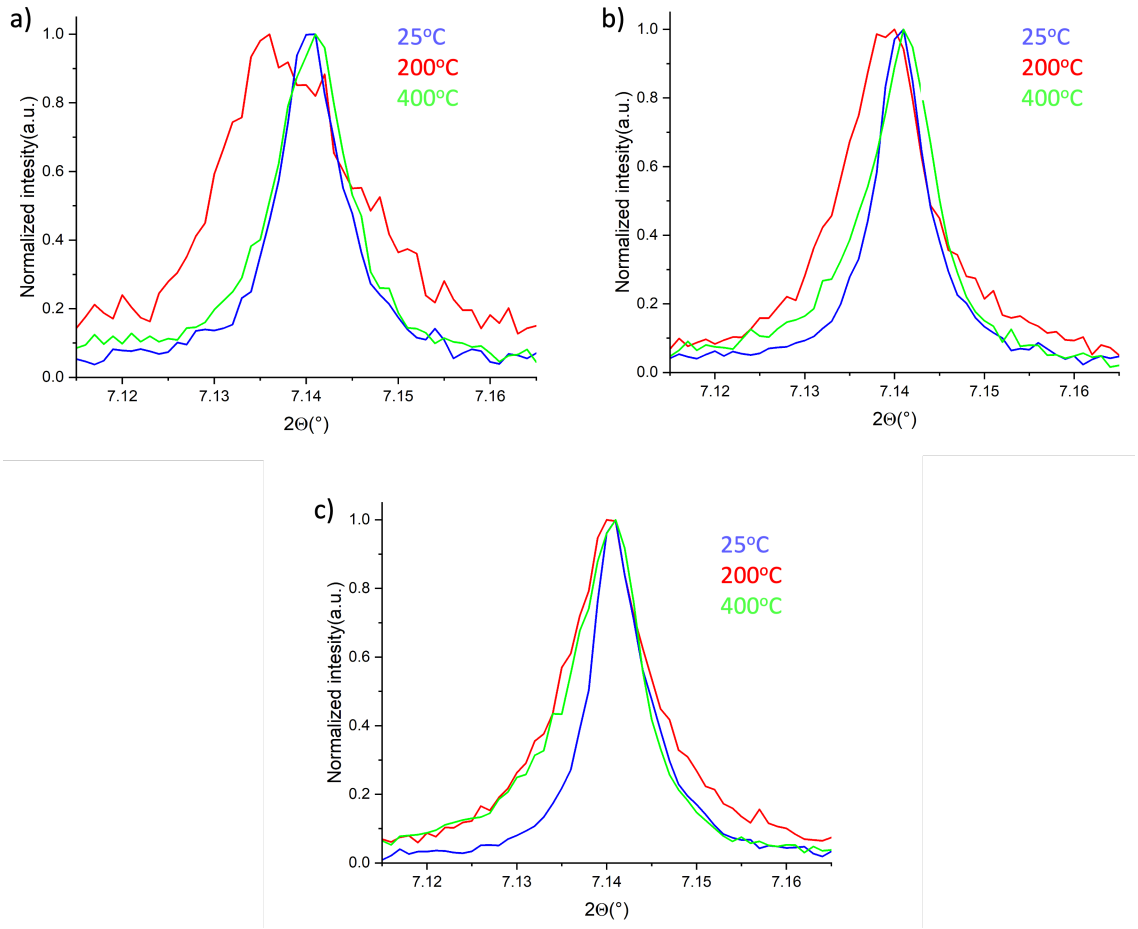

Figure 5.18. (006) reflection peak of the HR-XRD diffractograms at 25 °C, 200 °C and 400 °C with normalized intensity for calcite synthesized in the presence of, a) 0.09 mM spinochrome B, b) 0.07 mM echinochrome A, c) 0.07 mM spinochrome A.

5.4. Textile finishing by the bio-(hybrid) pigments

5.4.1. Synthesis of the hybrid pigments

A large-scale vapor diffusion synthesis of ACC-naphthazarin was conducted in ethanol to generate a hybrid pigment suitable for textile dyeing. The reaction setup was scaled up fivefold to ensure the yield of synthesis of hybrid pigment in grams, for conducting preliminary tests on various fabric types. Calcite-spinochrome hybrid pigment was synthesized using direct precipitation synthesis in water (M2).

5.4.2. Textile finishing

This work was carried out by Tony Jouanneau T. founder of ATELIER SUMBIOSIS, a lab merging science and textiles. This study aims to explore the color potential of natural pigments sourced from sea urchin waste (spinochrome A) and plants (naphthazarin) as well as hybrid pigments (ACC-naphthazarin and calcite-spinochrome A) in dyeing different textile substrates (silk, wool, and cotton). Here after, the natural pigments are also called colorants.

5.4.2.1. Fabric preparation and dyeing procedure

Fabrics (silk and cotton) were initially hand-washed at 40 °C, then placed in a non-reactive container while still damp and stirred to remove impurities. Rinsing of fabrics occurred in a hot soap (70 °C) bath with additional soda crystals. After cooling to RT, fabrics were rinsed in water baths. Following drying and weighing, mordant and pigment quantities were determined in respect to the fabric weight. For naphthazarin, the ratio of colorant:fabric was 1:1, whereas for spinochrome A, it was 0.01:1 because of the extraction that yields 60 mg in total (30 mg was used for synthesizing the calcite-spinochrome A hybrid pigments). Subsequently, the fibers underwent a 12-hour pre-wash to enhance their dye absorption capabilities, allowing mordants and adjuvants to provide consistent results. A "mordant" connects dye to the fiber through coordination bonds. Mordanting can occur before, during, or after coloring, with factors like experimental reactions, desired shade, and toxicity indicators influencing the method chosen. Mordants, commonly used are metallic salts. They create soluble complexes by chelation.

Dyeing technique: The process begins with diluting pigment material in 10 mL of ethanol. This initial mixture is introduced into a 2 L clear water bath at 40 °C with a pH of 7. A second dilution of 10 mL of ethanol is then performed using the container with the pigment material to ensure no residue remains. This second mixture is added to the clear water bath, which is gradually heated to 50 °C. Regular mixing is maintained to ensure proper dilution. After 15 minutes of heating without any residue, the bath is prepared for use in hot dyeing.

5.4.2.2. Textile coloration

5.4.2.2.1. Natural pigments

The process of dyeing fibers with natural pigments presents interesting outcomes. When utilizing naphthazarin (ratio 1:1), a noticeable disparity emerges in the coloration of cotton

compared to silk in terms of hues as well as in color intensity (Figure 5.19). Cotton exhibits a light purple color (Figures 5.19a) and silk an intense reddish-purple color especially after 2h of dyeing (Figure 5.19c). These results imply a more robust interaction between the natural pigments and animal proteins, such as silk and wool, in contrast to their interaction with plant-based carbohydrates, such as cotton.

In addition, for the silk fabric dyed for 30 min, a slight change in coloration from reddish-purple to pinkish is observed after acetic acid treatment at pH 3, likely due to the main presence of the NH_2 form of naphthazarin. However, when the dyeing is longer (2 h), this effect is less important. Notably, neither for 30 min nor 2 h dyeing procedure, the color of the cotton fiber is altered after undergoing the rigorous rinsing process with acetic acid (Figures 5.19b and 5.19d). This suggests different organic-organic interactions.

In the case of spinochrome A (ratio 0.01:1), encouraging results were obtained considering the very low amount of colorant used. Similarly, to naphthazarin, silk takes on a distinct purplish shade (Figure 5.20a), while wool acquires an intense reddish-purple color (Figure 5.20b) coloration. Similar results (not shown) to naphthazarin are also obtained after acetic acid treatment.

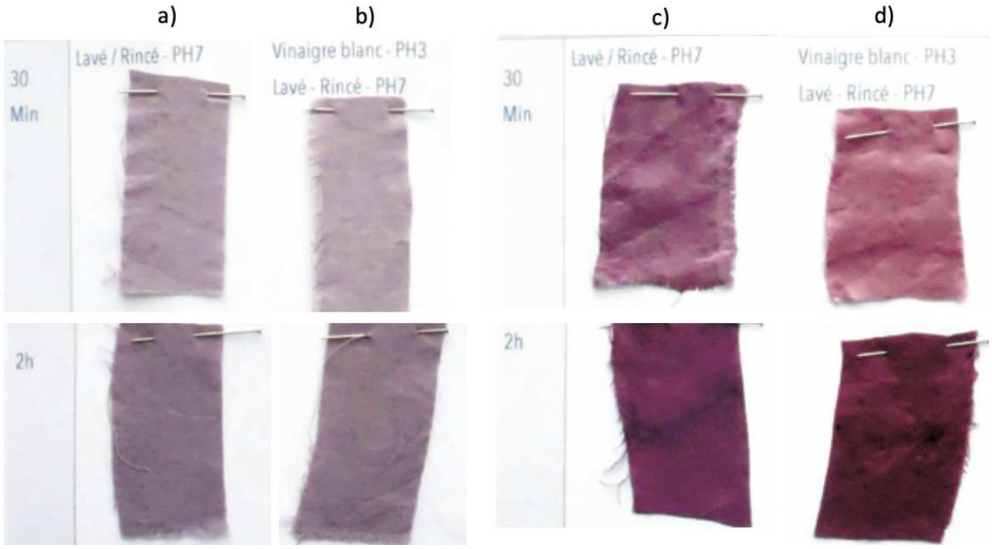

Figure 5.19. Dyeing of various fibers using naphthazarin. a) Cotton with naphthazarin for 30 min and 2 h (washed, rinsed), b) Cotton (washed, rinsed, and treated with acetic acid at pH 3) with naphthazarin for 30 min and 2 h, c) Silk with naphthazarin for 30 min and 2h (washed, rinsed), d) Silk (washed, rinsed, and treated with acetic acid at pH 3) with naphthazarin for 30 min and 2 h.

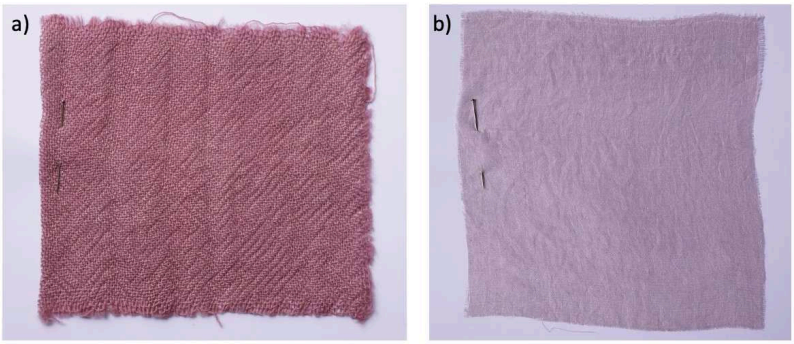

Figure 5.20. Dyeing of various fibers using spinochrome A, a) Wool with spinochrome A extracted from sea urchin spines for 2 h, b) Silk with spinochrome A extracted from sea urchin spines for 2 h.

5.4.2.2.2. Bio-hybrid pigments

When ACC-naphthazarin synthesized by vapor diffusion method was used for dyeing, cotton fibers showed no color likely due to lower naphthazarin concentration than when naphthazarin was used alone. However, silk fibers took on a purple shade (Figure 5.21a) that changed to pink after rinsing with acetic acid (Figure 5.21b)). However, when calcite-spinochrome A was used, the silk fibers exhibited no discernible coloration (Figure 5.22). These findings imply that dyes combined with ACC are more effective hybrid pigments than when paired with calcite, possibly due to the highest availability of the dye when associated with ACC than with calcite, in which some of the pigment is occluded within the calcite crystals.

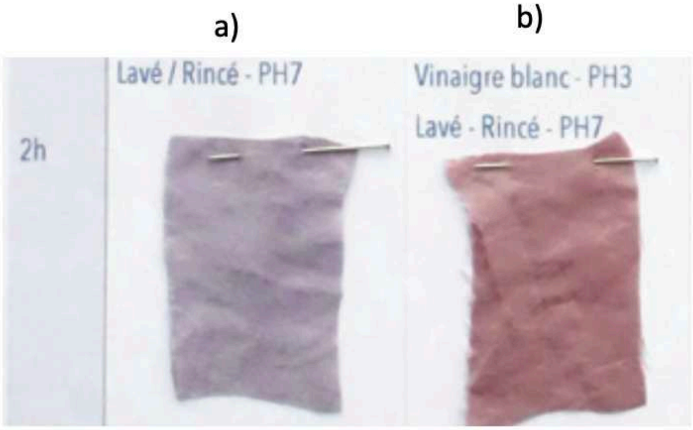

Figure 5.21. Dyeing of silk using ACC-naphthazarin synthesized by vapor diffusion a) washed, rinsed and b) washed, rinsed, and treated with acetic acid at pH 3.

Figure 5.22. Dyeing of silk using calcite-spinochrome A synthesized by direct precipitation method vapor diffusion a) washed, rinsed at pH 7.

These results underscore the potential of biogenic pigments and biohybrid pigments for meeting the demands of the textile industry. However, it is evident that further research and optimization efforts are necessary to fully harness their capabilities and achieve the desired outcomes in this field.

6

Conclusions and future perspectives

In this thesis, we seek to elucidate the intricate physicochemical mechanisms underpinning the chromatic phenomena manifested in sea urchin spines, a phenomenon presumably involving ACC precursors and naphthoquinone pigments. Concurrently, our pursuit is to acquire a comprehension of the intricate processes orchestrating the incorporation of naphthoquinones into calcite, culminating in the genesis of enduring, biogenic hybrid pigments. To elucidate this, we studied the impact of (poly)hydroxylated naphthoquinones on ACC crystallization into calcite, as well as the intricate multi-scale organic-inorganic interactions within the synthesized bioinspired hybrid pigments.

We demonstrate that naphthazarin, which is red at acidic pH and blue before ACC precipitation, leads to a lavender blue ACC powder that further crystallizes in solution into a purple mixture of calcite and vaterite that ultimately converts to a purplish-red calcite powder.

These color changes during ACC crystallization, suggest the important role pH plays as it continuously evolves during $CaCO_3$ synthesis (pH 11.5-8.5). This continuous change in pH during $CaCO_3$ synthesis leads to the incorporation/association of different species of naphthazarin (NH_2 (red color), NH^-(purple), N^{2-}(blue)), which are present at different pH (pK_1 = 8.3, pK_2 = 10.3). These *in-vitro* insights imply the possible role of pH in color transformation observed during biomineralization in sea urchins. In addition, we showed different trends of ACC stability in the presence of naphthazarin during its crystallization in solution *vs.* in air (heating). In solution, naphthazarin can stabilize as well as destabilize ACC depending upon the concentration, which was in stark contrast to the linear trend observed in air (heating) even if naphthazarin exhibited no discernible impact on the local structure of ACC. This indicates that ACC stability might arise from the interaction between ACC and naphthazarin at the surface, impeding crystallization in solution and in air. Increased ACC stability could be attributed to the presence of naphthazarin, which hinders the mobility of water molecules, or perhaps due to naphthazarin's hygroscopic nature, which may absorb moisture, keeping ACC hydration levels low and thus slowing down crystallization. Additionally, ACC formation and crystallization studies performed in the presence of lawsone and juglone revealed that the number of substituents and hydroxyl groups in a naphthoquinone plays an essential role in interaction with the Ca^{2+} ions, thus affecting the ACC formation and stability.

A thorough investigation of the organic-inorganic interactions across various scales, from the micron to atomic levels, was performed to decipher the mechanisms involved in the interaction and integration of naphthazarin molecules within calcite crystals during ACC crystallization in solution. Our observations highlighted a direct correlation between naphthazarin concentration and the color of calcite; higher naphthazarin concentrations yielded a darker purple-blue hue originating from different species of naphthazarin. The introduction of naphthazarin had a discernible impact on the crystal shape, leading to the emergence of elongated crystals. Only a minor fraction, approximately 5-10%, appeared to be incorporated within the calcite structure; the rest is adsorbed on the surface. These findings are consistent with the notion that most naphthazarin adheres to the crystal surface, potentially causing localized irregularities in crystal growth and giving rise to rhombohedral crystal-shaped voids at the surface. Even though most of the naphthazarin was adsorbed on the surface of the calcite, the interactions between calcite and naphthazarin were relatively strong as the mixing of ACC+naphthazarin or calcite-naphthazarin in water and ethanol did not lead to the leaching of color. Intriguingly, the incorporation did not induce significant lattice distortion, suggesting a low concentration of

naphthazarin incorporation. Subsequent analysis of FIB sections of calcite-naphthazarin revealed a non-homogeneous distribution of naphthazarin within the calcite as regions exhibited a higher organic signal than others. Our observations also indicated the presence of an additional phase within the calcite, which aligned well with the disappearance of Bragg peaks upon heating, implying a conversion of the amorphous phase into calcite. Through NMR, we found that naphthazarin might exist in different molecular states, i.e., deprotonated form. In calcite+naphthazarin, we observed the splitting of the carbonyl peak, suggesting the dynamic exchange of protons has stopped. Additionally, the downfield shifts in the peak position of naphthazarin on calcite+naphthazarin highlight the possible structural change in naphthazarin that could be induced by deprotonation or interaction between naphthazarin and $CaCO_3$. 2D NMR experiments confirmed the presence of water molecules and naphthazarin in close proximity to the carbonate ions of the calcite.

These findings have broad implications for biomineral pigmentation, color stability, and bio-inspired hybrid pigment applications. *In-vivo* insights highlight the intriguing color transformation in sea urchin spines during ACC formation, suggesting a possible role of pH in biomineral coloration. Additionally, our research opens possibilities for bio-inspired coloration, enabling the synthesis of diverse pigments for textiles, paints, and art. These pigments, inspired by sea urchin spines, offer photostability and thermal resistance (up to 400 ºC), catering to the demand for long-lasting and eco-friendly coloration methods in various industries.

Based on ACC formation and crystallization findings in the presence of naphthazarin, the study was extended to pigments extracted from sea urchin spines. These findings provide compelling evidence of spinochrome A's distinct interaction with calcite, setting it apart from its counterparts, spinochromes B and E. Spinochrome A emerges as a pivotal actor in the $CaCO_3$ crystallization process, notably hindering the transformation into the calcite phase. Furthermore, it exhibits a unique mode of interaction that leaves a relatively modest impact on the atomic structure and overall morphology of calcite crystals compared to the effects induced by spinochrome B and E. This unique behavior implies a potential rationale for the preferential incorporation of spinochrome A into *Paracentrotus lividus* sea urchin spines, which are synthesized by red spherule cells housing all three spinochromes. Spinochrome A's capacity to interact with calcite while preserving a closer resemblance to the original crystal structure positions it as an ideal candidate for influencing the coloration but not the structure of sea

urchin spines. This observation underscores the pivotal role of molecular-level interactions in the intricate processes governing biomineralization. It is essential to note that at this stage of our analysis, we lack information regarding whether the pigments are incorporated within the calcite or merely adsorbed on its surface. Further investigation, such as STEM-EELS, is required to shed light on the mechanisms of pigment molecule incorporation.

To delve deeper into our investigation, it is imperative to include the presence of PHNQ molecules when monitoring the formation and crystallization of ACC. This addition will enable the study of any color changes that occur during ACC formation and crystallization, resembling the processes that occur during biomineralization in sea urchins. Additionally, we need to adjust the synthesis methods, as biomineralization typically transpires within a pH range of 6 to 9. A proposed modification involves implementing an *in-situ* monitoring approach using the vapor diffusion method. This method is well-suited for observing the intricate processes and color changes associated with ACC formation, offering valuable insights into biomineralization akin to those found in sea urchins. Additionally, titration between Ca^{2+} and different PHNQs should be performed to analyse the affinity towards each other.

Furthermore, it is essential to explore the effect of macromolecules along with PHNQs extracted from sea urchin spines. The comprehensive analysis of these elements collectively will provide us with a more comprehensive understanding of the color changes that occur during the biomineralization process in sea urchin spines. By combining these various studies, we can gain deeper insights into the mechanisms behind this natural phenomenon.

References

A. P. Hammersley, A.N.F., S.O. Svensson, M. Hanfland, Hausermann, D., 1996. Two-dimensional detector software: From real detector to idealised image or two-theta scan. High Pressure Research 14, 235–248. https://doi.org/10.1080/08957959608201408

Abd-Elghany, M., Klapötke, T.M., 2018. A review on differential scanning calorimetry technique and its importance in the field of energetic materials. Physical Sciences Reviews 3. https://doi.org/10.1515/psr-2017-0103

Addadi, L., Aizenberg, J., Beniash, E., Weiner, S., 1999. On the Concept of a Single Crystal in Biomineralization, in: Braga, D., Grepioni, F., Orpen, A.G. (Eds.), Crystal Engineering: From Molecules and Crystals to Materials, NATO Science Series. Springer Netherlands, Dordrecht, pp. 1–22. https://doi.org/10.1007/978-94-011-4505-3_1

Addadi, L., Raz, S., Weiner, S., 2003. Taking Advantage of Disorder: Amorphous Calcium Carbonate and Its Roles in Biomineralization. Adv. Mater. 15, 959–970. https://doi.org/10.1002/adma.200300381

Aizenberg, J., Addadi, L., Weiner, S., Lambert, G., 1996. Stabilization of amorphous calcium carbonate by specialized macromolecules in biological and synthetic precipitates. Advanced Materials 8, 222–226. https://doi.org/10.1002/adma.19960080307

Aizenberg, J., Hanson, J., Ilan, M., Leiserowitz, L., Koetzle, T.F., Addadi, L., Weiner, S., 1995. Morphogenesis of calcitic sponge spicules: a role for specialized proteins interacting with growing crystals. FASEB j. 9, 262–268. https://doi.org/10.1096/fasebj.9.2.7781928

Aizenberg, Joanna, Hanson, J., Koetzle, T.F., Leiserowitz, L., Weiner, S., Addadi, L., 1995. Biologically Induced Reduction in Symmetry: A Study of Crystal Texture of Calcitic Sponge Spicules. Chem. Eur. J. 1, 414–422. https://doi.org/10.1002/chem.19950010705

Aizenberg, J., Hanson, J., Koetzle, T.F., Weiner, S., Addadi, L., 1997. Control of Macromolecule Distribution within Synthetic and Biogenic Single Calcite Crystals. J. Am. Chem. Soc. 119, 881–886. https://doi.org/10.1021/ja9628821

Aizenberg, J., Lambert, G., Weiner, S., Addadi, L., 2002. Factors Involved in the Formation of Amorphous and Crystalline Calcium Carbonate: A Study of an Ascidian Skeleton. J. Am. Chem. Soc. 124, 32–39. https://doi.org/10.1021/ja016990l

Aizenberg, J., Weaver, J.C., Thanawala, M.S., Sundar, V.C., Morse, D.E., Fratzl, P., 2005. Skeleton of Euplectella sp.: structural hierarchy from the nanoscale to the macroscale. Science 309, 275–278. https://doi.org/10.1126/science.1112255

Akhtar, K., Khan, S.A., Khan, S.B., Asiri, A.M., 2018. Scanning Electron Microscopy: Principle and Applications in Nanomaterials Characterization, in: Sharma, S.K. (Ed.), Handbook of Materials Characterization. Springer International Publishing, Cham, pp. 113–145. https://doi.org/10.1007/978-3-319-92955-2_4

Albeck, S., Aizenberg, J., Addadi, L., Weiner, S., 1993. Interactions of various skeletal intracrystalline components with calcite crystals. J. Am. Chem. Soc. 115, 11691–11697. https://doi.org/10.1021/ja00078a005

Albeck, S., Weiner, S., Addadi, L., 1996. Polysaccharides of Intracrystalline Glycoproteins Modulate Calcite Crystal Growth In Vitro. Chem. Eur. J. 2, 278–284. https://doi.org/10.1002/chem.19960020308

Albéric, M., Bertinetti, L., Zou, Z., Fratzl, P., Habraken, W., Politi, Y., 2018a. The Crystallization of Amorphous Calcium Carbonate is Kinetically Governed by Ion Impurities and Water. Advanced Science 5, 1701000. https://doi.org/10.1002/advs.201701000

Albéric, M., Caspi, E.N., Bennet, M., Ajili, W., Nassif, N., Azaïs, T., Berner, A., Fratzl, P., Zolotoyabko, E., Bertinetti, L., Politi, Y., 2018b. Interplay between Calcite, Amorphous Calcium Carbonate, and Intracrystalline Organics in Sea Urchin Skeletal Elements. Crystal Growth & Design 18, 2189–2201. https://doi.org/10.1021/acs.cgd.7b01622

Albéric, M., Stifler, C.A., Zou, Z., Sun, C.-Y., Killian, C.E., Valencia, S., Mawass, M.-A., Bertinetti, L., Gilbert, P.U.P.A., Politi, Y., 2019. Growth and regrowth of adult sea urchin spines involve hydrated and anhydrous amorphous calcium carbonate precursors. Journal of Structural Biology: X 1, 100004. https://doi.org/10.1016/j.yjsbx.2019.100004

Albéric, M., Zolotoyabko, E., Spaeker, O., Li, C., Tadayon, M., Schmitt, C.N.Z., Politi, Y., Bertinetti, L., Fratzl, P., 2022. Heat-Mediated Micro- and Nano-pore Evolution in Sea Urchin Biominerals. Crystal Growth & Design 22, 3727–3739. https://doi.org/10.1021/acs.cgd.2c00083

Anderson, H.A., Mathieson, J.W., Thomson, R.H., 1969. Distribution of spinochrome pigments in echinoids. Comp Biochem Physiol 28, 333–345. https://doi.org/10.1016/0010-406x(69)91347-4

Anderson, H.C., Garimella, R., Tague, S.E., 2005. The role of matrix vesicles in growth plate development and biomineralization. Front Biosci 10, 822–837. https://doi.org/10.2741/1576

Ashnagar, A., Shiri, A., 1941. Isolation and characterization of 2-hydroxy-1,4-naphthoquinone (lawsone) from the powdered leaves of henna plant marketed in Ahwaz city of Iran. International Journal of ChemTech Research 3, 974–4290.

Auyong, T.K., Westfall, B.A., Russell, R.L., 1963. Pharmacological aspects of juglone. Toxicon 1, 235–239. https://doi.org/10.1016/0041-0101(63)90005-9

Babula, P., Adam, V., Havel, L., Kizek, R., 2009. Noteworthy Secondary Metabolites Naphthoquinones-their Occurrence, Pharmacological Properties and Analysis. Current Pharmaceutical Analysis 5, 47–68. https://doi.org/10.2174/157341209787314936

Bahrom, H., Goncharenko, A., Fatkhutdinova, L., Peltek, O., Koval, O., Eliseev, I., Manchev, A., Gorin, D., Shishkin, I., Noskov, R., Timin, A., Ginzburg, P., Zyuzin, M., Fatkhutdinova, L., Muslimov, A., Koval, O., Barhum, H., 2019. Controllable Synthesis of Calcium Carbonate with Different Geometry: Comprehensive Analysis of Particle Formation, Cellular Uptake, and Biocompatibility. ACS Sustainable Chemistry & Engineering XXXX. https://doi.org/10.1021/acssuschemeng.9b05128

Bak, M., Rasmussen, J.T., Nielsen, N.C., 2000. SIMPSON: A General Simulation Program for Solid-State NMR Spectroscopy. Journal of Magnetic Resonance 147, 296–330. https://doi.org/10.1006/jmre.2000.2179

Bandaranayake, W.M., 2006. The nature and role of pigments of marine invertebrates. Nat. Prod. Rep. 23, 223–255. https://doi.org/10.1039/B307612C

Bauchau, V., 2001. Developmental stability as the primary function of the pigmentation patterns in bivalve shells? Belg. J. Zool. 131, 23–28.

Bazylinski, D.A., Frankel, R.B., 2003. Biologically Controlled Mineralization in Prokaryotes. Reviews in Mineralogy and Geochemistry 54, 217–247. https://doi.org/10.2113/0540217

Bechtel, P.J., Oliveira, A.C.M., Demir, N., Smiley, S., 2013. Chemical composition of the giant red sea cucumber, Parastichopus californicus, commercially harvested in Alaska. Food Science & Nutrition 1, 63–73. https://doi.org/10.1002/fsn3.12

Belcher, A.M., Wu, X.H., Christensen, R.J., Hansma, P.K., Stucky, G.D., Morse, D.E., 1996. Control of crystal phase switching and orientation by soluble mollusc-shell proteins. Nature 381, 56–58. https://doi.org/10.1038/381056a0

Beniash, E., Addadi, L., Weiner, S., 1999. Cellular control over spicule formation in sea urchin embryos: A structural approach. J Struct Biol 125, 50–62. https://doi.org/10.1006/jsbi.1998.4081

Beniash, E., Aizenberg, J., Addadi, L., Weiner, S., 1997. Amorphous calcium carbonate transforms into calcite during sea urchin larval spicule growth. Proc. R. Soc. Lond. B 264, 461–465. https://doi.org/10.1098/rspb.1997.0066

Bentes, A.L.A., Borges, R.S., Monteiro, W.R., De Macedo, L.G.M., Alves, C.N., 2011. Structure of Dihydrochalcones and Related Derivatives and Their Scavenging and Antioxidant Activity against Oxygen and Nitrogen Radical Species. Molecules 16, 1749–1760. https://doi.org/10.3390/molecules16021749

Benzerara, K., Skouri-Panet, F., Li, J., Férard, C., Gugger, M., Laurent, T., Couradeau, E., Ragon, M., Cosmidis, J., Menguy, N., Margaret-Oliver, I., Tavera, R., López-García, P., Moreira, D., 2014. Intracellular Ca-carbonate biomineralization is widespread in cyanobacteria. Proceedings of the National Academy of Sciences 111, 10933–10938. https://doi.org/10.1073/pnas.1403510111

Berman, A., Addadi, L., Kvick, Å., Leiserowitz, L., Nelson, M., Weiner, S., 1990. Intercalation of Sea Urchin Proteins in Calcite: Study of a Crystalline Composite Material. Science 250, 664–667. https://doi.org/10.1126/science.250.4981.664

Berman, A., Addadi, L., Weiner, S., 1988. Interactions of sea-urchin skeleton macromolecules with growing calcite crystals- a study of intracrystalline proteins. Nature 331, 546–548. https://doi.org/10.1038/331546a0

Berman, A., Hanson, J., Leiserowitz, L., Koetzle, T.F., Weiner, S., n.d. Biological Control of Crystal Texture: A Widespread Strategy for Adapting Crysta Properties to Function.

Berman, A., Hanson, J., Leiserowitz, L., Koetzle, T.F., Weiner, S., Addadi, L., 1993. Crystal-protein interactions: controlled anisotropic changes in crystal microtexture. J. Phys. Chem. 97, 5162–5170. https://doi.org/10.1021/j100121a052

Berna, F., 2017. Fourier Transform Infrared Spectroscopy (FTIR), in: Gilbert, A.S. (Ed.), Encyclopedia of Geoarchaeology, Encyclopedia of Earth Sciences Series. Springer Netherlands, Dordrecht, pp. 285–286. https://doi.org/10.1007/978-1-4020-4409-0_15

Bindschedler, S., Cailleau, G., Verrecchia, E., 2016. Role of Fungi in the Biomineralization of Calcite. Minerals 6, 41. https://doi.org/10.3390/min6020041

Blondeau, M., Sachse, M., Boulogne, C., Gillet, C., Guigner, J.-M., Skouri-Panet, F., Poinsot, M., Ferard, C., Miot, J., Benzerara, K., 2018. Amorphous Calcium Carbonate Granules Form

Within an Intracellular Compartment in Calcifying Cyanobacteria. Frontiers in Microbiology 9.

Blowes, L.M., Egertová, M., Liu, Y., Davis, G.R., Terrill, N.J., Gupta, H.S., Elphick, M.R., 2017. Body wall structure in the starfish Asterias rubens. J Anat 231, 325–341. https://doi.org/10.1111/joa.12646

Bolan, N.S., Kandaswamy, K., 2005. pH, in: Hillel, D. (Ed.), Encyclopedia of Soils in the Environment. Elsevier, Oxford, pp. 196–202. https://doi.org/10.1016/B0-12-348530-4/00210-1

Borukhin, S., Bloch, L., Radlauer, T., Hill, A.H., Fitch, A.N., Pokroy, B., 2012. Screening the Incorporation of Amino Acids into an Inorganic Crystalline Host: the Case of Calcite. Adv. Funct. Mater. 22, 4216–4224. https://doi.org/10.1002/adfm.201201079

Brasseur, L., Hennebert, E., Fievez, L., Caulier, G., Bureau, F., Tafforeau, L., Flammang, P., Gerbaux, P., Eeckhaut, I., 2017. The Roles of Spinochromes in Four Shallow Water Tropical Sea Urchins and Their Potential as Bioactive Pharmacological Agents. Marine Drugs 15, 179. https://doi.org/10.3390/md15060179

Broadbent, A.D., 2001. Basic principles of textile coloration. Society of Dyers and Colourists, Bradford, West Yorkshire.

Bumbrah, G.S., Sharma, R.M., 2016. Raman spectroscopy – Basic principle, instrumentation and selected applications for the characterization of drugs of abuse. Egyptian Journal of Forensic Sciences 6, 209–215. https://doi.org/10.1016/j.ejfs.2015.06.001

Bushuev, Y.G., Finney, A.R., Rodger, P.M., 2015. Stability and Structure of Hydrated Amorphous Calcium Carbonate. Crystal Growth & Design 15, 5269–5279. https://doi.org/10.1021/acs.cgd.5b00771

Camerini, R., Poggi, G., Chelazzi, D., Ridi, F., Giorgi, R., Baglioni, P., 2019. The carbonation kinetics of calcium hydroxide nanoparticles: A Boundary Nucleation and Growth description. Journal of Colloid and Interface Science 547, 370–381. https://doi.org/10.1016/j.jcis.2019.03.089

Carl, A.D., Kalan, R.E., Obayemi, J.D., Zebaze Kana, M.G., Soboyejo, W.O., Grimm, R.L., 2017. Synthesis and Characterization of Alkylamine-Functionalized Si(111) for Perovskite Adhesion With Minimal Interfacial Oxidation or Electronic Defects. ACS Appl. Mater. Interfaces 9, 34377–34388. https://doi.org/10.1021/acsami.7b07117

Chen, S.-F., Cölfen, H., Antonietti, M., Yu, S.-H., 2013. Ethanol assisted synthesis of pure and stable amorphous calcium carbonate nanoparticles. Chem. Commun. 49, 9564–9566. https://doi.org/10.1039/C3CC45427D

Chujo, Y., 2007. Organic – Inorganic Nano-Hybrid Materials.

Clarà Saracho, A., Haigh, S.K., Hata, T., Soga, K., Farsang, S., Redfern, S.A.T., Marek, E., 2020. Characterisation of CaCO3 phases during strain-specific ureolytic precipitation. Sci Rep 10, 10168. https://doi.org/10.1038/s41598-020-66831-y

Clark, A.M., Jurgens, T.M., Hufford, C.D., 1990. Antimicrobial activity of juglone. Phytotherapy Research 4, 11–14. https://doi.org/10.1002/ptr.2650040104

Clark, S., Colas, B., Jacob, D., Neuefeind, J., Wang, H.-W., Page, K., Soper, A., Schodder, P., Duchstein, P., Apeleo Zubiri, B., Yokosawa, T., Pipich, V., Zahn, D., Spiecker, E., Wolf, S., 2022. The nano- and meso-scale structure of amorphous calcium carbonate. Scientific Reports 12. https://doi.org/10.1038/s41598-022-10627-9

Coates, C.J., McCulloch, C., Betts, J., Whalley, T., 2018. Echinochrome A Release by Red Spherule Cells Is an Iron-Withholding Strategy of Sea Urchin Innate Immunity. J Innate Immun 10, 119–130. https://doi.org/10.1159/000484722

Colaric, M., Veberic, R., Solar, A., Hudina, M., Stampar, F., 2005. Phenolic Acids, Syringaldehyde, and Juglone in Fruits of Different Cultivars of Juglans regia L. J. Agric. Food Chem. 53, 6390–6396. https://doi.org/10.1021/jf050721n

Columbia Technology Ventures [WWW Document], n.d. URL https://inventions.techventures.columbia.edu/technologies/xpdfsuite-an-end-to--M11-120/licenses/113 (accessed 8.1.23).

Couradeau, E., Benzerara, K., Gérard, E., Moreira, D., Bernard, S., Brown, G.E., López-García, P., 2012. An early-branching microbialite cyanobacterium forms intracellular carbonates. Science 336, 459–462. https://doi.org/10.1126/science.1216171

Crenshaw, M.A., 1972. The Inorganic Composition of Molluscan Extrapallial Fluid. Biological Bulletin 143, 506–512. https://doi.org/10.2307/1540180

Crichton, R.R., 2012. Chapter 19 - Biomineralisation, in: Crichton, R.R. (Ed.), Biological Inorganic Chemistry (Second Edition). Elsevier, Oxford, pp. 359–378. https://doi.org/10.1016/B978-0-444-53782-9.00019-X

Cusack, M., Curry, G., Clegg, H., Abbott, G., 1992. An intracrystalline chromoprotein from red brachiopod shells: Implications for the process of biomineralization. Comparative Biochemistry and Physiology Part B: Comparative Biochemistry 102, 93–95. https://doi.org/10.1016/0305-0491(92)90278-Y

Darkins, R., Kim, Y.-Y., Green, D.C., Broad, A., Duffy, D.M., Meldrum, F.C., Ford, I.J., 2022. Calcite Kinetics for Spiral Growth and Two-Dimensional Nucleation. Crystal Growth & Design 22, 4431–4436. https://doi.org/10.1021/acs.cgd.2c00378

Dayan, F.E., Duke, S.O., 2014. Natural Compounds as Next-Generation Herbicides. PLANT PHYSIOLOGY 166, 1090–1105. https://doi.org/10.1104/pp.114.239061

de Frutos, M., Rodríguez-Navarro, A.B., Li, X., Checa, A.G., 2023. Nanoscale Analysis of the Structure and Composition of Biogenic Calcite Reveals the Biomineral Growth Pattern. ACS Nano 17, 2829–2839. https://doi.org/10.1021/acsnano.2c11169

De Queiroga, L.N.F., França, D.B., Rodrigues, F., Santos, I.M.G., Fonseca, M.G., Jaber, M., 2019. Functionalized bentonites for dye adsorption: Depollution and production of new pigments. Journal of Environmental Chemical Engineering 7, 103333. https://doi.org/10.1016/j.jece.2019.103333

De Yoreo, J.J., Gilbert, P.U.P.A., Sommerdijk, N.A.J.M., Penn, R.L., Whitelam, S., Joester, D., Zhang, H., Rimer, J.D., Navrotsky, A., Banfield, J.F., Wallace, A.F., Michel, F.M., Meldrum, F.C., Cölfen, H., Dove, P.M., 2015. Crystallization by particle attachment in synthetic, biogenic, and geologic environments. Science 349. https://doi.org/10.1126/science.aaa6760

Deng, Z., Jia, Z., Li, L., 2022. Biomineralized Materials as Model Systems for Structural Composites: Intracrystalline Structural Features and Their Strengthening and Toughening Mechanisms. Advanced Science 9, 2103524. https://doi.org/10.1002/advs.202103524

Devi, S.P., Kumaria, S., Rao, S.R., Tandon, P., 2016. Carnivorous Plants as a Source of Potent Bioactive Compound: Naphthoquinones. Tropical Plant Biol. 9, 267–279. https://doi.org/10.1007/s12042-016-9177-0

Differential Scanning Calorimeters - TA Instruments, n.d. URL https://www.tainstruments.com/products/thermal-analysis/differential-scanning-calorimeters/ (accessed 7.26.23).

Donnay, G., Pawson, D.L., 1969. X-ray Diffraction Studies of Echinoderm Plates. Science 166, 1147–1150. https://doi.org/10.1126/science.166.3909.1147

Drozdov, A.L., Sharmankina, V.V., Zemnukhova, L.A., Polyakova, N.V., 2016. Chemical composition of spines and tests of sea urchins. Biol Bull Russ Acad Sci 43, 521–531. https://doi.org/10.1134/S1062359016060078

Du, H., Amstad, E., 2020. Water: How Does It Influence the CaCO3 Formation? Angewandte Chemie International Edition 59, 1798–1816. https://doi.org/10.1002/anie.201903662

Du, H., Steinacher, M., Borca, C., Huthwelker, T., Murello, A., Stellacci, F., Amstad, E., 2018. Amorphous CaCO3: Influence of the Formation Time on Its Degree of Hydration and Stability. J. Am. Chem. Soc. 140, 14289–14299. https://doi.org/10.1021/jacs.8b08298

Dubois, P., Ameye, L., 2001. Regeneration of spines and pedicellariae in echinoderms: A review. Microscopy Research and Technique 55, 427–437. https://doi.org/10.1002/jemt.1188

Duffey, S.S., Stout, M.J., 1996. Antinutritive and toxic components of plant defense against insects. Archives of Insect Biochemistry and Physiology 32, 3–37. https://doi.org/10.1002/(SICI)1520-6327(1996)32:1<3::AID-ARCH2>3.0.CO;2-1

Dulo, B., Phan, K., Githaiga, J., Raes, K., De Meester, S., 2021. Natural Quinone Dyes: A Review on Structure, Extraction Techniques, Analysis and Application Potential. Waste Biomass Valor 12, 6339–6374. https://doi.org/10.1007/s12649-021-01443-9

Egorov, E.A., Alekhina, V.A., Volobueva, T.M., Fedoreev, S.A., Mishchenko, N.P., Kol'tsova, E.A., 1999. [Histochrome, a new antioxidant, in the treatment of ocular diseases]. Vestn Oftalmol 115, 34–35.

Eilenberg, H., Zilberstein, A., 2008. Carnivorous Pitcher Plants – Towards Understanding the Molecular Basis of Prey Digestion. pp. 287–294.

Elkhateeb, W., Elnahas, M.O., Daba, G., 2022. Fungal Calcium Carbonate Mineralization as a Microbial Approach for Concrete Self-Healing. Geomicrobiology Journal 39, 631–636. https://doi.org/10.1080/01490451.2022.2060383

El-Shaer, N.S., Badr, J.M., Aboul-Ela, M.A., Gohar, Y.M., 2007. Determination of lawsone in henna powders by high performance thin layer chromatography. J Sep Sci 30, 3311–3315. https://doi.org/10.1002/jssc.200700223

Falini, G., Albeck, S., Weiner, S., Addadi, L., 1996. Control of Aragonite or Calcite Polymorphism by Mollusk Shell Macromolecules. Science 271, 67–69. https://doi.org/10.1126/science.271.5245.67

Fang, F., Chen, S., Ma, J., Cui, J., Li, Q., Meng, G., Wang, L., 2018. Juglone suppresses epithelial-mesenchymal transition in prostate cancer cells via the protein kinase B/glycogen synthase kinase-3β/Snail signaling pathway. Oncology Letters 16, 2579–2584. https://doi.org/10.3892/ol.2018.8885

Feng, Q.L., Pu, G., Pei, Y., Cui, F.Z., Li, H.D., Kim, T.N., 2000. Polymorph and morphology of calcium carbonate crystals induced by proteins extracted from mollusk shell. Journal of Crystal Growth 216, 459–465. https://doi.org/10.1016/S0022-0248(00)00396-1

Fois, E., Gamba, A., Tilocca, A., 2003. On the unusual stability of Maya blue paint: Molecular dynamics simulations. Microporous and Mesoporous Materials - MICROPOROUS MESOPOROUS MAT 57, 263–272. https://doi.org/10.1016/S1387-1811(02)00596-6

Fontaine, A.R., 1962a. The Colours of Ophiocomina Nigra (Abildgaard): I Colour Variation and its Relation to Distribution. Journal of the Marine Biological Association of the United Kingdom 42, 1–8. https://doi.org/10.1017/S0025315400004422

Fontaine, A.R., 1962b. The Colours of Ophiocomina Nigra (Abildgaard): II. The Occurrence of Melanin and Fluorescent Pigments. Journal of the Marine Biological Association of the United Kingdom 42, 9–31. https://doi.org/10.1017/S0025315400004434

Foran, E., Weiner, S., Fine, M., 2013. Biogenic Fish-gut Calcium Carbonate is a Stable Amorphous Phase in the Gilt-head Seabream, Sparus aurata. Scientific Reports 3. https://doi.org/10.1038/srep01700

Fox, D.L., Hopkins, T.S., 1966. The comparative biochemistry of pigments. Physiology of echinodermata 277–300.

Fratzl, P., S. Gupta, H., P. Paschalis, E., Roschger, P., 2004. Structure and mechanical quality of the collagen– mineral nano-composite in bone. Journal of Materials Chemistry 14, 2115–2123. https://doi.org/10.1039/B402005G

Fratzl, P., Weinkamer, R., 2007. Nature's hierarchical materials. Progress in Materials Science 52, 1263–1334. https://doi.org/10.1016/j.pmatsci.2007.06.001

Fritsch, E., Rossman, G.R., 1987. An Update on Color in Gems. Part 1: Introduction and Colors Caused by Dispersed Metal Ions. Gems & Gemology 23, 126–139. https://doi.org/10.5741/GEMS.23.3.126

Frølich, S., Sørensen, H.O., Hakim, S.S., Marin, F., Stipp, S.L.S., Birkedal, H., 2015. Smaller Calcite Lattice Deformation Caused by Occluded Organic Material in Coccoliths than in Mollusk Shell. Crystal Growth & Design 15, 2761–2767. https://doi.org/10.1021/acs.cgd.5b00118

Fudouzi, H., 2011. Tunable structural color in organisms and photonic materials for design of bioinspired materials. Science and Technology of Advanced Materials 12, 064704. https://doi.org/10.1088/1468-6996/12/6/064704

Gal, A., Habraken, W., Gur, D., Fratzl, P., Weiner, S., Addadi, L., 2013. Calcite Crystal Growth by a Solid-State Transformation of Stabilized Amorphous Calcium Carbonate Nanospheres in a

Hydrogel. Angewandte Chemie International Edition 52, 4867–4870. https://doi.org/10.1002/anie.201210329

Gal, A., Kahil, K., Vidavsky, N., DeVol, R.T., Gilbert, P.U.P.A., Fratzl, P., Weiner, S., Addadi, L., 2014. Particle Accretion Mechanism Underlies Biological Crystal Growth from an Amorphous Precursor Phase. Advanced Functional Materials 24, 5420–5426. https://doi.org/10.1002/adfm.201400676

Gal, A., Sorrentino, A., Kahil, K., Pereiro, E., Faivre, D., Scheffel, A., 2018. Native-state imaging of calcifying and noncalcifying microalgae reveals similarities in their calcium storage organelles. Proceedings of the National Academy of Sciences 115, 11000–11005. https://doi.org/10.1073/pnas.1804139115

Gal, A., Wirth, R., Kopka, J., Fratzl, P., Faivre, D., Scheffel, A., 2016. Macromolecular recognition directs calcium ions to coccolith mineralization sites. Science 353, 590–593. https://doi.org/10.1126/science.aaf7889

Galano, A., Mazzone, G., Alvarez-Diduk, R., Marino, T., Alvarez-Idaboy, J.R., Russo, N., 2016. Food Antioxidants: Chemical Insights at the Molecular Level. Annual Review of Food Science and Technology 7, 335–352. https://doi.org/10.1146/annurev-food-041715-033206

García-Martínez, J.-M., Collar, E.P., 2021. Organic–Inorganic Hybrid Materials. Polymers 13, 86. https://doi.org/10.3390/polym13010086

Gebauer, D., Gunawidjaja, P.N., Ko, J.Y.P., Bacsik, Z., Aziz, B., Liu, L., Hu, Y., Bergström, L., Tai, C.-W., Sham, T.-K., Edén, M., Hedin, N., 2010. Proto-Calcite and Proto-Vaterite in Amorphous Calcium Carbonates. Angewandte Chemie International Edition 49, 8889–8891. https://doi.org/10.1002/anie.201003220

Geng, X., Liu, L., Jiang, J., Yu, S.-H., 2010. Crystallization of CaCO 3 Mesocrystals and Complex Aggregates in a Mixed Solvent Media Using Polystyrene Sulfonate as a Crystal Growth Modifier. Crystal Growth & Design - CRYST GROWTH DES 10, 3448–3453. https://doi.org/10.1021/cg100206y

Ghannam, L., Garay, H., Shanahan, M.E.R., François, J., Billon, L., 2005. A New Pigment Type: Colored Diblock Copolymer−Mica Composites. Chem. Mater. 17, 3837–3843. https://doi.org/10.1021/cm0478024

Gilbert, P.U.P.A., Bergmann, K.D., Boekelheide, N., Tambutté, S., Mass, T., Marin, F., Adkins, J.F., Erez, J., Gilbert, B., Knutson, V., Cantine, M., Hernández, J.O., Knoll, A.H., 2022. Biomineralization: Integrating mechanism and evolutionary history. Science Advances 8, eabl9653. https://doi.org/10.1126/sciadv.abl9653

Gill, P., Moghadam, T.T., Ranjbar, B., 2010. Differential Scanning Calorimetry Techniques: Applications in Biology and Nanoscience. Journal of Biomolecular Techniques : JBT 21, 167.

Gilow, C., Zolotoyabko, E., Paris, O., Fratzl, P., Aichmayer, B., 2011. Nanostructure of Biogenic Calcite Crystals: A View by Small-Angle X-Ray Scattering. Crystal Growth & Design 11, 2054–2058. https://doi.org/10.1021/cg200136t

Gong, Y.U.T., Killian, C.E., Olson, I.C., Appathurai, N.P., Amasino, A.L., Martin, M.C., Holt, L.J., Wilt, F.H., Gilbert, P.U.P.A., 2012. Phase transitions in biogenic amorphous calcium carbonate. Proc. Natl. Acad. Sci. U.S.A. 109, 6088–6093. https://doi.org/10.1073/pnas.1118085109

Goodwin, A.L., Michel, F.M., Phillips, B.L., Keen, D.A., Dove, M.T., Reeder, R.J., 2010. Nanoporous Structure and Medium-Range Order in Synthetic Amorphous Calcium Carbonate. Chem. Mater. 22, 3197–3205. https://doi.org/10.1021/cm100294d

Goodwin, T.W., Srisukh, S., 1950. A study of the pigments of the sea-urchins, *Echinus esculentus* L. and *Paracentrotus lividus* Lamarck. Biochemical Journal 47, 69–76. https://doi.org/10.1042/bj0470069

Gower, L.A., Tirrell, D.A., 1998. Calcium carbonate films and helices grown in solutions of poly(aspartate). Journal of Crystal Growth 191, 153–160. https://doi.org/10.1016/S0022-0248(98)00002-5

Gower, L.B., 2008. Biomimetic Model Systems for Investigating the Amorphous Precursor Pathway and Its Role in Biomineralization. Chem. Rev. 108, 4551–4627. https://doi.org/10.1021/cr800443h

Gower, L.B., Odom, D.J., 2000. Deposition of calcium carbonate films by a polymer-induced liquid-precursor (PILP) process. Journal of Crystal Growth 210, 719–734. https://doi.org/10.1016/S0022-0248(99)00749-6

Granite, n.d. What is Raman Spectroscopy? | Raman Spectroscopy Principle [WWW Document]. Edinburgh Instruments. URL https://www.edinst.com/us/blog/what-is-raman-spectroscopy/ (accessed 7.25.23).

Gürses, A., Açıkyıldız, M., Güneş, K., Gürses, M.S., 2016. Dyes and Pigments, SpringerBriefs in Molecular Science. Springer International Publishing, Cham. https://doi.org/10.1007/978-3-319-33892-7

Hachtel, J.A., Lupini, A.R., Idrobo, J.C., 2018. Exploring the capabilities of monochromated electron energy loss spectroscopy in the infrared regime. Sci Rep 8, 5637. https://doi.org/10.1038/s41598-018-23805-5

Han, T.Y.-J., Aizenberg, J., 2008. Calcium Carbonate Storage in Amorphous Form and Its Template-Induced Crystallization. Chem. Mater. 20, 1064–1068. https://doi.org/10.1021/cm702032v

Harris, J., Mey, I., Hajir, M., Mondeshki, M., Wolf, S.E., 2015. Pseudomorphic transformation of amorphous calcium carbonate films follows spherulitic growth mechanisms and can give rise to crystal lattice tilting. CrystEngComm 17, 6831–6837. https://doi.org/10.1039/C5CE00441A

Hartmann, S.R., Hahn, E.L., 1962. Nuclear Double Resonance in the Rotating Frame. Phys. Rev. 128, 2042–2053. https://doi.org/10.1103/PhysRev.128.2042

Hashem, E., Sedaira, H., Idriss, K.A., Soliman, S., 2000. Spectrophotometric study of the complexation equilibria of zinc(II) with lawsone, juglone and naphthazarin.

Hashimoto, H., Goda, M., Futahashi, R., Kelsh, R., Akiyama, T. (Eds.), 2021. Pigments, Pigment Cells and Pigment Patterns. Springer Singapore, Singapore. https://doi.org/10.1007/978-981-16-1490-3

Haunost, M., Riebesell, U., D'Amore, F., Kelting, O., Bach, L.T., 2021. Influence of the Calcium Carbonate Shell of Coccolithophores on Ingestion and Growth of a Dinoflagellate Predator. Frontiers in Marine Science 8.

Herbstein, F.H., Kapon, M., Reisner, G.M., Lehman, M.S., Kress, R.B., Wilson, R.B., Shiau, W. -i., Duesler, E.N., Paul, I.C., Curtin, D.Y., Dunitz, J.D., 1985. Polymorphism of naphthazarin and its relation to solid-state proton transfer. Neutron and X-ray diffraction studies on naphthazarin C. Proceedings of the Royal Society of London. A. Mathematical and Physical Sciences 399, 295–319. https://doi.org/10.1098/rspa.1985.0059

Hira, J., Wolfson, D., Andersen, A.J.C., Haug, T., Stensvåg, K., 2020. Autofluorescence mediated red spherulocyte sorting provides insights into the source of spinochromes in sea urchins. Sci Rep 10, 1149. https://doi.org/10.1038/s41598-019-57387-7

Hodson, M.E., Benning, L.G., Demarchi, B., Penkman, K.E.H., Rodriguez-Blanco, J.D., Schofield, P.F., Versteegh, E.A.A., 2015. Biomineralisation by earthworms – an investigation into the stability and distribution of amorphous calcium carbonate. Geochem Trans 16, 4. https://doi.org/10.1186/s12932-015-0019-z

Hou, Y., Carne, A., McConnell, M., Bekhit, A.A., Mros, S., Amagase, K., Bekhit, A.E.-D.A., 2020. In vitro antioxidant and antimicrobial activities, and in vivo anti-inflammatory activity of crude and fractionated PHNQs from sea urchin (Evechinus chloroticus). Food Chem 316, 126339. https://doi.org/10.1016/j.foodchem.2020.126339

Hou, Y., Vasileva, E.A., Carne, A., McConnell, M., Bekhit, A.E.-D.A., Mishchenko, N.P., 2018a. Naphthoquinones of the spinochrome class: occurrence, isolation, biosynthesis and biomedical applications. RSC Adv. 8, 32637–32650. https://doi.org/10.1039/C8RA04777D

Hou, Y., Vasileva, E.A., Carne, A., McConnell, M., El-Din A. Bekhit, A., Mishchenko, N.P., 2018b. Naphthoquinones of the spinochrome class: occurrence, isolation, biosynthesis and biomedical applications. RSC Adv. 8, 32637–32650. https://doi.org/10.1039/C8RA04777D

Hou, Y., Vasileva, E.A., Mishchenko, N.P., Carne, A., McConnell, M., Bekhit, A.E.-D.A., 2019. Extraction, structural characterization and stability of polyhydroxylated naphthoquinones from shell and spine of New Zealand sea urchin (Evechinus chloroticus). Food Chem 272, 379–387. https://doi.org/10.1016/j.foodchem.2018.08.046

Huang, J., Zhang, R., 2022. The Mineralization of Molluscan Shells: Some Unsolved Problems and Special Considerations. Frontiers in Marine Science 9.

Hubbard, B., Kuang, W., Moser, A., Facey, G.A., Detellier, C., 2003. Structural Study of Maya Blue: Textural, Thermal and Solid-State Multinuclear Magnetic Resonance Characterization of the Palygorskite-Indigo and Sepiolite-Indigo Adducts. Clays Clay Miner. 51, 318–326. https://doi.org/10.1346/CCMN.2003.0510308

Ihli, J., Bots, P., Kulak, A., Benning, L.G., Meldrum, F.C., 2013. Elucidating Mechanisms of Diffusion-Based Calcium Carbonate Synthesis Leads to Controlled Mesocrystal Formation. Advanced Functional Materials 23, 1965–1973. https://doi.org/10.1002/adfm.201201742

Ihli, J., Wong, W.C., Noel, E.H., Kim, Y.-Y., Kulak, A.N., Christenson, H.K., Duer, M.J., Meldrum, F.C., 2014. Dehydration and crystallization of amorphous calcium carbonate in solution and in air. Nat Commun 5, 3169. https://doi.org/10.1038/ncomms4169

Inbaraj, J.J., Chignell, C.F., 2004. Cytotoxic Action of Juglone and Plumbagin: A Mechanistic Study Using HaCaT Keratinocytes. Chem. Res. Toxicol. 17, 55–62. https://doi.org/10.1021/tx034132s

Ismail, A.A., van de Voort, F.R., Sedman, J., 1997. Chapter 4 Fourier transform infrared spectroscopy: Principles and applications, in: Paré, J.R.J., Bélanger, J.M.R. (Eds.), Techniques and Instrumentation in Analytical Chemistry, Instrumental Methods in Food Analysis. Elsevier, pp. 93–139. https://doi.org/10.1016/S0167-9244(97)80013-3

Ismail, R., Cionita, T., Shing, W.L., Fitriyana, D.F., Siregar, J.P., Bayuseno, A.P., Nugraha, F.W., Muhamadin, R.C., Junid, R., Endot, N.A., 2022. Synthesis and Characterization of Calcium Carbonate Obtained from Green Mussel and Crab Shells as a Biomaterials Candidate. Materials 15, 5712. https://doi.org/10.3390/ma15165712

Jahren, A.H., Gabel, M.L., Amundson, R., 1998. Biomineralization in seeds: developmental trends in isotopic signatures of hackberry. Palaeogeography, Palaeoclimatology, Palaeoecology 138, 259–269. https://doi.org/10.1016/S0031-0182(97)00122-3

Jensen, A.C.S., Imberti, S., Parker, S.F., Schneck, E., Politi, Y., Fratzl, P., Bertinetti, L., Habraken, W.J.E.M., 2018. Hydrogen Bonding in Amorphous Calcium Carbonate and Molecular Reorientation Induced by Dehydration. J. Phys. Chem. C 122, 3591–3598. https://doi.org/10.1021/acs.jpcc.7b10459

Jeon, D.-J., Paik, S., Ji, S., Yeo, J.-S., 2021. Melanin-based structural coloration of birds and its biomimetic applications. Appl Microsc 51, 14. https://doi.org/10.1186/s42649-021-00063-w

Jiang, J., Ma, Y., Zhang, T., Liang, Z., Cui, Z., 2015. Morphology and size control of calcium carbonate crystallized in a reverse micelle system with switchable surfactants. RSC Adv. 5, 80216–80219. https://doi.org/10.1039/C5RA15382D

Jimenez-Lopez, C., Rodriguez-Navarro, A., Dominguez-Vera, J.M., Garcia-Ruiz, J.M., 2003. Influence of lysozyme on the precipitation of calcium carbonate: a kinetic and morphologic study. Geochimica et Cosmochimica Acta 67, 1667–1676. https://doi.org/10.1016/S0016-7037(02)01275-9

Kahil, K., Varsano, N., Sorrentino, A., Pereiro, E., Rez, P., Weiner, S., Addadi, L., 2020. Cellular pathways of calcium transport and concentration toward mineral formation in sea urchin larvae. Proceedings of the National Academy of Sciences 117, 30957–30965. https://doi.org/10.1073/pnas.1918195117

Kanold, J.M., Guichard, N., Immel, F., Plasseraud, L., Corneillat, M., Alcaraz, G., Brümmer, F., Marin, F., 2015. Spine and test skeletal matrices of the Mediterranean sea urchin *Arbacia lixula* - a comparative characterization of their sugar signature. FEBS J 282, 1891–1905. https://doi.org/10.1111/febs.13242

Keeler, J., 2010. Understanding NMR Spectroscopy. John Wiley & Sons.

Khouzani, M.F., M. Chevrier, D., Güttlein, P., Hauser, K., Zhang, P., Hedin, N., Gebauer, D., 2015. Disordered amorphous calcium carbonate from direct precipitation. CrystEngComm 17, 4842–4849. https://doi.org/10.1039/C5CE00720H

Kim, H.L., Shin, Y.S., Yang, S.H., 2022. Effect of poly(acrylic acid) on crystallization of calcium carbonate in a hydrogel. CrystEngComm 24, 1344–1351. https://doi.org/10.1039/D1CE01687C

Kim, M.Y., Park, S.-J., Shim, J.W., Yang, K., Kang, H.S., Heo, K., 2015. Naphthazarin enhances ionizing radiation-induced cell cycle arrest and apoptosis in human breast cancer cells. International Journal of Oncology 46, 1659–1666. https://doi.org/10.3892/ijo.2015.2857

Kinoshita, S., Yoshioka, S., 2005. Structural Colors in Nature: The Role of Regularity and Irregularity in the Structure. ChemPhysChem 6, 1442–1459. https://doi.org/10.1002/cphc.200500007

Kogo, M., Uzawa, N., Nasu, A., Umegaki, T., Kojima, Y., 2022. Synthesis of colored calcium carbonate and its color. J. Ceram. Soc. Japan 130, 94–99. https://doi.org/10.2109/jcersj2.21106

Kojima, Y., Kanai, M., Nishimiya, N., 2012. Synthesis of novel amorphous calcium carbonate by sono atomization for reactive mixing. Ultrasonics Sonochemistry 19, 325–329. https://doi.org/10.1016/j.ultsonch.2011.05.002

Konrad, F., Gallien, F., Gerard, D.E., Dietzel, M., 2016. Transformation of Amorphous Calcium Carbonate in Air. Crystal Growth & Design 16, 6310–6317. https://doi.org/10.1021/acs.cgd.6b00906

Kuwahara, R., Hatate, H., Chikami, A., Murata, H., Kijidani, Y., 2010. Quantitative separation of antioxidant pigments in purple sea urchin shells using a reversed-phase high performance liquid chromatography. LWT - Food Science and Technology 43, 1185–1190. https://doi.org/10.1016/j.lwt.2010.03.005

Lam, R.S.K., Charnock, J.M., Lennie, A., Meldrum, F.C., 2007. Synthesis-dependant structural variations in amorphous calcium carbonate. CrystEngComm 9, 1226. https://doi.org/10.1039/b710895h

Lambert, G., 1998. Spicule Formation in the Solitary Ascidian Bathypera feminalba (Ascidiacea, Pyuridae). Invertebrate Biology 117, 341–349. https://doi.org/10.2307/3227036

Lamoureux, G., Perez, A.L., Araya, M., Agüero, C., 2008. Reactivity and structure of derivatives of 2-hydroxy-1,4-naphthoquinone (lawsone). Journal of Physical Organic Chemistry 21, 1022–1028. https://doi.org/10.1002/poc.1435

Land, E.J., Mukherjee, T., Swallow, A.J., Bruce, J.M., 1983. Reduction of the naphthazarin molecule as studied by pulse radiolysis. Part 1.—Addition of a single electron. J. Chem. Soc., Faraday Trans. 1 79, 391. https://doi.org/10.1039/f19837900391

Lang, A., Mijowska, S., Polishchuk, I., Fermani, S., Falini, G., Katsman, A., Marin, F., Pokroy, B., 2020. Acidic Monosaccharides become Incorporated into Calcite Single Crystals**. Chem. Eur. J. 26, 16860–16868. https://doi.org/10.1002/chem.202003344

Le Guillou, C., Bernard, S., De la Pena, F., Le Brech, Y., 2018. XANES-Based Quantification of Carbon Functional Group Concentrations. Anal. Chem. 90, 8379–8386. https://doi.org/10.1021/acs.analchem.8b00689

Lee, H.S., Ha, T.H., Kim, K., 2005. Fabrication of unusually stable amorphous calcium carbonate in an ethanol medium. Materials Chemistry and Physics 93, 376–382. https://doi.org/10.1016/j.matchemphys.2005.03.037

Lellis, B., Fávaro-Polonio, C.Z., Pamphile, J.A., Polonio, J.C., 2019. Effects of textile dyes on health and the environment and bioremediation potential of living organisms. Biotechnology Research and Innovation 3, 275–290. https://doi.org/10.1016/j.biori.2019.09.001

Leopoldini, M., Marino, T., Russo, N., Toscano, M., 2004. Antioxidant Properties of Phenolic Compounds: H-Atom versus Electron Transfer Mechanism. J. Phys. Chem. A 108, 4916–4922. https://doi.org/10.1021/jp037247d

Levi-Kalisman, Y., Raz, S., Weiner, S., Addadi, L., Sagi, I., 2002. Structural Differences Between Biogenic Amorphous Calcium Carbonate Phases Using X-ray Absorption Spectroscopy. Advanced Functional Materials 12, 43–48. https://doi.org/10.1002/1616-3028(20020101)12:1<43::AID-ADFM43>3.0.CO;2-C

Levi-Kalisman, Y., Raz, S., Weiner, S., Addadi, L., Sagi, I., 2000. X-Ray absorption spectroscopy studies on the structure of a biogenic "amorphous" calcium carbonate phase. J. Chem. Soc., Dalton Trans. 3977–3982. https://doi.org/10.1039/B003242P

Li, D.-M., Zhou, D.-Y., Zhu, B.-W., Miao, L., Qin, L., Dong, X.-P., Wang, X.-D., Murata, Y., 2013. Extraction, structural characterization and antioxidant activity of polyhydroxylated 1,4-naphthoquinone pigments from spines of sea urchin Glyptocidaris crenularis and Strongylocentrotus intermedius. Eur Food Res Technol 237, 331–339. https://doi.org/10.1007/s00217-013-1996-8

Liu, Q., Wang, H.-S., Zeng, Q., 2016. Vapor diffusion method: Dependence of polymorphs and morphologies of calcium carbonate crystals on the depth of an aqueous solution. Journal of Crystal Growth 449, 43–46. https://doi.org/10.1016/j.jcrysgro.2016.05.047

Liu, X., Chen, Y., Zhang, Y., Du, J., Lv, Y., Mo, S., Liu, Y., Ding, F., Wu, J., Li, J., 2017. Juglone potentiates TRAIL-induced apoptosis in human melanoma cells via activating the ROS-p38-p53 pathway. Molecular Medicine Reports 16, 9645–9651. https://doi.org/10.3892/mmr.2017.7806

Liu, Z., Zhang, Z., Wang, Z., Jin, B., Li, D., Tao, J., Tang, R., De Yoreo, J.J., 2020. Shape-preserving amorphous-to-crystalline transformation of CaCO3 revealed by in situ TEM. Proceedings of the National Academy of Sciences 117, 3397–3404. https://doi.org/10.1073/pnas.1914813117

Lowenstam, H.A., 1981. Minerals formed by organisms. Science 211, 1126–1131. https://doi.org/10.1126/science.7008198

Lowenstam, H.A., Weiner, S., 1989. On Biomineralization. Oxford University Press.

Lowenstam, H.A., Weiner, S., 1985. Transformation of amorphous calcium phosphate to crystalline dahillite in the radular teeth of chitons. Science 227, 51–53. https://doi.org/10.1126/science.227.4682.51

Ma, Y.R., Weiner, S., Addadi, L., 2007. Mineral Deposition and Crystal Growth in the Continuously Forming Teeth of Sea Urchins. Advanced Functional Materials 17, 2693–2700. https://doi.org/10.1002/adfm.200700234

Magdans, U., Gies, H., 2004. Single crystal structure analysis of sea urchin spine calcites: Systematic investigations of the Ca/Mg distribution as a function of habitat of the sea urchin and the sample location in the spine. ejm 16, 261–268. https://doi.org/10.1127/0935-1221/2004/0016-0261

Majdi, C., Duvauchelle, V., Meffre, P., Benfodda, Z., 2023. An overview on the antibacterial properties of juglone, naphthazarin, plumbagin and lawsone derivatives and their metal complexes. Biomedicine & Pharmacotherapy 162, 114690. https://doi.org/10.1016/j.biopha.2023.114690

Mann, S., 2001. Biomineralization: Principles and Concepts in Bioinorganic Materials Chemistry.

Mann, S., 1988. Mann, S. Molecular recognition in biomineralization. Nature 332, 119-124. Nature 332, 119–124. https://doi.org/10.1038/332119a0

Marin, F., Amons, R., Guichard, N., Stigter, M., Hecker, A., Luquet, G., Layrolle, P., Alcaraz, G., Riondet, C., Westbroek, P., 2005. Caspartin and calprismin, two proteins of the shell calcitic prisms of the Mediterranean fan mussel Pinna nobilis. J Biol Chem 280, 33895–33908. https://doi.org/10.1074/jbc.M506526200

Marin, F., Bundeleva, I., Takeuchi, T., Immel, F., Medakovic, D., 2016. Organic matrices in metazoan calcium carbonate skeletons: Composition, functions, evolution. Journal of Structural Biology 196, 98–106. https://doi.org/10.1016/j.jsb.2016.04.006

Marzec, B., Green, D.C., Holden, M.A., Coté, A.S., Ihli, J., Khalid, S., Kulak, A., Walker, D., Tang, C., Duffy, D.M., Kim, Y., Meldrum, F.C., 2018. Amino Acid Assisted Incorporation of Dye Molecules within Calcite Crystals. Angew. Chem. Int. Ed. 57, 8623–8628. https://doi.org/10.1002/anie.201804365

Mass, T., Giuffre, A.J., Sun, C.-Y., Stifler, C.A., Frazier, M.J., Neder, M., Tamura, N., Stan, C.V., Marcus, M.A., Gilbert, P.U.P.A., 2017. Amorphous calcium carbonate particles form coral skeletons. Proc Natl Acad Sci U S A 114, E7670–E7678. https://doi.org/10.1073/pnas.1707890114

Mayorova, T.D., Smith, C.L., Hammar, K., Winters, C.A., Pivovarova, N.B., Aronova, M.A., Leapman, R.D., Reese, T.S., 2018. Cells containing aragonite crystals mediate responses to gravity in Trichoplax adhaerens (Placozoa), an animal lacking neurons and synapses. PLoS One 13, e0190905. https://doi.org/10.1371/journal.pone.0190905

Meldrum, F.C., Cölfen, H., 2008. Controlling Mineral Morphologies and Structures in Biological and Synthetic Systems. Chem. Rev. 108, 4332–4432. https://doi.org/10.1021/cr8002856

Mergelsberg, S.T., Ulrich, R.N., Xiao, S., Dove, P.M., 2019. Composition Systematics in the Exoskeleton of the American Lobster, Homarus americanus and Implications for Malacostraca. Frontiers in Earth Science 7.

Merle, M., Soulié, J., Sassoye, C., Roblin, P., Rey, C., Bonhomme, C., Combes, C., 2022. Pyrophosphate-stabilised amorphous calcium carbonate for bone substitution: toward a doping-dependent cluster-based model. CrystEngComm 24. https://doi.org/10.1039/D2CE00936F

Metzler, R., Kim, I., Delak, K., Evans, J., Zhou, D., Beniash, E., Wilt, F., Abrecht, M., Chiou, J.-W., Guo, J., Coppersmith, S., Gilbert, P., 2008. Probing the Organic−Mineral Interface at the Molecular Level in Model Biominerals. Langmuir : the ACS journal of surfaces and colloids 24, 2680–7. https://doi.org/10.1021/la7031237

Michel, F.M., MacDonald, J., Feng, J., Phillips, B.L., Ehm, L., Tarabrella, C., Parise, J.B., Reeder, R.J., 2008. Structural Characteristics of Synthetic Amorphous Calcium Carbonate. Chem. Mater. 20, 4720–4728. https://doi.org/10.1021/cm800324v

Miller, V.R., 2013. Use of HSQC, HMBC, and COSY in Sophomore Organic Chemistry Lab, in: NMR Spectroscopy in the Undergraduate Curriculum, ACS Symposium Series. American Chemical Society, pp. 103–128. https://doi.org/10.1021/bk-2013-1128.ch008

Mohamed, M., Yusup, S., Maitra, S., 2012. DECOMPOSITION STUDY OF CALCIUM CARBONATE IN COCKLE SHELL 7.

Moir, M., Thomson, R.H., 1973. Naphthaquinones in Lomatia species. Phytochemistry 12, 1351–1353. https://doi.org/10.1016/0031-9422(73)80563-1

Morris, E.H., Charlot, J., Morris, A.A., 1931. Chemical Analysis of Pigments. KIP Articles.

Mullin, J.W., 2001. 6 - Crystal growth, in: Mullin, J.W. (Ed.), Crystallization (Fourth Edition). Butterworth-Heinemann, Oxford, pp. 216–288. https://doi.org/10.1016/B978-075064833-2/50008-5

Natsi, P.D., Koutsoukos, P.G., 2022. Calcium Carbonate Mineralization of Microalgae. Biomimetics 7, 140. https://doi.org/10.3390/biomimetics7040140

Nehrke, G., Poigner, H., Wilhelms-Dick, D., Brey, T., Abele, D., 2012. Coexistence of three calcium carbonate polymorphs in the shell of the Antarctic clam Laternula elliptica. Geochemistry, Geophysics, Geosystems 13. https://doi.org/10.1029/2011GC003996

Nielsen, M.H., Aloni, S., De Yoreo, J.J., 2014. In situ TEM imaging of CaCO3 nucleation reveals coexistence of direct and indirect pathways. Science 345, 1158–1162. https://doi.org/10.1126/science.1254051

Nitta, I., Kida, A., Fujibayashi, Y., Katayama, H., Sugimura, Y., 2006. Calcium carbonate deposition in a cell wall sac formed in mulberry idioblasts. Protoplasma 228, 201–208. https://doi.org/10.1007/s00709-006-0182-2

Niu, Y.-Q., Liu, J.-H., Aymonier, C., Fermani, S., Kralj, D., Falini, G., Zhou, C.-H., 2022. Calcium carbonate: controlled synthesis, surface functionalization, and nanostructured materials. Chemical Society Reviews 51, 7883–7943. https://doi.org/10.1039/D1CS00519G

Noh, M.Y., Muthukrishnan, S., Kramer, K.J., Arakane, Y., 2016. Cuticle formation and pigmentation in beetles. Current Opinion in Insect Science, Global change biology * Molecular physiology 17, 1–9. https://doi.org/10.1016/j.cois.2016.05.004

Nudelman, F., Chen, H.H., Goldberg, H.A., Weiner, S., Addadi, L., 2007. Spiers Memorial Lecture. Faraday Discuss. 136, 9–25. https://doi.org/10.1039/B704418F

Nudelman, F., Sommerdijk, N.A.J.M., 2012. Biomineralization as an Inspiration for Materials Chemistry. Angewandte Chemie International Edition 51, 6582–6596. https://doi.org/10.1002/anie.201106715

Nudelman, F., Sonmezler, E., Bomans, P.H.H., With, G. de, Sommerdijk, N.A.J.M., 2010. Stabilization of amorphous calcium carbonate by controlling its particle size. Nanoscale 2, 2436–2439. https://doi.org/10.1039/C0NR00432D

Nüsslein-Volhard, C., Singh, A.P., 2017. How fish color their skin: A paradigm for development and evolution of adult patterns. BioEssays 39, 1600231. https://doi.org/10.1002/bies.201600231

Obst, M., Dynes, J.J., Lawrence, J.R., Swerhone, G.D.W., Benzerara, K., Karunakaran, C., Kaznatcheev, K., Tyliszczak, T., Hitchcock, A.P., 2009. Precipitation of amorphous CaCO3 (aragonite-like) by cyanobacteria: A STXM study of the influence of EPS on the nucleation

process. Geochimica et Cosmochimica Acta 73, 4180–4198. https://doi.org/10.1016/j.gca.2009.04.013

Okumura, T., Suzuki, M., Nagasawa, H., Kogure, T., 2013. Microstructural control of calcite via incorporation of intracrystalline organic molecules in shells. Journal of Crystal Growth 381, 114–120. https://doi.org/10.1016/j.jcrysgro.2013.07.020

Olivieri, A., Paul, I.C., Curtin, D.Y., 1990. 13C CP-MAS study of the polymorphs of naphthazarin and of some methyl derivatives. Magnetic Resonance in Chemistry 28, 119–123. https://doi.org/10.1002/mrc.1260280206

Oral, Ç.M., Ercan, B., 2018. Influence of pH on morphology, size and polymorph of room temperature synthesized calcium carbonate particles. Powder Technology 339, 781–788. https://doi.org/10.1016/j.powtec.2018.08.066

Orme, C.A., Noy, A., Wierzbicki, A., McBride, M.T., Grantham, M., Teng, H.H., Dove, P.M., DeYoreo, J.J., 2001. Formation of chiral morphologies through selective binding of amino acids to calcite surface steps. Nature 411, 775–779. https://doi.org/10.1038/35081034

Ostertag, E., Scholz, M., Klein, J., Rebner, K., Oelkrug, D., 2019. Pigmentation of White, Brown, and Green Chicken Eggshells Analyzed by Reflectance, Transmittance, and Fluorescence Spectroscopy. ChemistryOpen 8, 1084–1093. https://doi.org/10.1002/open.201900154

Page, M.G., Nassif, N., Börner, H.G., Antonietti, M., Cölfen, H., 2008. Mesoporous Calcite by Polymer Templating. Crystal Growth & Design 8, 1792–1794. https://doi.org/10.1021/cg700899s

Parveen, S., Chakraborty, A., Chanda, D.Kr., Pramanik, S., Barik, A., Aditya, G., 2020. Microstructure Analysis and Chemical and Mechanical Characterization of the Shells of Three Freshwater Snails. ACS Omega 5, 25757–25771. https://doi.org/10.1021/acsomega.0c03064

Penkman, K.E.H., Kaufman, D.S., Maddy, D., Collins, M.J., 2008. Closed-system behaviour of the intra-crystalline fraction of amino acids in mollusc shells. Quaternary Geochronology 3, 2–25. https://doi.org/10.1016/j.quageo.2007.07.001

Piwoni-Piórewicz, A., Strekopytov, S., Humphreys-Williams, E., Kukliński, P., 2019. Elemental composition of invertebrates shells composed of different CaCO₃ polymorphs at different ontogenetic stages: a case study from the brackish Gulf of Gdansk (the Baltic Sea) (preprint). Biogeochemistry: Biomineralization. https://doi.org/10.5194/bg-2019-367

Pokroy, B., Fitch, A., Zolotoyabko, E., 2006. The Microstructure of Biogenic Calcite: A View by High-Resolution Synchrotron Powder Diffraction. Adv. Mater. 18, 2363–2368. https://doi.org/10.1002/adma.200600714

Pokroy, Boaz, Fitch, A.N., Marin, F., Kapon, M., Adir, N., Zolotoyabko, E., 2006. Anisotropic lattice distortions in biogenic calcite induced by intra-crystalline organic molecules. Journal of Structural Biology 155, 96–103. https://doi.org/10.1016/j.jsb.2006.03.008

Polette-Niewold, L.A., Manciu, F.S., Torres, B., Alvarado, M., Chianelli, R.R., 2007. Organic/inorganic complex pigments: Ancient colors Maya Blue. Journal of Inorganic Biochemistry, Special Issue in Memory of Edward I. Stiefel 101, 1958–1973. https://doi.org/10.1016/j.jinorgbio.2007.07.009

Politi, Y., Arad, T., Klein, E., Weiner, S., Addadi, L., 2004. Sea Urchin Spine Calcite Forms via a Transient Amorphous Calcium Carbonate Phase. Science 306, 1161–1164. https://doi.org/10.1126/science.1102289

Politi, Y., Metzler, R.A., Abrecht, M., Gilbert, B., Wilt, F.H., Sagi, I., Addadi, L., Weiner, S., Gilbert, P.U.P.A., 2008. Transformation mechanism of amorphous calcium carbonate into calcite in the sea urchin larval spicule. Proc. Natl. Acad. Sci. U.S.A. 105, 17362–17366. https://doi.org/10.1073/pnas.0806604105

Powell, C., Hughes, A.D., Kelly, M.S., Conner, S., McDougall, G.J., 2014. Extraction and identification of antioxidant polyhydroxynaphthoquinone pigments from the sea urchin, Psammechinus miliaris. LWT - Food Science and Technology 59, 455–460. https://doi.org/10.1016/j.lwt.2014.05.016

Qi, C., Zhu, Y.-J., Chen, F., 2014. Microwave Hydrothermal Transformation of Amorphous Calcium Carbonate Nanospheres and Application in Protein Adsorption. ACS Appl. Mater. Interfaces 6, 4310–4320. https://doi.org/10.1021/am4060645

Radha, A.V., Forbes, T.Z., Killian, C.E., Gilbert, P.U.P.A., Navrotsky, A., 2010. Transformation and crystallization energetics of synthetic and biogenic amorphous calcium carbonate. Proc. Natl. Acad. Sci. U.S.A. 107, 16438–16443. https://doi.org/10.1073/pnas.1009959107

Rahman, M.A., Oomori, T., 2008. Structure, crystallization and mineral composition of sclerites in the alcyonarian coral. Journal of Crystal Growth 310, 3528–3534. https://doi.org/10.1016/j.jcrysgro.2008.04.056

Raz, S., Hamilton, P. c., Wilt, F. h., Weiner, S., Addadi, L., 2003. The Transient Phase of Amorphous Calcium Carbonate in Sea Urchin Larval Spicules: The Involvement of Proteins and Magnesium Ions in Its Formation and Stabilization. Advanced Functional Materials 13, 480–486. https://doi.org/10.1002/adfm.200304285

Rieger, J., Frechen, T., Cox, G., Heckmann, W., Schmidt, C., Thieme, J., 2007. Precursor structures in the crystallization/precipitation processes of CaCO 3 and control of particle formation by polyelectrolytes. Faraday Discussions 136, 265–277. https://doi.org/10.1039/B701450C

Rødde, R., Einbu, A., Varum, K., 2008. A seasonal study of the chemical composition and chitin quality of shrimp shells obtained from northern shrimp (Pandalus borealis). Carbohydrate Polymers 71, 388–393. https://doi.org/10.1016/j.carbpol.2007.06.006

Rodriguez-Blanco, J.D., Shaw, S., Benning, L.G., 2011. The kinetics and mechanisms of amorphous calcium carbonate (ACC) crystallization to calcite, viavaterite. Nanoscale 3, 265–271. https://doi.org/10.1039/C0NR00589D

Rodriguez-Navarro, C., Kudłacz, K., Cizer, Ö., Ruiz-Agudo, E., 2014. Formation of amorphous calcium carbonate and its transformation into mesostructured calcite. CrystEngComm 17, 58–72. https://doi.org/10.1039/C4CE01562B

Rosário, J., da Luz, L.L., Geris, R., Ramalho, J.G.S., da Silva, A.F., Júnior, S.A., Malta, M., 2019. Photoluminescent organisms: how to make fungi glow through biointegration with lanthanide metal-organic frameworks. Sci Rep 9, 7302. https://doi.org/10.1038/s41598-019-43835-x

Rugabirwa, B., Murindababisha, D., Li, Y., Hong, Y., Su, Y., Wang, H., Li, J., 2019a. CO2-Responsive Switchable Solvents to Induce Self-Assembled Crystallization and Phase Control of CaCO3. ACS Sustainable Chem. Eng. 7, 6251–6258. https://doi.org/10.1021/acssuschemeng.8b06658

Rugabirwa, B., Murindababisha, D., Wang, H., Li, J., 2019b. A High-Pressure Gas–Solid Carbonation Route to Produce Vaterite. Crystal Growth & Design 19, 242–248. https://doi.org/10.1021/acs.cgd.8b01314

Saad, H., De Hoyos-Martinez, P.L., De Hoyos-Martinez, P.L., Srasra, E., Bouhtoury, F.C.-E., 2018. Advances in Bio-Nanohybrid Materials, in: Ahmed, S., Hussain, C.M. (Eds.), Green and Sustainable Advanced Materials. John Wiley & Sons, Inc., Hoboken, NJ, USA, pp. 289–332. https://doi.org/10.1002/9781119407089.ch11

Saeed, G., Sayeed, S., Ashraf, S., Naz, S., Siddiqi, R., Ali, R., Mesaik, A., 2013. A new method for the isolation and purification of Lawsone from Lawsonia Inermis and its ROS inhibitory activity. Pakistan Journal of Botany 45, 1431–1436.

Saharay, M., Yazaydin, A.O., Kirkpatrick, R.J., 2013. Dehydration-induced amorphous phases of calcium carbonate. J Phys Chem B 117, 3328–3336. https://doi.org/10.1021/jp308353t

Sanchez, C., Belleville, P., Popall, M., Nicole, L., 2011. Applications of advanced hybrid organic–inorganic nanomaterials: from laboratory to market. Chem. Soc. Rev. 40, 696–753. https://doi.org/10.1039/C0CS00136H

Schenk, A.S., Albarracin, E.J., Kim, Y.-Y., Ihli, J., Meldrum, F.C., 2014a. Confinement stabilises single crystal vaterite rods. Chem. Commun. 50, 4729–4732. https://doi.org/10.1039/C4CC01093K

Schenk, A.S., Cantaert, B., Kim, Y.-Y., Li, Y., Read, E.S., Semsarilar, M., Armes, S.P., Meldrum, F.C., 2014b. Systematic Study of the Effects of Polyamines on Calcium Carbonate Precipitation. Chem. Mater. 26, 2703–2711. https://doi.org/10.1021/cm500523w

Schmidt, C.A., Stifler, C.A., Luffey, E.L., Fordyce, B.I., Ahmed, A., Barreiro Pujol, G., Breit, C.P., Davison, S.S., Klaus, C.N., Koehler, I.J., LeCloux, I.M., Matute Diaz, C., Nguyen, C.M., Quach, V., Sengkhammee, J.S., Walch, E.J., Xiong, M.M., Tambutté, E., Tambutté, S., Mass, T., Gilbert, P.U.P.A., 2022. Faster Crystallization during Coral Skeleton Formation Correlates with Resilience to Ocean Acidification. J. Am. Chem. Soc. 144, 1332–1341. https://doi.org/10.1021/jacs.1c11434

Schottner, G., 2001. Hybrid Sol−Gel-Derived Polymers: Applications of Multifunctional Materials. Chemistry of Materials - CHEM MATER 13. https://doi.org/10.1021/cm011060m

Señorale-Pose, M., Chalar, C., Dauphin, Y., Massard, P., Pradel, P., Marín, M., 2008. Monohydrocalcite in calcareous corpuscles of Mesocestoides corti. Experimental Parasitology 118, 54–58. https://doi.org/10.1016/j.exppara.2007.06.011

Seto, J., Ma, Y., Davis, S.A., Meldrum, F., Gourrier, A., Kim, Y.-Y., Schilde, U., Sztucki, M., Burghammer, M., Maltsev, S., Jäger, C., Cölfen, H., 2012. Structure-property relationships of a biological mesocrystal in the adult sea urchin spine. Proceedings of the National Academy of Sciences 109, 3699–3704. https://doi.org/10.1073/pnas.1109243109

Sevilgen, D.S., Venn, A.A., Hu, M.Y., Tambutté, E., de Beer, D., Planas-Bielsa, V., Tambutté, S., 2019. Full in vivo characterization of carbonate chemistry at the site of calcification in corals. Sci Adv 5, eaau7447. https://doi.org/10.1126/sciadv.aau7447

Shamim, G., Ranjan, S.K., Pandey, D.M., Ramani, R., 2014. Biochemistry and biosynthesis of insect pigments. Eur. J. Entomol. 111, 149–164. https://doi.org/10.14411/eje.2014.021

Shan, W., Wang, B., Zhang, Y.-H., Wu, B.-Y., Tang, Y., 2004. Fabrication of Calcium Carbonate with Exquisite Morphologies and Colors through a New Controlled Precipitation Approach. Chem. Lett. 33, 1248–1249. https://doi.org/10.1246/cl.2004.1248

Shawkey, M., D'Alba, L., 2017. Interactions between colour-producing mechanisms and their effects on the integumentary colour palette. Philosophical Transactions of the Royal Society B: Biological Sciences 372, 20160536. https://doi.org/10.1098/rstb.2016.0536

Shen, C.-C., Syu, W.-J., Li, S.-Y., Lin, C.-H., Lee, G.-H., Sun, C.-M., 2002. Antimicrobial Activities of Naphthazarins from *Arnebia e uchroma*. J. Nat. Prod. 65, 1857–1862. https://doi.org/10.1021/np010599w

Shiau, W.-I., Duesler, E.N., Paul, I.C., Curtin, D.Y., Blann, W.G., Fyfe, C.A., 1980. Investigation of crystalline naphthazarin B by carbon-13 NMR spectroscopy using "magic angle" spinning techniques and by x-ray diffraction: evidence for a dynamic disordered structure. J. Am. Chem. Soc. 102, 4546–4548. https://doi.org/10.1021/ja00533a054

Shikov, A.N., Pozharitskaya, O.N., Krishtopina, A.S., Makarov, V.G., 2018. Naphthoquinone pigments from sea urchins: chemistry and pharmacology. Phytochem Rev 17, 509–534. https://doi.org/10.1007/s11101-018-9547-3

Silva, G.T.M., Silva, K.M., Silva, C.P., Gonçalves, J.M., Quina, F.H., 2020. Hybrid Pigments from Anthocyanin Analogues and Synthetic Clay Minerals. ACS Omega 5, 26592–26600. https://doi.org/10.1021/acsomega.0c03354

Simonet Roda, M., Ziegler, A., Griesshaber, E., Yin, X., Rupp, U., Greiner, M., Henkel, D., Häussermann, V., Eisenhauer, A., Laudien, J., Schmahl, W.W., 2019. Terebratulide brachiopod shell biomineralization by mantle epithelial cells. Journal of Structural Biology 207, 136–157. https://doi.org/10.1016/j.jsb.2019.05.002

Singh, H.B., Bharati, K.A., 2014. Handbook of Natural Dyes and Pigments 1–299.

Smith, C., Mcclure, S., Eaton-Magaña, S., Kondo, D., 2007. Pink-to-Red Coral: A Guide to Determining Origin of Color. Gems & Gemology 43, 4–15. https://doi.org/10.5741/GEMS.43.1.4

Soderquist, C.J., 1973. Juglone and allelopathy. J. Chem. Educ. 50, 782. https://doi.org/10.1021/ed050p782

Sone, E.D., Weiner, S., Addadi, L., 2007. Biomineralization of limpet teeth: a cryo-TEM study of the organic matrix and the onset of mineral deposition. J Struct Biol 158, 428–444. https://doi.org/10.1016/j.jsb.2007.01.001

Stephens, C.J., Kim, Y.-Y., Evans, S.D., Meldrum, F.C., Christenson, H.K., 2011. Early Stages of Crystallization of Calcium Carbonate Revealed in Picoliter Droplets. J. Am. Chem. Soc. 133, 5210–5213. https://doi.org/10.1021/ja200309m

Stipp, S.L., Hochella, M.F., 1991. Structure and bonding environments at the calcite surface as observed with X-ray photoelectron spectroscopy (XPS) and low energy electron diffraction (LEED). Geochimica et Cosmochimica Acta 55, 1723–1736. https://doi.org/10.1016/0016-7037(91)90142-R

Stuart-Fox, D., Moussalli, A., 2009. Camouflage, communication and thermoregulation: lessons from colour changing organisms. Philos Trans R Soc Lond B Biol Sci 364, 463–470. https://doi.org/10.1098/rstb.2008.0254

Sudhakar, P., Latha, P., Reddy, P.V., 2016. Chapter 15 - Plant pigments, in: Sudhakar, P., Latha, P., Reddy, P.V. (Eds.), Phenotyping Crop Plants for Physiological and Biochemical Traits. Academic Press, pp. 121–127. https://doi.org/10.1016/B978-0-12-804073-7.00015-6

Sun, R., Tai, C.-W., Strømme, M., Cheung, O., 2020. The effects of additives on the porosity and stability of amorphous calcium carbonate. Microporous and Mesoporous Materials 292, 109736. https://doi.org/10.1016/j.micromeso.2019.109736

Sun, X., Yang, A., Wu, B., Zhou, L., Liu, Z., 2015. Characterization of the Mantle Transcriptome of Yesso Scallop (Patinopecten yessoensis): Identification of Genes Potentially Involved in Biomineralization and Pigmentation. PLOS ONE 10, e0122967. https://doi.org/10.1371/journal.pone.0122967

Sutter, D., Mazzotti, M., 2017. Solubility and Growth Kinetics of Ammonium Bicarbonate in Aqueous Solution. Crystal Growth & Design 17, 3048–3054. https://doi.org/10.1021/acs.cgd.6b01751

Svenskaya, Y.I., Fattah, H., Inozemtseva, O.A., Ivanova, A.G., Shtykov, S.N., Gorin, D.A., Parakhonskiy, B.V., 2018. Key Parameters for Size- and Shape-Controlled Synthesis of Vaterite Particles. Crystal Growth & Design 18, 331–337. https://doi.org/10.1021/acs.cgd.7b01328

Swatland, H., 2010. Polarized-Light Interferometry of Calcium Carbonate Deposition in Moss from a Waterfall on the Niagara Escarpment. Microscopy and microanalysis : the official journal of Microscopy Society of America, Microbeam Analysis Society, Microscopical Society of Canada 16, 306–12. https://doi.org/10.1017/S1431927610000152

Tai, C.Y., Chen, C., 2008. Particle morphology, habit, and size control of CaCO3 using reverse microemulsion technique. Chemical Engineering Science 63, 3632–3642. https://doi.org/10.1016/j.ces.2008.04.022

Tamafo Fouegue, A.D., Ghogomu, J.N., Bikélé Mama, D., Nkungli, N.K., Younang, E., 2016. Structural and Antioxidant Properties of Compounds Obtained from Fe^{2+} Chelation by Juglone and Two of Its Derivatives: DFT, QTAIM, and NBO Studies. Bioinorganic Chemistry and Applications 2016, e8636409. https://doi.org/10.1155/2016/8636409

Tanaka, N., 2014. Scanning Transmission Electron Microscopy Of Nanomaterials: Basics Of Imaging And Analysis. World Scientific.

Taylor, M.W., Thacker, R.W., Hentschel, U., 2007. Evolutionary Insights from Sponges. Science 316, 1854–1855. https://doi.org/10.1126/science.1144387

Teng, H.H., Dove, P.M., 1997. Surface site-specific interactions of aspartate with calcite during dissolution; implications for biomineralization. American Mineralogist 82, 878–887. https://doi.org/10.2138/am-1997-9-1005

Terban, M.W., Billinge, S.J.L., 2022. Structural Analysis of Molecular Materials Using the Pair Distribution Function. Chem. Rev. 122, 1208–1272. https://doi.org/10.1021/acs.chemrev.1c00237

Tester, C.C., Brock, R.E., Wu, C.-H., Krejci, M.R., Weigand, S., Joester, D., 2011. In vitro synthesis and stabilization of amorphous calcium carbonate (ACC) nanoparticles within liposomes. CrystEngComm 13, 3975–3978. https://doi.org/10.1039/C1CE05153A

Tlili, M., Amor, M., Gabrielli, C., Joiret, S., Maurin, G., Rousseau, P., 2003. Study of Electrochemical Deposition of CaCO3 by In Situ Raman Spectroscopy II. Influence of the Solution Composition. Journal of The Electrochemical Society 150, C485–C493. https://doi.org/10.1149/1.1579483

Tobler, D.J., Blanco, J.D.R., Dideriksen, K., Sand, K.K., Bovet, N., Benning, L.G., Stipp, S.L.S., 2014. The Effect of Aspartic Acid and Glycine on Amorphous Calcium Carbonate (ACC) Structure, Stability and Crystallization. Procedia Earth and Planetary Science, Geochemistry of the Earth's surface GES-10 Paris France, 18-23 August, 2014. 10, 143–148. https://doi.org/10.1016/j.proeps.2014.08.047

Tobler, D.J., Rodriguez Blanco, J.D., Sørensen, H.O., Stipp, S.L.S., Dideriksen, K., 2016. Effect of pH on Amorphous Calcium Carbonate Structure and Transformation. Crystal Growth & Design 16, 4500–4508. https://doi.org/10.1021/acs.cgd.6b00630

Tobler, D.J., Rodriguez-Blanco, J.D., Dideriksen, K., Bovet, N., Sand, K.K., Stipp, S.L.S., 2015. Citrate Effects on Amorphous Calcium Carbonate (ACC) Structure, Stability, and Crystallization. Advanced Functional Materials 25, 3081–3090. https://doi.org/10.1002/adfm.201500400

Toby, B.H., Von Dreele, R.B., 2013. GSAS-II: the genesis of a modern open-source all purpose crystallography software package. J Appl Cryst 46, 544–549. https://doi.org/10.1107/S0021889813003531

Towe, K.M., 1967. Echinoderm calcite: single crystal or polycrystalline aggregate. Science 157, 1048–1050. https://doi.org/10.1126/science.157.3792.1048

Towe, K.M., Hamilton, G.H., 1967. Ultrastructure and inferred calcification of the mature and developing nacre in bivalve mollusks. Calc. Tis Res. 1, 306–318. https://doi.org/10.1007/BF02008102

Towe, K.M., Thompson, G.R., 1972. The structure of some bivalve shell carbonates prepared by ion-beam thinning. A comparison study. Calcif Tissue Res 10, 38–48. https://doi.org/10.1007/BF02012534

Trushina, D., Bukreeva, T., Kovalchuk, M., Antipina, M., 2014. CaCO3 vaterite microparticles for biomedical and personal care applications. Materials science & engineering. C, Materials for biological applications 45, 644–58. https://doi.org/10.1016/j.msec.2014.04.050

Tsafnat, N., Fitz Gerald, J.D., Le, H.N., Stachurski, Z.H., 2012. Micromechanics of Sea Urchin Spines. PLoS One 7, e44140. https://doi.org/10.1371/journal.pone.0044140

Unterlass, M.M., 2016. Green Synthesis of Inorganic-Organic Hybrid Materials: State of the Art and Future Perspectives (Eur. J. Inorg. Chem. 8/2016). European Journal of Inorganic Chemistry 2016. https://doi.org/10.1002/ejic.201690016

Vasileva, E.A., Mishchenko, N.P., Tran, V.T.T., Vo, H.M.N., Fedoreyev, S.A., 2021. Spinochrome Identification and Quantification in Pacific Sea Urchin Shells, Coelomic Fluid and Eggs Using HPLC-DAD-MS. Marine Drugs 19, 21. https://doi.org/10.3390/md19010021

Veis, A., 2003. Mineralization in Organic Matrix Frameworks. Reviews in Mineralogy and Geochemistry 54, 249–289. https://doi.org/10.2113/0540249

Versteegh, E.A.A., Black, S., Canti, M.G., Hodson, M.E., 2013. Earthworm-produced calcite granules: A new terrestrial palaeothermometer? Geochimica et Cosmochimica Acta 123, 351–357. https://doi.org/10.1016/j.gca.2013.06.020

Versteegh, E.A.A., Black, S., Hodson, M.E., 2014. Environmental controls on the production of calcium carbonate by earthworms. Soil Biology and Biochemistry 70, 159–161. https://doi.org/10.1016/j.soilbio.2013.12.013

Vinn, O., 2021. Biomineralization in Polychaete Annelids: A Review. Minerals 11, 1151. https://doi.org/10.3390/min11101151

Volkmer, D., Fricke, M., Huber, T., Sewald, N., 2004. Acidic peptides acting as growth modifiers of calcite crystals. Chemical Communications 0, 1872–1873. https://doi.org/10.1039/B405613B

Volkov, V.V., Chelli, R., Righini, R., Perry, C.C., 2020. Indigo chromophores and pigments: structure and dynamics. Dyes and Pigments 172. https://doi.org/10.1016/j.dyepig.2019.107761

Walker, J.M., Marzec, B., Nudelman, F., 2017. Solid-State Transformation of Amorphous Calcium Carbonate to Aragonite Captured by CryoTEM. Angewandte Chemie International Edition 56, 11740–11743. https://doi.org/10.1002/anie.201703158

Walker, J.M., Marzec, B., Ozaki, N., Clare, D., Nudelman, F., 2020. Morphological development of Pleurochrysis carterae coccoliths examined by cryo-electron tomography. J Struct Biol 210, 107476. https://doi.org/10.1016/j.jsb.2020.107476

Wang, J., Liu, K., Wang, X.-F., Sun, D.-J., 2017. Juglone reduces growth and migration of U251 glioblastoma cells and disrupts angiogenesis. Oncology Reports 38, 1959–1966. https://doi.org/10.3892/or.2017.5878

War, A.R., Paulraj, M.G., Ahmad, T., Buhroo, A.A., Hussain, B., Ignacimuthu, S., Sharma, H.C., 2012. Mechanisms of plant defense against insect herbivores. Plant Signaling & Behavior 7, 1306–1320. https://doi.org/10.4161/psb.21663

Weber, E., Pokroy, B., 2015. Intracrystalline inclusions within single crystalline hosts: from biomineralization to bio-inspired crystal growth. CrystEngComm 17, 5873–5883. https://doi.org/10.1039/C5CE00389J

Wefer, G., 1980. Carbonate production by algae Halimeda, Penicillus and Padina. Nature 285, 323–324. https://doi.org/10.1038/285323a0

Weiner, S., Addadi, L., 2011. Crystallization Pathways in Biomineralization. Annual Review of Materials Research 41, 21–40. https://doi.org/10.1146/annurev-matsci-062910-095803

Weiner, S., Dove, P.M., 2003. An Overview of Biomineralization Processes and the Problem of the Vital Effect. Reviews in Mineralogy and Geochemistry 54, 1–29. https://doi.org/10.2113/0540001

Weiner, S., Levi-Kalisman, Y., Raz, S., Addadi, L., 2003. Biologically formed amorphous calcium carbonate. Connect Tissue Res 44 Suppl 1, 214–218.

Williams, S.T., 2017. Molluscan shell colour. Biological Reviews 92, 1039–1058. https://doi.org/10.1111/brv.12268

Wise, M.L., 2011. Phenotypic and genetic diversity in the sea urchin Lytechinus variegatus. Duke University.

Wright, D., Mitchelmore, C., Dawson, R., Cutler, H.G., 2007. The Influence of Water Quality on the Toxicity and Degradation of Juglone (5-Hydroxy 1,4-Naphthoquinone). Environmental technology 28, 1091–101. https://doi.org/10.1080/09593332808618873

Wu, C.-C., Chen, S.-J., Yen, T., Kuo-Huang, L., 2006. Influence of Calcium Availability on Deposition of Calcium Carbonate and Calcium Oxalate Crystals in the Idioblasts of Morus Australis Poir. Leaves. Botanical Studies.

Xto, J.M., Borca, C.N., Van Bokhoven, J.A., Huthwelker, T., 2019. Aerosol-based synthesis of pure and stable amorphous calcium carbonate. Chem. Commun. 55, 10725–10728. https://doi.org/10.1039/C9CC03749G

Xu, X., Han, J.T., Cho, K., 2005. Deposition of Amorphous Calcium Carbonate Hemispheres on Substrates. Langmuir 21, 4801–4804. https://doi.org/10.1021/la047069v

Xu, X., Han, J.T., Kim, D.H., Cho, K., 2006. Two modes of transformation of amorphous calcium carbonate films in air. J Phys Chem B 110, 2764–2770. https://doi.org/10.1021/jp055712w

Yang, T., Fu, J., Ma, L., Du, H., Yue, X., Zhao, B., Wang, C., 2020. Biomimetic synthesis of calcium carbonate under phenylalanine: Control of polymorph and morphology. Materials Science and Engineering: C 114, 111019. https://doi.org/10.1016/j.msec.2020.111019

Yao, N., 2007. Focused Ion Beam Systems: Basics and Applications. Cambridge University Press.

Younis, S., Kauffmann, Y., Bloch, L., Zolotoyabko, E., 2012. Inhomogeneity of Nacre Lamellae on the Nanometer Length Scale. Crystal Growth & Design 12, 4574–4579. https://doi.org/10.1021/cg3007734

Zahedi Tabrizi, M., Tayyari, S.F., Tayyari, F., Behforouz, M., 2004. Fourier transform infrared and Raman spectra, vibrational assignment and density functional theory calculations of naphthazarin. Spectrochimica Acta Part A: Molecular and Biomolecular Spectroscopy 60, 111–120. https://doi.org/10.1016/S1386-1425(03)00186-0

Zeng, M., Kim, Y.-Y., Anduix-Canto, C., Frontera, C., Laundy, D., Kapur, N., Christenson, H.K., Meldrum, F.C., 2018. Confinement generates single-crystal aragonite rods at room temperature. Proceedings of the National Academy of Sciences 115, 7670–7675. https://doi.org/10.1073/pnas.1718926115

Zerlaut, G.A., Anderson, T.E., 1981. Multiple-integrating sphere spectrophotometer for measuring absolute spectral reflectance and transmittance. Appl. Opt. 20, 3797–3804. https://doi.org/10.1364/AO.20.003797

Zhang, J., Liu, Y., Shi, D., Hu, G., Zhang, B., Li, X., Liu, R., Han, X., Yao, X., Fang, J., 2017. Synthesis of naphthazarin derivatives and identification of novel thioredoxin reductase inhibitor as potential anticancer agent. European Journal of Medicinal Chemistry 140, 435–447. https://doi.org/10.1016/j.ejmech.2017.09.027

Zhao, D.-H., Gao, H.-W., 2010. Turning calcium carbonate into a cost-effective wastewater-sorbing material by occluding waste dye. Environ Sci Pollut Res 17, 97–105. https://doi.org/10.1007/s11356-009-0111-y

Zhu, Y.-P., Yuan, Z.-Y., 2015. Mesoporous Organic-Inorganic Non-Siliceous Hybrid Materials. https://doi.org/10.1007/978-3-662-45634-7

Zito, F., Koop, D., Byrne, M., Matranga, V., 2015. Carbonic anhydrase inhibition blocks skeletogenesis and echinochrome production in *Paracentrotus lividus* and *Heliocidaris tuberculata* embryos and larvae. Develop. Growth Differ. 57, 507–514. https://doi.org/10.1111/dgd.12229

Zolotoyabko, E., 2017. Anisotropic Lattice Distortions in Biogenic Minerals Originated from Strong Atomic Interactions at Organic/Inorganic Interfaces. Adv. Mater. Interfaces 4, 1600189. https://doi.org/10.1002/admi.201600189

Zou, Z., Bertinetti, L., Politi, Y., Fratzl, P., Habraken, W.J.E.M., 2017. Control of Polymorph Selection in Amorphous Calcium Carbonate Crystallization by Poly(Aspartic Acid): Two Different Mechanisms. Small 13. https://doi.org/10.1002/smll.201603100

Zou, Z., Bertinetti, L., Politi, Y., Jensen, A.C.S., Weiner, S., Addadi, L., Fratzl, P., Habraken, W.J.E.M., 2015. Opposite Particle Size Effect on Amorphous Calcium Carbonate Crystallization in Water and during Heating in Air. Chem. Mater. 27, 4237–4246. https://doi.org/10.1021/acs.chemmater.5b00145

Zou, Z., Habraken, W.J.E.M., Matveeva, G., Jensen, A.C.S., Bertinetti, L., Hood, M.A., Sun, C., Gilbert, P.U.P.A., Polishchuk, I., Pokroy, B., Mahamid, J., Politi, Y., Weiner, S., Werner, P., Bette, S., Dinnebier, R., Kolb, U., Zolotoyabko, E., Fratzl, P., 2019. A hydrated crystalline calcium carbonate phase: Calcium carbonate hemihydrate. Science 363, 396–400. https://doi.org/10.1126/science.aav0210

Zou, Z., Polishchuk, I., Bertinetti, L., Pokroy, B., Politi, Y., Fratzl, P., Habraken, W.J.E.M., 2018. Additives influence the phase behavior of calcium carbonate solution by a cooperative ion-association process. J. Mater. Chem. B 6, 449–457. https://doi.org/10.1039/C7TB03170J

Zou, Z., Yang, X., Albéric, M., Heil, T., Wang, Q., Pokroy, B., Politi, Y., Bertinetti, L., 2020. Additives Control the Stability of Amorphous Calcium Carbonate via Two Different Mechanisms: Surface Adsorption versus Bulk Incorporation. Advanced Functional Materials 30, 2000003. https://doi.org/10.1002/adfm.202000003

Appendices

Appendix 1

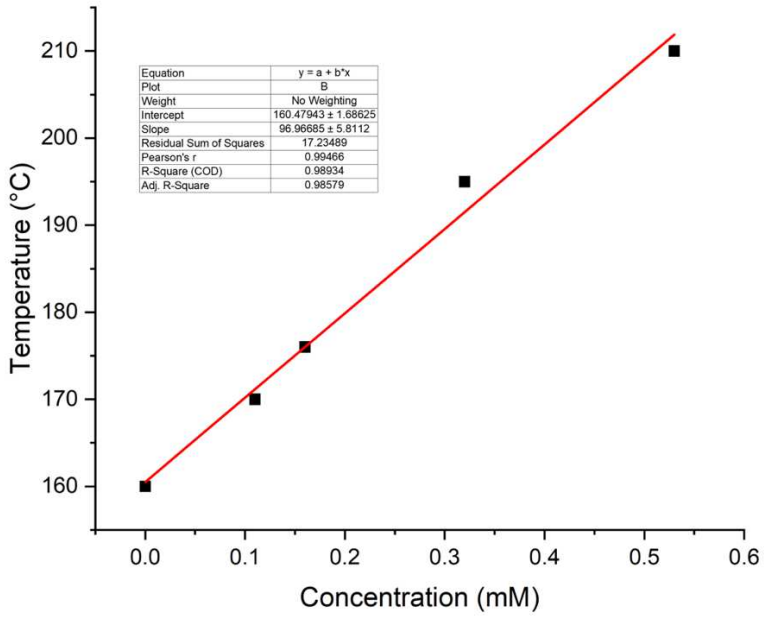

Figure 1. Crystallization temperature values extracted from DSC profiles showcasing linear trend with respect to concentration of naphthazarin.

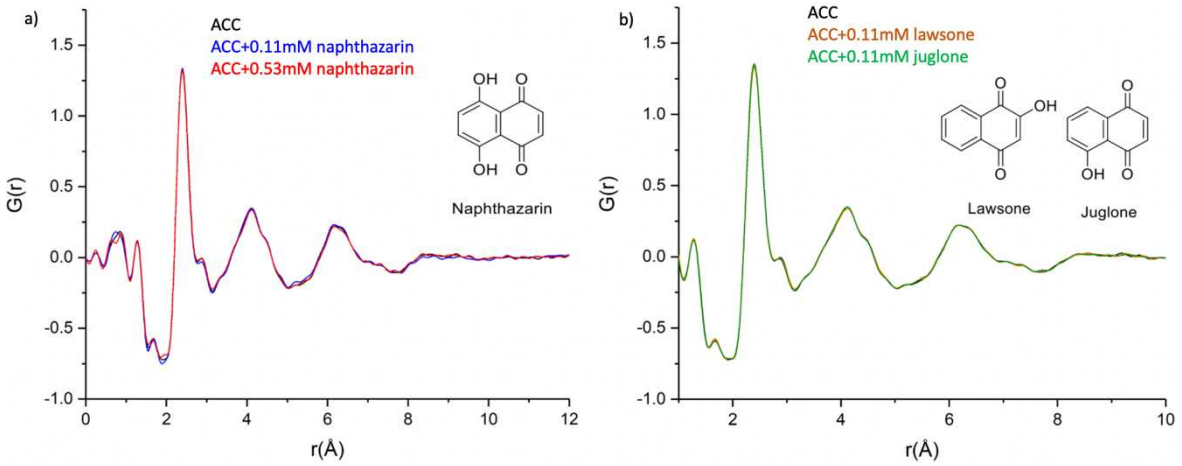

Figure 2. PDF calculated from X-ray scattering measurements at room temperature of a) pure ACC, ACC+0.11 mM of naphthazarin and ACC+0.53 mM of naphthazarin and b) ACC+0.11 mM of lawsone and juglone.

Table 1. Different parameters varied during the measurements to study the dose effect of naphthazarin:

Ronchicam current(pA)	Reel current (pA)	Dwell time (ms)	Sampling (nm)	Applied dose (e/A²)	Cumulated dose (e/A²)
8	7.6813	1	1	479	479
8	7.6813	5	1	2397	2877
8	7.6813	2	10	10	10
8	7.6813	5	5	96	105
8	7.6813	5	2	599	705
8	7.6813	20	1	9590	10294
8	7.6813	2	10	10	10
8	7.6813	5	5	96	105
8	7.6813	5	2.4	416	522
8	7.6813	5	1	2397	2919
8	7.6813	2	10	10	10
8	7.6813	5	5	96	105
8	7.6813	5	2	599	705
8	7.6813	5	1	2397	3102
8	7.6813	2	10	10	10
8	7.6813	2	10	10	10

Table 2. Rietveld refinement table for different samples

sample name	r_wp	r_exp	gof	a1	c1	a2	c2	w_cal	w_cal2
Calcite+0.055 mM naphtha	7.10630	3.64124	1.95162	4.99718	17.05790	4.99107	17.06720	23.12830	76.87170
Calcite+0.11 mM naphtha_100C	8.32045	2.98255	2.78971	4.99371	17.09570	4.98887	17.10450	32.90410	67.09590
Calcite+0.11 mM naphtha_200C	9.27201	3.05254	3.03748	4.98627	17.15610	4.98741	17.15230	52.18330	47.81670
Calcite+0.11 mM naphtha_300C	9.55357	3.00061	3.18388	4.98446	17.19380	4.98395	17.20960	19.61650	80.38350
Calcite+0.11 mM naphtha_400C	9.22820	3.10401	2.97300	4.98186	17.26820	4.98196	17.25750	31.41520	68.58480
Calcite+0.11 mM naphtha_25C	13.95610	3.02655	4.61122	5.03208	16.95900	4.99151	17.06700	0.08444	99.91560
Calcite+0.11 mM naphtha_25C after heating	8.91324	3.03430	2.93749	4.98946	17.08450	4.99065	17.06860	25.10380	74.89620
Calcite+0.22 mM naphtha	7.59593	3.41435	2.22471	4.99099	17.06790	4.99688	17.05820	77.18420	22.81580
Calcite+0.55 mM naphtha	7.76003	4.14944	1.87014	4.99566	17.05960	4.99098	17.06720	21.54920	78.45080
Calcite+0.055 mM Lawsone	12.80070	3.75736	3.40684	5.11340	17.78100	4.99137	17.06660	1.14086	98.85910
Calcite+0.11 mM Lawsone 100C	7.70990	3.41414	2.25823	4.98891	17.10350	4.99275	17.09610	75.89720	24.10280
Calcite+0.11 mM Lawsone 200C	8.54730	3.40003	2.51389	4.98627	17.15470	4.98715	17.15150	59.17880	40.82120
Calcite+0.11 mM Lawsone 300C	9.07110	3.43413	2.64146	4.98467	17.20010	4.98407	17.20940	24.32950	75.67050
Calcite+0.11 mM Lawsone 325C	9.18581	3.42863	2.67915	4.98416	17.21460	4.98353	17.22400	17.32080	82.67920
Calcite+0.11 mM Lawsone 350C	9.06891	3.41923	2.65233	4.98363	17.23040	4.98304	17.23740	17.12620	82.87380
Calcite+0.11 mM Lawsone 400C	9.39082	3.50101	2.68232	4.98224	17.26610	4.98216	17.26300	24.25700	75.74300
Calcite+0.11 mM Lawsone 25C	7.41886	3.35970	2.20819	4.99514	17.06020	4.99094	17.06740	20.15670	79.84330
Calcite+0.11 mM lawsone 25C after heating	8.93217	3.39374	2.63196	4.98987	17.08500	4.99098	17.06930	24.07120	75.92880
Calcite+0.22 mM Lawsone 100C	11.68010	3.79250	3.07978	5.11230	17.76170	4.99137	17.06660	0.79876	99.20120

Calcite+0.055 mM Juglone	6.97032	3.29685	2.11423	4.99729	17.05880	4.99113	17.06780	28.98830	71.01170
Calcite+0.11 mM Juglone 100C	8.19888	3.84330	2.13329	4.98900	17.10350	4.99469	17.09230	66.65990	33.34010
Calcite+0.11 mM Juglone 200C	9.14177	3.89562	2.34668	4.98639	17.15550	4.98761	17.15090	57.19710	42.80290
Calcite+0.11 mM Juglone 300C	9.39240	3.84614	2.44204	4.98382	17.19620	4.98409	17.21180	34.20720	65.79280
Calcite+0.11 mM Juglone 325C	9.29686	3.92448	2.36894	4.98310	17.21160	4.98346	17.22510	28.84880	71.15120
Calcite+0.11 mM Juglone 350C	9.55397	3.91252	2.44190	5.10868	17.81200	4.98285	17.23520	2.47215	97.52790
Calcite+0.11 mM Juglone 400C	9.51275	3.91276	2.43121	4.98170	17.24530	4.98187	17.26260	6.00979	93.99020
Calcite+0.11 mM Juglone 25C	7.95731	3.77852	2.10593	4.99673	17.05730	4.99105	17.06710	30.15770	69.84230
Calcite+0.11 mM Juglone 25C after heating	8.84068	3.84335	2.30026	4.98934	17.08450	4.99076	17.06730	22.78810	77.21190
Calcite+0.22 mM Juglone 100C	11.52300	3.20171	3.59901	5.05655	17.94030	4.99173	17.06790	1.22889	98.77110
calcite 25C	12.36070	3.93530	3.14097	5.19237	17.54490	4.99140	17.06710	0.55426	99.44570
calcite 100C	12.81250	3.35763	3.81594	5.08728	17.29100	4.98945	17.10330	0.00500	99.99500
calcite 150C	8.10405	3.31669	2.44342	4.98765	17.12940	4.99102	17.12390	68.73990	31.26010
calcite 200C	9.03368	3.34536	2.70036	4.98631	17.15630	4.98735	17.15270	55.02480	44.97520
calcite 300C	9.34355	3.33888	2.79841	4.98355	17.19040	4.98407	17.21030	14.94590	85.05410
calcite 350C	9.05585	3.39705	2.66580	4.98263	17.22350	4.98296	17.23720	17.31000	82.69000
calcite 400C	9.42578	3.40355	2.76940	4.98235	17.24620	4.98191	17.26330	5.70721	94.29280
Calcite 25C after heating	8.63123	3.29474	2.61970	4.98996	17.08070	4.99078	17.06810	23.02150	76.97850
calcite+ 0.035 mM Echinochrome A	7.83668	3.74750	2.09118	4.99161	17.06900	4.99097	17.06830	17.86790	82.13210
calcite+ 0.07 mM Echinochrome A 100C	7.81130	3.15611	2.47497	4.99008	17.10640	4.98897	17.10720	60.93280	39.06720
calcite+ 0.07 mM Echinochrome A150C	8.03233	3.20573	2.50561	4.98756	17.13650	4.98850	17.12830	52.54830	47.45170
calcite+ 0.07 mM Echinochrome A200C	8.19869	3.11556	2.63153	4.98653	17.16030	4.98680	17.15510	56.65450	43.34550
calcite+ 0.07 mM Echinochrome A 300C	7.99787	3.14058	2.54662	4.98389	17.20330	4.98422	17.21640	53.58550	46.41450
calcite+ 0.07 mM Echinochrome A 350C	8.04960	3.17862	2.53242	4.98315	17.24920	4.98288	17.23440	13.84200	86.15800

calcite+ 0.07 mM Echinochrome A 400C	8.39439	3.20811	2.61661	4.96049	17.30510	4.98195	17.26300	0.07524	99.92480
calcite+ 0.07 mM Echinochrome A 25C	7.34649	3.09516	2.37354	4.99660	17.06040	4.99102	17.06960	13.16020	86.83980
calcite+ 0.07 mM Echinochrome A 25C after heating	7.77913	3.10495	2.50540	4.98923	17.08720	4.99074	17.06720	20.51990	79.48010
calcite+ 0.14 mM Echinochrome A	7.80026	3.90042	1.99985	4.99632	17.06110	4.99107	17.07060	23.64080	76.35920
calcite+0.038 mM spinochrome E	7.56762	3.25193	2.32711	4.99703	17.05780	4.99103	17.06920	22.58330	77.41670
calcite+0.08 mM spinochrome E	7.57028	3.57738	2.11615	4.99707	17.05780	4.99108	17.06910	23.01340	76.98660
calcite+0.16 mM spinochrome E	7.20388	3.59429	2.00425	4.99638	17.06000	4.99105	17.07200	12.20180	87.79820
calcite+0.045 mM spinochrome B	7.71445	3.53790	2.18052	4.99636	17.05940	4.99110	17.06940	22.29110	77.70890
calcite+0.09 mM spinochrome B 100C	7.84635	3.32141	2.36236	4.99488	17.10120	4.98933	17.11120	24.95640	75.04360
calcite+0.09 mM spinochrome B 150C	8.02122	3.41060	2.35185	4.98815	17.13990	4.98987	17.12570	68.36880	31.63120
calcite+0.09 mM spinochrome B 200C	8.13152	3.34021	2.43443	4.98714	17.16940	4.98640	17.14590	55.19910	44.80090
calcite+0.09 mM spinochrome B 300C	8.24198	3.43578	2.39887	4.98396	17.19460	4.98425	17.21410	23.98930	76.01070
calcite+0.09 mM spinochrome B 350C	8.19184	3.35339	2.44285	4.98275	17.22850	4.98322	17.24260	45.42840	54.57160
calcite+0.09 mM spinochrome B 400C	8.34185	3.43442	2.42890	4.98198	17.27690	4.98192	17.26000	17.64440	82.35560
calcite+0.09 mM spinochrome B 25C	7.65723	3.34147	2.29158	4.99695	17.06170	4.99133	17.07140	25.30940	74.69060
calcite+0.09 mM spinochrome B 25C after heating	7.95749	3.53992	2.24793	4.98947	17.08910	4.99085	17.06750	18.70750	81.29250
calcite+0.18 mM spinochrome B	7.58143	3.73759	2.02843	4.99731	17.06240	4.99150	17.07100	18.71990	81.28010
calcite+0.04 mM spinochrome D	8.08579	3.68858	2.19211	4.99707	17.05810	4.99113	17.06750	26.96150	73.03850
calcite+0.08 mM spinochrome D	7.57830	3.68435	2.05689	4.99715	17.05890	4.99107	17.06820	19.87430	80.12570
calcite+0.16 mM spinochrome D	8.66505	3.22705	2.68513	4.99679	17.06170	4.99104	17.06970	19.20280	80.79720

calcite+0.035 mM spinochrome A	8.94829	3.37530	2.65111	5.11085	17.31900	4.99128	17.06780	0.01880	99.98120
calcite+0.07 mM spinochrome A 100C	7.80386	3.43805	2.26985	4.98917	17.10550	4.99470	17.09740	73.07920	26.92080
calcite+0.07 mM spinochrome A 200C	8.49739	3.42987	2.47746	4.98663	17.15590	4.98760	17.15830	58.06630	41.93370
calcite+0.07 mM spinochrome A 300C	8.30054	3.44171	2.41175	4.98445	17.22150	4.98416	17.20570	22.54850	77.45150
calcite+0.07 mM spinochrome A 325C	8.78031	3.45877	2.53856	5.09367	17.91520	4.98361	17.22300	1.45123	98.54880
calcite+0.07 mM spinochrome A 350C	8.77549	3.49023	2.51430	5.10092	18.00180	4.98304	17.23620	1.64047	98.35950
calcite+0.07 mM spinochrome A 400C	8.53527	3.43627	2.48388	4.98192	17.27660	4.98201	17.26060	17.38720	82.61280
calcite+0.07 mM spinochrome A 25C	7.41307	3.35895	2.20696	4.99684	17.06130	4.99113	17.06890	24.17090	75.82910
calcite+0.07 mM spinochrome A 25c after heating	8.17324	3.35467	2.43638	4.98878	17.09200	4.99086	17.06870	24.41600	75.58400
calcite+0.14 mM spinochrome A	13.47090	3.93072	3.42708	4.99724	17.05960	4.99105	17.06830	28.29180	71.70820
calcite aspartic 0.055 mM	19.32160	2.83817	6.80774	4.99048	17.06430	4.99519	17.05610	79.72660	20.27340
calcite aspartic 0.11 mM	42.09310	2.35465	17.87660	4.99048	17.06430	4.99519	17.05610	79.72660	20.27340
calcite aspartic 0.22 mM	29.28310	2.66052	11.00650	4.99048	17.06430	4.99519	17.05610	79.72660	20.27340
calcite aspartic 0.32 mM	23.36200	3.17958	7.34749	4.99048	17.06430	4.99519	17.05610	79.72660	20.27340
calcite aspartic 0.53 mM	28.19900	2.58936	10.89030	4.99048	17.06430	4.99519	17.05610	79.72660	20.27340
Calcite glycine 0.055 mM	22.31050	2.88577	7.73122	4.99048	17.06430	4.99519	17.05610	79.72660	20.27340
calcite glycine 0.11 mM	20.90570	3.00792	6.95022	4.99048	17.06430	4.99519	17.05610	79.72660	20.27340
Calcite_glycine 0.22 mM	25.47030	2.77186	9.18887	4.99048	17.06430	4.99519	17.05610	79.72660	20.27340
calcite glycine 0.32 mM	18.17920	2.87387	6.32570	4.99048	17.06430	4.99519	17.05610	79.72660	20.27340
calcite glycine 0.53 mM	34.34470	2.48390	13.82690	4.99048	17.06430	4.99519	17.05610	79.72660	20.27340
calcite aspartic 0.11 mM_150C exsitu	29.22640	2.71265	10.77410	4.99048	17.06430	4.99519	17.05610	79.72660	20.27340
calcite aspartic 0.11 mM 200C exsitu	18.33470	2.77323	6.61131	4.99048	17.06430	4.99519	17.05610	79.72660	20.27340
calcite aspartic 0.11 mM 250C exsitu	34.10720	2.48990	13.69820	4.99048	17.06430	4.99519	17.05610	79.72660	20.27340
calcite aspartic 0.11 mM 300C exsitu	23.93440	2.70620	8.84426	4.99048	17.06430	4.99519	17.05610	79.72660	20.27340

calcite aspartic 0.11 mM 400C exsitu	32.02880	2.62900	12.18290	4.99048	17.06430	4.99519	17.05610	79.72660	20.27340
Calcite	28.40600	2.50456	11.34180	4.99048	17.06430	4.99519	17.05610	79.72660	20.27340
ACC_400 C exsitu	5.57790	3.29257	1.69409	4.99017	17.06270	4.99006	17.05380	81.14070	18.85930
ACC_400C_naphtha 0.055 mM	5.70699	3.32296	1.71744	4.99039	17.06130	4.99056	17.06530	76.49950	23.50050
ACC_400C_naphtha 0.11 mM	5.39353	3.12819	1.72417	4.99025	17.06240	4.98987	17.06770	81.29810	18.70190
ACC_400C_naphtha 0.22 mM	5.70230	3.64856	1.56289	4.99021	17.06200	4.98971	17.06300	84.67440	15.32560
ACC_400C_naphtha 0.32 mM	5.51114	3.25413	1.69359	4.99023	17.06330	4.98727	17.06360	68.47940	31.52060
ACC_400C_naphtha 0.53 mM	8.69752	3.33067	2.61134	4.99041	17.06420	4.98883	17.06540	56.95230	43.04770

Appendix 2

Manuscript writing in progress

TITLE:

PHNQ-macromolecule complexes occluded within purple $CaCO_3$-biominerals of *Paracentrotus lividus* sea urchin spines

Marie Albéric[1,*], Claudio Dos Reis Ferreira[1], Vaskar Sardhalia[1] ,Alshaba Kakar[1], Romain Descamps[2], Lucrèce Matheron-Duriez[3,4], François Ribot[1], Delphine Talbot[5], Elena Vasileva[6], Natalia Mishchenko[6] and Frédéric Marin[7]

[1] Laboratoire Chimie de la Matière Condensée de Paris, Sorbonne Université, UMR CNRS 7574, 75005 Paris, France

[2] Plateforme de Chimie Analytique, Physique et Spectroscopie, Sorbonne Université, 75005 Paris, France

[3] Institut de Biologie Paris Seine, Sorbonne Université, UMR CNRS 7238, 75005 Paris, France

[4] Plateforme de Spectrométrie de Masse de Sorbonne Université Sciences (MS^3U), 75005 Paris, France

[5] Laboratoire de Physicochimie des Electrolytes et Nanosystèmes Interfaciaux, Sorbonne Université, UMR CNRS 8234, 75005 Paris, France

[6] Laboratory of the Chemistry of Natural Quinonoid Compounds, G.B. Elyakov Pacific Institute of Bioorganic Chemistry, Far Eastern Branch of Russian Academy of Sciences, 690022 Vladivostok, Russia

[7] Laboratoire Biogéosciences, UMR CNRS-EPHE 6282, Université de Bourgogne - Franche-Comté, 21000 Dijon, France

*corresponding author

INTRODUCTION

Marine invertebrates such as mollusks, brachiopods, crustaceans, crinoids and sea urchins show striking colors ranging from red, yellow to blue, purple and green (reviews Bandaranayake 2006, Williams 2017). This large palette of natural colors is due to the presence of small organic pigment molecules (typically < 1kDa) biosynthesized by the animals (e.g. porphyrins, bilins, melanin and quinonoid such as anthraquinones, polycyclic quinones, naphthoquinones and melanin) or obtained from food sources (e.g. carotenoids such as

canthaxanthin and astaxanthin) (Needham1974, Comfort, William, Stemmer, Hedegaard, Arma, Bonnard, Lemer, Affenzeller, Lederer, Goodwin, Mishenko, Vasileva, Cusack, Gaspard 2019, Zagalsky 1985, Cianci 2002, Wolkenstein 2009 2015 2019, Singh 2018, Ebada, Saenko2021, Jurg 1978, Ryberg1979, Matsuno and Tsushima, 2001, Verdes 2015, Soldati 2008). Of particular interest is the phylum Echinodermata whose members synthesize a large number of secondary metabolites such as hydroxyanthraquinone pigments identified in crinoids (Wolkenstein 2009, 2019 Singh 2018) and polyhydroxy-1,4-naphthoquinone molecules (PHNQs) found in sea urchins (Vasileva 2021).

Biosynthesized via enzymatic pathways (Salaque 1967, Ageenko2011, Li2022), PHNQs have antimicrobial, anti-inflammatory, antioxidant and UV-absorption properties (Lebedev 2001, Zhou 2011, Coates 2018, Powell 2014, Brasseur 2017) making them interesting bioactive compounds for pharmaceutical applications (Hou 2018, Vasileva 2021, Shikov 2018). Consequently, about 40 different PHNQ molecules have been already identified across various species of adult sea urchins (for reviews see Anderson 1969, Hou 2018, Vasileva 2021, Ageenko 2022) once isolated from their gonads (Brasseur), digestive system (Brasseur 2017a), immune red-spherule cells (Matranga 2000, Pinsino 2015, Calestani, Coates 2018, Brasseur, Ageenko 2022,Vasileva 2021) and colorful skeletal biominerals (test and spines) with their surrounding soft tissues (Vasileva, Brasseur, Goodwin).

However, PHNQ-macromolecule complexes have not been yet evidenced, to the best of our knowledge, and could be of further interest not only for pharmaceutical applications but also for food (Zhou 2011, 2012, review Mejia2020), cosmetic and dyeing textile industries that are actively turning to natural products (Li 2021). Protein-associated pigments have been already identified in some marine invertebrates (Comfort 1950, Cusack 1992, Zagalsky 1985, Cianci 2002, Jackson 2006, Mann 2014, Hedegaard 2006, book Needham1974). Specifically, carotenoproteins were extracted from the calcified tissues of blue lobster carapaces (Zagalsky 1985, Cianci 2002) and brachiopod red shells (Cusack 1992) after calcium carbonate ($CaCO_3$) mineral dissolution. The occlusion of organic pigments within the biogenic mineral phase indisputably occurs during its growth (Fox and Hopkins 1965, Towe 1990) *i.e.*, biomineralization processes, which involve a set of organic macromolecules such as proteins, glycoproteins and polysaccharides that subsequently also get incorporated within the mature biominerals and are part of the so-called intracrystalline organic matrix (Crenshaw 1972, Weiner 1975, Lowenstan and Weiner 1988). Although biomineral pigmentation and biomineralization pathways appear to be two metabolic processes intimately linked during the life time of these animals (Towe 1990, Zito, Sun), the detailed mechanism of pigment's

occlusion in $CaCO_3$ and association with macromolecules potentially directly involved in crystal growth, is not known. Attested to play a crucial role in biomineralization, some macromolecules of the intracrystalline organic matrix were shown to control *in vitro* crystal nucleation, growth, orientation, polymorph selection, structure and morphology (Berman, Aizenberg, Politi, Kanold, Karakostis, Nudelman, Gong). However, the role of secondary metabolites in biomineralization processes such as pigment molecules has not been thoroughly addressed yet.

Using an adapted biochemical extraction protocol, we first evidence the presence of PHNQ-macromolecules complexes occluded within the mass-colored $CaCO_3$-biominerals of *Paracentrotus lividus* sea urchin purple spines by UV-visible spectroscopy and SDS-PAGE. After thorough characterization of both free PHNQs and PHNQ-macromolecules complexes by FT-IR, NMR in solution and HR-MS, we further compare the effect of both extracts on $CaCO_3$ crystal growth and thus assess the likely role of intracrystalline PHNQs and PHNQ-macromolecule complexes on biomineralization processes.

RESULTS AND DISCUSSION

Mass-coloration of purple sea urchin spines reveals the presence of intracrystalline pigments

As most echinoderm skeletal elements, sea urchin spines exhibit a three-dimensional arrangement of mineralized $CaCO_3$-trabeculae, the so-called stereom that provides light-weight properties to the biominerals. Specifically, *Paracentrotus lividus* primary spines comprise an imperforate stereom (the septa) consisting of dense mineral wedges radially arranged around an inner laminar stereom having a connected porosity of 5 to 25 µm (Albéric 2022) (Figure 1). During the life time of sea urchins, soft tissues also defined as connective tissues (epidermis and dermis) (Heatfield, Ameye) cover the septa and fill the stereom's porosity. These organic soft tissues, also defined as the inter-crystalline organic fraction, comprise different cell types and a large number of extracellular vesicles (Dubois and Ameye, 2001; Heatfield and Travis, 1975b; Heatfield and Travis, 1975a; Märkel and Röser, 1983; Märkel *et al*., 1989) that tightly adhere to the surface of the $CaCO_3$-trabeculae. Inter-crystalline organics have been previously removed by collagenase (Weiner 1985), NH_4OH (Weiner 1979) or H_2O_2 treatment (Penkman2008), but a 12% NaClO cleaning of powdered biominerals for 48h was shown to be the most efficient for mollusk shells (Penkman2008). In contrast, the so-called intracrystalline organic fraction resists prolongated chemical oxidation and is thus, considered occluded with

the mineral phase (Crenshaw 1952, Weiner 1975, Towe 1990, Berman 1993, Sykes 1995, Stern 1999, Marin 2016).

Fresh *P. lividus* sea urchin spines of purple color were first treated for few hours with 5% NaClO to remove most of the soft tissues (Figure 1A). This mild oxidative treatment enhanced the purple color of the spines (Figure SI) showing that the purple hue originates from the pigment molecules occluded within the biominerals rather than the ones possibly present in the soft tissues. Indeed, different pigment cells have been already observed in the spine's connective tissues such as the red-spherule cells that contain dense red vesicles filled with PHNQs (ref.) and chromatophores with melanin granules (Millott 1952).

After resin embedding, cross-sections were then obtained perpendicular to the long axis of the spines and further polished under water (Figure 1B). Observed under light microscopy, the entire septa show a homogeneously distributed intense purple color (Figure 1C). The longitudinal trabeculae of the stereom also show intense purple color whereas the transverse bridges that connect the trabeculae appear transparent (Figure 1D). These differences might be due to different concentrations of occluded pigments but also to different mineral thicknesses. Indeed, the compact wedges of the septa and the longitudinal trabeculae of the stereom run almost all along the spine length of about 1 cm whereas the transverse bridges are only few microns wide. This mass-colored pigmentation of the spines contrasts with the one observed only within the outer surface of the shells of sea urchins (Figure SI) and mollusks (Stemmer, Budd 2004, Zhao Oyster, Komura 2018, Milano 2018, Sakalauskaite 2020). This suggests that the pigment molecules are continuously deposited and further encapsulated during the entire growth of the spines.

In order to appreciate the micron spatial distribution of organics within the $CaCO_3$ biominerals and possibly identify their molecular nature, we performed Raman confocal microscopy of polished cross-sections. Indeed, the spatial distributions of polyenes, porphyrin and melanin within biominerals have been commonly evidenced by Raman spectroscopy thanks to their characteristic spectral signatures (Fürst, Stemmer, Hedegaard, Kamuro 2018, Gaspard 2019, Ishikawa 2019, Karampelas 2019, Milano 2018, William). Figure 1E shows two characteristic averaged Raman spectra of the outer (brown spectrum) and the inner septa (yellow spectrum). Both areas exhibit a very high fluorescence in the 2000 - 4000 cm^{-1} region that prevents the detection of any characteristic organic signal and only allows for the detection of the main calcite peak at 1089 cm^{-1}. This high fluorescence, which is likely due to the organic

molecules (ref.) can however be spatially visualized by obtaining a fluorescence map obtained in the [2000-4000] cm^{-1} region (Figure 1F). Thus, Figure 1F reveals the two-dimensional spatial distribution of the intra-crystalline organics at the surface of the polished cross-section. Concentrical wavy lines of 1µm thick showing high fluorescence signal (yellow) are observed all along the septa length and in the stereom. Similar concentric laminations or onion like patterns have been previously identified after mild acidic *etc*hing or/and fracture of the stereom surface of sea urchin test plates (Nissen 1969, Pearse and Pearse 1975) and spines (Gorzelak 2011, Weiner 1997, Ameye 2001). They have been attributed to mineralization deposition lines alternating between "laminar accretion of calcite and organic thin concentric layers". Although previously first reported that such features were absent in the septa and suggested to be due to less controlled mineralization than in the stereom (Weiner 1997), Ameye *et al.* 2001 did observe concentric wavy layers in the septa as well. Our results thus suggest that the formation of the septa also occur through a delicate deposition of $CaCO_3$ minerals intertwined with organic layers of organics. In addition, we measured higher fluorescence signals in the stereom and in the septa close to the stereom than in most of the septa (Figure 1E and F). This suggests different organic concentrations or compositions in the different zones as already observed by lectin-gold labeling concerning the presence of N- and O-glycoproteins as well as sialic acid (Ameye 2001).

Nevertheless, as for most skeletal organic matrix (Marin 2015, William), a detailed analysis of the sea urchin intracrystalline organics requires its prior extraction from the biominerals.

Extraction of the intra-crystalline free PHNQs and PHNQ-macromolecule complexes

In order to exclusively extract the intracrystalline PHNQs and PHNQ-macromolecule complexes occluded within purple *P. lividus* sea urchin spines, we first ensured the complete removal of the soft tissues tightly bound to the convoluted trabeculae of the spine's stereom. In order to do so, we performed several cleaning cycles from 4h to 100h of intact and powdered spines with 5 and 12%-NaClO solutions. SEM micrographs of fractured spines treated with 5%-NaClO for 4h still reveal the presence of soft tissues at the surface of the biominerals (Figure 2A). The organic contents remaining after the different oxidative treatments were further quantified by TGA. Fresh spines before and after cleaning with 5%-NaClO for 4h show 3.2 wt.% and 1.5 wt.% total weight losses, respectively whereas powdered spines treated with 12%-NaClO for 48h and 100h have both 1 wt.% weight losses (Figure 2B). Similarly to

mollusk shells (Penkman2008), these results evidence that a 12%-NaClO treatment for 48h is therefore needed, but sufficient, to accurately remove all the inter-crystalline organics of *P. lividus* primary spines.

Notably, the relatively strong oxidation treatment does not alter the color of the biominerals as revealed by UV-visible diffuse reflectance spectroscopy measurements of untreated and treated powdered samples (fresh spines, 5%-NaClO cleaned spines for few hours and 12%-NaClO cleaned ones for 48h). Indeed, the UV-visible absorbance spectra of the three powdered samples are very similar. They show three UV bands at 245, 295 and 355 nm as well as a small and a broad band in the visible range, respectively at 480 and 570 nm (Figure 2C). The visible bands are indicative of the purple color whereas the UV ones originate from the well-known UV- absorption properties of PHNQs once extracted (Zhou2011, 2012). This suggests that when occluded within the $CaCO_3$ biominerals, PHNQs still show UV-absorption properties, which verifies one of the hypotheses about their physiological function as UV-protectants (Brasseur).

Then, we combined and adapted two established protocols for the extraction of $CaCO_3$ skeletal matrix macromolecules in one hand (Marin) and for the isolation of pure PHNQs (Goodwin, review Vasileva 2021) in another hand. This combination allows for extracting the intracrystalline macromolecules, preserving their eventual association with the PHNQs as well as isolating small molecules which are the free and pure PHNQs. Indeed, the macromolecules are otherwise destroyed when using strong acid such as concentrated HCl primarily used for the extraction of PHNQ only (Goodwin 1950).

Therefore, we used dilute acetic acid to completely and mildly dissolve of the $CaCO_3$ powder in order to extract and preserve all the intracrystalline organic molecules. Being more soluble in ethanol than in water, PHNQs have been also extracted with 4-10% H_2SO_4 acidified ethanol (Mischenko 2005, 2014, Vasileva 2017), but which only allows for a partial mineral dissolution and the extraction of PHNQs exclusively, as proteins, glycoproteins, lipids and polysaccharides are poorly soluble in ethanol.

After complete mineral dissolution, a dark purple solution is obtained at pH 4 (Figure 3A) and then separated by centrifugation into an acid-soluble matrix (ASM) and an acid-insoluble matrix (AIM). The solid pellet consisting of the AIM fraction has a dark purple color with some grey parts (Figure 3B), which can be quite important in some extraction (Figure SI).

In contrast, the solution containing the total ASM fraction is pink-orange (Figure 3C). Interestingly, the separation of the ASM from the AIM is not complete as a dark purple colloidal suspension is still observed in the ASM after centrifugation and separation from the AIM (Figure 3C). We propose that this intermediate fraction might consist of lipopolysaccharides that may form colloidal suspension in aqueous media. These different colors observed may reveal different pigment composition, concentration, ionic forms or/and association to macromolecules.

The total ASM fraction is further ultrafiltrated on a 1kDa cut-off membrane allowing for the separation of the free PHNQs mixture (<1kDa) from the PHNQ-macromolecule complexes (>1kDa). While the ASM<1kDa fraction exhibits an intense and clear pink color (Figure $3D_{1.}$), the ASM > 1kDa fraction shows a biphasic coloration dark purple/pinkish due to the presence of the highly concentrated dark colloidal suspension within the pinkish acetic acid solution (Figure $3E_{1.}$). After slow agitation (Figure $3E_{2.}$), an intense opaque dark purple (almost black) color can be obtained due to the resuspension of the lipopolysaccharide like molecules that precipitate again after some time (Figure $3E_{3.}$).

In order to further remove the acetic acid and the dissolved salts from both ASM fractions, ASM >1kDa is dialyzed against distilled water in 1kDa cut-off membrane tubes and ASM<1kDa is purified by solvent extraction with diethyl ether and Na_2CO_3 (see exp.). Notably, during solvent extraction the later changes from pink at pH 2 to purple at pH 11(Figure $3D_{2.}$). This change of colors according to pH is likely due to the different ionic forms of the pigment molecules. Indeed, PHNQs are halochromic pigments that change the color of the solution according to pH (Zhou, Lebedev). For example, echinochrome A changes from orange to purple to yellow at pH 4 and 6 (Vlès and Vellinger 1928). Once concentrated in the ether phase it finally shows an intense ruby color (Figure 3F) in agreement with (Goodwin).

All three fractions are finally freeze-dried.

Structure elucidation of the free pigments from the ASM <1kDa fraction

Among the large number of PHNQ molecules previously identified in various species, six different PHNQs have been in total reported for the spines and test plates of *P. lividus* sea

urchins, independently of their color: Echinochrome A, Spinochrome A (two isomers), B, C and E, (Anderson 1969) (Goodwin, Lederer, Louise, Anderson, Shikov). More recently, only spinochrome A and B were identified in the spines and test plates of *P. lividus* sea urchins from the Italian coast (Marzorati 2021). In addition, echinochrome A was extracted from the red-spherules cells present in the coelomic of *P. lividus* sea urchins (Coates 2018, Mantraga). These variations of PHNQ composition within even one species might depend on the specimen itself, the tissue considered but also on the protocol used for the extraction of such molecules. Here, we isolated and further characterized the intracrystalline PHNQs of purple *P. lividus* spines only as our protocol ensures first the complete removal of the spine's surrounding soft tissues that are known to contain numerous red-spherule cells (Heatfield).

The characterization of the ASM <1kDa fraction by HPLC (Figure SI) and ^{1}H, ^{13}C NMR (Figure 4) show the presence of one main PHNQ molecule, spinochrome A ($C_{12}O_7H_8$, 3-Acetyl-2,5,7,8-tetrahydoxy-1,4-naphthoquinone). Another PHNQ is detected by NMR (*, Figure 4A), but its low quantity does not allow HMBC measurements making difficult its complete structure elucidation. In addition to spinochrome A, further HR-MS analysis show the presence of two minor PHNQs, spinochrome B ($C_{10}O_6H_6$, 2,3,5,7-Tetrahydroxy-1,4-naphthoquinone) and C ($C_{12}O_8H_8$, 2-Acetyl-3,5,6,7,8-pentahydroxy-1,4-naphthoquinone). However, neither echinochrome A nor spinochrome E were detected as intra-crystalline PHNQs of purple spine, which suggest that these two molecules are possibly only present in the surrounding soft tissues.

Characterization of the intra-crystalline macromolecules

The intracrystalline ASM fraction of *Paracentrotus lividus* biominerals has been investigated through biochemical and proteomic approaches. The amino acid composition of the protein constituents was first determined (Weiner 1985, Berman 1993, Albeck 1993, 1996) and diverse proteins, glycoproteins and free polysaccharides were further identified such as alkaline protein (SM50), MSP-130 proteins, metalloenzymes (carbonic anhydraze), cytoskeletal proteins, terminal sialic acids, O-, N- and C-type lectin glycoproteins (Benson 1987, Albeck 1996, Ameye 1999, Ameye 2001, Karakostis 2016, others). In contrast, the AIM fraction has been poorly studied (Weiner 1985, Karakostis, Kanold) and was first identified as mainly composed of nonproteinaceaous material (Weiner 1985) although some proteins (and monosaccharides) were later evidenced in the AIM of the test plates of *P. lividus* as well as in the spines and test plates of *Arbacia lixula* (Kanold, Karakostis).

Although FT-IR spectroscopy is not the best technique for identifying PHNQs that shows characteristic bands only between 1890-1480 cm^{-1}, it has been successfully used for characterizing the freeze-dried AIM and ASM fractions extracted from $CaCO_3$ skeletons (Fred's paper, Aizenberg 2002). The FT-IR spectra of the AIM and ASM >1kDa fractions show characteristic vibration bands of protein backbone, polysaccharide moieties and sulfate or phosphate groups (Figure 5 A, Table). In particular, the ASM fraction > 10kDa presents bands identified as amide A (N-H str*etc*hing) at 3290 cm^{-1}, amide B (N-H str*etc*hing) at 3090 cm^{-1}, amide I (C=O str*etc*hing) at 1627 cm^{-1}, amide II (C-N str*etc*hing/N-H bending) at 1537 cm^{-1} and amide III (C-N str*etc*hing/N-H bending) at 1226 cm^{-1}. Bands attributed to ν-C-H and δ-C-H (asymmetric and symmetric) are also observed, they are also all detected in the AIM dark purple portion with additional important band at 1093 cm^{-1} indicative of some polysaccharide moiety (ν -C-O). The grey portion of the AIM fraction shows two very intense bands at 1204 and 1150 cm^{-1}, together with smaller bands at 638 and 552 cm^{-1}, they suggest the presence of sulfate or phosphate groups. Finally, the FT-IR spectra of the ASM < 1kDa fraction shows characteristic bands of PHNQ at 1725, 1632 and 1597 cm^{-1} attributed to ν-C=C, δ-C-O-H and ν-C=O (Glazunov 2014).

Evidence for the presence of intra-crystalline PHNQ-macromolecule complexes

The intense and different colors of the AIM and ASM > 1kDa fractions already suggest that some PHNQ are associated with different macromolecules (Figure 3). Further UV-visible spectroscopy measurements of the ASM > 1kDa and ASM < 1kDa before ether extraction and dialysis respectively confirm this observation. The UV-visible spectra of ASM <1kDa composed mainly of spinochrome A shows two relatively defined UV bands at 273 and 311 nm and a broad visible band with two maximum at 450 and 510 nm, in agreement with (Vasileva2021, Goodwin) (Figure 6A). These bands are also present in the spectra of the ASM > 1kDa (pink curve) especially when measured after precipitation of the black colloid suspension. An additional broad band is detected around 650 nm, which is becoming more intense when the dark colloid suspension is suspended (navy curve) (Figure 6A).

***In vitro* $CaCO_3$ crystallization assay - Effect of PHNQs and PHNQ-macromolecule on $CaCO_3$ crystal growth**

Because, they resist relatively strong NaClO treatments, PHNQs are considered as part of the intracrystalline matrix and are therefore potentially involved in biomineralization processes

(Cusack 1992). The complexity of such biologically controlled mechanisms implies numerous players, in particular organic molecules, at different levels. Some organics may be directly involved in biomineralization by controlling the final crystal structure and morphology or even as simple nucleation sites but some others may be indirectly crucial for biomineralization to occur *e.g.,* by providing the ideal conditions (pH regulation, bacterial decontamination, *etc*). All being incorporated within the final biominerals and thus part of the intracrystalline matrix, these organic molecules may interact differently with the mineral phase either coherently by matching the crystal lattice or in the form of localized inclusions, if fortuitously trapped (Marin 2016).

Although the potential role of echinoderm pigments in biomineralization has been at first discarded based on similar skeletal structures between colored and albinos' sea urchin specimens (Dubois and Chen 1989), it was later shown that PHNQs can complex Ca^{2+} ions (Ledebev 2001, 2003, Zhou 2012), promote mineralized nodule formation in osteogenic sarcoma cells in the presence of $CaCl_2$ (Hou 2020) and are released from the RSC when high levels of intracellular Ca^{2+} ions are measured (Coates 2018).

EXPERIMENTAL SECTION

Sample preparation. *Paracentrotus lividus* sea urchins were obtained from the biological station of Sorbonne University (Roscoff, France). After dissection of the Aristotle lantern, the ceolomic fluid, the gonads and the internal organs were removed. The shells with the spines of each sea urchins were soaked in 200 mL of 5% sodium hypochlorite (NaClO) solution overnight in order to remove most of the organic tissues (podia, muscles, epidermis, *etc.*) allowing the spines to detach from the shells. The spines were further cleaned from their soft tissues by NaClO (12%) under rotative shaking with a tube rotator (Stuart® rotator SB3) for 3 hours and then rinsed extensively with mili-Q water and finally air-dried. Spines of 1cm long were selected from five different sea urchins, the uncolored base of each spine was removed and the shafts were crushed within an agate mortar and sieved into a <200 µm powder. The <200 µm powder was then suspended in a 12% NaClO solution (50 mL/per gram of powder) within several centrifuge tubes. The suspended powder was shaken for 48h at 15 rpm using the tube rotator. After centrifugation with a MIKRO 220R Hettich® centrifuge (6000 rpm, 10 min), the 12% NaClO solution was pipetted off from each tube, the powder rinsed five times with

mili-Q water under rotative shaking for 1h30 and once with MeOH for 5min and finally air-dried (Penkman 2008).

Extraction and isolation of the intra-crystalline organic matrix. After the oxidation treatment, 13.6 grams of the <200 µm powder was slowly dissolved at 4°C with 470 mL of 10% acetic acid solution added at a rate of 1.2 mL/min using a digital burette TITRONIC® 300 until complete dissolution. The dissolved dark purple solution whose pH was 4.4, was distributed within centrifuge tubes, which were centrifuged at 6000 rpm for 15 min at 4°C. The pink supernatant containing the acido-soluble matrix (ASM) was collected and the dark purple pellets containing the acido-insoluble matrix (AIM) were rinsed several times with 10% acetic acid (40 mL) until the supernatant was transparent and then with mili-Q water. The supernatant was then added to the ASM fraction whose final volume was 510 mL. The ASM fraction was further separated at 4°C by ultrafiltration at 2 to 4 bars using a 400mL Millipore® Amicon stirred cell with first, a 10kDa membrane and second, a 1kDa membrane, both previously rinsed and soaked in mili-Q water for 1h. Therefore, three ASM fractions were obtained: F_1>10kDa, 1kDa<F_2<10kDa and F_3<1kDa.

The ASM fractions F_1 and F_2 were then dialyzed at 4°C against mili-Q water using 0.5-1kDa molecular weight cut-off dialysis tubes in order to remove the dissolved salts. Several water changes were done until the volume within the dialysis tubes remain constant. The volume of the F_1 and F_2 increased by XX, respectively. Both fractions were then concentrated by ultrafiltration on the 10KDa and 1KDa membrane, respectively, measured by liquid UV-visible spectroscopy and then freeze dried for further characterization (FTIR and SDS-PAGE gels).

The ASM fraction F_3<1KDa was acidified to pH 2 by adding hydrochloric acid 37% and then partitioned between water and diethyl ether to remove the dissolved salts. The diethyl ether phase containing the PHNQ molecules was collected and another solvent extraction was performed involving equal volume of 4wt% sodium carbonate (Na_2CO_3) solution (pH 11) and diethyl ether to purify the PHNQ fraction from remaining small lipids and peptides. The Na_2CO_3 aqueous phase containing the PHNQs was collected, acidified to pH 2 and then partitioned between water and diethyl ether. The diethyl ether was finally evaporated.

The PHNQs content of the AIM, ASM F_1 and F_2 fraction was finally isolated by destroying the intracrystalline macromolecules by XX% HCl, extracted and purified as for the ASM F_3<1KDa described above.

FIGURES

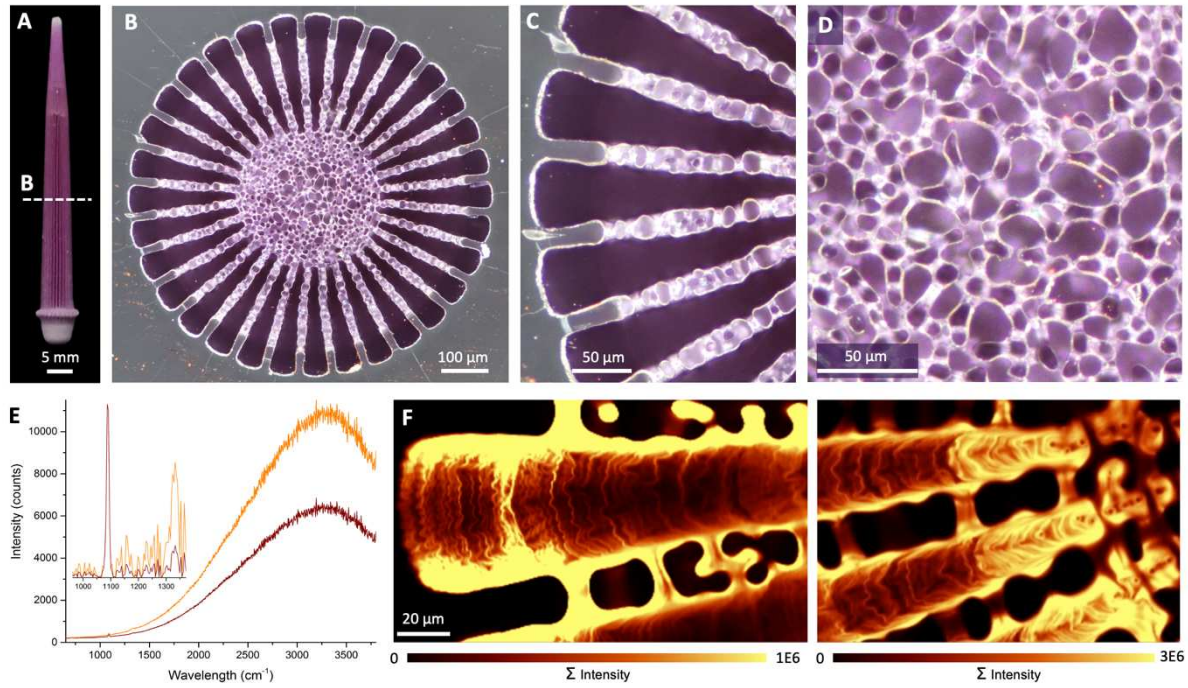
A
B
5 mm
B
100 µm
C
50 µm
D
50 µm
E
Intensity (counts)
Wavelength (cm-1)
F
20 µm
0
1E6
Σ Intensity
0
3E6
Σ Intensity

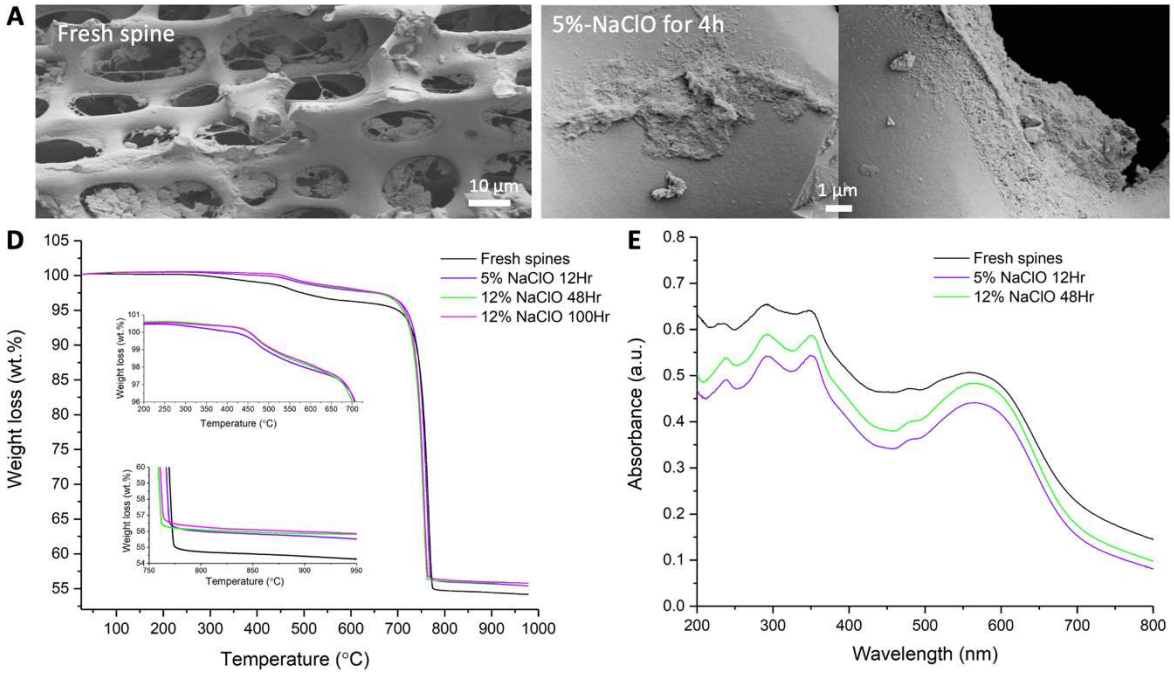
A
Fresh spine
10 µm
5%-NaClO for 4h
1 µm
D
Weight loss (wt.%)
Temperature (°C)
Fresh spines
5% NaClO 12Hr
12% NaClO 48Hr
12% NaClO 100Hr
E
Absorbance (a.u.)
Wavelength (nm)
Fresh spines
5% NaClO 12Hr
12% NaClO 48Hr

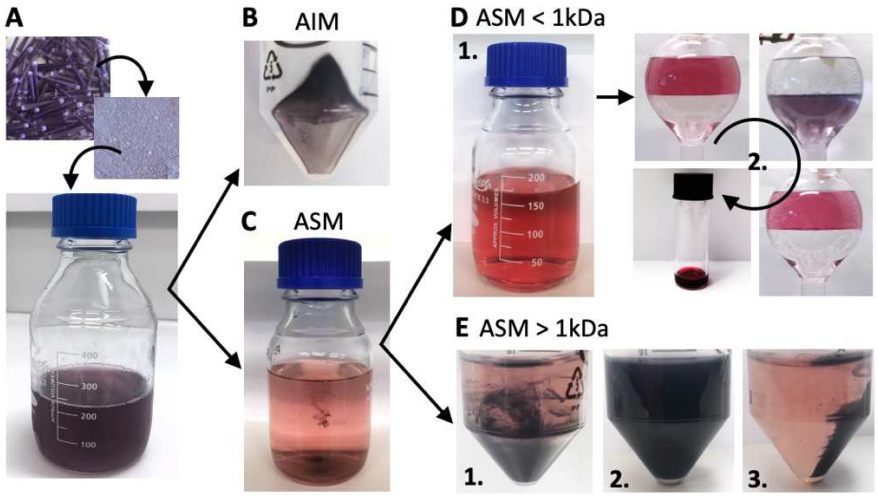
A
B AIM
C ASM
D ASM < 1kDa
1.
2.
E ASM > 1kDa
1.
2.
3.

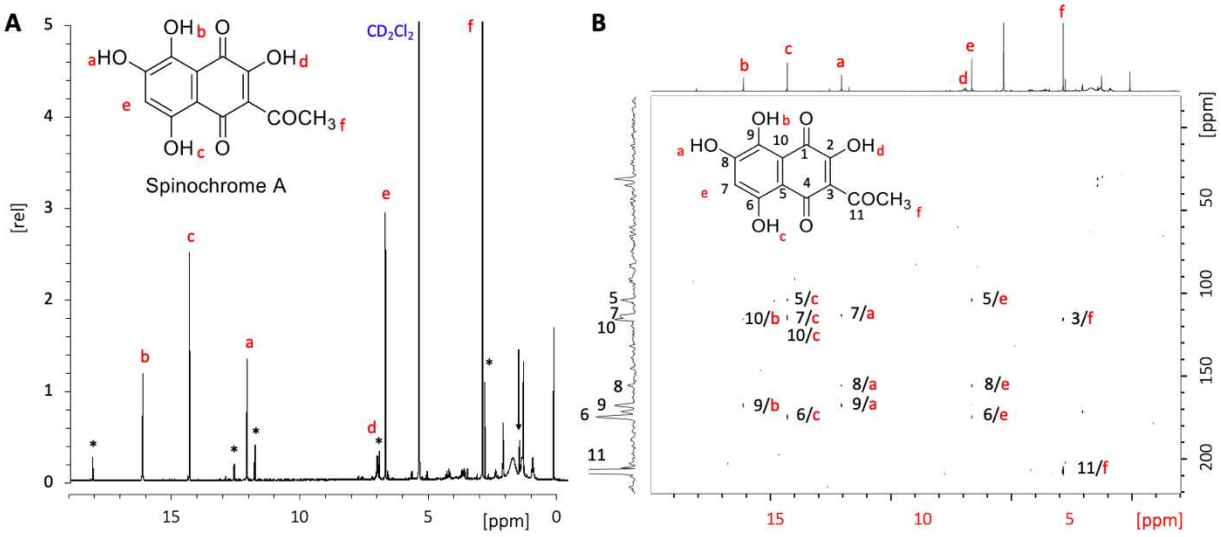
A
Spinochrome A
CD2Cl2
[rel]
[ppm]
B
[ppm]
5/c
10/b
7/c
10/c
7/a
5/e
3/f
8/a
9/a
8/e
9/b
6/c
6/e
11/f

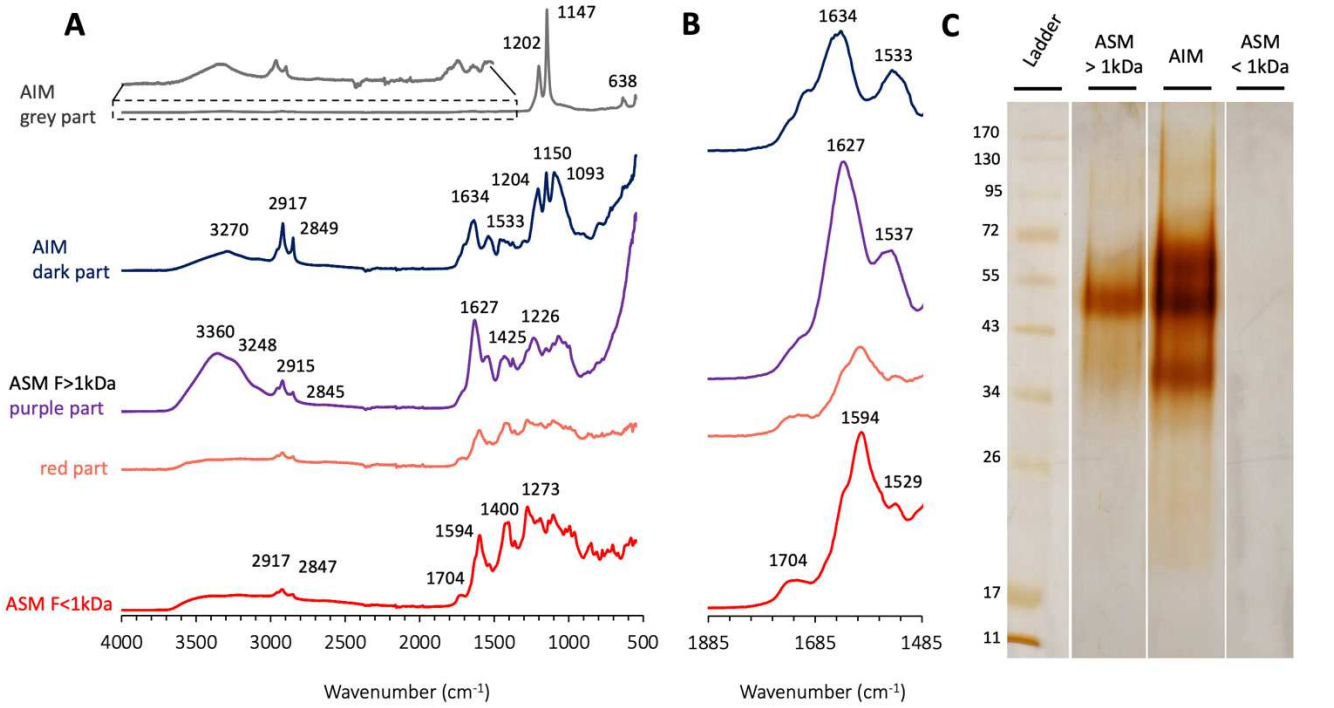
A
AIM
grey part
1147
1202
638
AIM
dark part
1150
1204
1093
2917
3270
2849
1634
1533
ASM F>1kDa
purple part
3360
3248
2915
2845
1627
1425
1226
red part
ASM F<1kDa
2917
2847
1273
1400
1594
1704
4000 3500 3000 2500 2000 1500 1000 500
Wavenumber (cm-1)
B
1634
1533
1627
1537
1594
1529
1704
1885 1685 1485
Wavenumber (cm-1)
C
Ladder
ASM > 1kDa
AIM
ASM < 1kDa
170
130
95
72
55
43
34
26
17
11

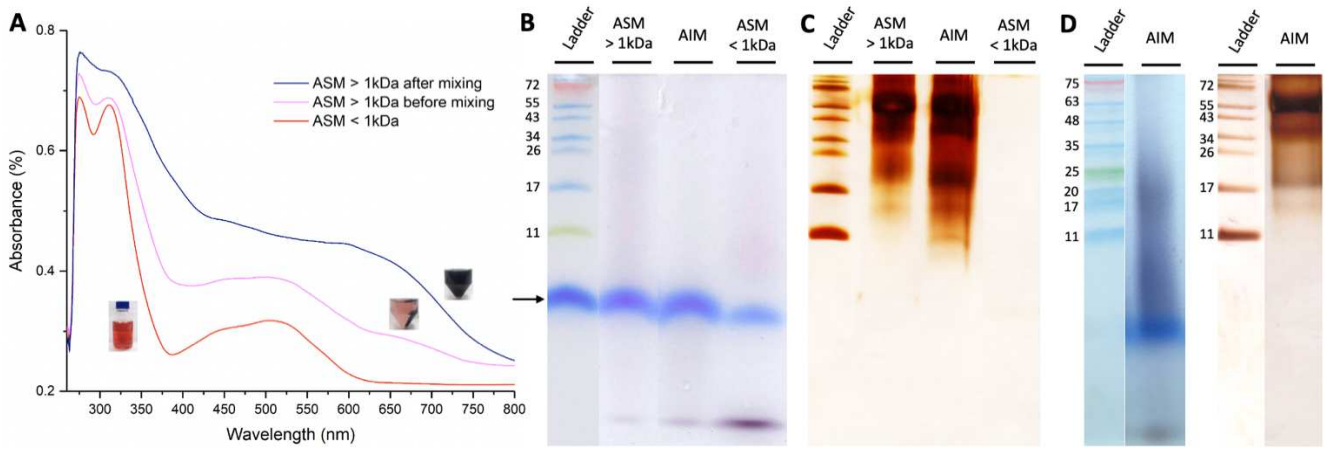
A
Absorbance (%)
0.8
0.6
0.4
0.2
ASM > 1kDa after mixing
ASM > 1kDa before mixing
ASM < 1kDa
300 350 400 450 500 550 600 650 700 750 800
Wavelength (nm)
B
Ladder
ASM > 1kDa
AIM
ASM < 1kDa
72
55
43
34
26
17
11
C
Ladder
ASM > 1kDa
AIM
ASM < 1kDa
D
Ladder
AIM
75
63
48
35
25
20
17
11
Ladder
AIM
72
55
43
34
26
17
11

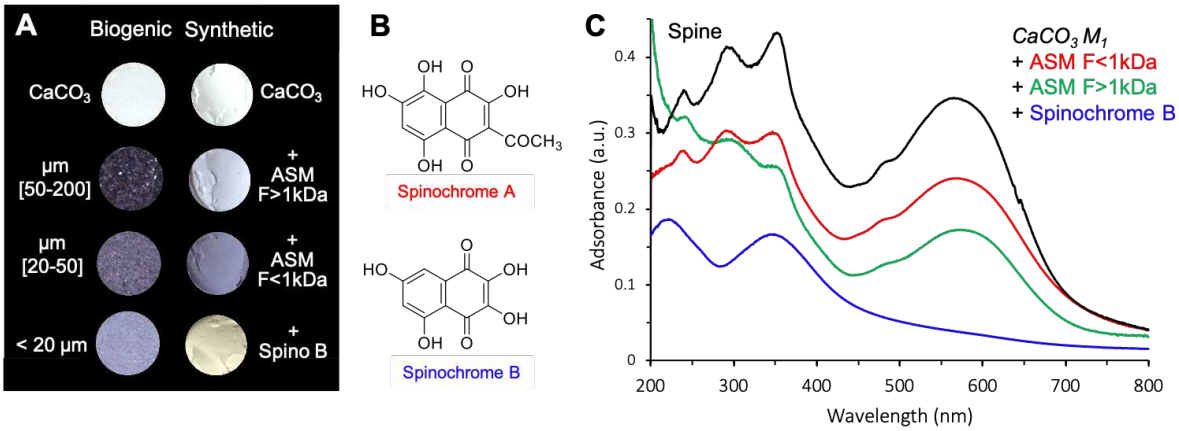
A
Biogenic
Synthetic
CaCO3
CaCO3
µm
[50-200]
+
ASM
F>1kDa
µm
[20-50]
+
ASM
F<1kDa
< 20 µm
+
Spino B
B
HO
OH
O
OH
COCH3
OH
O
Spinochrome A
HO
OH
O
OH
OH
O
Spinochrome B
C
Spine
CaCO3 M1
+ ASM F<1kDa
+ ASM F>1kDa
+ Spinochrome B
Adsorbance (a.u.)
0.4
0.3
0.2
0.1
0
200 300 400 500 600 700 800
Wavelength (nm)

Fig. 7. A) Photographs of biogenic $CaCO_3$ (white test plate and purple spine powder of different granulometry) and $CaCO_3$ powders synthesized by Method 1 in the absence or presence of ASM F>1kDa, ASM F<1kDa or spinochrome B (0.04 mg/mL), B) structure of spinochrome A and B and C) UV-visible spectra of the spine powder and the synthetic $CaCO_3$ powders synthesized by Method 1 in the presence of extracted ASM F<1kDa and ASM F>1kDa as well as pure spinochrome B.

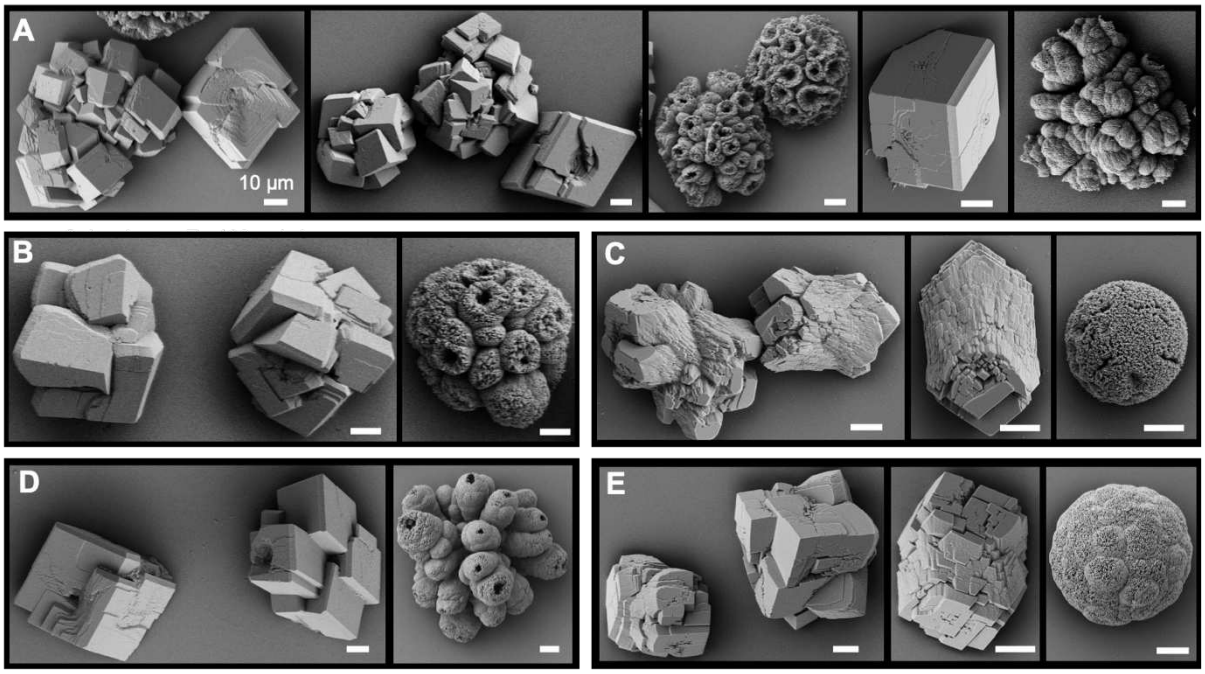

Fig. 8. SEM micrographs of $CaCO_3$ crystals synthesized by Method 2 A) in the absence of pigment and in the presence of B) ASM F<1kDa at 25 µg/mL, C) ASM F<1kDa at 100 µg/mL, D) Spinochrome B 25 µg/mL and E) Spinochrome B 100 µg/mL – scale bar 10 µm.

Appendix 3

Manuscript writing in progress

TITLE:

Halochromic amorphous calcium carbonate crystallization inspired by biomineral pigmentation in sea urchins

Vaskar Sardhalia[1], Shahrouz Amini[2], Peter Fratzl[2], Thierry Azaïs[1,*], Marie Albéric[1,*]

[1]Laboratoire Chimie de la Matière Condensée de Paris Sorbonne Université, CNRS, France

[2]Department of Biomaterials, Max Planck Institute of Colloids and Interfaces, Potsdam, Germany

1. Introduction

Marine life fascinates by its ability of producing a large variety of multifunctional biomineralized structures that often exhibit striking colors whose functions remain unclear (ref.). The wide range of hues observed in calcium carbonate ($CaCO_3$)-based biominerals can be the result of several factors (physical and chemical) (ref.). Among those, is the presence of small organic pigment molecules (<1kDa) of different classes such as carotenoids, bilins, porphyrins, melanin and naphthoquinones (ref). They are found in low quantity (<0.1wt%) within the $CaCO_3$ skeletal elements of mollusks, brachiopods, crustaceans, red corals, crinoids and sea urchins (ref.) in which they are likely occluded during biomineral's crystal growth (Towe). Of particular interest are the polyhydroxy-1,4-naphthoquinone molecules (PHNQs) (Anderson, Vasileva 2021) biosynthesized by sea urchins via enzymatic pathways (ref.) and well-known for their UV-absorption, antioxidant and antibacterial properties (Lebedev 2001, Zhou 2011, Coates 2018, Powell 2014, Brasseur 2017, review Hou). These bio-active secondary metabolites are also responsible for the multiple colors observed in sea urchins from red in the immune red-spherule cells (ref.) to yellow, pink, purple and green in the $CaCO_3$ biomineralized spines (Goodwin, Lederer, Louise, Brasseur). Indeed, PHNQs display intense colors resulting from important electron delocalization in their quinoid structure (Dulo 2021) and which vary in solution according to pH due to successive deprotonations of their numerous hydroxyl groups (Vlès 1928, Zhou 2012, Ledebev 2003). For example, once extracted from

Paracentrotus lividus spines of purple color, spinochrome A (3-acetyl-2,5,7,8-tetrahydroxy-1,4-naphthoquinone), which is red at acidic pH (Goodwin) turns purple at basic pH (our results). Although little is known about biomineral pigmentation mechanisms, this observation suggests that the pH required for $CaCO_3$ crystal's growth (pH>7) (Hu, LeGoff2017, Georgiou2015, Tobler) could play a role, at least in the final biomineral color. On the contrary, mineral formation by organisms, *i.e.* biomineralization pathways have been largely studied (reviews). In sea urchins (Elia, Yael, Gong, Marie), as in other marine organisms (Stan, Pupa, Ingrid…), they occur through the initial deposition of metastable amorphous calcium carbonate (ACC) nanoparticles, which have been shown to be temporarily stabilized by inorganic (ref.) and organic additives (Raz, Yael, Gong) before to crystallize into calcite or aragonite (ref). In particular, the role of organic molecules (*e.g*. citrate, pAsp, pyrophosphate, *etc. big/small molecules* Xu. 1998, poly(acrylic) *etc*.) on biogenic and synthetic ACC formation, composition, structure, stabilization and crystallization mechanisms has been then extensively investigated (ref.). In addition, calcite crystals of different colors have been previously obtained *in vitro* by direct precipitation in the presence of synthetic sulfonated dyes shown to preferentially interact with calcite planes (Marzec 2018, Shan 2004). However, the role of secondary metabolites, such as natural organic pigments on ACC formation and crystallization remains unexplored although it could greatly contribute to our better understanding of biomineralization processes and the development of innovative materials.

Therefore, inspired by the growth of pigmented calcite in sea urchins through ACC in the presence of PHNQs, we here first study the effect of naphthazarin on ACC's color, composition, structure and stability against crystallization. Second, we follow color changes occurring during ACC precipitation and crystallization in solution and induced by mild-annealing. We chose naphthazarin (5,8-dihydroxy-1,4-naphthoquinone) because it is a natural secondary metabolite commercially available, which presents an analogue molecular structure to PHNQs and changes of colors from red to purple at similar pH (Land 1983) than spinochrome A (our results).

Using a wide range of mostly *in situ* techniques, we show that naphthazarin used in biologically relevant concentrations produces intense colored hybrid pigments but have little effect on ACC structure and stability against crystallization, especially in solution. More strikingly, we demonstrate that naphthazarin, which is red at acidic pH (<7.9) and blue before ACC precipitation (pH>10.7), leads to a lavender blue ACC powder that further crystallizes in

solution into a purple mixture of calcite and vaterite that ultimately converts to a purplish-red calcite powder. We propose that these remarkable changes in color are due to successive OH deprotonations of naphthazarin driven by pH variations imposed by ACC precipitation, crystallization and calcite formation in solution and thus, during a likely redissolution/precipitation mechanism. In contrast, when ACC crystallization is induced by mild-annealing, shown to proceed *via* solid-state transformation (ref.), purple calcite is obtained. Thus, by controlling the speciation of naphthazarin in solution and capturing its partial deprotonation state within amorphous and then crystalline hybrid pigments, we here reveal an halochromic ACC crystallization pathway that could unveil color changes during the pigmentation of $CaCO_3$-biominerals formed through amorphous phases. Blue colors that mostly originate from structural color in nature (ref.), can thus be obtained by tweaking red pigments using pH shift, a strategy already used by some plants (Basilio 2021). Reproducing such *in vivo* strategies, *in vitro* is of high interest for building advanced bioinspired amorphous hybrid pigments with halochromic properties upon crystallization for applications such as bio-sourced and potentially bio-active material's coloration.

2. Results and Discussion

2.1. Influence of naphthazarin on ACC color, composition and structure

Amorphous calcium carbonate (ACC) powders were synthesized with the direct and fast precipitation method widely used for ACC precipitation (Koga, Zou, *etc*.). Briefly, the different powder samples were recovered shortly after the fast addition of $CaCl_2$ to a Na_2CO_3 solution containing different concentrations of naphthazarin [0-0.53 mM] the different (for details see Material and Methods).

The amorphous nature of the samples after synthesis in the absence or presence of naphthazarin was confirmed by the absence of Bragg peaks in the XRD pattern (SI, Fig. 1 A).

Figure A) show the striking difference of colors between the red naphthazarin powder, the white pure ACC sample and the blue-lavender color displayed by the ACC sample synthesized in the presence of 0.53 mM naphthazarin and named here after ACC-0.53 mM Naphtha. These colors were confirmed and further quantified by visible diffuse reflectance measurements which allow further calculation of the xy values reported on the CIE diagram 1931 (Fig. 1B). In addition, distinct signatures in the UV range were also observed. The white ACC powder displays no

characteristic absorbance while ACC-0.53 mM Naphtha shows two bands at 225 nm and 300 nm and a multiple broad band at 600 nm, therefore all attributed to the presence of naphthazarin. However, these bands are different from the ones of the spectra of pure naphthazarin at 275 nm, 425 and 585 nm. This result suggests that the molecular state of naphthazarin has been modified during ACC precipitation.

To investigate the effect of naphthazarin on the local structure of ACC, SAXS/WAXS measurements for Pair Distribution Functional analysis provide insight into the effect of naphthazarin on the inter-atomic distances. The PDF analyses also give the characteristic signature of ACC (ref.) with MRO up to 10 A and the Ca-O, O-O, Ca-O and Ca-Ca inter) atomic distances peaks (Fig. 1 A).

At room temperature, ACC and ACC+naphthazarin show very similar PDF exhibiting characteristic short and medium-range order up to 10Å with typical positions for main maxima around 2.4Å, 2.9Å, 4.1Å and 6.2Å mainly containing contributions from Ca-O pairs, O-O pairs, Ca-O/Ca-Ca pairs (1st shell) and Ca-O/Ca-Ca pairs (2nd shell), respectively.

Using TGA measurements, we monitored the removal of water, and the crystallization of ACC into calcite, on this basis we quantified the relative weight fractions of water associated with colored ACC having different concentrations of naphthazarin. The TGA-IR measurements were performed on ACC, ACC+0.01mg Naphtha, ACC+.02mg/ml Naphtha and 0.1mg/ml Naphtha. It was observed that there was no difference in the relative amount of water associated with the different ACC samples. However, there was a slight difference in the amount of water adsorbed on ACC and the structural water lost during the ACC crystallization into the calcite which was calculated using the first derivative of the TGA data. During the crystallization, the water lost for ACC+0.1mg/ml Naphtha was ~2.5wt.% which compared to pure ACC ~3wt%. This result suggests that the higher the concentration of naphthazarin the higher the amount of water adsorbed as naphthazarin is hygroscopic and therefore it lowers the amount of structural water thus making the ACC phase more stable which is in correlation with the results obtained from DSC measurement.

2.2. Effect of naphthazarin concentrations on ACC stabilization against crystallization in solution versus in air (Figure. 2 and 3)

The synthesis of $CaCO_3$ was performed in a Metrohm titrando setup that allows monitoring the pH and free [Ca^{2+}] during the fast precipitation of ACC after the addition of $CaCl_2$ into a Na_2CO_3 solution and the successive crystallizations in solution into a mixture of calcite and vaterite (2min) that further crystallize into calcite only (2days).

The addition of $CaCl_2$ solutions in the Na_2CO_3 solution resulted in an immediate decrease in pH from ~11.5 to 10.2 and simultaneously an increase in the [Ca^{2+}]. As soon as the precipitation of ACC starts the free [Ca^{2+}] decreases leading to an increase in pH from 10.2 to 10.4. After this, a plateau is observed for both pH and [Ca^{2+}] which corresponds to the stable ACC phase, which converts to a mixture of calcite and vaterite at around 350-400s.

It was observed that with the addition of naphthazarin, the ACC crystallization into calcite and vaterite is delayed by 30-the 50s. The pH and [Ca^{2+}] were monitored for 50000s and at around 33000s the mixture of calcite and vaterite gets converted to calcite only. This change corresponds to a small decrease in pH and [Ca^{2+}] on the profiles(**fig.3**). Importantly the effect of naphthazarin addition on the ACC phase stability does follow a linear trend. It was observed that the addition of naphthazarin up to 0.02mg/ml concentration stabilizes the |ACC phase and any concentration greater than 0.03mg/ml naphthazarin has an opposite effect on the stability of the ACC phase meaning that the crystallization into vaterite and calcite mixture occurs faster.

The presence of different polymorphs of $CaCO_3$ at different time intervals of the reaction was confirmed by carrying out PXRD measurements. The $CaCO_3$ collected at the plateau of the pH profile showed no Bragg's peak in the diffractogram. ACC was also characterized by the FT-IR spectroscopy which showed a characteristic band i.e. -OH bending around 1650 cm^{-1} and asymmetric CO_3^{2-} at 1540 cm^{-1}. The XRD diffractograms of $CaCO_3$ powder filtered at around 700s, predicted the presence of a mixture of vaterite and calcite (**SI**). The conversion of the mixture of calcite+vaterite into calcite was confirmed by XRD on powder filtered after 48hrs (**SI**).

The effect of naphthazarin on ACC crystallization temperature was studied by performing DSC measurements. In the DSC profile of ACC (**fig.X**), the peak around 100°C corresponds to the loss of water which is an endothermic process, and the peak at ~150°C is for ACC crystallization which is an exothermic process. The enthalpy of hydration for ACC: 179.2 J/g, ACC+0.02mg/ml naphthazarin: 186.7 J/g, ACC +0.1mg/ml naphthazarin: 242.8 J/g. The crystallization temperature for ACC, ACC+0.02mg/ml naphthazarin, and ACC +0.1mg/ml

naphthazarin were 152ºC, 160ºC, 200ºC respectively, and enthalpy of crystallizations were 29.3J/g, 36.8J/g, 48.38J/g respectively. Comparing the ACC DSC profile with ACC+naphthazarin, it can be observed that with an increase in naphthazarin concentration, the ACC crystallization temperature increases suggesting that the addition of naphthazarin stabilizes the ACC phase. The trend in the effect of naphthazarin on the stability of the ACC phase against crystallization by heating is linear in comparison with the trend obtained in solution i.e with an increase in naphthazarin concentration the ACC phase stability against crystallization increases. Zou *et al*. demonstrated that the stability of the ACC can also be affected by the size of the ACC nanoparticles. ACC with smaller nanoparticles has greater stability in air as compared to larger nanoparticles. To confirm that the stability of ACC was not increasing because naphthazarin was affecting the ACC particle SEM-FEG micrographs were obtained for ACC, ACC+0.02mg/ml naphthazarin, and ACC+0.1mg/ml naphthazarin. It revealed that the average size for ACC particles was between 95-110 nm which was very close to the particle size for ACC+ naphthazarin 95-105 nm.

and nanoparticles were observed under SEM-FEG with a relative broad size distribution with an average size of 142 ±42 nm for pure ACC and of 144±45 nm for ACC-0.53 mM Naphtha.

These results suggest that the naphthazarin does not affect the size of the ACC nanoparticles suggesting stabilization of the ACC phase by naphthazarin is not related to the size effect of ACC nanoparticles**(Zou_2014)**.

Heat-assisted crystallization of ACC was carried out to mimic the solid-state crystallization mechanism occurring *in vivo*. To evidence small local ordering during the heat-induced ACC crystallization, dPDF/dT maps were generated (**Fig X**). In the dPDF/dT maps the blue color corresponds to negative change and the red color represents positive change. The most important changes in the dPDF/dT maps are related to the crystallization which corresponds to the sudden increase in the PDF intensities. The structural rearrangement before the crystallization is accompanied by the loss of water from the ACC phase. The crystallization of ACC varies in terms of onset temperature and length according to different samples. In the dPDF/dT maps, crystallization starts at 180°C and last 30°C for pure ACC, whereas with the addition of naphthazarin, ACC crystallization onset temperatures increases to 200°C and last for more than 30°C. Regarding the local rearrangements, the ACC+naphthazarin show small differences in the degree of SRO rearrangement from pure ACC, and significant differences are observed in the MRO around 6-7 Å which corresponds to the interatomic distances for Ca-

O/Ca-Ca pairs (2nd shell). However, we did observe a naphthazarin peak at around 0.8Å, which might be appearing due to the presence of crystalline naphthazarin deposited on the ACC powder. During the *in-situ* heating, the peak belonging to the naphthazarin moves and ultimately disappears at higher temperatures suggesting naphthazarin undergoes structural change due to heating and at high temperatures, it decomposes leading to the disappearance of the naphthazarin peak. Here we say naphthazarin adsorbed on the ACC because, at the end of the *in-situ* heating cycle, the ACC powder is still colored meaning naphthazarin is still present.

2.3. Protonation state of naphthazarin and color changes during ACC formation and crystallization in solution and in air

The protonation state of the naphthazarin was also analyzed using UV-Vis spectroscopy **(figure X)**. Naphthazarin in an aqueous solution can exist in the fully protonated form or other forms i.e. singly deprotonated or doubly deprotonated form **(Land 1983)**. Protonation to naphthazarin might occur in very acid solutions. The color of the naphthazarin varies depending upon the pH, the solution is blue-violet in dilute alkali (~pH 8.5), deep blue in strong alkali (~pH 11) rose-red at mildly acid (~pH 5), and neutral pH. To get the complete picture of the behavior of the naphthazarin molecules in aqueous solution absorption spectroscopy was performed on a naphthazarin solution prepared at different pH. It can be evidenced that with an increase in pH on going from acidic to alkaline or as each hydroxy group ionizes the visible absorption band shifts further into the red and there is an increase in the extinction coefficient. The interplay between the intensity of the two bands in the visible region corresponds to the protonation state of the naphthazarin. For singly protonated species the band around 570 nm has higher intensity whereas when the intensity of the band at **630** nm becomes higher it corresponds to the doubly deprotonated species. This study provides evidence of the molecular state of naphthazarin incorporated within the calcite could be a mixture of single and double-deprotonated naphthazarin as the synthesis occurs between pH 11.4 and pH 9.5.

To confirm the incorporation of naphthazarin into calcite polymorph bleaching experiments were carried out. It was concluded that in the case of calcite, the color did not degrade. The UV-Vis measurements also confirmed the degradation of naphthazarin as for the bleached ACC there was no absorbance band in the visible region.

We measured cross-polarization ^{13}C NMR for pure naphthazarin. The proton exchange between the hydroxyl and keto groups generates three chemically different carbons. In the NMR

spectra, we observed three distinct peaks at 112 (9,10), 173 (2,3,6,7), and 137 (1,4,5,8) ppm corresponding to carbons in three chemical enviro nments.

To study how naphthazarin interacts with calcite, 13C ss NMR was measured on calcite+0.1mg/ml naphthazarin system. We evidenced the characteristic peak for carbonate at 168ppm, coming from hydrated and disordered $CaCO_3$ domains. Interestingly, the peak from 2,3,6,7 was now composite. But the more important change in the spectrum was the splitting of the 1,4,5,8 peak in two resonances: 1) at 180 ppm (C=O) and 2) at 170 ppm (=C-OH) seen as a shoulder on the left of the carbonate peak. The exchange between hydroxyl and keto groups not happening anymore. There could be two explanations for the above phenomenon, 1) the naphthazarin molecules in the calcite system are rigid and the system is stopping or making it difficult for this exchange to occur, 2) the naphthazarin molecules in the calcite system are deprotonated which generates more chemically different Carbon atoms resulting in the splitting of peaks on the spectra.

To confirm the molecular state of naphthazarin incorporated within the calcite, we measured cross-polarization ^{13}C NMR on naphthazarin_basic. We observed the characteristic peak for carbonates at around 168ppm and for bicarbonates at around 164ppm which appear due to the presence of Na_2CO_3 and $NaHCO_3$ respectively. Interestingly We evidenced the characteristic peak for carbonate at 168ppm, coming from hydrated and disordered $CaCO_3$ domains. Interestingly, the peak from 2,3,6,7 naphtha carbons is in a very similar position to that of calcite_naphthazarin. We also evidenced the same splitting of the 1,4,5,8 naphtha peak in two resonances: 1) at 180 ppm (C=O) and 2) at ~170 ppm (=C-OH). The results obtained suggest that the second explanation regarding the nature of the naphthazarin molecules incorporated in the calcite system is more likely to be true i.e., deprotonation of naphthazarin generates more chemically different carbon atoms resulting in the splitting of peaks on the spectra.

3. Discussion

5. Experimental Section

6. Figures

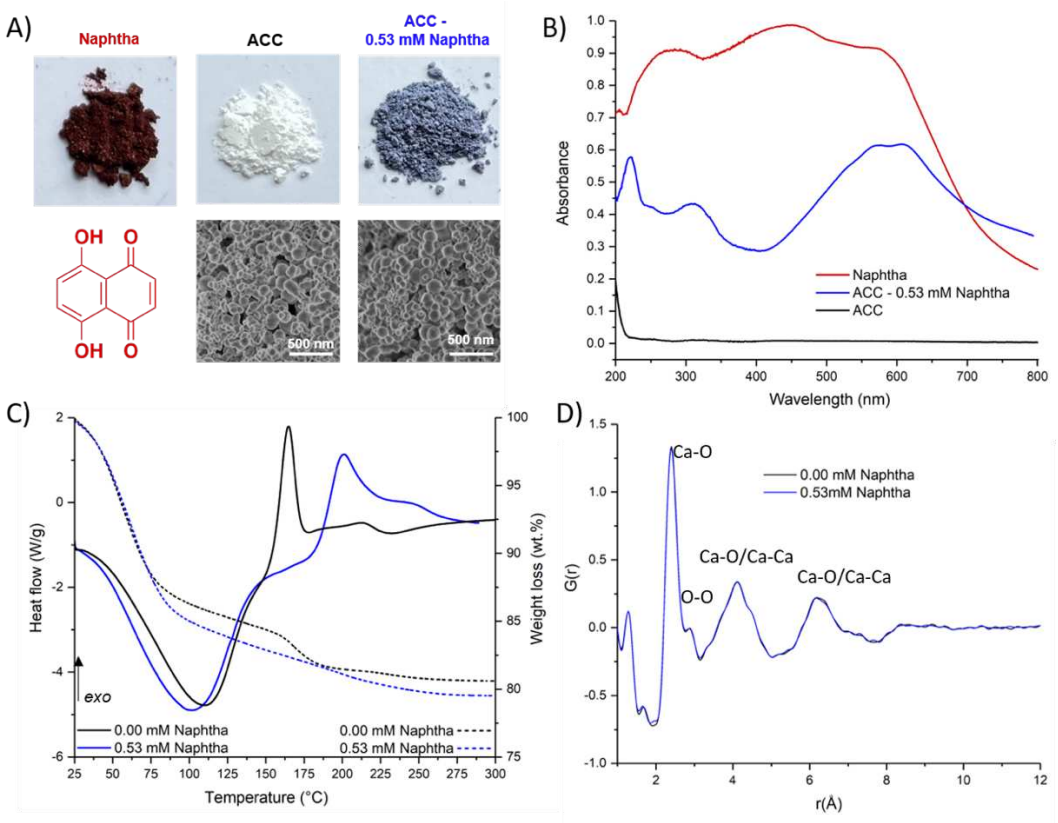

Fig. 1. A) Powder photographs of naphthazarin, pure ACC and ACC synthetized in the presence of 0.53 mM naphthazarin, B) diffuse reflectance spectra of naphthazarin powder in red, pure ACC powder in black and ACC powder with 0.53 mM naphthazarin in blue, C) DSC measurements (solid line) and TGA (dashed line) of ACC synthesized without (in black) and with (in blue) 0.53 mM naphthazarin and D) PDF of ACC synthesized without (in black) and with (in blue) 0.53 mM naphthazarin.

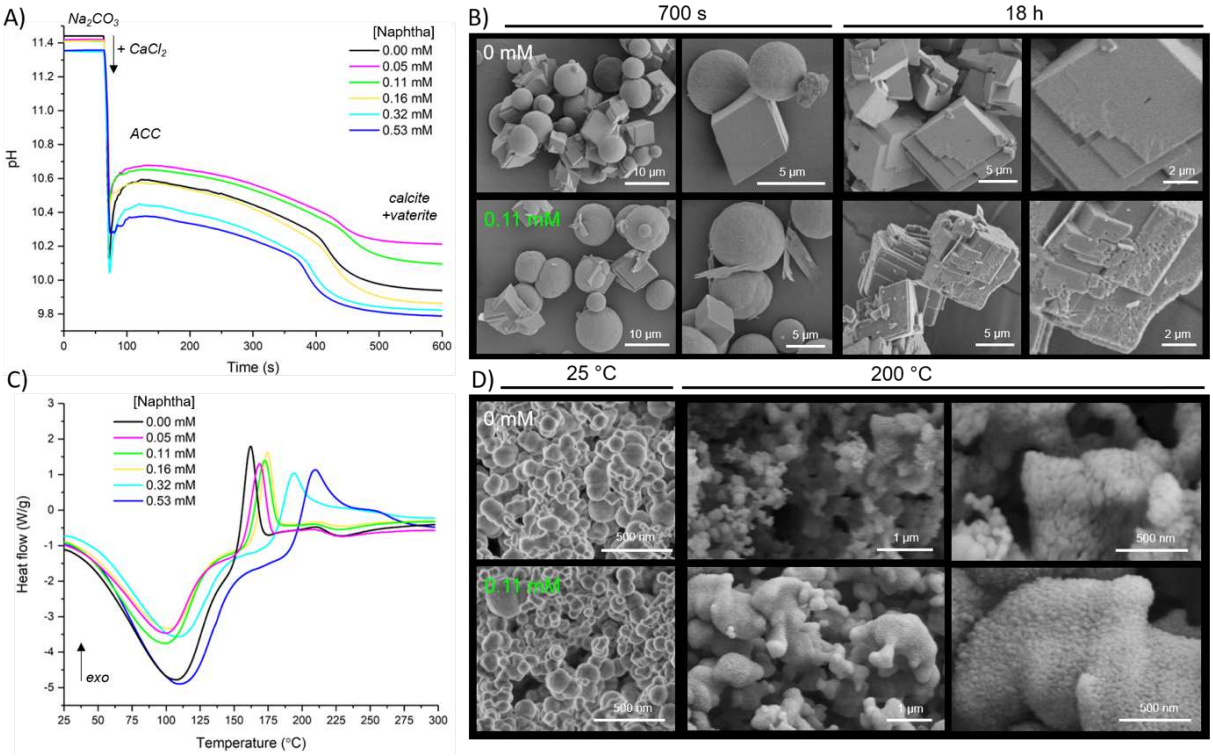

Fig. 2. A) pH profiles as a function of time (s) during the addition of $CaCl_2$ into a Na_2CO_3 solution having different naphthazarin concentrations ranging from 0 to 0.53 mM, the formation and the plateau of stability of ACC as well as its crystallization into a mixture of calcite and vaterite are indicated, B) SEM micrographs of the resulting $CaCO_3$ powders synthesized in the absence (0 mM) and presence (0.53 mM) of naphthazarin recovered at 700s and 18h of the reaction, C) DSC measurements of ACC powders synthesized in the presence of different naphthazarin concentrations from 0 to 0.53 mM, exothermic peaks due to ACC crystallization are detected between 150°C and 275°C, D) SEM micrographs of the ACC powders synthesized in the absence (0 mM) and presence (0.53 mM) of naphthazarin at 25°C and after heat-treatment at 200°C for 1h.

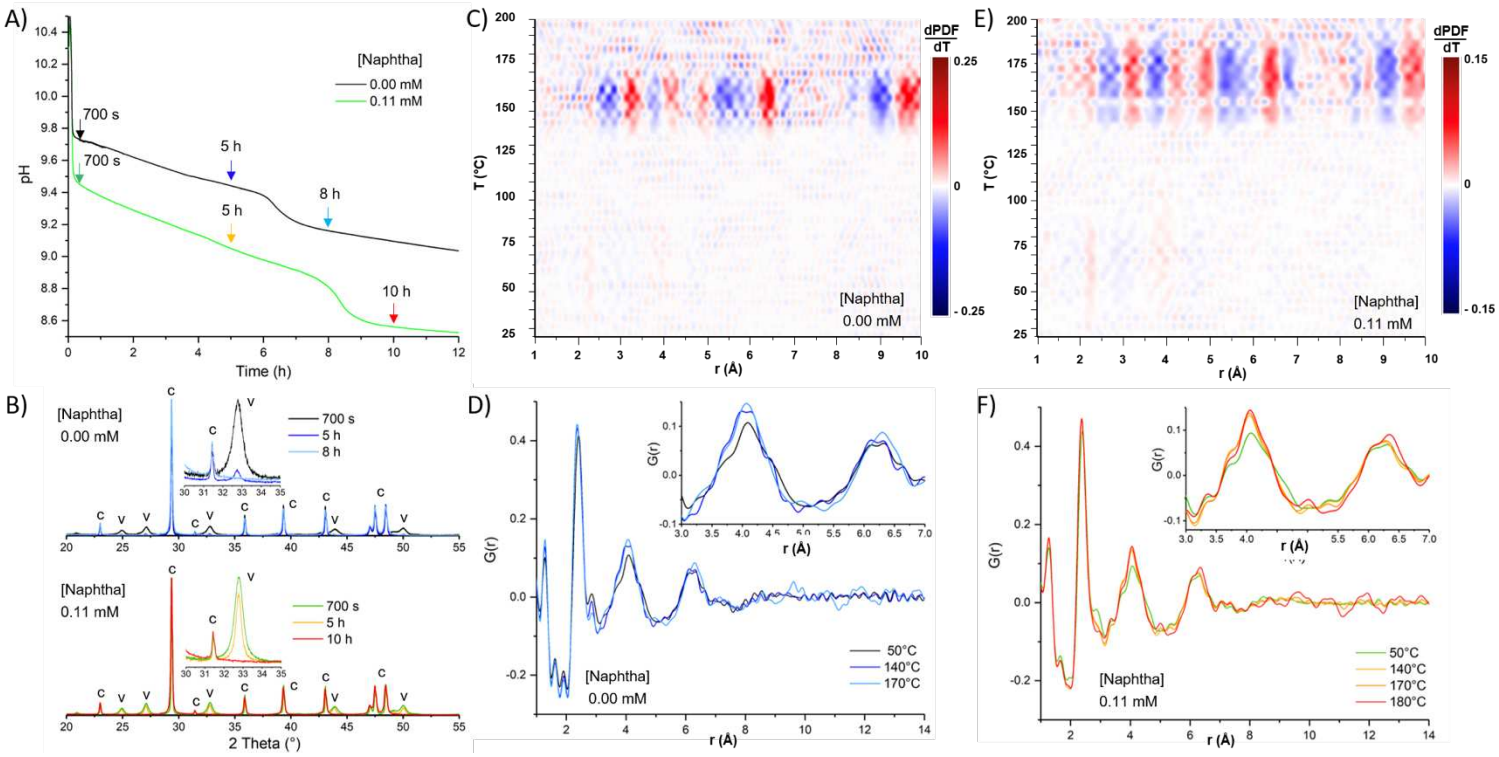

Fig. 3. A) pH profiles as a function of time (h) during $CaCO_3$ formation in the absence (in black) and presence (in green) of 0.11 mM naphthazarin, the first plateau corresponds to the crystallization of ACC into a mixture of calcite and vaterite and the second one to the complete conversion into calcite only as confirmed by B) XRD laboratory measurements taken at 700s, 5h, 8h and 10h, the vaterite (v) and calcite (c) reflection peaks are indicated, C) differential dPDF/dT maps of ACC with D) selected PDFs at 50°C, 140°C and 170°C and E) differential dPDF/dT maps of ACC + 0.11 mM naphthazarin with F) selected PDFs at 50°C, 140°C and 170°C.

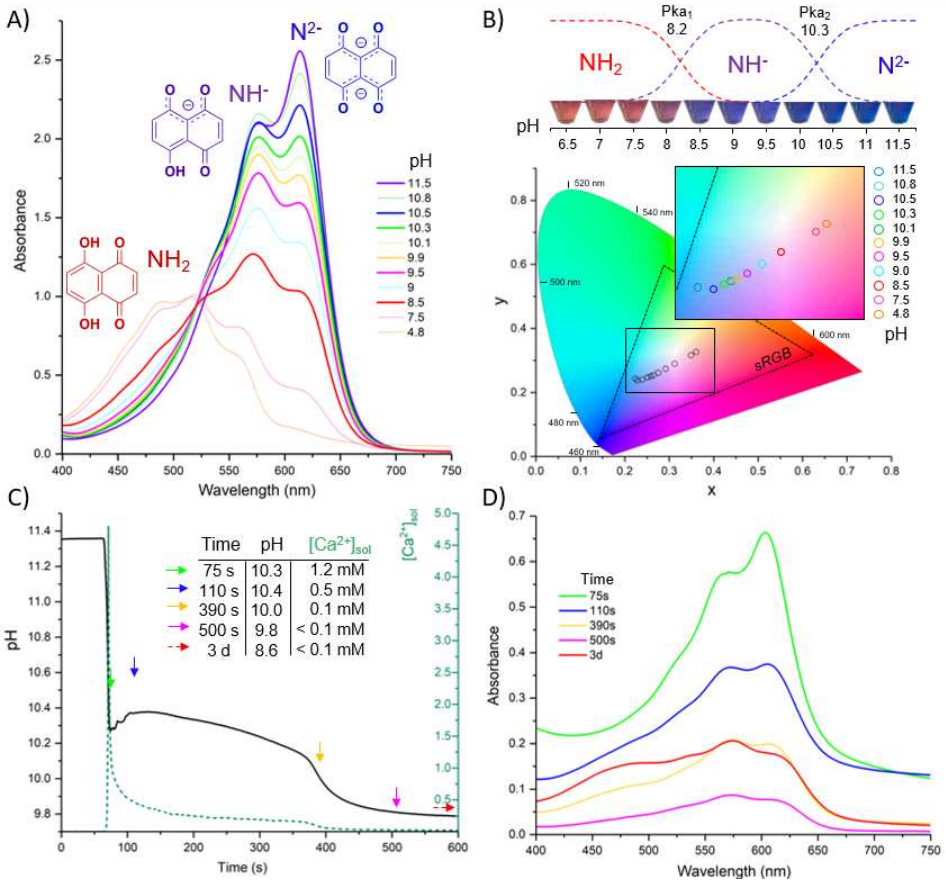

Fig. 4. A) UV-visible spectra of 0.53 mM naphthazarin in water at different pH from 11.5 to 4.8 adjusted with HCl and NaOH, B) speciation diagram of NH_2, NH^- and N^{2-} forms, color changes according to pH of a 0.11 mM naphthazarin solution and the CIE 1931 diagram obtained based on the spectra shown in A), C) pH and [Ca^{2+}] profiles as a function of time (s) during the precipitation of ACC in the presence of 0.53 mM naphthazarin and its crystallization into a mixture of calcite and vaterite and D) UV visible spectra of the titrant taken at different times of the reaction indicated by colored arrows in C).

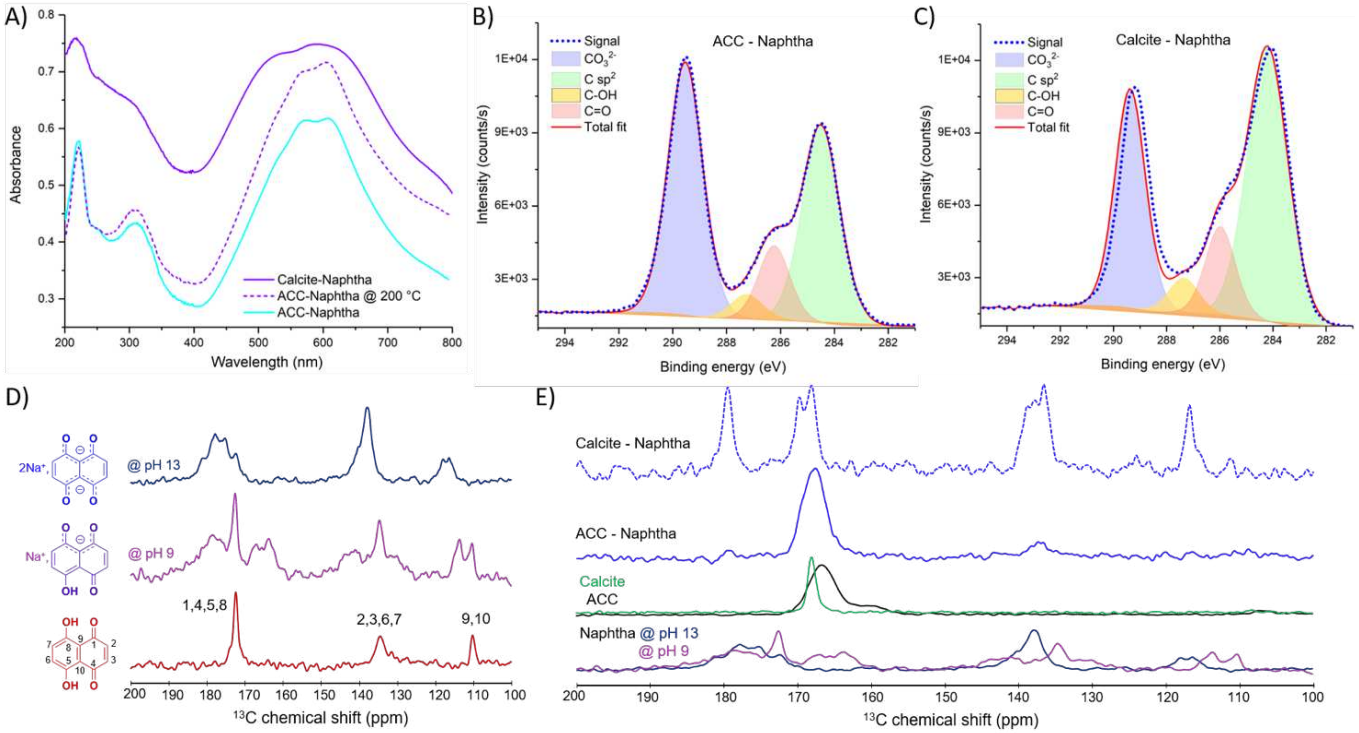

Fig. 5. A) UV-visible diffuse reflectance spectra of $CaCO_3$-0.53 mM naphthazarin powders, X-ray photoemission spectra for carbon, C 1s, and fitted components (CO_3^{2-}, C sp^2, C-OH and C=O) of B) ACC-0.53 mM naphthazarin powder and C) Calcite-0.53 mM naphthazarin powder, ^{13}C CP-MAS NMR spectra of D) naphthazarin and Na-naphthazarin salts prepared at pH 9 and 13 and of E) $CaCO_3$ powders synthesized in the absence and presence of 0.53 mM naphthazarin.

Supplementary Information

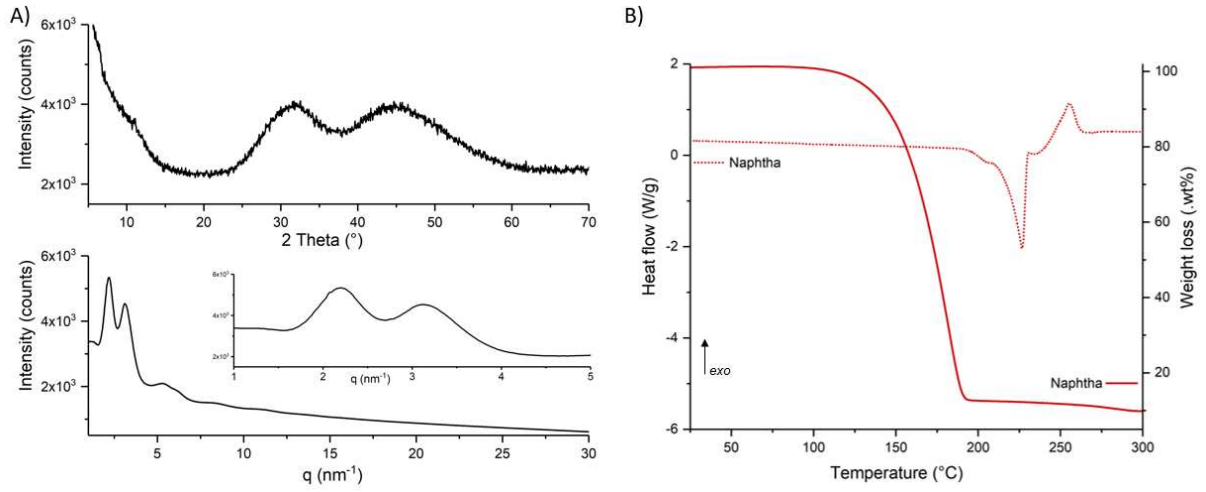

Fig. SI1. A) Characteristic XRD profile of ACC acquired with a laboratory D8 instrument (top) and at ID15A beamline (ESRF, France) (bottom), B) TGA (solid line) and DSC (dotted line) measurements of naphthazarin powder.

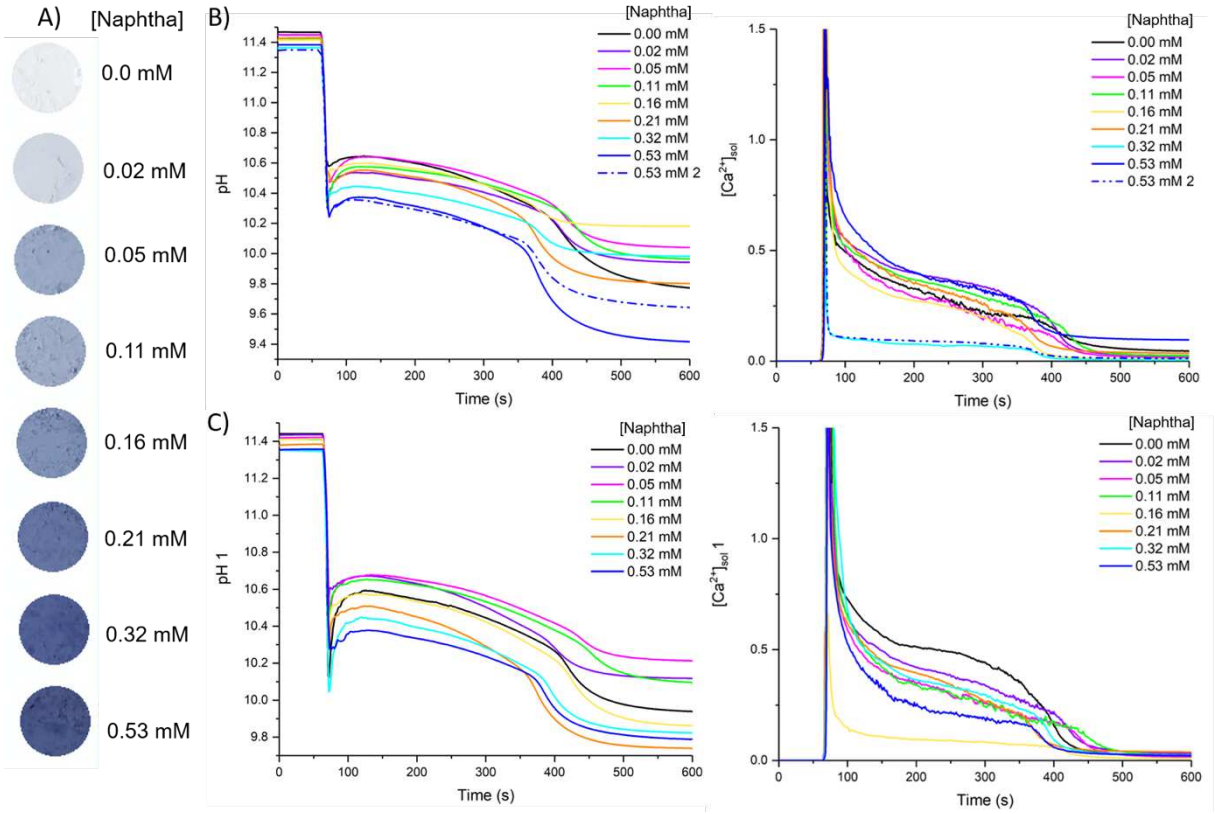

Fig. SI2. A) Photographs of the ACC powder synthesized in the presence of naphthazarin from

0 to 0.53 mM, B and C) series of pH and Ca^{2+} profiles as a function of time (s) during the addition of $CaCl_2$ into a Na_2CO_3 solution having different naphthazarin concentrations ranging from 0 to 0.53 mM and acquired in two different days respectively.

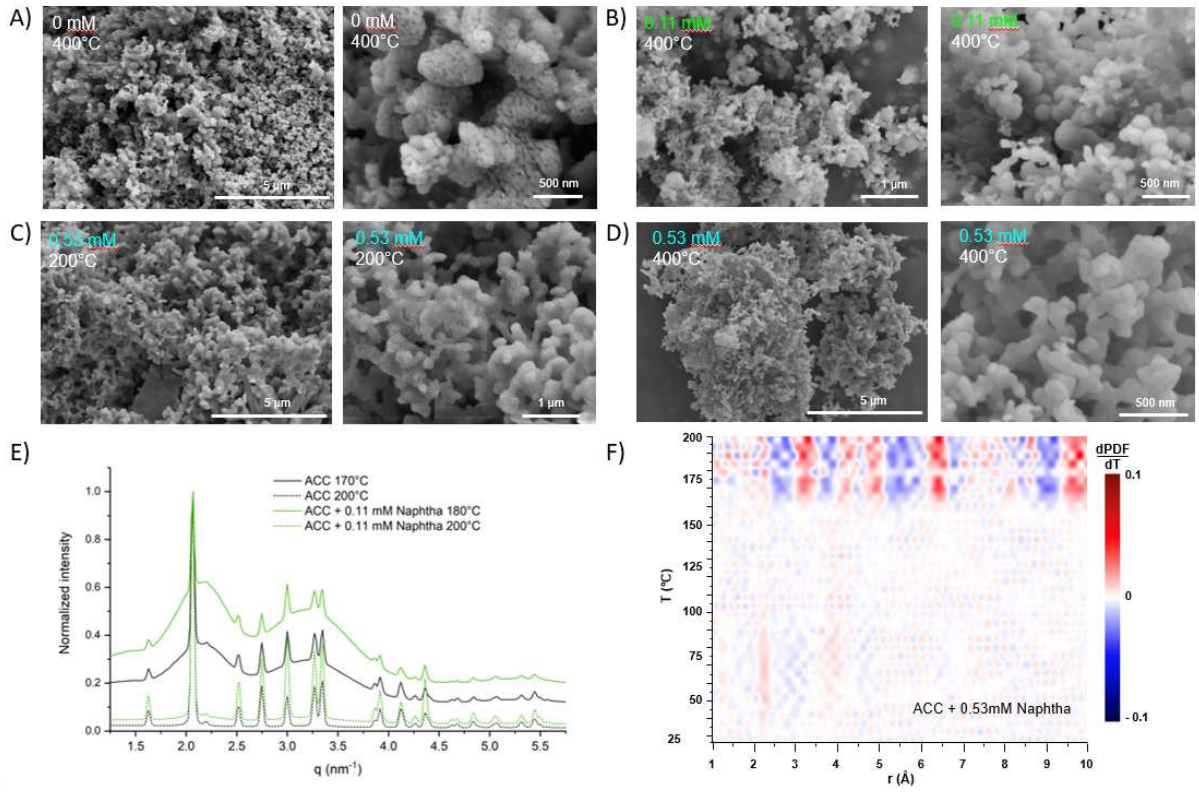

Fig. SI3. A-D) SEM micrographs obtained after heat-treatments at 200°C and 400°C of ACC powders synthesized in the absence (0 mM) and presence (0.11 mM and 0.53 mM) of naphthazarin, E) XRD profiles acquired at ID15A beamline (ESRF) around the temperature of ACC crystallization (200°C) of pure ACC and ACC – 0.11 mM naphthazarin and F) differential dPDF/dT maps of ACC-0.53 mM naphthazarin sample.

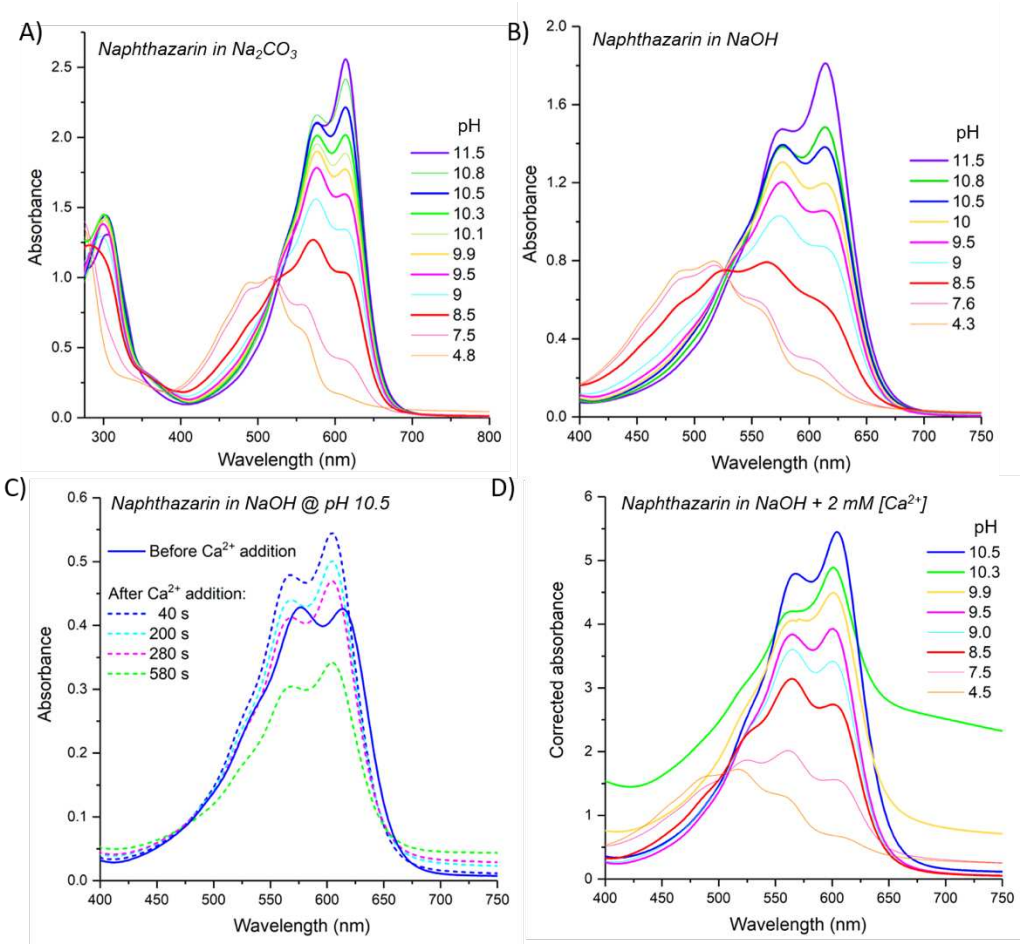

Fig. SI4. UV-visible spectra of 0.53 mM naphthazarin solution at different pH from 11.5 to ~4.5 adjusted with HCl and NaOH A) in Na_2CO_3 and B) in NaOH, and UV-visible spectra of naphthazarin in NaOH before and after the addition of 2 mM Ca^{2+} C) at pH 10.5 and at different time points from 40 to 580 s and D) at different pH from 10.5 to 4.5 right after 2 mM Ca^{2+} addition.

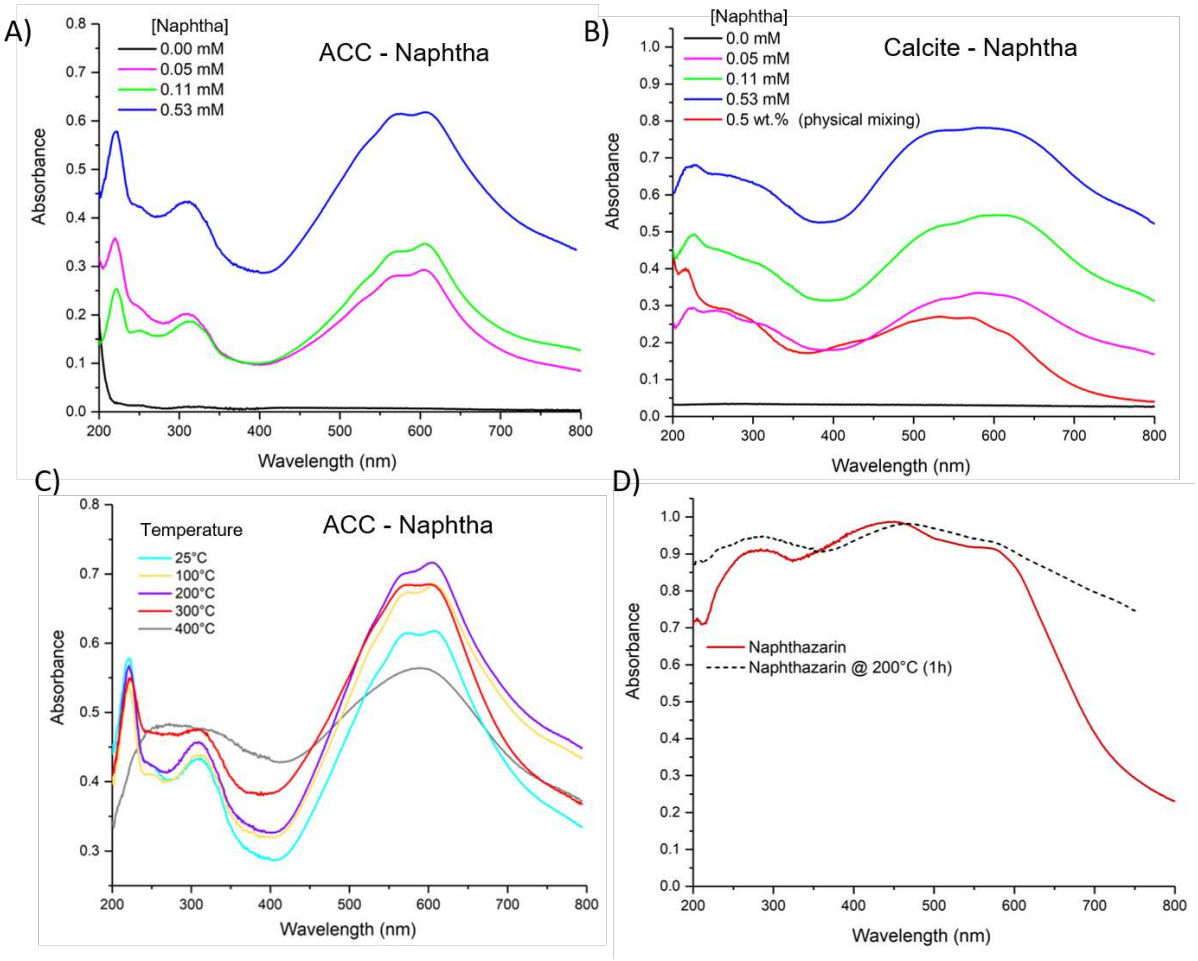

Fig. SI5. UV-visible diffuse reflectance spectra of A) ACC-naphthazarin samples, B) Calcite-naphthazarin samples obtained by direct precipitation with naphthazarin concentrations from 0 to 0.53 mM and by physical mixing with 0.5wt% naphthazarin, C) ACC- 0.53 mM naphthazarin at 25°C and after heat-treatments at 100°C – 400°C for 1h, D) Naphthazarin before and after heat-treatment at 200°C for 1h.

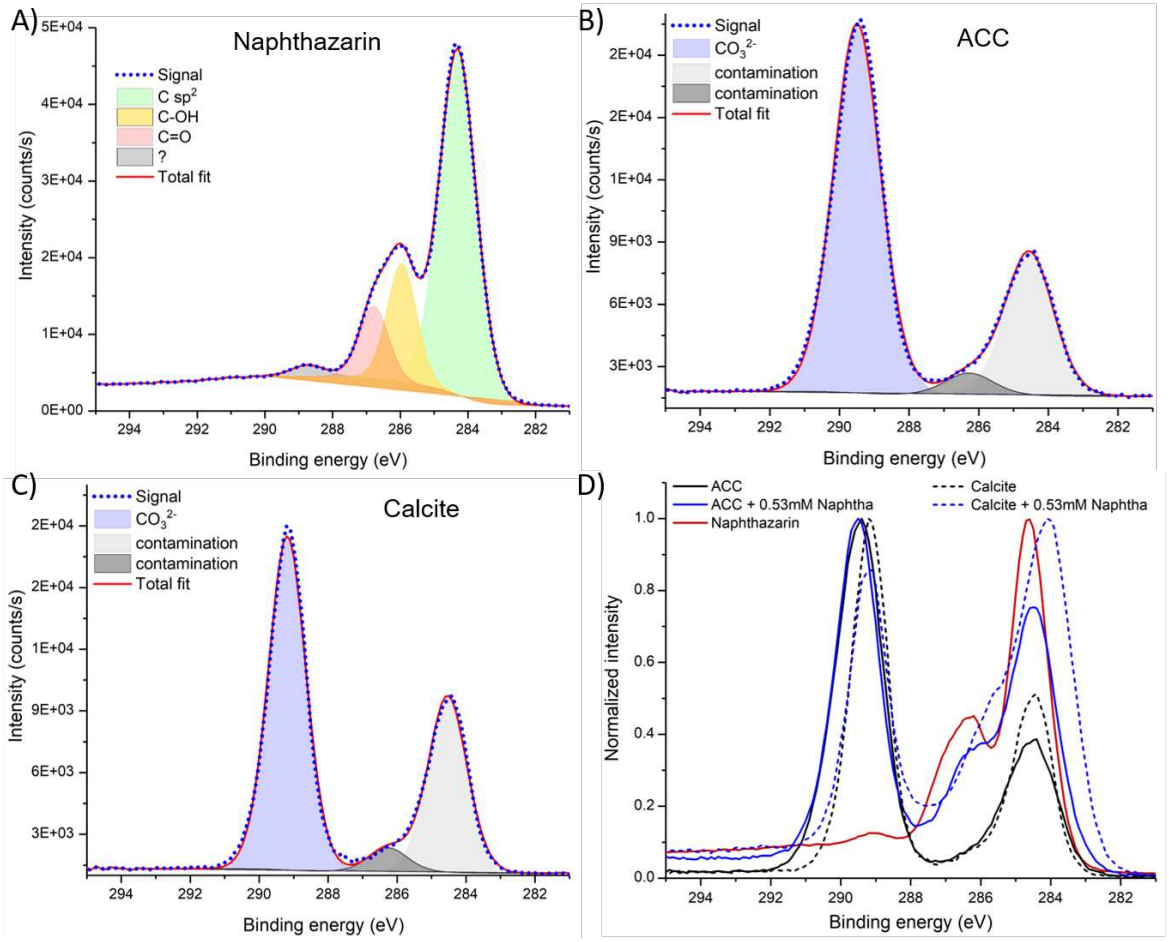

Fig. SI6. X-ray photoemission spectra for carbon, C 1s, and fitted components (CO_3^{2-}, C sp^2, C-OH and C=O) of A) pure naphthazarin, B) ACC and C) Calcite. D) comparison of the different spectra.

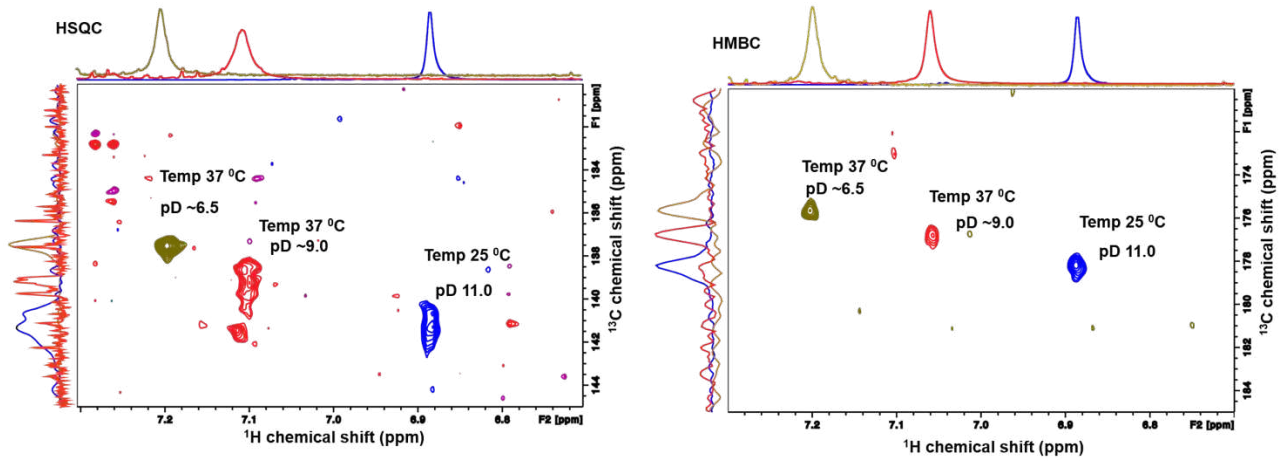

Fig. SI7. Cryo-sonde NMR measurements in solution of naphthazarin solution prepared at pD 6.5, 9 and 11. HSQC and HMBC maps at 25°C and 37 °C to increase naphthazarin solubility.